IMPORTANCE OF MANGANESE OXIDES IN CARBON REMINERALIZATION IN RIVER-DOMINATED CONTINENTAL MARGINS AND THE BIOGEOCHEMICAL CYCLING OF ARSENIC

A Dissertation
Presented to
The Academic Faculty

by

Shannon Marie Owings

In Partial Fulfillment
of the Requirements for the Degree
Doctor of Philosophy in the
School of Earth and Atmospheric Sciences

Georgia Institute of Technology
[May 2020]

IMPORTANCE OF MANGANESE OXIDES IN CARBON

REMINERALIZATION IN RIVER-DOMINATED CONTINENTAL MARGINS

AND THE BIOGEOCHEMICAL CYCLING OF ARSENIC

Approved by:

Dr. Martial Taillefert, Advisor
School of Earth and Atmospheric Sciences
Georgia Institute of Technology

Dr. George W. Luther, III
School of Marine Science and Policy
University of Delaware

Dr. Thomas DiChristina
School of Biological Sciences
Georgia Institute of Technology

Dr. Christophe Rabouille
Laboratoire des Sciences du Climat et de l'Environnement, LSCE/IPSL
CEA-CNRS-UVSQ-Université de Paris
Gif-sur-Yvette, France

Dr. Yuanzhi Tang
School of Earth and Atmospheric Sciences
Georgia Institute of Technology

Dr. Frank Stewart
School of Biological Sciences
Georgia Institute of Technology

Date Approved: [February 27, 2020]

[To the fellow chemists in my family,

especially my grandfather, Dr. George A. Ward, III]

ACKNOWLEDGEMENTS

I would first like to thank my thesis advisor, Martial Taillefert. Thank you for all the opportunities to expand my skills beyond the lab including field expeditions and networking opportunities. There were tough times involved in troubleshooting instruments, rough seas, long days of analysis and multiple rounds of edits on manuscripts, but I'm appreciative how each difficulty was a chance to learn new lessons and improve. Thank you for letting me explore my interest in teaching and allowing me to TA for multiple courses in the department to gain experience although it may have pulled me away from the lab. I have learned valuable skills involved in research as well as communication and mentoring that will benefit my future career endeavors.

I would like to thank Dr. Don Nuzzio for the research presentation he gave during my freshman seminar at the University of Delaware. After his presentation I reached out to Dr. George Luther whom graciously allowed me to start undergrad research in his lab. I attribute my scientific career in geochemistry starting with Dr. Nuzzio's talk and the opportunities and mentorship I received during my undergraduate research with Dr. Luther. Now, 10 years later, I have utilized Dr. Nuzzio's technology for my thesis research and have continued to consult with Dr. Luther regarding his expertise in inorganic chemistry. It is an honor to have Dr. Luther on my thesis committee. I would like to thank Dr. Thomas DiChristina for sharing his expertise in microbiology and enthusiasm for pairing geochemical and microbiology techniques to solve important environmental questions. I would like to thank Dr. Yuanzhi Tang for introducing me to the important topics in her mineral surface geochemistry course, which was foundational for each of my research

projects. I would like to thank Dr. Frank Stewart for the opportunity to participate in my first research cruise in the Gulf of Mexico which lead to a fruitful and insightful collaboration to link sediment geochemistry and microbiology. I would like to thank Dr. Christophe Rabouille for the productive stay at LSCE during my Chateaubriand Fellowship, I appreciate the conversations regarding the Gulf of Mexico data, and I am additionally thankful for all the extra efforts you implemented to ease my stay including the administrative assistance, translations and especially the wine and cheese lunches. I would also like my colleagues at LSCE for making my stay in France scientifically and culturally successful: Laurie Bréthous, Bruno Bombled, Bruno Lansard, and Eric Viollier.

I would also like to thank all of my current and past lab mates for sharing their knowledge in analytical techniques as well as support throughout the ups and downs of grad school, especially my friend Emily Saad. I couldn't have gotten started without the patience and expertise of Eryn Eitel and Keaton Belli, and I've enjoyed working together with Joel Craig, Jordon Beckler, Nan Xie, Ben Fields, and Tony Boever. Additionally, I would like to thank all the past and current members and leaders of the Graduate Women's group at the counseling center for their support, encouragement and comradery.

Finally, I would like to thank my family. Words cannot do justice for the gratefulness I feel for all the ways you've provided support from phone calls, visits, holidays, family dinners and helping me move from apartment to apartment. Thank you for being along for the ride of grad school and all the support you have provided in so many ways!

TABLE OF CONTENTS

LIST OF TABLES

LIST OF FIGURES

LIST OF SYMBOLS AND ABBREVIATIONS

AVS	Acid volatile sulfide
BMO	Biogenic manganese oxides
CFU	Colony forming units
CTD	Conductivity, Temperature, Depth
DMA	dimethylarsinate
DOU	Dissolved oxygen uptake
ESS	Effective surface sites
FeRB	Iron reducing bacteria
GOM	Gulf of Mexico
HFO	Hydrous ferrous oxides
HMDE	Hanging Mercury Drop Electrode
HMO	Hydrous mangansese oxides
HPLC	High Performance Liquid Chromatography
ICP-MS	Inductively Coupled Plasma- Mass Spectroscopy
LCS	Louisiana Continental Shelf
MCL	Markov clustering method
MDL	Minimum Detection Limit
MMA	monomethylarsonate
nGoM	northern Gulf of Mexico
OPD	Oxygen Penetration Depth
PEEK	PolyEtherEtherKetone

pHpzc	point of zero charge pH
RiOMars	Riverine-dominated ocean margins
ROS	Reactive Oxygen Species
SOB	Sulfide oxidizing bacteria
SRB	Sulfate reducing bacteria
SSA	Specific Surface Area
SWI	Sediment-Water Interface
TA	Total Alkalinity
US	United States
XRD	X-ray diffraction

SUMMARY

Manganese oxides (MnO_2) are ubiquitous in the environment and play an important role in the transformation and transport of contaminants in the environment and the biogeochemical cycling of carbon. This study investigated both aspects of these roles using a combination of laboratory experiments and field work. First, the kinetics of oxidation of the more toxic arsenic form, arsenite (As(III)), to the less mobile form, arsenate (As(V)), by MnO_2 was determined and compared to literature data to investigate the mechanism of the reaction. Subsequently, the effect of low As(V) concentrations on the anaerobic microbial respiration of MnO_2 and iron oxides, $Fe(OH)_3$, were investigated to shed light into the mechanism of As(V) toxicity in aquatic environments. At low As(V) concentrations, microbial reduction rates were increased compared to arsenic-free treatments suggesting As(V) at low concentrations stimulates metal reduction (MnO_2, $Fe(OH)_3$) in sediments as a result of a catalytic cycle in which arsenic is constantly reduced via microbial detoxification and re-oxidized by MnO_2. The cumulative findings from this study suggest that arsenic is not simply immobilized in sediments and that a suite of complex abiotic and microbial processes including adsorption, intracellular transport, and redox reactions may affect the transport of arsenic in the environment, and ultimately the quality of drinking water resources.

In parallel, manganese cycling, and the dominant redox pathways involved in carbon remineralization processes were characterized in marine sediments across the Louisiana shelf and slope that are exposed to mineral and terrestrial organic inputs from the Mississippi River. Although sulfate reduction dominates on the continental shelf,

denitrification and microbial manganese reduction appear equally significant anaerobic respiration processes along the continental slope the closest to the Mississippi River. This study emphasizes how the differential oxidation kinetics of Mn^{2+} (slow) and Fe^{2+} (fast) as well as sediment transport processes influence the main pathways of carbon degradation in these regions. Overall this thesis emphasizes the importance of characterizing the fundamental molecular processes of complex systems to better understand large scale global biogeochemical cycles.

CHAPTER 1. INTRODUCTION

1.1 Manganese in the environment

Manganese (Mn) is an essential component of many chemical and biological processes. Mn(II/III/IV) are found in photosystem II of photosynthetic organisms and Mn(III) is important in bacterially mediated decomposition of organic matter (Trouwborst et. al. 2006). In aqueous environments Mn(II) is stable to oxidation by O_2 at pH values below 8 (Morgan, 2005; Stumm and Morgan, 1996) though heterogenous oxidation via iron, silica and aluminum oxides enhance the oxidation compared to the rate solely with O_2 (Davies and Morgan, 1989). In turn, the microbial oxidation of Mn(II) proceeds more rapidly by fungi and bacteria utilizing multi-copper oxidases (MCO), therefore most manganese oxides in the environment are considered to be biogenic (Spiro et al., 2010; Tebo et al., 2004). Furthermore, bacterially-produced reactive oxide species (ROS) catalyze the oxidation of Mn(II) (Learman et al., 2011). In addition to Mn(II), Mn(III) is an important one electron transfer redox species which can act as either a reductant or an oxidant (Trouwborst et al., 2006). Reduction of Mn(IV) to Mn(II) and oxidation of Mn(II) to Mn(IV) involving two one-electron transfer steps which involve the formation of Mn(III) as an intermediate, is more thermodynamically favorably than a one-step two-electron transfer reaction (Luther, 2005, 2010). Previously, Mn(III) was considered negligible in water because the fast disproportionation of its free hydrated ion to Mn(II) and MnO_2. However, recent studies have uncovered Mn(III) as an important component and potential player to facilitate electron transfer reactions in aqueous marine environments, (Dellwig et al., 2012; Jones et al., 2019; Oldham et al., 2017; Oldham et

al., 2015; Trouwborst et al., 2006). Mn(III) is potentially ubiquitous in sediment if stabilized by ligands (Luther et al., 2018; Madison et al., 2011a; Madison et al., 2013; Oldham et al., 2019). Indeed, production of Mn(III) as an intermediate via bacterial oxidation of Mn(II) to Mn(IV) (Webb et al., 2005) and bio-reduction of Mn(IV) to Mn(II) (Lin et. al. , 2012) have been demonstrated.

Manganese oxides in the environment are ubiquitous and consist mainly of birnessite, δ-MnO_2, and manganite, MnOOH (Turekian and Wedepohl, 1961). The point of zero charge pH (pH_{pzc}) of these Mn(IV) oxides range from 1.85 to 3.1 (Jones et al., 2012; Morgan and Stumm, 1964; Murray, 1973; Scott and Morgan, 1995; Yao and Millero, 1993), indicating that the surface of Mn(IV) oxides are overall negative at the circumneutral pH of most aquatic systems (pK_{a1}=-1.6 and pK_{a2}=4.6; Yao & Millero, 1993; Yao and Millero 1996; Catts and Langmuir 1986). Manganese oxides are important scavengers of inorganic contaminants including lead, arsenic, cadmium, and others (Tebo et al., 2004). In addition, manganese oxides are oxidants of many environmental organic contaminants including phenols, pharmaceuticals, pesticides, etc. (Remucal and Ginder-Vogel, 2014). Furthermore, manganese oxides serve as efficient oxidants of biogeochemically important elements (i.e. Fe(II), ΣH_2S) in the environment (Siebecker et al., 2015; Yao and Millero, 1993).

1.2 Sedimentary redox reaction including thermodynamically favorable electron acceptors coupled to carbon remineralization

Sediment diagenetic processes are important players in the global carbon cycle as they control the remineralization and, thus, preservation of natural organic matter. The

series of consumption of the electron acceptors the terminal acceptor proceeds via oxygen (O_2), nitrate (NO_3^-), manganese oxides (MnO_2), iron oxides ($Fe(OH)_3$), sulfate (SO_4^{2-}) and methane (CH_4), ordered by decreasing energy production per mole of organic carbon oxidized (Froelich et al., 1979). MnO_2, $Fe(OH)_3$, and SO_4^{2-} become the main reduction pathways of organic matter degradation in the absence of oxygen in early diagenesis in anoxic sediments (natural organic matter based on the Redfield ratio where the C:N ratio is represented by coefficients x:y) (Eqs.1-1,1-2,1-3).

$$(CH_2O)_x(NH_3)_y(H_3PO_4) + 4xFe(OH)_{3(s)} + (7x + y - 2)H^+ \rightarrow 4xFe^{2+} + xHCO_3^- + yNH_4^+ + HPO_4^{2-} + 10xH_2O \quad (1\text{-}1)$$

$$(CH_2O)_x(NH_3)_y(H_3PO_4) + 2xMnO_{2(s)} + (3x + y - 2)H^+ \rightarrow 2xMn^{2+} + xHCO_3^- + yNH_4^+ + HPO_4^{2-} + 2xH_2O \quad (1\text{-}2)$$

$$2(CH_2O)_x(NH_3)_y(H_3PO_4) + xSO_4^{2-} \rightarrow xHS^- + 2xHCO_3^- + 2yNH_4^+ + 2HPO_4^{2-} + (x - 2y + 4)H^+ \quad (1\text{-}3)$$

Due to high sulfate concentrations in seawater, sulfate reduction has been observed to play a large role in marine sediments (Bowles et al., 2014; Ferdelman et al., 1999; Jørgensen, 1982; Lee et al., 2008; Lin et al., 2002). However, evidence has increasingly suggested the role of Mn and Fe cycling in sediments may have been previously underestimated in continental margins and constitutes a large percentage of the carbon oxidation pathways (Aller et al., 1990; Beckler et al., 2016; Canfield et al., 1993a; Canfield et al., 1993b; Devereux et al., 2015; Hyun et al., 2017; Law et al., 2009; Oldham et al., 2019; Sørensen and Jeørgensen, 1987; Thamdrup et al., 2000). As one mole of SO_4^{2-} can

oxidize two moles of carbon (Eq. 1-3), carbon remineralization via dissimilatory sulfate reduction processes more carbon than via dissimilatory iron and manganese reduction (Eqs. 1-1,1-2,1-3). Due to the varying efficiencies of anaerobic carbon remineralization and their potential impacts on CO_2 production, it is important to identify which terminal electron accepting process dominates under different water column redox regimes. However, it is difficult to identify the main biotic reactions solely by following the production of reduced metabolites due to the simultaneous occurrence of ancillary abiotic and biotic reactions (Beckler et al., 2016). For example, dissolved sulfide (HS^-) reduce iron oxides (Eq.1-5, (Pyzik and Sommer, 1981; Yao and Millero, 1996b)) and manganese oxides (Eq.1-6, (Herszage and dos Santos Afonso, 2003; Yao and Millero, 1993)) and precipitate with Fe(II) to form FeS and ultimately pyrite (Eq. 1-6,1-7), (Theberge and Luther, 1997)). The reduction of manganese oxides by Fe(II) (Eq. 1-8, (Postma, 1985; Postma and Appelo, 2000; Siebecker et al., 2015)), ammonium (Bartlett et al., 2008; Hulth et al., 1999; Javanaud et al., 2011), or nitrite (Luther and Popp, 2002) is also possible. Furthermore, metals are trapped by adsorption onto solid phase minerals (van der Zee et al., 2001) or re-oxidized by oxygen microbially (Hedrich et al., 2011; Tebo et al., 2004) or abiotically (Millero et al., 1987; Morgan, 2005; Sundby and Silverberg, 1985) upon diffusion to the aerobic zone. Finally, reduced metals can precipitate as mixed Mn-Ca-CO_3 and $FeCO_3$ phases (Jakobsen and Postma, 1989; Mucci, 2004; Suess, 1979).

$$2Fe(OH)_3 + HS^- + 5H^+ \rightarrow 2\,Fe^{2+} + \,S^0 + 6\,H_2O \qquad 1\text{-}4$$

$$MnO_2 + HS^- + 3H^+ \rightarrow Mn^{2+} + S^0 + 2H_2O \qquad 1\text{-}5$$

$$HS^- + Fe^{2+} \leftrightarrow \,FeS_{aq} + H^+ \,\rightarrow \,FeS_{am} \qquad 1\text{-}6$$

$$FeS_{am} + H_2S \rightarrow FeS_2 + H_2 \quad \text{1-7}$$

$$\delta MnO_2 + 2Fe^{2+} + 4H_2O \rightarrow Mn^{2+} + 2Fe(OH)_3 + 2H^+ \quad \text{1-8}$$

1.3 River dominated continental margins

Riverine-dominated ocean margins (RiOMars) represent carbon remineralization hot spots as a result of the significant input of natural organic matter and inorganic particulate material from terrestrial origin (Bianchi et al., 2018). In addition, the nutrient supply from the underlying sediment (Aller et al., 1996; Grégoire and Friedrich, 2004; Morse and Rowe, 1999) or riverine inputs (Turner et al., 2007) promotes primary production on continental shelves that may enhance the overall input of natural organic matter to the seafloor (Aller et al., 1996; Waterson and Canuel, 2008) and increase diagenetic reactivity by a priming effect (Bianchi, 2011). The supply of organic matter and lithogenic material to continental shelves depends on the intensity of riverine discharge, which typically varies seasonally (Bianchi et al., 2007; Mossa, 1996). At low discharge, the density difference between freshwater and seawater impedes the seaward transport of freshwater and its particulate load such that freshwater and sediment are both trapped in the estuary or backwater reach of rivers (Allison et al., 2012; Geyer et al., 2004). In contrast, the momentum of the river outflow at high discharge is strong enough to overcome this effect and export water and sediment offshore. As a result, sediment trapped in estuaries or backwater reach during low discharge seasons is biogeochemically processed until the next high discharge, such that the inorganic (Allison and Pratt, 2017; Meiggs and Taillefert, 2011; Sutula et al., 2004) and organic (Cowie and Hedges, 1984, 1992; Sampere et al., 2011) content of surrounding shelf sediments is seasonally altered.

In turn, the lithologic input to continental shelves is greater during high discharge as a result of increased weathering upstream (Meiggs and Taillefert, 2011). Riverine dissolved and particulate material eventually delivered to the ocean flocculates and aggregates into fine-grained material that settles into the benthic boundary layer (BBL) 0.1-2 m above the seabed and forms mobile muds, an ephemeral layer that is often remobilized by physical mixing generated by tidal currents or storms (Aller, 1982, 1998; McKee et al., 2004). These mobile muds are eventually deposited on continental shelves and slopes, with selective dispersal that depends on particle size, density, morphology, or composition (McKee et al., 2004), and enhance carbon remineralization by exposing sediment to oxygenated bottom waters (Aller, 1998; Blair and Aller, 2012; Hartnett et al., 1998) and co-metabolizing fresh, planktonic organic carbon (Canfield, 1994). As a result, sediment distribution across continental margins and their associated diagenetic processes may vary widely depending on the organic carbon and lithologic composition of the top sediment layers (Canfield, 1994; Grégoire and Friedrich, 2004; Taillefert et al., 2017).

The complex interplay between abiotic and biotic processes influences the availability of electron acceptors and efficiency of carbon remineralization processes. After aerobic respiration, sulfate reduction often plays a large role in marine sediments exposed to significant inputs of natural organic matter (Bowles et al., 2014; Ferdelman et al., 1999; Jørgensen, 1982; Lee et al., 2008; Lin et al., 2002) mainly due to the high concentration of sulfate in seawater and the efficient carbon remineralization yield of this process (i.e., 2 mole of carbon per mole of sulfate reduced). In RiOMars and shelf to slope transition zones of passive continental margins, however, manganese (Mn) and iron (Fe) reduction may contribute to a large fraction of carbon remineralization processes (Aller et al., 1990;

Beckler et al., 2016; Canfield et al., 1993a; Canfield et al., 1993b; Devereux et al., 2015; Hyun et al., 2017; Law et al., 2009; Oldham et al., 2019; Sørensen and Jeørgensen, 1987; Thamdrup et al., 2000). The differential kinetics of manganese and iron transformations also separates Mn^{2+} and Fe^{2+} vertically in the sediment column, as microbial Mn(III/IV) oxide reduction is thermodynamically more favorable and much faster than microbial Fe(III) reduction (Arnold et al., 1988; Dollhopf et al., 2000; Larsen et al., 1998; Lovley and Phillips, 1988; Myers and Nealson, 1988) and abiotic Mn^{2+} oxidation is much slower than Fe^{2+} oxidation (Stumm and Morgan, 1996). As a result, Mn^{2+} diffuses out of the sediment and is slowly reoxidized either close to the sediment surface (Mouret et al., 2009) or in the overlying waters (Trefry and Presley, 1982), whereas Fe^{2+} is oxidized immediately at the oxic-anoxic transition (Millero et al., 1987). Simultaneously, Fe^{2+} is less mobile in comparison to Mn^{2+} due to rapid precipitation with H_2S (Pyzik and Sommer, 1981). Mn(III, IV) oxides are therefore dispersed and redeposited in surface sediments where they become important electron acceptors for organic carbon oxidation (Hyun et al., 2017; Law et al., 2009), whereas Fe(III) oxides are typically immobilized below the oxygen penetration depth in the sediment. Differentiating these processes in RiOMar sediments may help quantify anaerobic carbon remineralization processes more accurately.

The Gulf of Mexico is a unique region to study diagenetic processes in deep sediments because the transport of materials from the Mississippi Atchafalaya River System (MARS) provides fuel for carbon remineralization processes. The plume of the Mississippi River extends from its outlet at the ‘bird foot’ of Louisiana westward across the shelf. The Mississippi River drains ~47% of the US and provides ~65% of suspended solids and dissolved solutes that enter the oceans from the US (Dagg et al., 2004).

Additionally, the Atchafalaya River provides approximately 30% of the input into the Gulf of Mexico (Turner et al., 2007). The northern Gulf of Mexico receives 230 million tons of sediment per year (Meade and Parker 1985) and an annual mass load of 7.38 $x10^7$ tons of metals (Reiman et al., 2018) from the MARS. The input of inorganic and organic materials, nutrients, and metals to the northern Gulf of Mexico via the MARS induces seasonal hypoxia (<63 µM oxygen) in this region (Rabalais et al., 2007). However, the transport of material extends beyond the hypoxic region and can be transferred to the nearby Mississippi slope and canyon (Bianchi et al., 2006) via lateral down-slope accretion of material from the margins and or mass wasting (Rowe et al., 2008).

1.4 Arsenic in the environment

Modern crustal material consists of only 0.0005% arsenic, making it the 20th most abundant element (Ballantyne and Moore, 1987). Arsenic is most commonly associated with sulfide, in arsenopyrite minerals, but can also be found in high concentrations in shales and at smaller concentrations in different mineral types including sedimentary, igneous, sandstone and limestone (Gomez-Caminero et al., 2001). Naturally occurring arsenic in minerals is prevalent around the world especially in regions such as India, Taiwan and Bangladesh, where As in drinking water from natural sources poisons millions of people (Nordstrom, 2002; Smith et al., 2000b). To a lesser extent, As occurs in ground water in the US as a result of the reaction of iron oxides with organic carbon which releases As adsorbed to the surface (Welch et al., 2000). Few systems exist that naturally contain millimolar levels of arsenic, for example the hypersaline and alkaline Mono Lake in California, an environmental extreme. Background arsenic levels range around 133nM in pristine rivers and lakes, 13-30 nM in groundwater, 0.1-40 mM kg^{-1} in sediments, and 0.1

mM kg^{-1} in soils (Gomez-Caminero et al., 2001). Higher concentrations are found in areas near anthropogenic pollution or geological sources. Anthropogenic sources of As include herbicidal agents, anti-microbial agent in chicken feed, smelter by-products, coal fly ashes, runoff from mine tailings, hide tanning waste, paints and dyes, and pressure-treated wood (Bode and Dong, 2002; Christen, 2001; Mukhopadhyay et al., 2002; Oremland and Stolz, 2003).

1.5 Arsenic Speciation in Solution, at Mineral-Water Interfaces, and Redox Transformations

The oxidation states of arsenic include As(III), As(V), As(0) and As(-III). Arsenite, As(III), and arsenate, As(V) represent the most common forms, whereas elemental arsenic, As(0), and arsines, As(-III) are rare (Cotton et al., 1999). The acid-base chemistry of arsenic is important as it affects its reactivity with mineral and natural organic matter ((Dixit and Hering, 2003; Mikutta and Kretzschmar, 2011; Redman et al., 2002; Thanabalasingam and Pickering, 1986b). The pK_a's of H_3AsO_4 are 2.24, 6.76, and 11.6, whereas the pK_a's of H_3AsO_3 are 9.2, 12.1, and 13.41 (Stumm and Morgan, 1996). Therefore, in the majority of circumneutral pH aquatic environments $H_2AsO_4^-$, $HAsO_4^{2-}$, and H_3AsO_3 are the most commonly found species. Given its neutral charge, As(III) represents the more hydrologically mobile form of arsenic, whereas the anions of As(V) readily adsorb to mineral surfaces such as clays and Fe(III) (pHpzc=7-9 (Pedersen et al., 2006), Al(III), and Mn(IV/III) (pHpzc=2-4) oxides and, consequently, is less mobile (Amirbahman et al., 2006; Arai et al., 2001; Raven et al., 1998). Arsenite does not adsorb easily to mineral surfaces and is therefore less mobile (Smedley and Kinniburgh, 2002; Tufano et al., 2008). Considering amorphous iron oxides and goethite, As(V) adsorption is

greater than As(III) below pH 5-6, but above pH 7-8 As(III) has a higher adsorption affinity (Dixit and Hering, 2003).

In parallel with bacterial processing of arsenic, chemical transformations influence the speciation of arsenic. In reducing environments, mackinawite (FeS) and dissolved sulfides reduce arsenate to arsenic sulfide minerals or thioarsenite species (Troyer et al., 2014; Wilkin et al., 2003). The rate of abiotic As(III) oxidation by dissolved oxygen is slow, with a half-life of up to 1-3 years (Eary and Schramke, 1990) (Eq. 1-9).

$$H_3AsO_3 + 2O_2 \rightarrow H_2AsO_4^- + H^+ \quad (\Delta G = -80.9) \qquad 1\text{-}9$$

Conversely, arsenite oxidation by Fe(III) oxyhydroxides proceeds faster compared to dissolved O_2(Amstaetter et al., 2010), however, the reaction is much faster with MnO_2 (Owings et al., 2019).. Overall, manganese oxides are important environmental oxidants of arsenite and contain a surface with a high affinity for arsenate adsorption and these processes are studied intensively. Due to the overall negative surface of manganese oxides in environmental settings, arsenite, H_3AsO_3, is less likely to adsorb on manganese oxides surfaces than arsenate, $HAsO_4^{2-}$, but arsenite oxidation proceeds rapidly on the surface of manganese oxides followed by the adsorption of arsenate. The overall reaction is written (Eq.1-10) (Scott and Morgan, 1995)

$$MnO_2 + H_3AsO_3 + 2H^+ \rightarrow Mn^{2+} + H_3AsO_4 + H_2O \qquad 1\text{-}10$$

One proposed mechanism of the interaction between birnessite and arsenite involves the formation of an Mn(III)-oxyhydroxide intermediate during a two-step reductive dissolution reaction (Nesbitt et al., 1998). The first step includes the reduction of Mn(IV) to Mn(III) by splitting the two electrons of As(III) to reduce two Mn(IV) atoms

(Eq 1-11), followed by another reduction step involving another H_3AsO_3 molecule to reduce the two MnOOH intermediate species (Eq 1-12).

$$2Mn^{IV}O_2 + H_3AsO_3 \rightarrow 2Mn^{III}OOH + H_3AsO_4 \quad 1\text{-}11$$

$$2MnOOH + H_3AsO_3 = 2MnO + H_3AsO_4 + H_2O \quad 1\text{-}12$$

Subsequently, one electron reduction of Mn(III) to MnO and Mn(II) which is released into solution. Mn(III) formation on the surface due to Mn(IV) oxidation of As(III) was not found previously (Lafferty et al., 2010b), but the formation of Mn(III) was was determined to be the result of conproportionation of sorbed Mn(II) to Mn(IV) (Eq 1-13). Over time, as the reaction proceeds, it appeared that more Mn(III) ions occupied the surface of the MnO_2. This observation leads to the conclusion the oxidation takes place via one 2-electron transfer with no formation of an Mn(III) intermediate (Lafferty et al., 2010b). An alternative suggestion indicates that the reactiontakes place via a ligand exchange between As(III) and the manganese oxide surface group (Amirbahman et al., 2006)

$$> Mn^{IV} - OH + Mn^{II}(aq) + H_2O + H^+ \rightarrow 2(> Mn^{III} - OH_2) \quad 1\text{-}13$$

The reduction product Mn(II) and oxidation product As(V) represent the main species competing for vacancy sites on the surface of the manganese oxides (Lafferty et al., 2011). Mn(II) preferentially binds to vacancy sites while both species will bind to Mn(III) if the ion is available at the surface (Lafferty et al., 2010a; Manceau et al., 2002). These species passivate the manganese oxide surface, decreasing the available sites for rapid arsenite oxidation. The structure of the adsorption complex between arsenate and the manganese oxide is assumed to be bidendate binuclear, double corner sharing polyhedral, at the edges and interlayers of the MnO_2 solid where the oxidation state of Mn in the

complex is assumed to be Mn(IV) (Manning et al., 2002). Although, evidence exists of a monodentate mononucluear complex which occurs more commonly after 4 hours of reaction (Lafferty et al., 2010b), at six hours or greater Mn(II) at edge reacts with Mn(III), which adsorbs As(V) and increases As-Mn bond length.

Rates of arsenite oxidation by manganese oxides vary significantly. The fastest rate published observes 50% of the reaction occurs within the first minute (Parikh et al., 2008), while other studies report the reaction progresses over multiple hours (Villalobos et al., 2013). The disagreement of reaction mechanism and published rates indicate the kinetics of the reaction need to be better constrained. The reaction (Eq. 1-10) is assumed to be pseudo first order, and the overall rate equation assumes first order with respect to H_3AsO_3, MnO_2 and proton concentration, $[H^+]$ (Eq 1-14).

$$MnO_2 + H_3As^{III}O_3 + H^+ \rightarrow Mn^{2+} + H_2As^{V}O_4^- + H_2O \quad \text{1-10}$$

$$Rate = k * [MnO_2]^1 * [As(III)]^1 * [H^+]^1 \quad \text{1-14}$$

Interestingly, these assumptions have not been verified experimentally. In addition, the pH typically remains constant or is only varied between low and high values. Trends cannot be explained mechanistically when only two pH values are studied. Furthermore, literature lacks kinetic studies, the first few minutes of reaction is where the majority of the oxidation takes place, but few studies have appropriate time resolution to follow the reaction products appropriately. Overall, a comprehensive kinetic study of the manganese oxide/arsenite/arsenate system is needed over a pH range 4-8,

1.6 Cellular Arsenic Uptake and Toxicity

Arsenate is isoelectronic to the phosphate molecule and, consequently, inhibits oxidative phosphorylation. The arsenate anion, $H_2AsO_4^-$, chemically resembles phosphate, $H_2PO_4^-$, with the main atom bound by four oxygens in a tetrahedral arrangement. The similarity of the two anions allows arsenate to enter cells via phosphate transporters (Willsky and Malamy, 1980b). The two main inorganic phosphate (Pi) transport systems present in bacterial cells includes the high affinity phosphate specific transporter, Pst, and the low affinity inorganic phosphate transporter, Pit, systems (Willsky and Malamy, 1980a). The *phoS* and *phoT* genes that are part of the *pho* operon in the Pst transport system are involved in the regulation and synthesis of the phosphatase (in low Pi conditions) (Willsky and Malamy, 1980a). The Pit system is a low affinity-high velocity system which favors arsenate uptake into the cell (Willsky and Malamy, 1980b). As(III) is proposed to enter prokaryotic cells via the glycerol facilitator, GlpF, in a similar fashion as the trivalent antimonite, Sb_2O_3, which was recognized as a polyol in *E. Coli* (Sanders et al., 1997) and in yeast arsenite entered through glycerol channel (Wysocki et al., 2001). Arsenite, $As(OH)_3$, toxicity derives from the fact arsenite resembles glycerol, a simple sugar also known as polyol, and enters cells via aqua-glyceroporins that regulate the entrance or exit of glycerol through the plasma membrane. Once in the cell, arsenite binds to sulfhydryl groups which are found in many proteins and therefore disrupts enzyme functions.

1.6.1 Arsenic Detoxification

Once inorganic arsenic enters the bacterial cell different detoxification pathways are available. First, As(V) can be removed from the cell by methylation, a process

that is well understood for fungi and eukaryotes, but not absolute in the prokaryotic world (Stolz et al., 2006). Methylation for eukaryotes is proposed to involve a series of steps involving the reduction of arsenate and the oxidative addition of a methyl group (via S-adenosylmethionine methyltransferases aka SAM) to lead to methyl arsenite, dimethyl arsenate, dimethyl arsenite, and trimethyl arsine oxide (Challenger, 1945). This pathway is also proposed for bacteria, although arsine, Me_xAsH_{3-x} (where x=0-2), represents the most commonly formed product (Bentley and Chasteen, 2002). In addition to the Challenger mechanism, it has been proposed that instead of the oxidation of As(III), glutathione (GSH) is oxidized by SAM during the methylation process (Ajees and Rosen, 2015; Hayakawa et al., 2005). Prokaryotic *arsM* gene expression is regulated by the As(III)-responsive transcriptional repressor ArsR, which is a component of the As detoxification pathway. Four conserved cysteine residues in ArsM (including two N-terminal cysteine residues CysA and CysB) are required for As(III) (but not MMA methylation (Dheeman et al., 2014; Marapakala et al., 2015). Two C-terminal cysteine residues (CysC and CysD) bind As(III) and are required for ArsM activity (Dheeman et al., 2014). In addition to ArsM-catalyzed methylation of As(III), MMA is synthesized via reduction of monosodium methylarsenate, which is widely applied as a herbicide with toxic and carcinogenic properties (Chen et al., 2015b). Additional bacterial enzymes for MMA detoxification include the C-As bond lyase ArsI (a member of the dioxygenase superfamily that cleaves MMA to As(III) and formaldehyde (Yoshinaga and Rosen, 2014)), NADPH/FMN-dependent oxidoreductase ArsH (oxidizes MMA to MAs(V) (Chen et al., 2015a)), and MMA efflux permease ArsP (exports MMA and Roxarsone, a pentavalent aromatic arsenical species from *Campylobacter jejuni* and *Shewanella putrefaciens* (Chen et al., 2015b; Chen and Rosen,

2016)).The better understood detoxification mechanism involves the reduction of As(V) to As(III) followed by As(III) expulsion from the cell. The first reduction step is performed by the arsenate reductase ArsC, an enzymatic cytoplasmic protein encoded by the *arsC* gene (Ji and Silver, 1992). A bacterial cell removes the reduction product, As(III), from the interior using the repressor protein, ArsR, and membrane bound structural proteins ArsA and ArsB. The cell is most efficient at removing As(III), when ArsA and ArsB are coexpressed as ArsAB and create an oxyanion translocating ATPase (Rosen et al., 1995; Rosen, 2002). The amino acid sequences of the *ars*C and *ars*B putative genes were identified in *Shewanella oneidensis* strain MR-1 and *S. putrefaciens* strain 200 but those of the *ars*A and *ars*D genes were only identified in *S. putrefaciens* strain 200 (Jiang et al., 2013).

In addition to the arsenate reduction enzyme, the arsenite oxidase enzyme, Aox, a molybdenum enzyme similar to the dimethylsulfoxide reductase family that consists of a large subunit with Mo and [3Fe-4S] clusters and a small subunit homologous to [2Fe-2S] proteins is sometimes used for detoxification (Ellis et al., 2001; Hoke et al., 2004). Interestingly, some heterotrophic arsenite oxidizers (HAOs) express similar enzymes (vanden Hoven and Santini, 2004).

1.6.2 Arsenic Respiration

A variety of prokaryotes gain energy during dissimilatory arsenate reduction using the respiratory arsenate reductase gene, *arr*. The Arr enzyme was characterized as a heterodimer with two subunits, ArrA and ArrB. The reductase is composed of molybdenum, iron, acid-labile sulfur and zinc, leading to the conclusion that ArrA is

similar to proteins consisting of cysteine clusters and ArrB is similar to iron-sulfur proteins (Krafft and Macy, 1998). Although it is surprising that bacteria would use 'toxic' chemicals to grow, the redox potential of the As(V)/As(III) is +135mV and heterotrophic arsenate reduction is thermodynamically favorable (Oremland and Stolz, 2003). *Shewanella* species strain ANA-3 couples lactate oxidation to the reduction of As(V) (Saltikov et al., 2003). The presence of *arr*A and *arr*B putative genes and respiration activity were also identified in *S. putrefaciens* strain 200 but not in *S. oneidensis* strain MR-1 (Jiang et al., 2013).

Interestingly, some species contain multiple arsenic respiratory genes that are activated independently depending on oxygen concentrations. For example, *Shewanella* species strain ANA-3 expresses *ars* in oxic and anoxic conditions, whereas the *arr* system is only expressed in anaerobic conditions (Saltikov et al., 2005). Additionally, a *Thermus* isolate has been observed to oxidize As(III) in aerobic conditions and subsequently grow in anaerobic conditions by coupling arsenate reduction to lactate oxidation (Gihring and Banfield, 2001). Genomes from arsenate respiring bacteria *Alkaliphilus oremlandii* and *Shewanella* sp. strain ANA-3 suggest Arr is reversible and can act either as a reductase or oxidase among (Richey et al., 2009). The presence of these bacteria in arsenic-rich environments may therefore impact the cycling of arsenic greatly in both aerobic and anaerobic conditions.

Prokaryotes are also able to utilize As(III) oxidation to gain energy. The rate of abiotic As(III) oxidation by dissolved oxygen is slow, although the redox process is thermodynamically favorable, which explains why bacteria would utilize this kinetically slow but thermodynamically favorable process (Eq. 1-9) (Cherry et al., 1979; Santini et al., 2000; Stumm and Morgan, 1996).

$$H_2AsO_3^- + NO_3^- \rightarrow HAsO_4^{2-} + NO_2^- + H^+ \ (\Delta G^0 = -56.5\ kJ/mol) \qquad 1\text{-}15$$

Nitrate reduction coupled to arsenite oxidation represents another thermodynamically favorable reaction for bacterial arsenite respiration (Eq.**Error! Reference source not found.**) (Oremland et al., 2002; Senn and Hemond, 2002). Although these processes are important to characterize for the design of efficient bioremediation strategies, little is known about the mechanisms involved in arsenite oxidation (Oremland and Stolz, 2003).

Respiration on As(III) was likely active before the Great Oxidation Event ((Sforna et al., 2014), and after oxygenation As(V) was likely introduced as an environmental toxin leading to the development of detoxification pathways discussed above. Arsenic pathways have been extensively studied in arsenic rich, extreme environments including Mono Lake, CA, and acid mine drainage (Fahy et al., 2015; Hoeft et al., 2002). However, recent metagenomic studies have found arsenic cycling genes in environmental settings with low arsenic concentrations, including oxygen deficient zones of the ocean (Saunders et al., 2019), and soil and rice rhizospheres (Jia et al., 2013). These findings suggest arsenic transformation genes may be more widespread than previously considered and are thus underestimated in current biogeochemical cycles.

1.7 Research objectives of this dissertation

The bacterial arsenic respiration processes from Mono Lake are intensively studied, yet a gap of knowledge exists on the effect of arsenic on the chemical and biological systems in natural aquatic environments with minute levels of arsenic. In these natural systems iron oxides, oxygen, and more importantly manganese oxides are the most efficient oxidants of arsenite. As a result, this study fills some gaps in this knowledge by

developing a rate law of arsenite by manganese oxides with respect to pH, MnO_2 and initial arsenite concentration.

The release of arsenite increases with the dissolution of ferrihydrite, due to the change of the mineral structure (Tufano and Fendorf, 2008; Tufano et al., 2008). Few studies have shown a link between microbial iron reduction and arsenic speciation (Senn and Hemond, 2002). Field and laboratory studies using Chattahoochee River sediments show small concentrations of arsenic (< 1 µM) increase rates of iron reduction by up to four fold and consequently release As(V) (Chow and Taillefert, 2005, 2009). This effect could be the consequence of bacteria using Fe oxides as an energy source to supplement energy lost from detoxifying As(III) which is oxidized abiotically on the Fe oxides. Leading to the hypothesis of this study that ***a catalytic cycle involving manganese oxides and microbial detoxification of arsenic may affect microbial respiration processes in sediments.***

In addition, this study investigated the main redox pathways prevalent in marine sediments along the northern Gulf of Mexico using voltammetric profiling, pore water analysis and solid phases extractions. Stations were selected along a transect influenced by the Mississippi River and another transect to the east of the Mississippi River plume to compare the changing redox environments in regions with contrasting nutrient and sediment loadings from the Mississippi River. ***The objective of this study is to identify if sulfate reduction is pervasive in marine sediments, or conversely if the supply of terrigeneous material supplied by the Mississippi River is sufficient to sustain metal reduction and outcompete sulfate reduction.*** Additionally, during the 2016 sampling campaign, metagenomics samples were collected with ***the goal to elucidate the***

geochemical and microbial processes responsible for the main carbon remineralization pathways in addition to abiotic processes in sediments in the Gulf of Mexico after a period of high riverine discharge.

1.8 Organization of this dissertation

Following this introduction this dissertation contains chapters exploring each objective identified throughout the introduction. Chapter 2 explains the analytical procedures utilized and details the methods utilized for field measurements and laboratory experiments. Chapter 3, published in *Geochimica et Cosmochimica Acta* (Owings et al., 2019), develops a rate law for the oxidation of arsenite by manganese oxides with respect to initial arsenite concentration, effective surface sites of manganese oxides, and pH. Tthis chapter also explores the likely electron transfer mechanism based on the experimental data.

Chapter 4 investigates the effect of As(V) concentrations on anaerobic electron acceptors by metal reducing bacteria. This chapter presents incubations with model metal-reducing microorganism *Shewanella* strains with varying arsenic resistances to reproduce the effects of As(V) on iron reduction observed in the field and expands this investigations with alternate terminal electron acceptor nitrate and manganese oxide.

Chapter 5 presents data on early sediment diagenesis on the Louisiana shelf and slope during seasonal hypoxia in 2016 using both geochemical and metagenomic approaches in collaboration with microbiologists at Georgia Tech. Studies with comprehensive data sets at high spatial resolution both on kilometer (across shelf) and millimeter (core depth) scales are rare. This chapter determines the main biogeochemical pathways along the northern

Gulf of Mexico sediments based on the chemical and microbial data collected. This chapter is in preparation to be submitted to Geomicrobiology.

Chapter 6, under review for Marine Chemistry (Owings et al., 2020), investigates the differential manganese and iron recycling and transport in continental margin sediments in the northern Gulf of Mexico. Similar to Chapter 5, sediments were analyzed for geochemical proxies after a high riverine discharge period from the Mississippi River. The existing sediment diagenetic model (MATSEDLAB) was used to quantify rates of microbial respiration. While many studies assume sulfate reduction is the main carbon remineralization pathway, this study took into account all important electron acceptors in order to accurately represent carbon oxidation pathways in these sediments. Chapter 6 also includes a synthesis of the geochemical observations across the Northern Gulf of Mexico during similar sampling times between 2016 (Chapter 5) and 2017 (Chapter 6) that will be synthesized in another manuscript submitted by colleagues from the Laboratoire des Sciences du Climat et de l'Environnement (CEA, CNRS, U. Versailles, Paris, France).

Chapter 7 provide a synthesis of the main findings of this thesis and the novel findings provided to the scientific community and concludes with recommendations for future work.

CHAPTER 2. ANALYTICAL TECHNIQUES

2.1 Voltammetry

Voltammetry is a comprehensive tool to measure a suite of redox active species with one measurement. A potential was applied to a sample (water/sediment) and current is measured. When an electron transfer occurs at the electrode, an increase in current occurs which corresponds to the number of electrons transferred. In order to apply potentials and measure current this study used a mercury-plated gold (Au/Hg) working electrode (Brendel and Luther, 1995; Luther et al., 2008) in a three-electrode system (Ag/AgCl reference, Pt counter, and Au/Hg working electrodes) coupled to a computer-controlled DLK 70 or 100 potentiostat from Analytical Instrument Systems, Inc. (AIS, Inc.). The working electrode was made of 100 µm diameter gold wire (GoodFellow Corp.) soldered to RG-50 coax cable encased in either PolyEtherEtherKetone tubing (PEEK electrodes) or in a 30 cm long pyrex glass tube pulled to a 5 cm long and ≤ 1 mm in diameter tip with marine epoxy (West System brand) as reported previously (microelectrodes) (Beckler et al., 2016; Brendel and Luther, 1995; Luther et al., 1999). The working electrodes were plated with Hg by applying a potential of -0.2 V for 4 minutes in a 0.1 M $Hg(NO_3)_2$ solution in 2% HNO_3, followed by a polarization step at -9 V for 90 s in 1 M NaOH to ensure amalgamation of the Hg to the Au wire (Brendel and Luther, 1995). Electrodes are tested in oxygen saturated solutions as well as calibrated with $MnCl_2$ (0-400 µM) in degassed seawater to ensure plating occurred correctly. PEEK working electrodes are durable and used for incubations, laboratory experiments or field measurements for water column work, whereas, glass microelectrodes

are minimally invasive and optimal for sediment core profiling in the lab or deployed on benthic landers.

In this study microelectrodes were used for ex-situ sediment core profiles. Sediment cores were collected from their respective environments and secured in lab. Profiles began approximately 3-5 mm above the sediment water interface in the overlying water and the electrodes were lowered with a micromanipulator (AIS Inc.) in millimeter increments. Dissolved oxygen was detected using linear sweep scans from -0.1 to -1.8V and a scan rate of 200 mV/s after a conditioning step at -0.1 V for 10 seconds (Minimum Detection Limit: MDL ~ 5 µM) (Luther et al., 2008). At each depth, cathodic square wave scans with a preconditioning step at -0.1 V for 10 seconds were run in at least triplicate from -0.1 to -1.8 V with a scan rate of 200 mV s^{-1}. These scans are able to quantify dissolved manganese(II) (Mn^{2+}, MDL ~ 15 µM), dissolved iron(II) (Fe^{2+}, MDL ~ 25 µM), thiosulfate ($S_2O_3^{2-}$, MDL ~ 10 µM), and total dissolved sulfide ($\Sigma H_2S=H_2S+HS^- + S^0 + S_x^{2-}$, MDL ~ 0.2 µM) in addition to qualitatively detect organic complexes of Fe(III) (org-Fe(III) (Taillefert et al., 2000a) and aqueous iron sulfide clusters ($FeS_{(aq)}$) (Theberge and Luther, 1997). For ΣH_2S or org-Fe(III) species measurements, an additional preconditioning step was applied for 10 seconds at -0.9 V before each analytical measurement to avoid memory effects (Brendel and Luther, 1995). Voltammetric signals were integrated using a semi-automated VOLTINT software package (Bristow and Taillefert, 2008). Before profiling, working electrodes were calibrated in a cell stand with $MnCl_2$ (0.1 M), and Fe^{2+}, ΣH_2S, and $S_2O_3^{2-}$ were quantified from the pilot ion method with Mn^{2+} as pilot ion (Brendel and Luther, 1995). Oxygen concentrations for the overlying water were calibrated using the oxygen concentrations of the bottom water determined by Winkler titration or by

calculating the maximum oxygen saturation using temperature and salinity. As the chemical composition of org-Fe(III) complexes and $FeS_{(aq)}$ is unknown, these species cannot be quantified and are reported in normalized current intensities (Taillefert et al., 2000a; Theberge and Luther, 1997).

2.2 Hanging Mercury Drop Electrodes

Dissolved As(III) concentrations were determined voltammetrically with a Metrohm VA 663 Hanging Mercury Drop Electrode (HMDE) coupled to an Ecochemie Autolab PGSTAT 12 potentiostat in a three electrode configuration, using a glassy carbon counter electrode and an Ag/AgCl/KCl (3M) reference electrode with a 2 M NaCl glass bridge. Samples were spiked to solutions pre-purged with N_2 gas that contained 0.8 mM $CuCl_2$, 2 M HCl, and 40 µM hydrazine (Chow and Taillefert, 2005; Li and Smart, 1996). A potential was applied for 30 seconds at -0.4 V to form a copper-arsine complex, then the potential was scanned cathodically from -0.4 to -1.2 V at a scan rate of 177 mV s^{-1} to reoxidize the copper-arsine complex. A minimum of triplicate scans were performed per sample. External calibration curves were obtained every 10 samples to ensure reproducibility. Detection limits of 300 nM with typical relative standard deviations of 0.5-8.0% (n=3) were obtained using this procedure.

2.3 Inductively coupled plasma-mass spectrometry (ICP-MS)

Total dissolved arsenic (As, mass to charge ratio (m/z): 75) and manganese (Mn, m/z: 55) concentrations were determined by an Agilent 7500a Inductively Coupled Plasma-Mass Spectrometer (ICP-MS). Standards and samples were prepared in 2% nitric acid (Trace Metal Grade, Fisher) and included scandium (Sc, m/z: 45) and yttrium (Y, m/z: 89)

internal standards (500 ppt, SPEX CertiPrep) to account for the drift of the instrument. A peristaltic pump flowed samples into a nebulizer which created a mist of sample using the carrier gas (argon) and continuously flowed excess sample into the waste container. A sample mist flowed through the spray chamber where large droplets are removed and the finer mist particles continued to the quartz torch. A radio frequency (RF) current was maintained around the torch which heated and energized the argon gas creating collisions of Ar atoms which generated a plasma (temperatures ranging from 8,000 to 10,000 K). The sample mist is desolvated and ionized in the plasma. The resulting ions are then lead to the first vacuum stage (evacuated by a vacuum pump) through the sample and skimmer cones with orifices diameters of 10 and 0.4 mm, respectively. The ion beam was focused using a series of ion lenses, the last of which deflects the ion beam to the front plate of the quadrapole. The quadrapole mass analyzer has RF and direct current (DC) currents applied to parallel, long metal rods which, depending on the charge, allow certain m/z ions to pass through to the electron multiplier detector. The detector operated in either pulse or analog mode for low or high concentrations samples respectively. The instrument was programmed to automatically correct As (m/z:75) counts for the interference of $ArCl^+$ (m/z: 75 and 77), and a selenium isotope (Se, m/z: 77) using the ratios of the abundance of the known isotopes of As and Se (Eq. 2-1)) (Agilent 7500 ICP-MS ChemStation Operator's Manual and Tuning and Application Handbook).

$$As(75) = [(75) * 1] - [(77) * 2.9] + [(82) * 2.3] - [(83) * 2.23] \qquad \textbf{2-1}$$

Calibration curves for As (low range: 0-250 ppb, high range: 3000-1,000 ppb) and Mn (low: 0-10 ppb and high: 20-100 ppb) were run approximately every 20 samples. Blanks and quality controls (mid-range calibration concentrations) were run every 10

samples with 97-106% recovery. Minimum detection limits (MDL, 3σ of blank counts) for dissolved Mn and As were 0.05 ppb (n=17) and 0.18 ppb respectively (n=28).

2.4 High Performance Liquid Chromatography coupled with Inductively Coupled Mass Spectrophotometry (HPLC-ICP-MS)

A high performance liquid chromatography instrument (Shimadzu LC-20AT) with autosampler (Shimadzu SIL-20AC HT) was paired with an inductively coupled mass spectrometer (HPLC-ICP-MS) to simultaneously quantify inorganic and organic arsenic species: arsenate (As(V)), arsenite (As(III)), monomethylarsonate (MMA) and dimethylarsinate (DMA) (Bednar et al., 2004; Fang et al., 2016) (Figure 2-1). As(III) and As(V) standards were prepared by dissolving As_2O_3 and As_2O_5 (Sigma) in 0.1 M NaOH. DMA standards were prepared by dissolving cacodylic acid (Sigma) in water, and MMA standards were prepared by dissolving methyl arsonic acid disodium salt (TRC Canada) in water. A Hamilton PRP-X100 (10 µm, 4.1 x 250mm) anion exchange column with a PRP-X100 guard column was used to separate As(III), As(V), DMA, and MMA. This column includes a 55% cross-linked polystyrene-divinylbenzene copolymer that is functionalized with quaternary ammonium anion-exchanger group to couple reverse phase separation of the methylated species with anion exchange properties to separate negatively charged arsenate species (Fang et al., 2016). The optimized eluent contained 6 mM ammonium phosphate buffer (pH 6.2) and 1% methanol to ensure that As(V) (pKas of 2.3, 6.8, and 11.6), DMA (pKas of 6.2), and MMA (pKas of 2.6 and 8.2) were mildly negatively charged and organic species not retained on the column. The eluent also contained 0.1 mM EDTA to complex indium (50 ppb, 436 nM) added to all standards and samples as internal standard to ensure its free elution through the column. Indium was used to correct for the

drift of the ICP-MS by normalizing the peaks of interest to the In peak (Figure 2-2). The eluent was run at a flow rate of 1.0 mL min^{-1} to keep pressure under 1,200 psi, and a 50 µL loop was used to inject samples. As As(III) (pKa of 11.9) was neutral, it was eluted first, followed by DMA, the larger methylated species, MMA, and As(V), the most negatively charge species (Figure 2-1). Calibration curves tested between 0-3 µM for each As species determined the linear range was between 0-3 µM (Figure 2-3, Table 2-1) and MDL for each species was calculated by three times the error on the y-intercept of the calibration curves (Table 2-1).

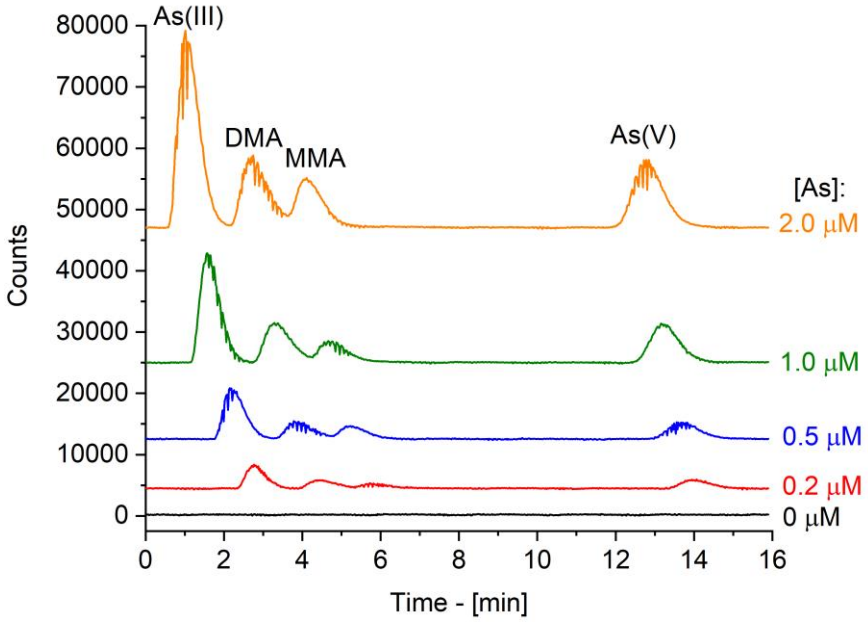

Figure 2-1 HPLC-ICP-MS chromatographs of standards containing As(III), DMA, MMA and As(V) in increasing concentrations from 0-2 µM. The eluent consisted of 6 mM ammonium phosphate buffer (pH 6.2), 0.1 mM EDTA and 1% methanol. Flow rate: 1 ml min^{-1}.

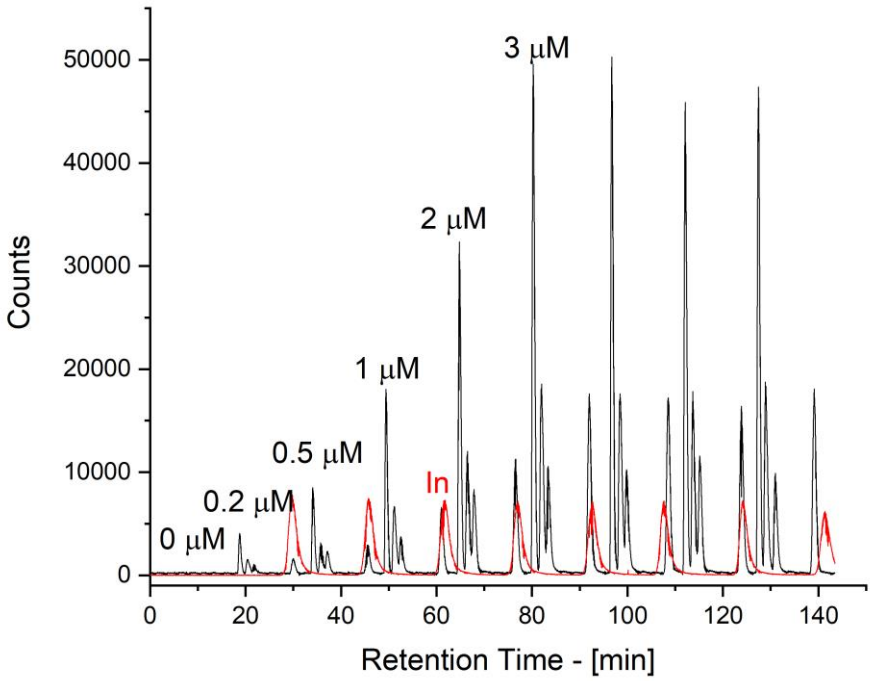

Figure 2-2 HPLC-ICP-MS chromatograph of As counts (black) overlain with In counts (red) to illustrate how In was used as an internal standard to normalize As concentrations during analysis.

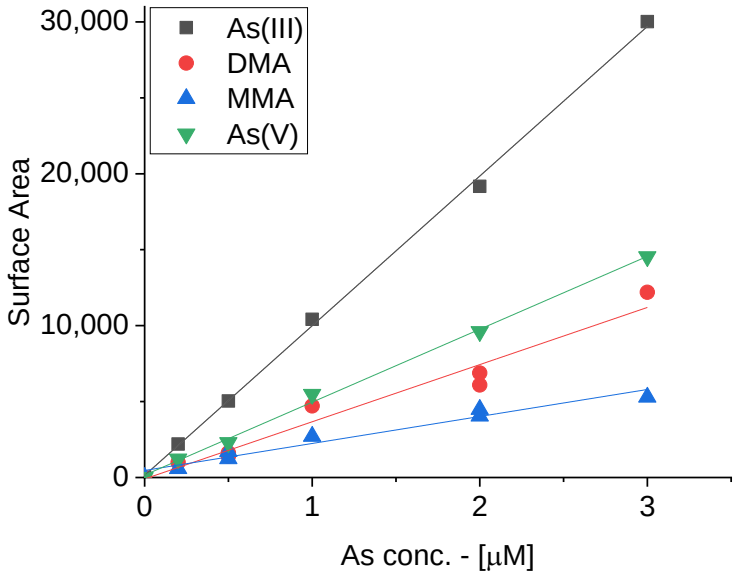

Figure 2-3 Calibration curves of surface area under the peak versus concentration (μM) of As(III) (gray square), DMA (red circle), MMA (blue triangle) and As(V) (green inverse triangle). Straight lines represent the linear regression. Regression statistics are listed in Table 2-1.

Table 2-1: Linear regression statistics and minimum detection limits (MDL) of As species determined by HPLC-ICP-MS calibrations (Figure 2-3)

Species	Slope	Intercept	MDL (nM)[a]
As(III)	9,855 ± 166	139 ± 256	78.0
DMA	3,764 ± 307	-93 ± 467	142.3
MMA	1,777 ± 152	464 ± 232	70.6
As(V)	4,802 ± 120	159 ± 185	56.3

[a]MDL: minimum detection limit, calculated as 3 times the standard deviation of the intercept.
Calibration curves based on surface area.

2.5 Determination of Mn(II), Mn(III) and total Mn using a spectrophotometric porphyrin ligand exchange method

Simultaneous speciation of dissolved Mn(II), dissolved Mn(III), and total dissolved Mn ($Mn(II)_d$, $Mn(III)_d$, and Mn_d) was based on a spectrophotometric protocol (Madison et al., 2011) which monitors the slow transition of a Cd-porphyrin complex with the ligand α,β,γ,δ-tetrakis(4-carboxyphenyl)porphine (T4CPP) to a Mn(III)-porphyrin (Mn(III)-T4CPP) complex by ligand exchange according to an exponential rise to a maximum over time (Figure 2-4a). At time zero before sample was added, the reagent matrix includes 24 µM T4CPP, 24 µM $CdCl_2$ and 5 mM imidazole borate buffer (pH 8). When Mn(II) is present in the sample, Mn(II) substitutes the Cd-porphyrin complex to form a Mn(II)-T4CPP complex which is oxidized to the Mn(III)-T4CPP complex (Eq. 2-2). In turn, when Mn(III) is present in the sample, usually complexed by ligands (Mn(III)-L), Mn(III) substitutes in the Cd-T4CPP complex via ligand exchange reaction (Eq. 2-3). The ligand exchange reaction takes longer, therefore, the rate of formation of the Mn(III)-porphyrin complex is slower in comparison to the Mn(II) substitution pathway as observed in the behavior of the absorbance curve (Madison et al., 2011a). Speciation of manganese is made possible by fitting with Eq. 2-4 (derivation can be found in Madison et al. 2011) the exponential rise to a maximum absorbance versus time data after converted to concentrations (Mn_d) versus time data after converting to concentrations. The fitting parameters required in the model include the initial concentrations of Mn(II) ($Mn(II)_0$) and Mn(III) ($Mn(III)_0$) as well as the corresponding ligand exchange rate constants k_1 and k_2 (Madison et al., 2011a) (Eq. 2-4). For this study, a MATLAB code was developed to fit

the exponential rise to a maximum using a non-linear least square optimization procedure that optimizes the four parameters (script provided in Appendix A).

$$Mn(II) + Cd - T(4-CP)P \xrightarrow{\uparrow Cd(II)} Mn(II) - T(4-CP)P + O_2 \rightarrow Mn(III) - T(4-CP)P \quad (2\text{-}2)$$

$$Mn(III) + Cd - T(4-CP)P \xrightarrow{\uparrow Cd(II)} Mn(III) - T(4-CP)P \quad (2\text{-}3)$$

$$[Mn]_d = [Mn(III) - T(4-CP)P]_{Total} = Mn(II)_0(1 - e^{-k_1 t}) + Mn(III)_0(1 - e^{-k_2 t}) \quad (2\text{-}4)$$

Occasionally, the code input an initial guess that remained constant for the time series of the reaction (rather than dynamic with time as expected due to reaction mechanism, Figure 2-4b). In these cases, Mn(III) was overestimated leading to a higher calculated concentration of Mn_d compared to the actual concentration measured (Table 2-2). As k_1, the kinetic constant for the binding of Mn(II) by the porphyrin, can be determined from calibration curves (e.g., Figure 2-5), a code based on a 3-parameter fit of the non-linear exponential rise to a maximum was developed to optimize the remaining variables: $Mn(II)_0$, $Mn(III)_0$, and k_2. In the cases where a straight-line guess was determined by the 4 parameter code, the 3 parameter code typically provided a dynamic fit to the data as expected, yet overestimated Mn(III) percentages in the standards. Therefore, the 4 parameter fit to the curve outputs only are reported in this work. Finally, it is important to note the 4 parameter code detected 1.5 µM Mn(III) in Mn(II) standards that were run as samples (Table 2-2). Due to this issue, the MDL for Mn(III) is operationally defined as 1.5 µM.

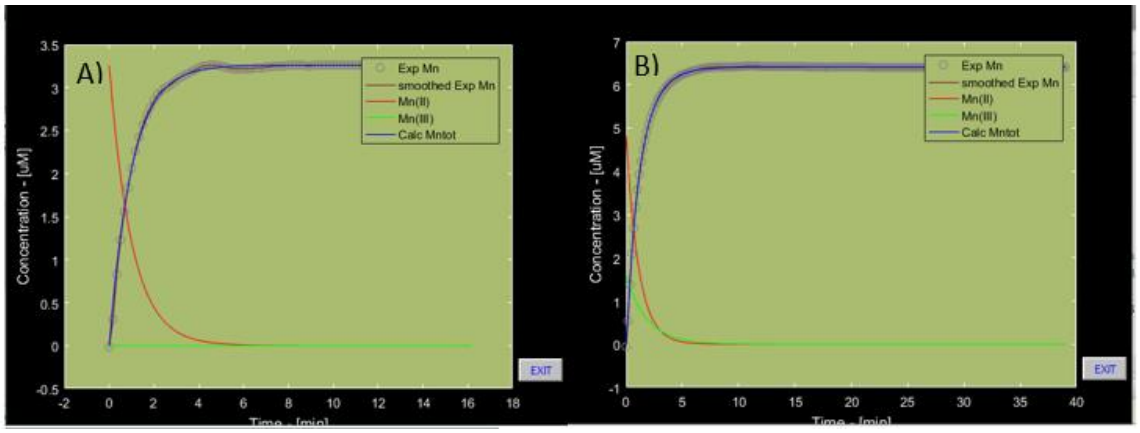

Figure 2-4 Typical model outputs for the fitting of pore water samples as a function of time with: (A) only Mn(II) (no Mn(III) detected) and (B) Mn(II) (red) and Mn(III) detected (green line) (station 11, section 13, depth 127 mm) The experimental Mn concentrations (open circles) are plotted along with the smoothed experimental data (black line), model Mn(II) fit (red line), model Mn(III) fit (green line), and calculated total Mn concentrations (blue line).

Table 2-2: Mn(II) only standards ran as samples with Mn(II/III) speciation code*

[NaCl] (mM)	Mn(II) [µM]	k_1 (min^{-1})	k_2 (min^{-1})	$Mn(II)_0$ [µM]	$Mn(III)_0$ [µM]	$Mn(II)_0$ +$Mn(III)_0$ [µM] (calc)	% $Mn(III)_0$/ % err
0	1	2.54	0.00	1.02	0.00	1.02	0.00
0	3	2.21	0.00	3.01	0.00	3.01	0.00
0	5	2.31	0.53	4.59	0.45	5.04	8.92
9	1	1.14	0.00	0.98	0.00	0.98	0.00
9	3	1.11	0.00	3.04	0.72[a]	3.75	23.88
9	5	1.01	0.00	4.94	1.28[a]	6.22	25.66
18	1	0.71	0.00	1.01	0.00	1.01	0.00
18	3	0.70	0.00	2.99	0.00	2.99	0.00
18	5	0.83	0.25	4.43	0.60	5.03	11.99
36	1	0.41	0.00	1.01	0.00	1.01	0.00
36	3	0.41	0.20	2.72	0.28	3.00	9.36
36	5	0.43	0.20	4.11	0.95	5.06	19.00

*analyzed with 4 parameter fit, upper bounds: $k_1=2*k_{1standards}$, $k_2=0.5*k_{1standards}$
[a] Mn(III) guess is straight line

2.5.1 Correction for Cl^- and Fe^{2+} interferences

Excess chloride present during the reaction interferes with the kinetics of the reaction via Cd-chloride complexation (Madison et al., 2011a). Calibration curves with Mn(II) standards (Figure 2-5b) revealed an increase in chloride concentrations decreases Mn(II) substitution rates and exponentially decreases k_1 values (Figure 2-5c). Complexation of chloride with Cd^{2+}, however, does not affect the final absorbance value of the Mn(III)-T4CPP complex (Figure 2-5a) or the molar absorptivity of the complex (Figure 2-5b). NaCl concentrations of 0, 9, 18 and 36 mM NaCl correspond to the analysis of freshwater samples, or 60, 30 and 15 times dilutions of pore water (seawater, 0.54M) samples respectively (Figure 2-5). A similar effect was observed in microbial incubation

samples with M1 media and exaggerated with M1 media and 0.5 mM As(V) in solution (Figure 2-6). M1 media contains inorganic salts (Ionic strength of approximately 0.1) which would interfere with the Cd-substitution similar to the effect of the NaCl interference. At this point further tests would need to be performed to understand the mechanism of the As(V) interference, however, the interference could be caused by the complexation of As(V) with the porphyrin complex. The calibration function of the MATLAB code extracts the k_1 value of the standards assuming only Mn(II) was present in the sample (disregarding the Mn(III) term in Eq 2-4). To normalize the change in kinetics with increasing Cl^- concentrations in samples, the extracted k_1 values were input as bounds when samples were speciated, the upper bound was $k_1=2*k_{1,standards}$, and the lower bound was 0. An upper bound of $k_2=0.5*k_1$ was placed on k_2 due to the fact k_2 is inherently lower than k_1 due to the reaction mechanism, and previously reported k_2 values did not exceed one third of the k_1 value (Madison et al., 2013). All scans were run for speciation using the 4 parameter MATLAB code.

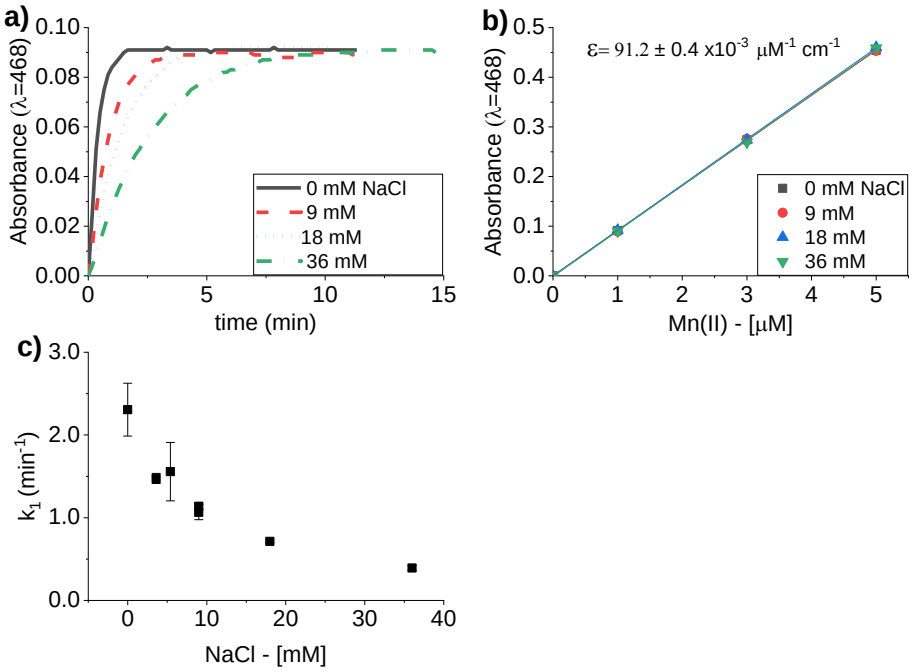

Figure 2-5 (a) Absorbance of the Mn(III)-T4CPP complex (λ=468) corrected for reagent blank measured over time with 1 µM Mn(II) in the presence of increasing NaCl concentrations. (b) Calibration curves (0-5 µM Mn(II)) in varying NaCl concentrations (0, 9, 18, and 36 mM) used to quantify Mn_d demonstrate an average molar absorptivity of 91.2 ± 0.4 x10^3 µmol cm^{-1}. (c) k_1 values as a function of NaCl concentration determined using the calibration feature of the speciation code that assumes only Mn(II) is present in the sample. Error bars represent the standard deviation of the average k_1 obtained for 1, 3, and 5 µM Mn(II) standards (n=3).

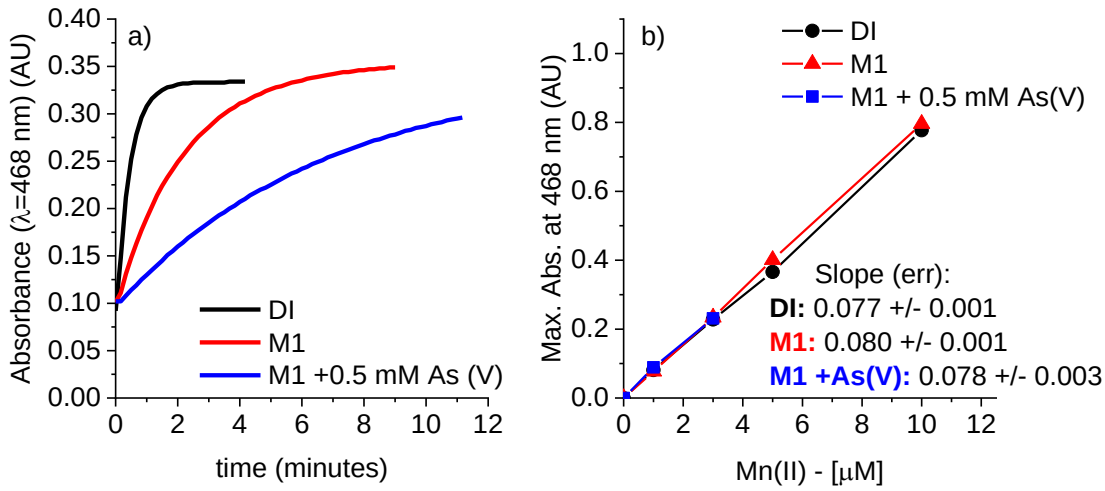

Figure 2-6 (a) Absorbance of the Mn(III)-T4CPP peak at 468 nm (absorption units, AU) measured over time with 3 μM Mn(II) and (b) calibration curves between 0 and 10 μM Mn(II) in the reagent matrix with either DI (black), M1 media (red) or M1 media and 0.5 mM As(V) (blue). Regardless of the medium, the maximum absorbance of the Mn(III)TCPP complex at steady-state remains the same. Maximum absorbances used for the calibration curves were corrected by subtracting the absorbance at t=0 (approx. 0.10 AU).

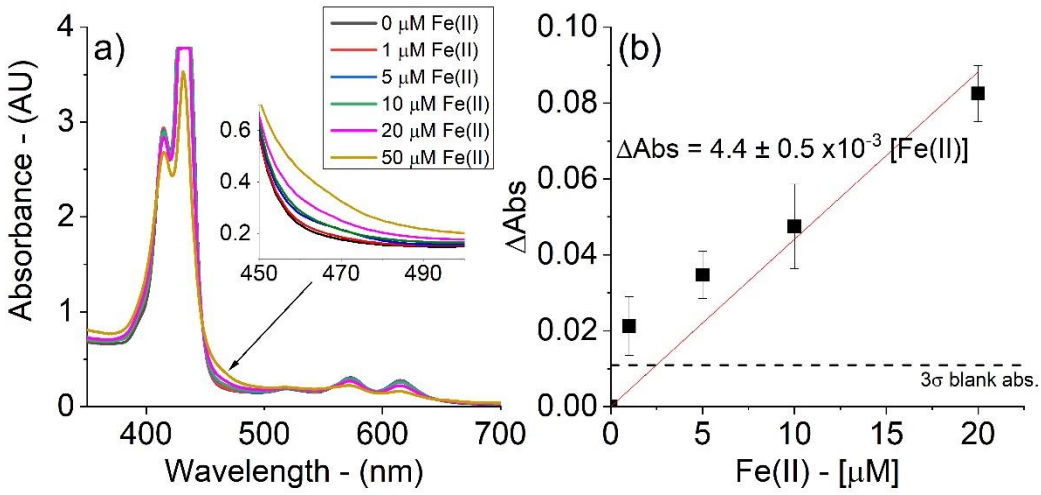

Figure 2-7 (a) Spectrophotometric scans of the Mn(II)-free Cd-porphyin reagent amended with increasing Fe(II) concentrations. The baseline increases (see inset) at the same wavelength as the expected Mn(III)-T4CPP peak (λ=468 nm). (b) Change in absorbance (Δabs) of each Mn(II) standard (0, 1, 5, 10 µM Mn(II)) (n=4) amended with Fe compared to the unamended standard as a function of Fe(II) concentration. Error bars represent standard deviation of the average change in absorbance of each standard (n=4). Dashed line represents 3σ error in the absorbance of the blanks (0 µM Mn(II), 0 µM Fe(II)) (n=24).

Additionally, Fe(II) interfered with the soret band at the absorbance of the Mn(III)-T4CCP complex (λ=468 nM) (Figure 2-7a). Different Fe(II) concentrations (1, 5, 10, 20 µM) were amended in Mn(II) standards (0, 1, 5, 10 µM) to determine the average increase in absorbance compared to Fe(II)-unamended Mn(II) standards. The average and standard deviations of the change in absorbance (Δabs) of Mn(II) standards increased linearly with increasing Fe(II) concentration where Δabs =4.4 ± 0.5 $x10^{-3}$ [Fe(II)] (R^2=0.95) (Figure 2-7b). The standard error of the blank absorbance (3σ, n=24) was 0.011 absorbance units (Figure 2-7b), which input into the trendline equation corresponds to a value of 2.5 ± 0.3 µM Fe(II) (Figure 2-7b). Therefore, if the total dissolved Fe (Fe_d) concentration determined by the ferrozine method (Stookey, 1970) in the cell during Mn measurement (corrected for dilution factor) was above 2.5 µM, the Fe concentration was input into the trendline, and the Δabs of the Mn(III)-T4CPP complex was subtracted from the final absorbance value. Only 20% of pore water samples were corrected for an Fe interference from the Gulf of Mexico 2017 research cruise.

2.5.2 Method validation with environmental samples

Total dissolved Mn (Mn_d) was determined in duplicate Gulf of Mexico pore water samples from three different stations (St. 4, St. MK, and St. 13) with the porphyrin method by converting the final absorbance (λ=468) with the molar absorptivity (Figure 2-5b, ε=91.2 ±0.4 $x10^{-3}$ µM cm^{-1}). Leftover frozen unacidified pore water samples were analyzed for total dissolved Mn via ICP-MS for comparison (Table 2-3, Table 2-4) even thoughacidifying samples for ICP work precipitates humics and Mn eventually bound to them (Buffle, 1988). Porphyrin sample dilution factors ranged between 15 and 60 times,

whereas ICP-MS samples were diluted 1,000 times. Only one replicate per sediment section was analyzed via ICP-MS, therefore, the reported error represents error propagated from the calibration curve. Mn_d concentrations between the two methods varied between 0-10% for St. 4 and St. MK, (with the exception of a 20% difference for section 1 at St. 4 (Table 2-3)). However, Mn_d concentrations at St. 13 measured by the porphyrin method were consistently higher compared to the ICP-MS measurements (Table 2-4).

Table 2-3: Pore water Mn_d concentrations measured by ICP-MS compared to the porphyrin method and the relative difference in concentration relative to the ICP-MS measurement

	St. 4			St. MK		
Section	ICP-MS (μM)	Mn porp (μM)	% err	ICP-MS (μM)	Mn porp (μM)	% err
0	BDL	16.3 ± 0.0		BDL	NA	
1	104.9 ± 0.3	124.1 ± 4.6	18.2	44.5±0.5	49.3±0.1	10.7
2	74.8 ± 0.6	84.7 ± 1.4	13.3	29.8±0.4	28.6±0.6*	4.1
3	58.7 ± 1.2	65.6 ± 0.5	11.8	24.7±0.4	22.9±0.5*	7.1
4	45.4 ± 0.6	47.5 ± 0.0	4.7	12.5±0.1	15.6±0.5	25.2
5	32.4 ± 0.4	35.3 ± 0.5	8.9			
6	27.3 ± 0.4	31.0 ± 0.0	13.5	10.3±0.3	11.4±0.6	10.6
7	24.5 ± 0.3	28.8 ± 0.2	17.9	9.5±0.1	11.2±0.1	17.3
8	25.1 ± 0.2	27.5 ± 0.2	9.8	8.4±0.1	8.4±1.4	0.2
9	25.6 ± 0.3	26.2 ± 3.5	2.5	9.2±0.1	9.5±0.7	3.8
10	26.5 ± 0.2	31.6 ± 0.0	19.5		8.8±0.1	
11	22.2 ± 0.2	26.5 ± 0.7	19.5		9.6±0.6	
12	23.0 ± 0.2	25.7 ± 0.5	12.0		9.9±0.1	
13	20.6 ± 0.1	24.9 ± 0.7	20.8	10.6±0.1	12.6±0.1	19.0
14	20.0 ± 0.1	20.4 ± 4.2	2.4	10.4±0.2	10.1±3.4	2.3
15	20.4 ± 0.2	24.9 ± 0.2	21.8		12.3±0.1	
16	20.6 ± 0.2	23.7 ± 0.5	15.0		8.6±8.8	
17	18.1 ± 0.1	20.9 ± 0.2	15.5	13.5±0.2	NA	

*corrected for Fe interference. Average relative difference (%) per core: 13 ± 6 (St. 4), 10 ± 8 (St. MK), 28 ± 15 (St. 13).

Table 2-4 Pore water Mn_d concentrations measured by ICP-MS compared to the porphyrin method and the relative difference in concentration relative to the ICP-MS measurement for St. 13

Section	ICP-MS (μM)	Mn porp (μM)	% err
0	BDL	1.7 ± 0.3	
1	BDL	2.7 ± 2.0	
2	60.4 ± 1.5	64.1 ± 1.7	6.1
3	112.0 ± 1.4	141.2 ± 1.4	26.1
4	141.9 ± 2.2	174.8 ± 1.4	23.2
5	172.9 ± 1.3	231. 5± 6.1	33.9
6	189.4 ± 1.5	239.1 ± 6.5	26.2
7	163.7 ± 2.8	203.8 ± 0.5	24.5
8	118.5 ± 1.3	199.9 ± 0.5	68.7
9	NA	182.4 ± 0.0	
10	143.0 ± 0.4	164.3 ± 5.1	14.9
11	139.5 ± 1.0	176.5 ± 0.9	26.5
12	147.5 ± 0.5	181.4 ± 0.5	23.0
13	150.8 ± 0.6	196.9 ± 1.9	30.5
14	165.5 ± 1.4	208.4 ± 1.4	26.0
15	178.1 ± 2.0	220.6 ± 4.7	23.9
16	NA	229.2 ± 8.4	
17	199.6 ± 1.1	248.3 ± 0.9	24.4
18	171.1 ± 0.7	271.1 ± 2.3	58.5
19	231.1 ± 2.1	286.6 ± 5.6	24.0
20	234.8 ± 2.0	276.7 ± 5.6	17.8

2.6 Acid Volatile Sulfide (AVS) extractions

The 'acid volatile sulfides' (AVS) fraction represents monosulfide compounds consisting of hydrogen sulfide trapped by Fe(II) and other divalent metals (Cornwell and Morse, 1987). The AVS fraction is extracted from 0.5-0.7 gram of wet sediment in the presence of 3 M HCl added to a N_2-degassed (using a heated Cu trap to remove residual O_2 from N_2 gas) cold distillation vial. The hydrogen sulfide (H_2S) gas formed is carried by the N_2 gas stream under low flow conditions and trapped into a N_2-degassed 1 M NaOH solution positioned at the output of the distillation vial (Henneke et al., 1991) during a 4 hour extraction period (Carey and Taillefert, 2005). Dissolved sulfide was detected by measuring absorption at 230 nm (Figure 2-8a) (Ellis and Golding, 1959) and quantified using external calibration curves obtained daily with fresh NaS_2 standards partially dissolved in degassed DI water to remove impurities and diluted in 1 M NaOH (Figure 2-8b). The average sensitivity of calibrations was $7.2 \times 10^{-3} \pm 6.4 \times 10^{-4}$ AU μM^{-1} (n=22). Blanks were set to 0 AU for each measurement, therefore the minimum detection limit was calculated as 3 times the standard deviation of the intercept of the linear regression used for the calibrations (n=22). The detection limit for this method was 2.5 µM HS^-. Each extraction was performed in triplicate. Samples were analyzed immediately after extraction, as HS^- is susceptible to oxidation by dissolved O_2 at high pH (Cline and Richards, 1969; Luther et al., 2011) despite being more stable in trace metal clean conditions (Luther et al., 2011).

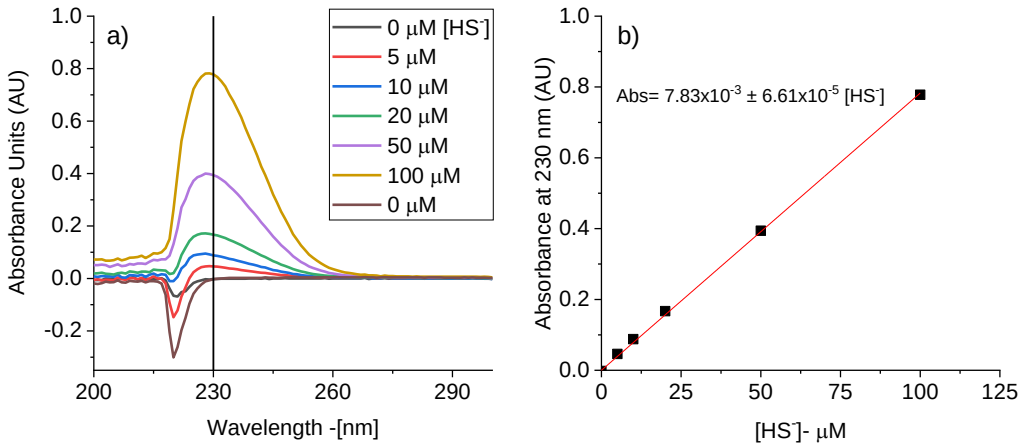

Figure 2-8 (a) absorbance vs wavelength of HS^- at increasing HS^- concentrations (10-20 mM stock NaS_2 dissolved in water) in 1 M NaOH. Absorbance at 230 nm (vertical black line) at each concentration was used to create (b) calibration curves.

CHAPTER 3. DEVELOPMENT OF A RATE LAW FOR ARSENITE OXIDATION BY MANGANESE OXIDES

This is the reprint of an article published in *Geochimica et Cosmochimica Acta*, authored by Shannon Owings[1], George W. Luther[2], and Martial Taillefert[1] entitled "Development of a rate law for arsenite oxidation by manganese oxides".

[1]School of Earth and Atmospheric Sciences, Georgia Institute of Technology, Atlanta, GA 30332-0340 [2]College of Earth, Ocean, and Environment, University of Delaware, Lewes, DE 19958

3.1 Abstract

Arsenite (As(III)), may be rapidly oxidized to arsenate (As(V)) by manganese oxides over a wide range of pH. Interestingly, pseudo-first order rate constants for Mn(IV) oxides (MnO_2) reported in the literature differ by orders of magnitude, mainly due to the fact that experimental conditions have not been normalized and surface passivation may hinder the reaction rate. As a result, a formal kinetic rate law for the oxidation of As(III) by MnO_2 does not exist. In this study, a comprehensive rate law that describes the abiotic oxidation of As(III) by vernadite (δ-MnO_2) was developed by systematically varying pH and the concentrations of δ-MnO_2 and As(III). Experiments were performed with excess δ-MnO_2 compared to As(III) in buffered solutions with an ionic strength typical of freshwater environments to reflect the geochemical conditions of most environments. The half-life of the pseudo-first order reaction is less than three minutes in all experiments. Results show the initial reaction rate is proportional to the concentrations of δ-MnO_2 and

As(III) and independent of pH in the pH range 4-9. However, below pH 6 and above pH 8 the pseudo-first order rate constant is slightly lower due to the protonation of the surface δ-MnO_2 and the deprotonation of As(III). Overall, the reaction follows a first order rate law with respect to As(III) and effective surface sites of δ-MnO_2 and zeroth order with respect to pH. The overall second order rate constant, k, was calculated to be 0.36 ± 0.11 L hr^{-1} m^{-2}. This rate constant is comparable to the vast majority of rate constants derived from previously published data when using the effective surface sites of MnO_2 as reactive species only, indicating the most influential factors of As(III) oxidation by MnO_2 are constrained in the developed rate law. Based on the present experiments, the oxidation of As(III) by MnO_2 is proposed to proceed as one two-electron transfer reaction between As(III) and Mn(IV) to eventually form As(V) and Mn^{2+} species. Two steps of one-electron transfer, however, may be possible though it is likely that both Mn(IV) and Mn(III) species are ultimately reduced to Mn^{2+}. Comproportionation of Mn^{2+} and Mn(IV) to Mn(III) does not seem to be important on the time scale of these experiments.

3.2 Introduction

Arsenic may naturally accumulate above the World Health Organization guideline of 10 ppb (WHO, 2000) in aquifers around the world (Ahmed et al., 2004; Nickson et al., 2000) and therefore presents a global risk to human health(Nordstrom, 2002; Rasheed et al., 2017; Smith et al., 2000a). Arsenic is also introduced anthropogenically into the environment by mining, manufacturing, and agricultural practices (Bode and Dong, 2002; Christen, 2001; Mukhopadhyay et al., 2002; Oremland and Stolz, 2003) and generally accumulates in low, yet detectable concentrations in aquatic environments (Chow and Taillefert, 2005; Donner et al., 2017; Smedley and Kinniburgh, 2002).

Arsenite (As(III)), under the form of the neutral H_3AsO_3 species across the pH of most aquatic environments (pKa values 9.2, 12.1, and 13.4), and arsenate (As(V)), under the form of the weak acid $H_2AsO_4^-$ (pKa of 2.24, 6.76, 11.6), represent the two most common oxidation states of arsenic in the environment (Stumm and Morgan, 1996). Given its neutral charge, As(III) represents the more hydrologically mobile form of arsenic, whereas As(V) readily adsorbs to mineral surfaces such as clays and Fe(III), Al(III), and Mn(IV/III) oxides and, consequently, is less mobile (Amirbahman et al., 2006; Arai et al., 2001; Raven et al., 1998). As As(V) is only reduced abiotically by dissolved sulfide with a half-life of several months (Newman et al., 1997; Rochette et al., 2000), and poorly reduced by structural S^{2-} from mackinawite (FeS) (Troyer et al., 2014). As(V) in aquatic systems is considered to be mainly reduced microbially via respiration (Krafft and Macy, 1998) or detoxification (Saltikov et al., 2005) processes. On the other hand, As(III) may be chemically oxidized to As(V) by dissolved oxygen (half-life of days) (Kim and Nriagu, 2000), Mn(IV) oxides (half-life of minutes to hours) (Kim and Nriagu, 2000; Oscarson et al., 1981b; Oscarson et al., 1981c; Oscarson et al., 1983), $Mn^{III}OOH$ (half-life of hours) (Chiu and Hering, 2000), and freshly formed iron oxyhydroxides (Amstaetter et al., 2010). These findings indicate that manganese oxides represent the main abiotic oxidant of As(III) in aquatic systems.

In sediments, manganese oxides are mainly formed biogenically (Tebo et al., 2004), as Mn^{2+} is largely inert to abiotic oxidation below pH 8-9 (Diem and Stumm, 1984). Synthetic analogs to biogenically produced Mn(IV) oxides include vernadite (synthesized in alkaline solution, δ-MnO_2) and acid birnessite (synthesized in acidic conditions) (McKenzie, 1971; Scott and Morgan, 1995; Villalobos et al., 2014; Villalobos et al., 2003).

The point of zero charge pH (pH_{pzc}) of these Mn(IV) oxides range from 1.85 to 3.1 (Jones et al., 2012; Morgan and Stumm, 1964; Murray, 1973; Scott and Morgan, 1995; Yao and Millero, 1993), indicating that the surface of Mn(IV) oxides are overall negative at the circumneutral pH of most aquatic systems (pK_{a1}=-1.6 and pK_{a2}=4.6; (Catts and Langmuir, 1986; Yao and Millero, 1993, 1996a). Simultaneously, the pK_as of As(III) species are high enough (i.e. 9.2, 12.1, and 13.41) (Stumm and Morgan, 1996) to allow adsorption of As(III) onto the negatively charged MnO_2 surface species above pH 5 and promote the abiotic oxidation of As(III) according to the overall reaction (Eq. 3-1) (Scott and Morgan, 1995):

$$MnO_2 + H_3AsO_3 + H^+ \rightarrow Mn^{2+} + H_2AsO_4^- + H_2O \qquad 3\text{-}1$$

Elemental arsenic has the configuration [Ar] $3d^{10}4s^24p^3$, whereas As(III) has no electrons in the 4p orbitals and has the configuration [Ar]$3d^{10}4s^2$. The formation of As(V) therefore requires loss of two '4s' electrons to form the extremely stable [Ar] $3d^{10}$ configuration. The oxidant in this reaction is $Mn^{(IV)}O_2$ with the inert electron configuration of $t_2g^3e_g^{*0}$ such that H_2O or OH^- does not readily dissociate from the metal center valence band (Cotton et al., 1999). As electrons have to be transferred to the e_g^* (σ symmetry) of Mn(IV), the relative good symmetry between the 4s orbital (also with σ symmetry) of As(III) indicates that outer sphere electron transfer is possible but has yet to be observed experimentally. The proposed mechanisms for the oxidation of As(III) by MnO_2 involve either a single two-electron transfer step (Lafferty et al., 2010b; Scott and Morgan, 1995)to form As(V) and Mn^{2+} or the formation of a Mn(III)-oxyhydroxide (MnOOH) intermediate in successive one-electron transfer reactions (Nesbitt et al., 1998). The two-electron transfer mechanism involves the attachment of As(III) to the surface and the single transfer of two electrons from the 4s orbitals of As(III) to Mn(IV) to form surface-bound Mn^{2+} and

$H_2AsO_4^-$. Finally, $H_2AsO_4^-$ detaches from the surface and is released into solution (Amirbahman et al., 2006; Scott and Morgan, 1995) mainly because the first two pK_as of As(V) are low enough (i.e. 2.24, 6.76) that the product of As(III) oxidation is not expected to remain strongly adsorbed to the MnO_2 surface (Power et al., 2005). The first step in the one-electron transfer mechanism includes the splitting of two electrons of As(III) to reduce two Mn(IV) atoms to MnOOH (Eq. 3-2), followed by another reduction step involving another As(III) to reduce the two MnOOH intermediate species and release Mn^{2+} into solution (Eq 3-3).

$$2Mn^{IV}O_2 + H_3AsO_3 + H_2O \rightarrow 2Mn^{III}OOH + H_2AsO_4^- + H^+ \quad 3\text{-}2$$

$$2MnOOH + H_3AsO_3 + 3H^+ \rightarrow 2Mn^{2+} + H_2AsO_4^- + 3H_2O \quad 3\text{-}3$$

As Mn(IV) includes a band of orbitals (conduction band) rather than discrete orbitals to accept electrons during reduction, the one electron transfer to two different Mn(IV) ions is also possible as proposed with hydrogen sulfide as the reductant (Luther et al., 2018). Mn(III) formation has also been proposed to result from the comproportionation of sorbed Mn^{2+} to the Mn(IV) oxide surface (Eq. 3-4), as structural changes of birnessite ($Mn^{IV}O_2$) to feitknechite (β-$Mn^{III}OOH$) with the addition of Mn^{2+} was observed after 24 hours of reaction (Elzinga, 2011). Additionally, the comproportionation-disproportionation reactions occur much faster at pH 7.5 compared to pH 5, with a difference of equilibrium from days to months (Elzinga, 2016; Elzinga and Kustka, 2015). These findings therefore suggest that As(III) oxidation either takes place via a single two-electron transfer without formation of Mn(III) intermediate over short time scales, followed by eventual formation of Mn(III) by comproportionation, or occurs via two single-electron transfer steps to the

conduction band of the most energetically favorable Mn(IV) centers with formation of Mn(III) surface sites that may eventually be reduced to Mn^{2+}.

$$> Mn^{IV} - OH + Mn^{2+}(aq) + H_2O + H^+ \rightarrow 2(> Mn^{III} - OH_2) \quad 3\text{-}4$$

In both mechanisms, Mn^{2+} may either remain surface-bound above the pH_{pzc} of MnO_2 or released into solution at pH values lower than the pH_{pzc} (Scott and Morgan, 1995). The Mn^{2+} and As(V) products may therefore compete for vacancy sites on the surface of the manganese oxides (Lafferty et al., 2011). Although, a monodentate mononuclear complex intermediate between As(V) and Mn(IV) may exist (Lafferty et al., 2010b), a bidendate binuclear, double corner-sharing polyhedral complex preferentially forms between As(V) and Mn(IV) at the edges and in the interlayers of the MnO_2 (Manning et al., 2002; Zhu et al., 2009), and As(V) may bind to Mn(III) if the ion is available at the surface (Lafferty et al., 2010a; Lafferty et al., 2010b; Manceau et al., 2002). The presence of adsorbed cations may also create positive surface sites that favor adsorption of the negatively charged As(V) (Scott and Morgan, 1995; Villalobos et al., 2014). Finally, the adsorption of high concentrations of As(V) may decrease the availability of sites for rapid As(III) oxidation, even in excess As(III) (Manning et al., 2002; Oscarson et al., 1981a). Similarly, pre-equilibrating MnO_2 with Mn^{2+} or other cations may passivate the surface and affect the reaction rate (Power et al., 2005; Scott and Morgan, 1995).

As MnO_2 is prevalent in the environment and the oxidation state of arsenic greatly affects its transport, it is important to accurately characterize the rate and mechanism of As(III) oxidation by MnO_2 over a range of pH and MnO_2 and As concentrations. Remarkably, the pseudo-first order rate constants (k_{obs}) published in the literature differ significantly (Table 3-1 and Schacht and Ginder-Vogel, 2018). For example, the reaction

is reported to occur within minutes (Parikh et al., 2008) or over several hours (Lafferty et al., 2010a; Villalobos et al., 2014), and the rate may decrease after an initial rapid oxidation period (Oscarson et al., 1983; Thanabalasingam and Pickering, 1986a). In addition, pseudo-first order rate constants are often reported only, and experiments are either conducted at fixed pH or in low and high pH conditions (i.e. 3 and 6), such that the effect of pH on the mechanism cannot be inferred (Manning et al., 2002; Power et al., 2005; Villalobos et al., 2014). Simultaneously, the passivation of the manganese oxide surface by cations or reaction products may misrepresent the effect of As(III) concentration on the rate of the reaction (Lafferty et al., 2010a; Scott, 1991). Furthermore, considering the concentration of MnO_2 in the rate law may not be accurate as: (i) As(III) oxidation only takes place on the edge sites of MnO_2 (Tournassat et al., 2002; Villalobos et al., 2014) which total about 60% of the mineral surface (Tournassat et al., 2002; Villalobos et al., 2014); and (ii) the crystallinity of MnO_2 and its surface area vary based on synthesis (Villalobos et al., 2014). Finally, the majority of analytical techniques available to quantify As(III) are unable to collect data within the first few minutes of the reaction, this crucial time frame in kinetic studies. The disagreement between reaction mechanisms and published rates indicates the kinetics of the reaction needs to be better constrained to conclude on the reaction mechanism or determine the most important geochemical factors in the oxidation of As(III) by MnO_2.

Table 3-1 Literature values summary including Experimental Conditions, Specific Surface Area (SSA), Effective Surface Sites (ESS), Pseudo-First Order Rate Constants (k_{obs}), Calculated Initial Rates (R_0) and Overall Second Order Rate Constants (*k*)

Reference	Mn type[a]	pH	As(III)$_i$ (μM)	MnO_2 (g L^{-1})	Mn:As molar ratio[b]	k_{obs} (h^{-1})	SSA (m^2 g^{-1})	ESS (m^2 L^{-1})[c]	R_0 (μM h^{-1})	*k* (L m^{-2} h^{-1})
Power et al. (2005)	acid birn	4.5	100	0.1	11.49	7.60	32.6	1.96	81.7 ± 4.4	0.42 ± 0.02
Power et al. (2005)	acid birn	4.5	300	0.1	3.83	5.40	32.6	1.96	171.6 ± 10.4	0.29 ± 0.02
Power et al. (2005)	acid birn	6	100	0.1	11.49	4.60	32.6	1.96	54.4 ± 2.3	0.28 ± 0.01
Power et al. (2005)	acid birn	6	300	0.1	3.83	2.40	32.6	1.96	69.0 ± 3.2	0.12 ± 0.01
Villalobos et al. (2014)	δ-MnO_2	3	300	0.1	3.83	1.20	114	6.84	298.3 ± 52.7	0.15 ± 0.03
Villalobos et al. (2014)	δ-MnO_2	6	300	0.1	3.83	0.53	114	6.84	302.7 ± 65.6	0.15 ± 0.03
Villalobos et al. (2014)	acid birn	3	300	0.1	3.83	1.16	39	2.34	388.8 ± 66.6	0.55 ± 0.09
Villalobos et al. (2014)	acid birn	6	300	0.1	3.83	0.37	39	2.34	320.1 ± 99.9	0.46 ± 0.14
Villalobos et al. (2014)	acid birn	3	300	0.29	11.11	3.49	39	6.79	896.6 ± 108.3	0.44 ± 0.05
Villalobos et al. (2014)	acid birn	6	300	0.29	11.11	2.12	39	6.79	590.5 ± 39.9	0.29 ± 0.02
Manning et al. (2002)	acid birn	6.5	100	0.1	11.49	0.78	32	1.92	88.6 ± 13.3	0.46 ± 0.07
Manning et al. (2002)	acid birn	6.5	100	0.25	28.74	10.90	32	4.8	374.7 ± 63.1	0.78 ± 0.13
Scott and Morgan (1995)	acid birn	4	99.3	0.17	19.74	0.27	72	7.34	315.0 ± 92.8	0.32 ± 0.09
Ginder-Vogel et al. (2009)	HMO, δ-MnO_2	7	5000	1	11.49	9.00	273.5[d]	164.1	366,000.0 ± 0.0	0.45 ± 0.00
Ginder-Vogel et al. (2009)	HMO, δ-MnO_2	7	5000	1	11.49	16.92	273.5[d]	164.1	586,285 ± 124,849	0.71 ± 0.15
Jones et al. (2012)	δ-MnO_2	7.2	65–77	0.05	7.46	1.33	273.5	8.21	N/A	0.16 ± 0
Scott (1991)	acid birn	4	398	0.22	6.35	0.85	72	9.50	364.8 ± 42.5	0.10 ± 0.01
Scott (1991)	acid birn	5	99.4	0.14	16.20	1.94	72	6.05	145.9 ± 30.4	0.24 ± 0.05
Scott (1991)	acid birn	5.85	99.4	0.36	41.63	1.97	72	15.55	156.1 ± 18.9	0.10 ± 0.01
Scott (1991)	acid birn	6.8	99.3	0.17	19.68	2.17	72	7.344	149.0 ± 21.1	0.20 ± 0.03
Scott (1991)	acid birn	7.7	99.9	0.37	42.57	1.95	72	15.984	150.3 ± 9.3	0.09 ± 0.01
Scott (1991)	acid birn	8.2	99.9	0.15	17.26	1.88	72	6.48	208.4 ± 49.1	0.32 ± 0.08
Watanabe et al. (2013)	BMO	7	16	0.04–0.08	30–64	2.2–4.7	98[e]	2.5–5.2	23.6–50.0	0.62 ± 0.26

N/A: raw data not provided in study to calculate initial rate (R_0).

Abbreviations: acid birn: acid birnessite; HMO: hydrous manganese oxides; BMO: biogenic manganese oxides.

[a] Manganese oxide definitions from Villalobos et al. (2003).

[b] Mn:As molar ratio after converting MnO_2 from g L^{-1} to mol L^{-1} using FW of MnO_2 (82 g mol^{-1}).

[c] Effective surface sites (ESS) = 0.6 * g L^{-1} * SSA (m^2 g^{-1}).

[d] 273.5 m^2 g^{-1} from Lafferty et al. (2010a).

[e] BMO surface area from Villalobos et al. (2003).

In this paper, a comprehensive kinetic study of the MnO_2/As(III)/As(V) system was conducted over a pH range between 4 and 9 using excess MnO_2 to simulate natural environmental settings. The order of the reaction with respect to each component was determined, the overall rate constant of the reaction calculated and compared to other constants derived from the literature, and the mechanism of the reaction discussed based on experimental observations and molecular orbital considerations.

3.3 Methods

3.3.1 Preparation and Characterization of MnO_2

Unless otherwise noted, all chemicals used were ACS grade. Hydrous manganese oxides were prepared by titrating basic 0.2 M $KMnO_4$ (Fisher Scientific) with 0.3 M $MnCl_2$ (Fisher Scientific), the solution was stirred overnight with a magnetic stirrer and stir plate to allow the reaction to reach completion (Murray, 1973). The black precipitate formed from the reaction was rinsed three times, each with 0.1 M $MgCl_2$ (OmniPur) and milliQ water to remove excess Mn^{2+} ions (Tessier et al., 1979), then dried at 50^{o}C for 3-5 days. The dried MnO_2 was crushed with a mortar and pestle, and its surface area was determined by BET (Gemini VII) to be 186 ± 5.6 m^2/g. The structure was verified as vernadite, δ-MnO_2, by X-Ray Diffraction (XRD) spectra using reference spectra from the literature (Manning et al., 2002; Villalobos et al., 2006). Fresh MnO_2 were synthesized every month, even though XRD spectra of 2-6 month old dried MnO_2 did not show significant aging (data not shown). The average oxidation state (x in MnO_x) determined from a modified Winkler titration (J.D.H Strickland, 1972) was found to be 1.9 ± 0.1, thus verifying the oxidation state of the synthesized δ-MnO_2. Although MnO_2 was synthesized in the same

way for all experiments, about 50 µM dissolved Mn was initially detected in solution in the experiments performed at pH 4.6 that could have been caused by partial dissolution of the MnO_2 at this lower pH. To isolate the Mn^{2+} produced via As(III) oxidation from total dissolved Mn measured, 50 µM was subtracted from the measured dissolved Mn as a function of time in the pH 4.6 experiments only. Dissolved Mn was not detected in the background in all other conditions.

3.3.2 Abiotic Batch Experiments

As(III) stock solutions of 50 mM were prepared weekly by dissolving As_2O_3 (Aldrich) into 0.12 M NaOH. Control experiments at pH 7 (5 mM PIPES) demonstrated As(III) oxidation by dissolved oxygen did not take place over 12 days at room temperature (data not shown). Batch experiments were performed in buffered solution of PIPES (Acros Organics, 5mM) for pH 6-8 or MES (Sigma, 5 mM) for pH 4-6 investigations, 10 mM NaCl, and different concentrations of MnO_2, ranging from 0.1 to 1 g L^{-1}. PIPES was chosen as a buffer as it does not adsorb to the MnO_2 surface significantly in the 1-10 mM range (Ying et al., 2012). MES was chosen for lower pH values because it does not complex with metals (Kandegedara and Rorabacher, 1999). After adding the MnO_2 solid to the buffered solution, the pH was adjusted using HCl or NaOH to reach the desired pH. Incubations were conducted in glass Biological Oxygen Demand (BOD) bottles which were purged with ultra-high purity N_2 gas for two hours to remove dissolved oxygen before the addition of As(III) and sealed and crimped with rubber septa. The BOD bottles were then transferred into an anaerobic chamber (ThermoFisher), and small aliquots of 50 mM As(III) were added to the buffered MnO_2 slurry to reach the desired final concentration (60-175 µM). The BOD bottles were stirred continuously with a magnetic stir bar during the incubations.

Small aliquots (~1 mL) were removed at each time point and filtered using nitrocellulose membrane 0.22 µM filters (Millipore). Samples were stored at 4°C until analysis of As(III), then stored at -20°C until analysis of total soluble arsenic and manganese by ICP-MS (see below). Experiments were conducted in four sets: (A) varying initial As(III) concentrations at constant pH and in excess MnO_2 to keep its concentration constant, (B) varying initial, yet in excess of As(III), MnO_2 concentrations at constant pH in the presence of the same initial As(III) concentration, and (C &D) varying pH in the presence of the same initial As(III) concentration and two different excess MnO_2 concentrations (Table 3-2). The pH measured at the end of each experiment confirmed it varied by less than 0.2 pH units in these buffered solutions.

3.3.3 Analytical Techniques and Arsenic and Manganese Speciation

The pH was measured with a combination pH electrode (Orion) calibrated with pH 4.0, 7.0, and 10.0 standards (Fisher Scientific) at the same temperature as the samples. Dissolved As(III) concentrations were determined voltammetrically with a Metrohm VA 663 Hanging Mercury Drop Electrode coupled to an Ecochemie Autolab PGSTAT 12 potentiostat in a three electrode configuration, using a glassy carbon counter electrode and an Ag/AgCl/KCl (3M) reference electrode with a 2 M NaCl glass bridge. Samples were spiked to solutions pre-purged with N_2 gas that contained 0.8 mM $CuCl_2$, 2 M HCl, and 40 µM hydrazine (Chow and Taillefert, 2005; Li and Smart, 1996). A potential was applied for 30 seconds at -0.4 V to form a copper-arsine complex, then the potential was scanned cathodically from -0.4 to -1.2 V at a scan rate of 177 mV s^{-1} to reoxidize the copper-arsine complex. A minimum of triplicate scans were performed per sample. External calibration curves were obtained every 10 samples to ensure reproducibility. Detection limits of 300

nM with typical relative standard deviations of 0.5-8.0% (n=3) were obtained using this procedure. Total dissolved arsenic and manganese concentrations were determined in triplicate measurements by an Agilent 7500a Inductively Coupled Plasma-Mass Spectrometer. Standards and samples were prepared in 2% nitric acid (Trace Metal Grade, Fisher) and included Sc and Y internal standards (SPEX CertiPrep) to account for the drift of the instrument. Blanks were run every 10 samples, and calibration curves were run every 20 samples. Minimum detection limits (3σ of blank) for dissolved Mn and As were 0.5 and 0.3 nM. Dissolved As(V) was determined by difference between total dissolved arsenic and dissolved As(III). The sorbed fraction of arsenic was determined by difference of the initial concentration of added As(III) and total dissolved arsenic.

Assuming total dissolved Mn (Mn_d) measured by ICP-MS was mainly under the form of Mn^{2+} and that As(III) removal from the solution was due to its oxidation, the total concentration (µM) of As(III) removed ($As(III)_{removed}$) from solution at steady-state (t=15-60 minutes) corresponds to the total concentration of Mn^{2+} (µM) produced according to the 1:1 stoichiometric ratio of the overall reaction (Eq. 3-1). Thus, the difference between the concentrations of As(III) removed and total dissolved Mn produced at any point during the course of the reaction should represent the concentration of Mn^{2+} removed by adsorption or incorporated in the crystal lattice during comproportionation, or the concentration of partially reduced Mn(III) collectively termed [$Mn(II/III)_{surf}$] (Eq. 3-5, units of µM):

$$\left[Mn(II/III)_{surf}\right] = [As(III)removed] - [Mn_d] \qquad 3\text{-}5$$

3.4 Results

3.4.1 Speciation of Arsenic and Manganese

Typical examples of the evolution of the arsenic and Mn^{2+} speciation over time during the kinetic experiments at two different pHs are shown in Figure 3-1, while Table 3-2 lists all experiments performed and their respective conditions.

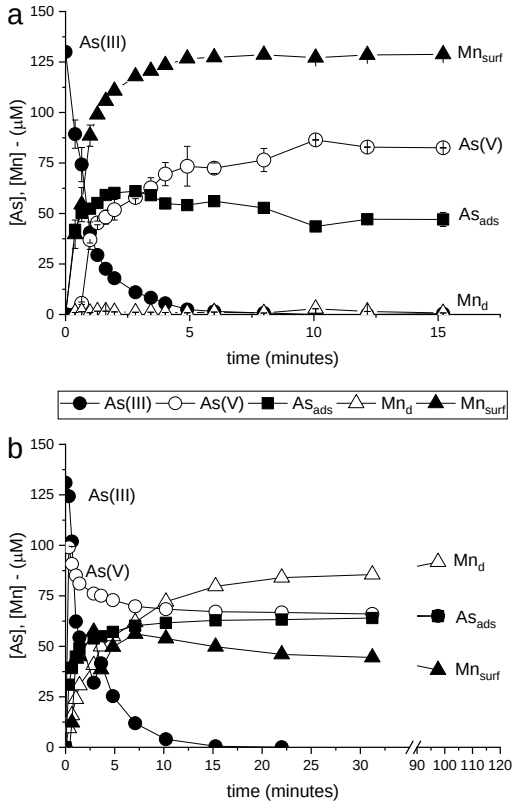

Figure 3-1 Concentrations of dissolved As(III) (closed circle), dissolved As(V) (open circle), adsorbed As (closed square), total dissolved Mn (open triangle) and surface Mn (closed triangle) over the course of an experiment in the presence of 10 mM NaCl, 0.5 g L^{-1} manganese oxides and 130 µM initial As(III) at: (a) pH 6.1 (PIPES); and (b) pH 4.6 (MES). For As(III), error bars represent the standard deviation between triplicate measurements of each sample. For As(V) and Mn(II), error bars represent instrumental error.

Table 3-2 Experimental Conditions, Effective Surface Site (ESS) Concentrations, Concentrations of Total Dissolved Manganese (Mn_d) and of Total Adsorbed Arsenic (As_{ads}) at Steady-State, Half-life of the Reaction, Pseudo-first Order Rate Constants (k_{obs}), Initial Rates (R_0), and Overall Second Order Rate Constants (k).

Condition	pH	$As(III)_i$ (μM)	MnO_2 (g L^{-1})	Mn:As Molar ratio	ESS (m^2 L^{-1})	Mn_d (μM)[b]	As_{ads} (%)[b]	half-life (min)	k_{obs} (h^{-1})	R_0 (μM h^{-1})	k (L m^{-2} h^{-1})
(A) As(III) varied	7.1	60	0.5	101.6	55.8	0.9 ± 0.2	66 ± 6	0.6 ± 0.0	74.9 ± 1.9	1551 ± 412	0.46 ± 0.12
	6.9	80	0.5	76.2	55.8	0.8 ± 0.1	44 ± 1	0.7 ± 0.0	63.8 ± 3.3	2155 ± 439	0.48 ± 0.10
	6.9	100	0.5	61.0	55.8	1.0 ± 0.4	38 ± 1	1.8 ± 0.1	23.5 ± 1.7	2216 ± 424	0.40 ± 0.08
	7.1	130	0.5	46.9	55.8	2.2 ± 0	29 ± 2	0.9 ± 0.1[a]	48.1 ± 6.5[a]	3599 ± 1134	0.50 ± 0.16
	7.1	175	0.5	34.8	55.8	0.1 ± 0	62 ± 1	1.1 ± 0.1	37.1 ± 1.6	4916 ± 403	0.50 ± 0.04
(B) MnO_2 varied	6.1	130	0.2	18.76	22.3	3.8 ± 0.0	27 ± 1	2.0 ± 0.3	21.3 ± 3.7	1008 ± 412	0.35 ± 0.14
	6.3	130	0.4	37.52	44.64	5.7 ± 0.1	36 ± 1	2.1 ± 0.2	19.6 ± 1.7	1154 ± 242	0.20 ± 0.04
	6.1	130	0.5	46.90	55.8	0.8 ± 0.0	36 ± 1	0.8 ± 0.0	54.5 ± 2.6	1862 ± 376	0.26 ± 0.05
	6.4	130	0.8	70.36	89.28	0.8 ± 0	47 ± 1	0.8 ± 0.0	51.0 ± 2.3	2303 ± 459	0.21 ± 0.04
	6.2	130	1.0	93.81	111.6	1.4 ± 0.2	57 ± 1	0.5 ± 0.0	84.6 ± 3.8	4163 ± 1128	0.29 ± 0.08
(C) pH varied	5.8	130	1.0	93.81	111.6	n.a.	n.a.	0.6 ± 0.0	71.1 ± 2.0	3943 ± 817	0.27 ± 0.06
($[MnO_2]$ = 1 g L^{-1})	7.2	130	1.0	93.81	111.6	n.a.	n.a.	0.6 ± 0.1	67.7 ± 5.1	4486 ± 864	0.31 ± 0.06
	7.9	130	1.0	93.81	111.6	n.a.	n.a.	1.0 ± 0.1	43.6 ± 3.3	3682 ± 597	0.25 ± 0.04
(D) pH varied	4.6	130	0.5	46.90	55.8	89.2 ± 0.4	50 ± 1	1.8 ± 0.2	22.8 ± 2.1	3652 ± 480	0.50 ± 0.07
($[MnO_2]$ = 0.5 g L^{-1})	5.8	130	0.5	46.90	55.8	3.1 ± 0.0	31 ± 1	1.4 ± 0.1	29.2 ± 1.4	2672 ± 538	0.37 ± 0.07
	6.3	130	0.5	46.90	55.8	1.6 ± 0.0	45 ± 1	0.9 ± 0.4	46.4 ± 2.1	1862 ± 376	0.26 ± 0.05
	7.1	130	0.5	46.90	55.8	2.2 ± 0	29 ± 2	0.9 ± 0.1[a]	48.1 ± 6.5[a]	3599 ± 1134	0.50 ± 0.16
	7.6	130	0.5	46.90	55.8	0.6 ± 0	18 ± 1	0.8 ± 0.1	53.4 ± 3.8	2612 ± 939	0.36 ± 0.13
	8	130	0.5	46.90	55.8	0.6 ± 0.2	17 ± 3	0.9 ± 0.0	48.7 ± 2.4	3284 ± 716	0.45 ± 0.10
	8.5	130	0.5	46.90	55.8	0.7 ± 0.0	34 ± 1	1.1 ± 0.1	36.8 ± 1.9	2964 ± 662	0.41 ± 0.09

Errors represent instrumental error, unless otherwise noted.

n.a: not measured.

[a] This data is an average of 3 separate experiments in the same conditions.

[b] Mn_d and As_{ads} were determined by ICP-MS at steady state. Standard deviations represent the variation of the last three data points of a time series.

The oxidation of As(III) by MnO_2 was rapid, and As(III) decreased according to an exponential decay in all experiments conducted (e.g. Figure 3-1), suggesting a pseudo-first order reaction. Although the concentration of As(V) in solution increased proportionally to the decrease in As(III), a significant fraction of arsenic was retained on the solid phase (Figure 3-1, Table 3-2). As As(III) oxidation is rapid following contact with MnO_2, adsorbed As(III) has yet to be observed in dilute solutions (Feng et al., 2018; Lafferty et al., 2010b; Manning et al., 2002; Wu et al., 2018). In addition, the oxidation of As(III) by MnO_2 (Eq. 3-2) was thermodynamically favorable in all experimental conditions (ΔG_{rxn}=-99 to -122 KJ mol^{-1}, Appendix B) as shown previously in acidic and basic conditions (Schacht and Ginder-Vogel, 2018). As a result, the disappearance of As(III) from solution was assumed to be solely due to oxidation and the adsorbed As fraction to consist of the As(V) product only. Speciation measurements determined that the adsorbed fraction of arsenic accounted for approximately 35 ± 13% of total As concentrations at the end of the experiments ($t \geq 15$minutes) conducted with 0.5 g L^{-1} of MnO_2 (Table 3-2). Simultaneously, the concentration of total dissolved Mn did not exceed 10 µM in all experiments conducted at pH > 5 (Figure 3-1a) but was much higher at lower pH (Figure 3-1b, Table 3-2). Total dissolved Mn reached a maximum concentration of c.a. 85 µM at the same time As(III) was completely oxidized to zero, and remained constant at steady state (Figure 3-1b). Adsorbed Mn(II/III) surface species at steady-state averaged 97±4% for each experiment conducted at pH > 5 (Table 3-2). At pH 4.6, however, dissolved Mn was mainly produced in solution over time (Figure 3-1b), indicating that Mn^{2+} did not adsorb significantly to the excess MnO_2 below pH 5.

3.4.2 Overall order of the reaction

The oxidation of As(III) by MnO_2 (Eq. 1) should be expressed by a general rate law that is a function of the As(III), MnO_2, and proton concentrations (Eq. 3-6). As the current experiments were conducted in excess of Mn(IV) compared to As(III), however, it is more realistic to express the rate law as a function of the effective surface sites of the MnO_2 (ESS) according to (Eq. 3-6):

$$R = -\frac{d[As(III)]}{dt} = k[As(III)]^a[ESS]^b[H^+]^c \quad \text{3-6}$$

where R is the rate of the reaction, k represents the rate constant, [As(III)] and $[H^+]$ the concentration of As(III) and H^+ (mol L^{-1}), the exponents a, b, and c are the rate orders with respect to each variable, and ESS is the effective surface sites term (m^2 L^{-1}) which is related to the ratio of edge sites to surface sites (assumed to be 0.6), the specific surface area (SSA in m^2 g^{-1}), and the concentration of MnO_2 (in g L^{-1}) (Tournassat et al., 2002; Villalobos et al., 2014) (Eq. 3-7):

$$[ESS] = 0.6 * SSA * [MnO_2] \quad \text{3-7}$$

3.4.3 Order with respect to As(III)

In the presence of excess MnO_2 and at constant pH, the rate law can be reduced and expressed with the pseudo-first order constant, k_{obs} (min^{-1}) (Eq. 3-8):

$$R = \frac{d[As(III)]}{dt} = -k_{obs}[As(III)]^a \quad \text{3-8}$$

where:

$$k_{obs} = k[ESS]^b\,[H^+]^c \quad \text{3-9}$$

To determine the order of the reaction with respect to As(III) concentrations, the effect of varying the initial As(III) concentration ($[As(III)]_0$) on the initial rate of As(III) oxidation (R_0) was determined at pH 7.1 in the presence of 0.5 g L^{-1} of MnO_2 (Figure 3-2a). The linearization of Eq. 3-8 leads to Eq.3-10:

$$logR_0 = logk_{obs} + a\,log[As(III)]_0 \quad 3\text{-}10$$

which was represented graphically (Figure 3-2b) to determine the order with respect to As(III) from the slope. A slope of 0.83 ± 0.08, rounded up to 1, indicates the reaction is first order with respect to [As(III)]. Eq. 3-8 can then be integrated into:

$$ln\left(\frac{[As(III)]}{[As(III)]_0}\right) = -k_{obs}t \quad 3\text{-}11$$

The integrated form of the rate law (Eq. 3-11) represented as a function of time (t, min) was linear in all experimental conditions (Figure 3-2c,e), in agreement with the behavior of a pseudo-first order rate reaction with respect to As(III) and justifying rounding up the order determined experimentally. As a result, the half-life ($t_{1/2}$, minutes) of each reaction (Eq. 3-12) was less than 3 minutes (Table 3-2).

$$t_{1/2} = \frac{ln\,(2)}{k_{obs}} \quad 3\text{-}12$$

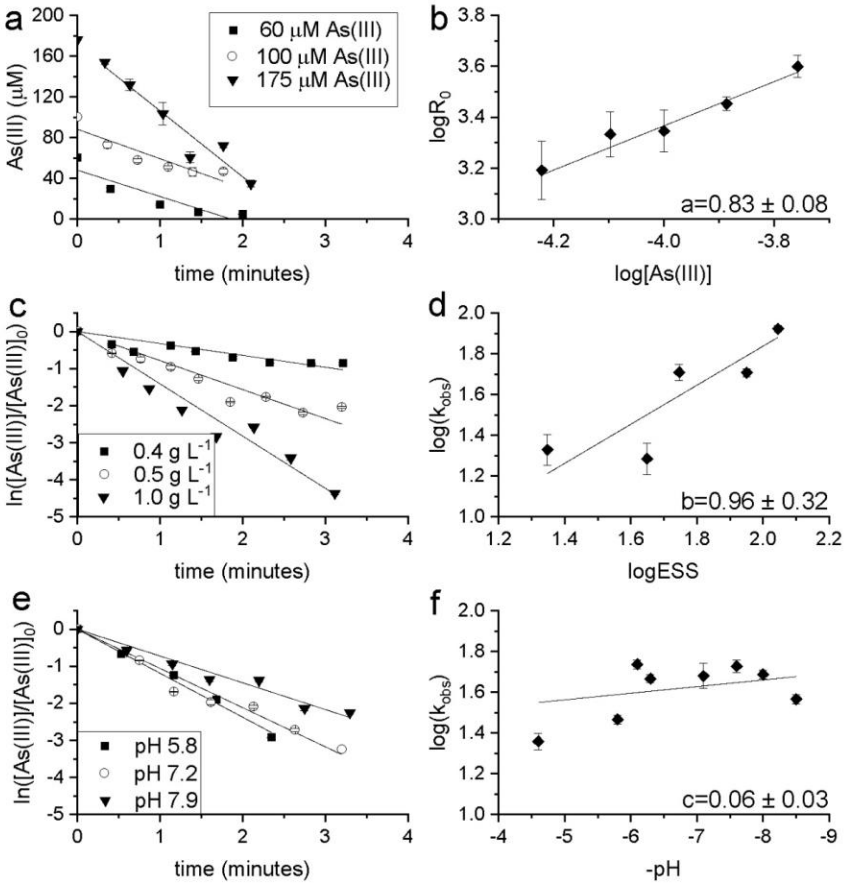

Figure 3-2 (a) Evolution of As(III) concentration vs time in the first few minutes of the reaction to determine the initial rate of the reaction. Experiments were conducted at pH 7.1 (5 mM PIPES), in the presence of 0.5 g L^{-1} MnO_2, and at varying concentrations of As(III) (60-175 µM); (b) Log of the initial rate of oxidation of As(III) (R_0) determined from each experiment as a function of the log of initial As(III) concentration to determine the order of the reaction with respect to As(III); (c) Linear regression of the integrated rate law for experiments conducted at pH 6.2 ± 0.1 (5 mM PIPES) in the presence of 130 µM As(III) and different concentrations of MnO_2 (0.4-1.0 g L^{-1}). (d) Log of the pseudo-first order rate constants (k_{obs}) determined from each experiment versus the log of the effective surface sites to determine the order of the reaction with respect to the mineral.(e) Linear regression of the integrated rate law for experiments conducted with 130 µM As(III) and 1.0 g L^{-1} MnO_2 at different pH; (f) Log of the pseudo-first order rate constants (k_{obs}) versus the negative of the pH value to determine the order of the reaction with respect to pH. Error bars of each data point represents the standard deviation of triplicate measurements. All experiments were performed in 10 mM NaCl.

3.4.4 Order with Respect to the Effective Surface Sites of MnO_2

To determine the order of the reaction with respect to the MnO2 effective surface sites (ESS), As(III) oxidation experiments in the presence of 130 µM As(III) were conducted at different concentrations of MnO_2 and constant pH. Linear regression of the integrated form of the pseudo-first order rate law (Eq. 3-11) over the first 3 minutes of the reaction (initial rate) was used to calculate the pseudo-first order rate constant, k_{obs} (Figure 3-2c). Equation 3-9 was then linearized in its logarithmic form to obtain Eq. 3-13:

$$log k_{obs} = b\, log(ESS) + log(k[H^+]^c) \qquad 3\text{-}13$$

A slope of 0.96 ± 0.32, rounded to 1, equivalent to a first order reaction with respect to the effective surface sites of the MnO_2 (exponent b), was obtained from the linear regression between log k_{obs} and the log of the effective surface sites (Eq. 3-13, Figure 3-2d). The reaction rate (Figure 3-2c) and pseudo-first order rate constant (Figure 3-2d) increased with the concentration of effective surface sites on the MnO_2, in agreement with previous studies (Manning et al., 2002; Villalobos et al., 2014), due to the increased availability of edges sites for As(III) oxidation (Lafferty et al., 2010b).

3.4.5 Order with Respect to pH

Experiments were performed over a range of pH with the same concentrations of MnO_2 (0.5 g L^{-1}) and As(III) (130 µM), and the evolution of As(III) concentrations was represented graphically (Figure 3-2e) using the integrated equation (Eq. 3-11) to determine the pseudo-first order rate constant (k_{obs}). Subsequently, Eq. 3-13 was rearranged and represented graphically (Eq. 3-14, Figure 3-2f) to determine the order of the reaction with respect to the log of the proton concentration (negative of the pH):

$$log k_{obs} = -c\ pH + log\left(\mathrm{k[ESS]^b}\right) \quad 3\text{-}14$$

The pseudo-first order rate constant did not change significantly over the pH range 4.6-8.5, (Figure 3-2f). The linear regression of the log of the pseudo-first order rate constant as a function of pH returned an order of 0.06 ± 0.03 (Figure 3-2f) in agreement with previous studies that showed the pH did not affect the As(III) oxidation rate significantly between pH 4 to 8.2 (Scott and Morgan, 1995). A similar set of experiments were performed with 1 g L^{-1} MnO_2 and 130 µM initial As(III) (Table 3-2C). The order with respect to the proton concentration for this set of experiments was also determined to be zero, based on a slope of 0.09 ± 0.06.

3.4.6 Overall Rate law and Second Order Rate Constant

The oxidation of As(III) by MnO_2 was experimentally determined to follow an overall second order rate law, including a first order reaction with respect to As(III) concentration and the effective surface sites of the MnO_2 and a zero order reaction with respect to the proton concentration (Eq. 3-15).

$$R = -\frac{d[As(III)]}{dt} = k[ESS][As(III)] \quad 3\text{-}15$$

The true rate constant, k, was then calculated from each experiment (Table 3-2) with this rate law (Eq. 3-15) and the initial reaction rate. Using this approach, an average overall second order rate constant of 0.36 ± 0.11 L hr^{-1} m^{-2} was obtained from all experiments performed in this study (Table 3-2).

3.5 Discussion

In this study, the speciation of arsenic and the production of Mn^{2+} were monitored during the oxidation of As(III) by MnO_2, and a kinetic rate law that describes the effect of pH on the reaction was determined. Although previous studies investigated the kinetics of this reaction, only pseudo-first order observed rate constants were reported (Table 3-1) and the effect of pH was not systematically investigated. The rate law developed in this study allows experiments to be compared across different published studies to help characterize the reaction mechanism.

3.5.1 The Effect of pH on the Reaction Rate

Although the reaction was zero order with respect to pH across the studied range, the pseudo-first order rate constants below pH 6 and above pH 8 were lower than around circumneutral pH (Figure 3-2f), suggesting mechanistic differences that affect the rate of the reaction. MnO_2 plays an important role in controlling the rate of As(III) oxidation because of its surface charge. As the first pK_a of the MnO_2 surface species ($> MnOH_2^+$) is extremely low (Eq. 3-16) and the second pK_a ($>$ MnOH) is mildly acidic (Eq. 3-17), the surface of the oxide is mainly neutrally charged below pH 4.6 and deprotonated above pH 4.6.

$$> Mn - OH_2^+ \rightarrow \ > Mn - OH + \ H^+ \quad pK_{a1} = -1.6 \qquad 3\text{-}16$$

$$> Mn - OH \rightarrow \ > MnO^- + \ H^+ \quad pK_{a2} = 4.6 \qquad 3\text{-}17$$

As demonstrated previously (Balistrieri and Murray, 1982; Murray et al., 1984; Smith and Jenne, 1991), the concentration of the double-protonated surface sites ($> MnOH_2^+$) is negligible above pH 2.0 (Figure A1), and an excess negative charge dominates the MnO_2

surface at most of the environmentally relevant pH investigated in the study (pH > 4.6). In contrast, As(III) remains protonated across most of the pH range studied, as its first acid dissociation constant is high (pK_{a1} = 9.2). As the first step in the oxidation mechanism is adsorption of As(III) to the MnO_2 surface, the following reactions illustrate the possible adsorption of each As(III) species on each MnO_2 surface species (precursor complexes represented as pairs with the • symbol) in the conditions of this study (Eq. 3-18-3-21):

$$> Mn - OH + H_3AsO_3 \overset{k_1}{\rightarrow} > MnOH \bullet As(OH)_3 \rightarrow > Mn - OAsO_3H + 3H^+ \quad (3\text{-}18)$$

$$> Mn - O^- + H_3AsO_3 \overset{k_2}{\rightarrow} > MnO^- \bullet As(OH)_3 \rightarrow > Mn - OAsO_3H + 2H^+ \quad (3\text{-}19)$$

$$> Mn - OH + H_2AsO_3^- \overset{k_3}{\rightarrow} > MnOH \bullet H_2AsO_3^- \rightarrow > Mn - OAsO_3H + 2H^+ \quad (3\text{-}20)$$

$$> Mn - O^- + H_2AsO_3^- \overset{k_4}{\rightarrow} > MnO^- \bullet H_2AsO_3^- \rightarrow > Mn - OAsO_3H + H^+ \quad (3\text{-}21)$$

Given the half-life of the reaction, it is assumed the adsorption is the rate-limiting step (Stumm and Morgan, 1996), suggesting the rate of the reaction is directly proportional to the concentration of adsorbate, itself controlled by the availability of surface sites and the As(III) concentration. The rate of formation of the adsorbed precursor complex may then be represented by (Eq. 3-22)

$$\begin{aligned} R_1 &= k_1[MnOH][H_3AsO_3] + k_2\,[MnO^-][H_3AsO_3] \\ &\quad + k_3[MnOH][H_2AsO_3^-] + k_4[MnO^-][H_2AsO_3^-] \\ &= \left(k_1\alpha_{MnOH}\alpha_{H_3AsO_3} + k_2\alpha_{MnO^-}\alpha_{H_3AsO_3} + k_3\alpha_{MnOH}\alpha_{H_2AsO_3^-} \right. \\ &\quad \left. + k_4\alpha_{MnO^-}\alpha_{H_2AsO_3^-}\right)S_T[As(III)]_T \end{aligned} \quad (3\text{-}22)$$

$$= k_{obs} S_T [As(III)]_T$$

where α_x represent the mole fractions of each species x (Eq 3-23-3-26) involved in the precursor complex formation reactions (Eq 3-18-3-21) and S_T and $[As(III)]_T$ represent the total concentration of MnO_2 (m^2 L^{-1}) and As(III) (M). The mole fractions (α_x) were calculated using the proton concentration ($[H^+]$, M) and acid dissociated constants (K_{ax}, dimensionless) (Eq 3-23-3-26) (detailed calculations in Supplementary Data Section S2).

$$\alpha_{MnOH} = \frac{K_{a1}[H^+]}{[H^+]^2 + K_{a1}[H^+] + K_{a1}K_{a2}} \quad 3\text{-}23$$

$$\alpha_{MnO^-} = \frac{K_{a2}}{K_{a2} + [H^+]} \quad 3\text{-}24$$

$$\alpha_{H_3AsO_3} = \frac{[H^+]}{[H^+] + K_{a1}} \quad 3\text{-}25$$

$$\alpha_{H_2AsO_3^-} = \frac{K_{a1}[H^+]}{[H^+]^2 + K_{a2}K_{a1} + K_{a1}[H^+]} \quad 3\text{-}26$$

It is therefore valuable to compare the experimentally determined pseudo-first order constant to the distribution of the precursor complexes (i.e. the arsenite surface species) as a function of pH to predict how the pH affected the reaction rate (Luther et al., 2018; Yao and Millero, 1993). To this end, the individual rate constants, k_1 to k_4, were calculated by fitting the k_{obs} data within the pH range where each individual rate constant is dominant using Eq. 3-22. The mole fractions of each surface and As(III) species (Eqs. 3-23-3-26) (vanLoon and Duffy, 2011) compared to the experimentally determined pseudo-first order rate constant (Figure 3-3) indicate that the dominant adsorption couple in the pH range 6-

8 was formed from the [MnO^-][H_3AsO_3] couple (k_2 = 51.8 ± 3.8 min^{-1}). In turn, the [MnOH][H_3AsO_3] couple was prominent at pH < 6, and the [MnO^-][$H_2AsO_3^-$] couple was prominent at pH > 8, though rate constants k_1 and k_4 were negligible in the fitting of the pseudo-first order rate constant. Additionally, the formation of the precursor complex based on the adsorption of $H_2AsO_3^-$ onto the neutral surface species (Eq. 3-20) was insignificant as >MnOH is present at low pH while $H_2AsO_3^-$ is formed at high pH. Overall, the expected second-order rate constant calculated over the entire pH range demonstrates the surface complex yielding k_2 is the dominant driver of the reaction in all conditions (Eq. 3-22, Figure 3-3).

The slightly lower pseudo-first order rate constants below pH 6 and above pH 8 can be reconciled by considering that below pH 6 the oxide surface and As(III) species are mainly protonated ([MnOH][H_3AsO_3] couple) and that the lack of attraction between two neutral species lowers the reaction rate. In contrast, when the surface is deprotonated (MnO^-), the neutral species H_3AsO_3 is more likely to be attracted to the surface, in agreement with the observation the pseudo-first order rate constants were highest around pH 7. At pH increases above 8, however, As(III) is deprotonated, promoting repulsion between the two negative species ([MnO^-][$H_2AsO_3^-$] couple) and ultimately decreasing the pseudo-first order rate constant (Figure 3-3).

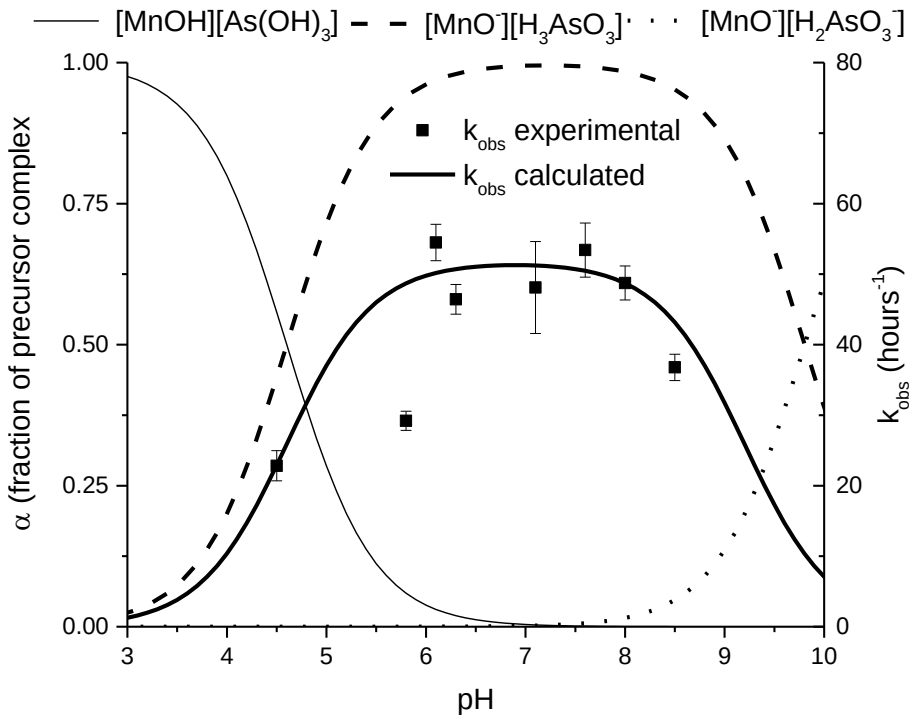

Figure 3-3 Predicted precursor species of the MnO_2 and As(III) surface complexes represented as a function of pH, compared to the pseudo-first order rate constant (k_{obs}) experimentally determined in the presence of 0.5 g L^{-1} MnO_2 and 130 µM As(III) at different pH. Error bars represent standard variations of the slope used to determine k_{obs} (Figure 3-2e). The calculated k_{obs} is represented by the thick line. The k_{obs} value at pH 7 represents the average and standard deviation of three sets of experiments conducted in the same conditions.

3.5.2 Effect of the Mn:As Molar Ratio on the Adsorption of Mn^{2+} and As(V)

Above pH 5.0, 97% of the reduced manganese was under the form of Mn(II/III) surface species at the end of the reaction (Table 3-2, Figure 3-1a) due to the negatively charged surface of the MnO_2 and its excess concentration, thus allowing for sufficient surface sites for both Mn^{2+} and As(III) adsorption. Near the pH_{pzc}, however, only 31% of reduced manganese was under the form of Mn(II/III) surface species at steady-state (Table

3-2, Figure 3-1b), likely because the surface of the oxide was mostly protonated (> MnOH) at lower pH, therefore decreasing the affinity of the surface for Mn^{2+}. Previous studies demonstrated similar trends (Manning et al., 2002; Scott and Morgan, 1995), though the little amount of Mn^{2+} released into solution was previously postulated to be evidence for the formation of Mn(III) species on the mineral surface by comproportionation of Mn^{2+} and Mn(IV) (Manning et al., 2002). Alternately, negatively charged vacancy sites could be present on the surface (Manceau et al., 2002) or in the interlayers (Elzinga, 2011) of the oxide that could readily adsorb Mn^{2+} ions.

Interestingly, the relative fraction of adsorbed As(V) at steady-state increased proportionally to the initial MnO_2 concentrations (Figure 3-4a), likely a result of the increase in reactive surface sites for both As(III) oxidation and As(V) adsorption as expected from the excess MnO_2 used in these experiments (Mn:As molar ratios of 19-102, Table 3-2). These findings are confirmed by the observation that As(III) did not oxidize completely within one hour in the presence of 0.1 g L^{-1} MnO_2 (Mn:As molar ratio 9.5) at pH 5.3, 7.1, or 8.3 (data not shown) even if the fraction of adsorbed As(V) remained proportional to the MnO_2 concentration (Figure 3-4a). In turn, the fraction of adsorbed As(V) at steady-state followed an inverse parabolic relationship with increasing As(III) concentrations in the presence of 0.5 g L^{-1} MnO_2 (Figure 3-4b). This behavior could be explained by the simultaneous increase adsorption of Mn^{2+} proportionally to the initial concentration of As(III) (Figure 3-4b). At low initial As(III) concentrations, enough edge sites were available for As(V) to adsorb and proportionally less Mn^{2+} was produced that competed with As(III) or As(V) for surface sites. When initial As(III) concentrations were increased, however, the concentration of Mn^{2+} produced may have been high enough to

decrease the availability of binding sites for As(V) adsorption, but not significant enough to change the overall charge of the mineral surface, such that the fraction of adsorbed As(V) decreased (Figure 3-4b). Above a critical As(III) threshold (~100 µM As(III), corresponding to a Mn:As ratio < 60), the continuous increase in adsorbed Mn^{2+} on the surface likely changed the overall charge of the surface and promoted As(V) adsorption. The reverse parabolic relationship between the fraction of adsorbed As(V) versus the total As supports the hypothesis that Mn(III) was not formed by comproportionation of Mn^{2+}, at least on the short time scale of these experiments. If Mn(III) was formed by comproportionation on the mineral surface, the surface charge would have not changed significantly as a result of the increased concentration of initial As(III) (Zhu et al., 2009). In these conditions, adsorption of As(V) should have therefore increased proportionally with the initial concentration of As(III) until surface sites were saturated. On the other hand, the adsorption of As(V) should have decreased proportionally to the initial concentration of As(III) as As(V) displays a lower adsorption affinity for Mn(III) compared to Mn(IV) surface species (Zhu et al., 2009). These findings do not imply that Mn(III) was not formed as intermediate during the reduction of MnO_2. It is entirely conceivable that the one-electron transfer reaction mechanism may have led to the formation of Mn(III) as surface intermediate, but its high reactivity may have precluded accumulation and led to the ultimate formation of Mn^{2+}.

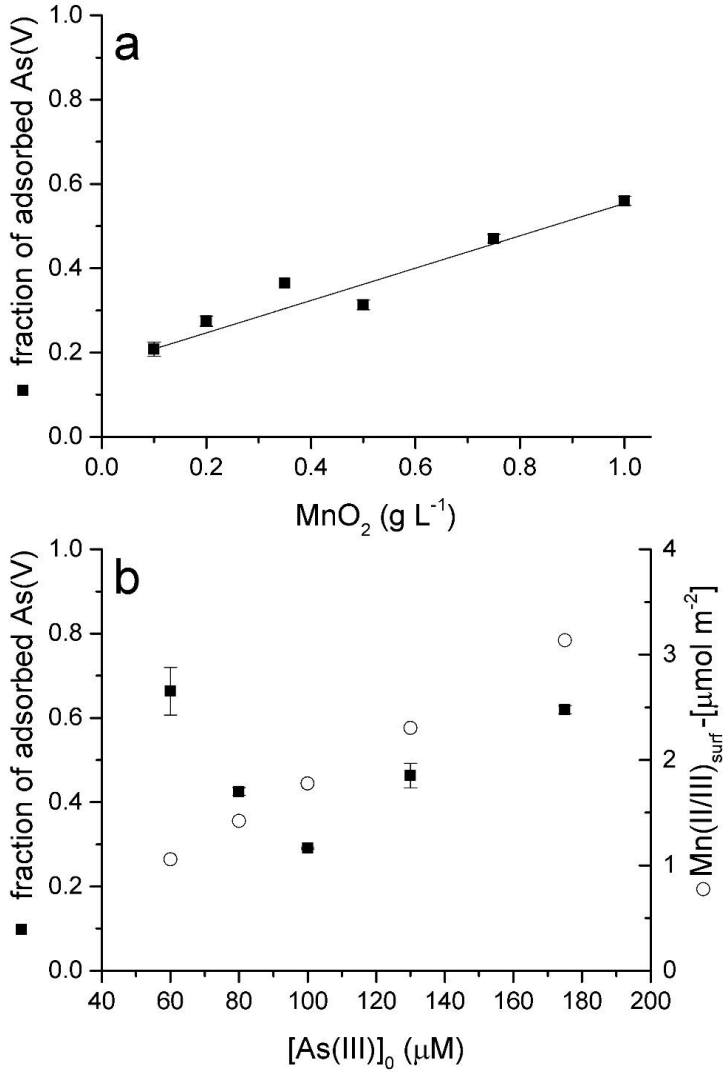

Figure 3-4 Fraction of adsorbed As(V) at steady-state (closed squares) as a function of: a) the initial concentration of MnO_2 (g L^{-1}) for experiments with 130 µM As(III) at pH 6.2 ± 0.2 (5 mM PIPES) except for the 0.1g L^{-1} MnO_2 data which was obtained at pH 7.1; and b) the initial concentration of As(III) at pH 7.1 (5 mM PIPES) in the presence of 0.5 g L^{-1} MnO_2. Mn(II/III) surface species calculated from Eq. 5 are represented as open circles.

3.5.3 Kinetics of the Reaction and Comparison to the Literature

The overall second order rate constants obtained in this study were compared to constants derived from the literature. Literature rate constants were calculated using the rate law (Eq. 3-15) and the initial rate of disappearance of As(III) if the data were provided (Ginder-Vogel et al., 2009; Manning et al., 2002; Power et al., 2005; Scott, 1991; Scott and Morgan, 1995; Villalobos et al., 2014). If the time series data were not available and only the pseudo-first order rate constant was reported, Eq. 3-9 was used along with the geochemical conditions to calculate the overall second order rate constant (Jones et al., 2012; Watanabe et al., 2013). When MnO_2 concentrations (g L^{-1}) were used instead of effective surface sites (ESS, m^2 L^{-1}), the disparity between rate constants of the present study and the literature became apparent (Figure 3-5a). Experiments of the present study, however, were conducted with MnO_2 of much larger surface area (186 ± 5.6 m^2/g) and in much higher excess Mn(IV) (i.e., Mn:As molar ratio of 19-102, Table 3-2) compared to the majority of studies from the literature (Table 3-1), suggesting that the surface area along with possible surface defects of the synthesized mineral plays a significant role in the kinetics of the reaction. Indeed, the overall second order rate constants calculated from the literature data using effective surface sites of MnO_2 (Table 3-1) compared robustly to the rate constants obtained in this study (Table 3-2, Figure 3-5b). As a result, the rate law developed from this study shows consistency across studies derived from an array of techniques, including X-ray Absorption Spectroscopy, extended X-ray absorption fine structure (EXAFS) (Manning et al 2002), HPLC-ICP-MS (Jones et al., 2012) ICP-AES (Power et al., 2005), and spectrophotometric measurements (Dhar et al., 2004; Power et al., 2005; Villalobos et al., 2014). More importantly, the proposed rate law accounts

correctly for the high As(III)-loading conducive to surface passivation (Ginder-Vogel et al., 2009; Power et al., 2005) providing that the frequency of data acquisition is high enough to determine initial rates. Finally, the proposed rate law demonstrates that the concentration of edge sites and the surface area of the mineral, rather than the concentration or the type of manganese oxides, control the kinetic of the reaction. In fact, the second order rate constant from this study (average of 0.36 ± 0.11 L m^{-2} hr^{-1}, Figure 3-5b) is even comparable to that (0.62 ± 0.26 in Table 3-1) obtained with biogenic manganese oxides (BMOs), likely the most prevalent Mn(IV) mineral in sedimentary environments, despite the likely high surface area of biogenic MnO_2 (Watanabe et al., 2013). In turn, the second order rate constant for the reduction of MnO_2 by As(III) is lower than that of H_2S (437 M^{-1} min^{-1}, Yao and Millero, 1993), NO_2^- (493 M^{-1} min^{-1}, Luther and Popp, 2002), and Fe^{2+}, perhaps because the arsenic atom of H_3AsO_3 is sterically hindered from the MnO_2 surface by the hydroxyl groups.

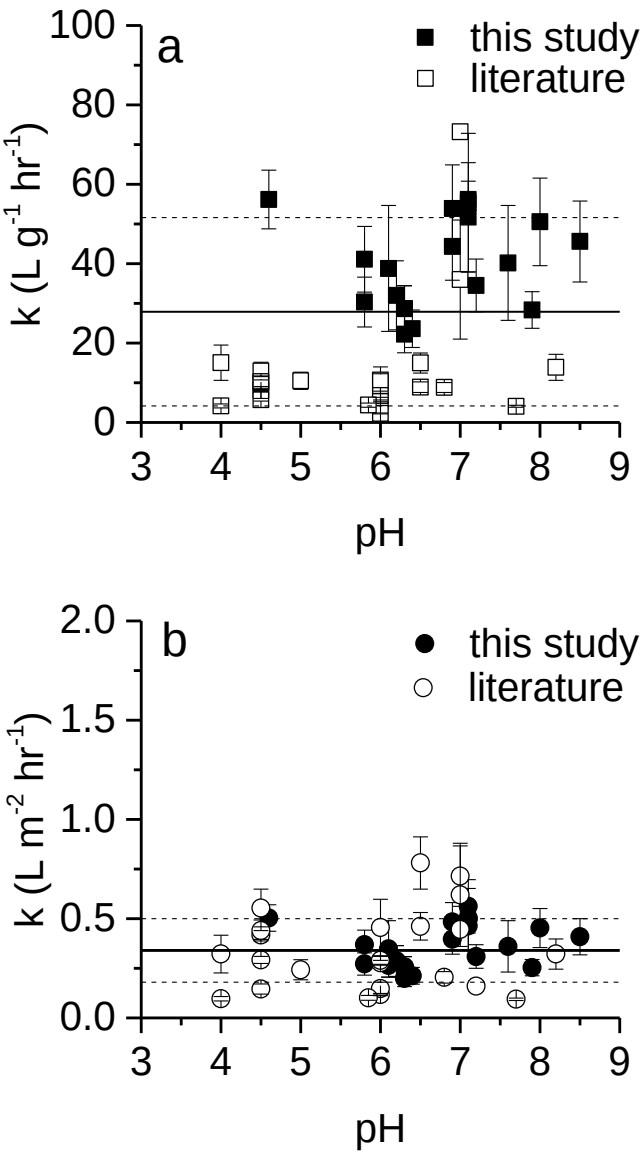

Figure 3-5 Comparison of overall second-order rate constants calculated from literature data (open symbols) and data obtained in the present study (closed symbols) using: (a) concentrations of MnO_2 (g L^{-1}); and (b) effective surface sites of MnO_2 (m^2 L^{-1}). Experimental conditions for rate constants from the literature are found in Table 3-1 whereas details of each experiment from this study are found in Table 3-2. Solid and dashed lines represent the average and standard deviations from the average rate constants.

3.5.4 Proposed Mechanism: Molecular Considerations

Based on the evidence from this study, the reaction proceeds mainly via interaction of the deprotonated Mn(IV) (> MnO^-) surface with the fully protonated As(III) (H_3AsO_3), with small contributions from the neutral Mn(IV) surface species (>MnOH) at pH < 6 and the deprotonated $H_2AsO_3^-$ species at pH > 8 (Figure 3-3). To transfer electrons, As(III) must be first drawn towards the MnO_2 surface via formation of a precursor complex. This attraction is created between the empty sigma antibonding (σ*) orbitals of the Lowest Unoccupied Molecular Orbitals (LUMO) of As(III) that are available for coordination and the Highest Occupied Molecular Orbital (HOMO) of the oxygen groups of the > MnO^- and > MnOH surface species (dashed line in Figure 3-6a). A Mn(IV) atom on the surface of a MnO_2 mineral has an inert $t_{2g}^3e_{g*}^0$ electronic configuration that decreases lability of its oxygen atoms (Figure 3-6a). The precursor complexes are therefore formed either by monodentate mononuclear adsorption or bidentate binuclear adsorption of As(III) on one or two surface oxygen groups via nucleophilic substitution (Zhu et al., 2009). After formation of the precursor complex, the lone pair of electrons from the s orbitals of As(III) may be transferred to the Mn(IV) center via different pathways depending on the structure of the mineral surface. If defects are present on the surface, the As(III) molecule may fit nicely between missing surface oxygen atoms and be in close contact with Mn(IV) to encourage the two-electron transfer pathway of the lone s pair of As(III) to the empty e_g^* orbitals of the Mn(IV) metal center (Figure 3-6b). The two-electron transfer pathway should be facilitated by the presence of a band of orbitals on the MnO_2 surface (Luther et al., 2018). Electron transfer may also be established via bidentate binuclear binding of As(III) and two one-electron transfers to neighboring Mn(IV) metal centers using two

different oxygen atoms as bridging ligands. As(V) and two surface Mn(III) species may form as products of this reaction (Figure 3-6c). Electrons transferred from As(III) may also go to surface or interior Mn(IV) atoms as electron transfer depends on which atoms make up the lower orbitals of the conduction band of orbitals (Luther et al., 2018). Lastly, if Mn(III) atoms are formed on the mineral surface or in the crystal lattice, the $t_{2g}^{3}e_{g*}^{1}$ electronic configuration becomes much more reactive and readily donates or accepts electrons. As a result, one As(III) could split its lone pair between two neighboring Mn(III) atoms and form two Mn^{2+} ions (Figure 3-6d). Following the electron transfer, between 20 and 50% of As(V), depending on the concentration of MnO_2 but regardless of the pH (Table 3-2), is adsorbed onto the remaining Mn(IV) surface sites. Above the pH_{pzc}, the majority of the Mn^{2+} adsorbs to the surface and, possibly, vacancy sites, whereas Mn^{2+} is mainly released into solution below the pH_{pzc}. It is less likely that the reaction mechanism may change from one two-electron transfer step above the pH_{pzc} to two one-electron transfer steps with formation of Mn(III) intermediate below the pH_{pzc} considering the little effect of the pH on the rate of the reaction and the presence of Mn(IV) bands of orbitals at all pH (Cotton et al., 1999). If a change of mechanism was occurring across the pH_{pzc}, a corresponding change in the reaction rate would have been observed. These findings suggest that the Mn^{2+} product was mainly removed by adsorption onto the MnO_2 surface.

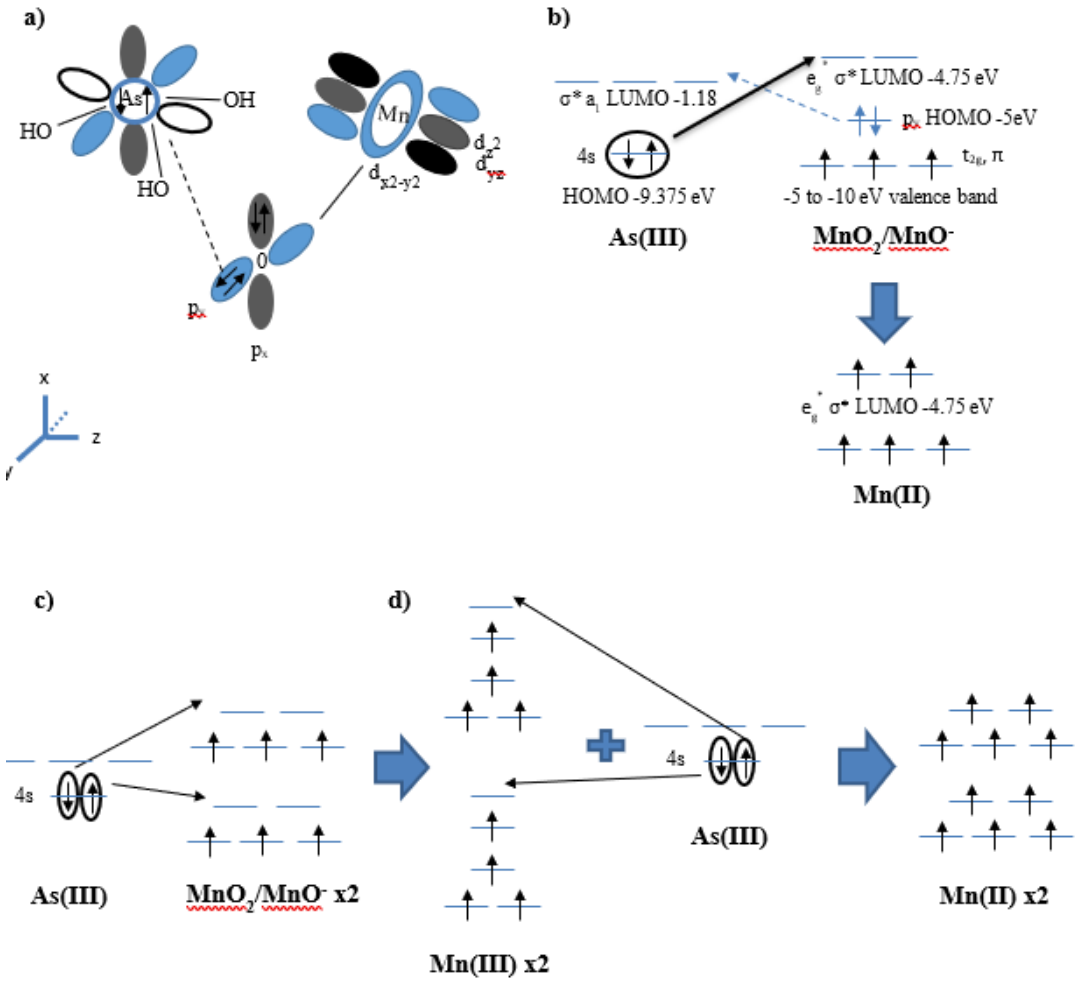

Figure 3-6 a) Formation of the precursor complex between the LUMO of As(III) and HOMO of the oxygen in the > MnO- or > MnOH surface species identified experimentally (Figure 3-3). A lone pair of electrons is found in the s orbitals of As(III); (b) Electron organization before transfer and resulting Mn(II) electron configuration. Energies for As(III) were computed using HyperChemTM program version 8.0.10 from Hypercube, Inc®; (c) Electron transfer from one As(III) molecule to two Mn(IV) atoms resulting in two Mn(III) atoms; and (d) Two Mn(III) atoms accept one electron each from the lone pair of electrons on As(III) to form two Mn(II) molecules.

3.5.5 Environmental Implications

Manganese oxides are pervasive in sedimentary environments and represent a strong oxidant of any As(III) introduced anthropogenically or via natural geochemical or microbial processes. The findings of this study demonstrate that small concentrations of As(III) introduced to a manganese-rich sedimentary environment should be efficiently oxidized to As(V) over the wide range of pH usually encountered in natural environments. Under these conditions, the As(V) product may be readily adsorbed to the excess Mn(IV) surface sites available, thus providing an effective natural attenuation mechanism. If the concentration of As(III) increases relative to the Mn(IV) oxide concentration such that the Mn:As molar ratio dips below 60, however, the pH and the concentration of the Mn^{2+} product or any other divalent cation present in solution may control the overall mobilization of As(V). In addition, the rate of As(III) oxidation is proportional to the surface area of the Mn(IV) oxide and concentration of edge sites available on its surface, indicating that crystalline Mn(IV) oxides with smaller surface area should be less reactive than poorly crystalline minerals such as BMOs. In the presence of large concentrations of As(III) and at the circumneutral pH of most environments, however, the reactive surface sites of Mn(IV) oxides may become saturated with the Mn^{2+} or As(V) reaction products. Under these conditions, the oxidation of As(III) may be incomplete and As(III), which is more toxic and mobile than As(V), may spread over a wider surface area in the environment.

Divalent cations (e.g., Mn^{2+}, Zn^{2+}, Pb^{2+}) commonly occurring in natural or contaminated environments may passivate the mineral surface and decrease the As(III) oxidation rate by MnO_2 (Power et al., 2005; Villalobos et al., 2014). The proposed rate law could easily account for this passivation effect by adjusting the ESS concentration (Eq. 3-

7). Indeed, initial rates of -27.4 and -78.5 µM As(III) hr^{-1} determined for the oxidation of 100 and 300 µM As(III) by 0.1 g L acid birnessite at pH 4.5 in the presence of 100 µM Zn^{2+} (Power et al., 2005) required to decrease the ratio of available surface sites to 0.2 to reflect less surface sites were available for reaction. In turn, naturally-occurring ligands that stabilize Mn(III) in solution (Duckworth and Sposito, 2005, 2007; Oldham et al., 2017; Oldham et al., 2015) could affect the mechanism of As(III) oxidation and facilitate two one-electron transfer reactions (Figure 3-6c). Stabilization of Mn(III) in solution may therefore enhance the number of vacancy sites on the mineral surface and increase mineral reactivity. Simultaneously, enhanced production of surface Mn(III) may increase As(III) oxidation rates as recently demonstrated (Lan et al., 2018), though comproportionation of Mn(II) and Mn(IV) may not play a significant role in the time frame of these experiments (< 15 minutes). In this case, the proposed rate law could also be adapted by simply increasing the ESS concentration. Finally, the presence of redox inactive mineral surfaces-such as aluminum oxides, silicates, and clays may affect the application of this rate law in natural environments. For example, As(III) adsorbs to Al oxides which may decrease its availability for reaction with MnO_2 (Arai et al 2000). Although As(V) adsorbs minimally to SiO_2 (Nair et al., 2014), As(V) adsorbs to Al oxides (Arai et al., 2000) and clay mineral surfaces (smectite and kaolinite) (Mukhopadhyay et al., 2017). Furthermore, ternary complexes may form with adsorbed cations (e.g., Fe(II)) on mineral surfaces, potentially increasing the removal of As(V) via non redox reactions (Zhu and Elzinga, 2015). If redox inactive surfaces are available for the adsorption of As(V), passivation of the MnO_2 surface with the reaction product will be prevented and the As(III) oxidation potential will increase. The presence of these parallel reactions could easily be considered in the current rate law

by using the effective concentration of As(III) available for reaction or by varying the ESS concentration according to the changes in availability of surface sites.

3.6 Conclusions

The kinetics of As(III) oxidation by manganese oxides has been investigated in a variety of contexts but not well constrained, nor systematically studied with respect to pH and MnO_2 and As(III) concentrations. As As(III) is more mobile and toxic than As(V) and manganese oxides are the most efficient oxidants of As(III), a universal rate law is imperative to understand and predict the chemical transformation of arsenic in the environment. In this study, the speciation of As(III) and As(V) was determined within the first few minutes of the reaction to determine the order of the reaction with respect to As(III), MnO_2, and proton concentrations as well as the overall rate constant of the reaction using the initial rate method. Experiments were performed in excess MnO_2 relative to As(III) to reflect the geochemical conditions of the vast majority of environments and eliminate the effect of surface passivation by the reaction products on the reaction rate. Results revealed that the rate law is first order with respect to the concentrations of As(III) and the effective Mn(IV) surface sites and zero order with respect to the proton concentration. Although the pH did not have a significant effect on the rate of the reaction, small variations in the pseudo-first order rate constant below pH 6 and above pH 8 suggest that the changes in speciation of As(III) and the protonation of the MnO_2 reactive surface sites affect the reaction mechanism. The developed rate law was applied to previously published data sets that were obtained in a wide variety of geochemical conditions with different mineral phases to calculate the overall second order rate constant of the reaction. The overall second order kinetic constants of published studies were comparable to that

obtained in this study when using the concentration of effective surface sites only, demonstrating that the concentration of edge sites and the surface area of Mn(IV) oxides mainly control the rate of the reaction. Speciation calculations as a function of pH revealed the main surface precursor complexes is the deprotonated MnO^- species bound to the fully protonated H_3AsO_3. Given the high rate of these reactions, a two-electron transfer reaction may be preferred, especially if vacancy sites are available to promote fast electron transfer. Two steps of one-electron transfer, however, may be possible though it is likely that both Mn(IV) and Mn(III) species are ultimately reduced to produce Mn^{2+}. Comproportionation of Mn^{2+} and Mn(IV) to Mn(III) does not seem to be important on the time scale of these experiments. Finally, increasing the concentration of As(III) may have important consequences on the reaction rate and mechanism, as experiments demonstrated that As(V) and Mn^{2+} products both passivate the surface of the mineral, even in excess concentration of MnO_2 compared to As(III). As the concentration of As(III) increased, a proportionally higher concentration of the As(V) product was released into solution. Above an As(III) concentration threshold (corresponding to a Mn:As molar ratio below 60), however, the concentration of the adsorbed Mn^{2+} product was likely high enough to reverse the surface charge of the MnO_2 and increase its affinity for As(V). As Mn(IV) oxides are the most efficient oxidants of As(III), the findings of this study have important environmental implications. First, the second order rate law developed in this study should be able to predict the fate of As(III) in a variety of geochemical conditions with different Mn(IV) minerals, including biogenic manganese oxides which are most prevalent in sedimentary environments. Second, As(III) introduced to a Mn(IV)-rich sedimentary environment should be efficiently oxidized to the less toxic and less mobile As(V), though at Mn:As

molar ratios below 60, the overall adsorption of As(V) may be controlled by the concentration of the Mn^{2+} product or any other divalent cation in solution. Finally, the mobility of As(III) may be enhanced in the presence of more crystalline MnO_2 phases or in the presence of large As(III) concentrations which decrease the rate of As(III) oxidation. Although the presence of excess cations (Mn^{2+}, Zn^{2+}, etc.), Mn(III)-stabilizing ligands, and non-redox inactive mineral surfaces may affect the rate of As(III) oxidation by MnO_2, these effects may be account for by modifying the effective surface species concentration.

3.7 Acknowledgements

This work was funded by the Low Temperature Geochemistry and Geobiology (EAR-1325098 to MT) and Chemical Oceanography (OCE 1558738 to GWL) Programs of the National Science Foundation. The authors thank the three anonymous reviewers for their thoughtful suggestions to improve an earlier version of this paper.

CHAPTER 4. ENHANCED ANAEROBIC MICROBIAL REDUCTION PROMOTED BY AS(V) TOXICITY

This chapter is authored by Shannon Owings[1], Jordon Beckler[2], Grace McNamee[1], Seng K. Wee[3], Hyun-Dong Shin[4], Thomas DiChristina[4], Martial Taillefert[1]

[1]School of Earth and Atmospheric Sciences, Georgia Institute of Technology, Atlanta GA 30332 [2]Florida Atlantic University, Harbor Branch Oceanographic Institute, Boca Raton, FL 33431 [3]Faculty of Bioengineering and Technology, Universiti Malaysia Kelantan, Kelantan, Malaysia [4]School of Biological Sciences, Georgia Institute of Technology, Atlanta GA 30332

4.1 Abstract

To elucidate the effect of arsenic on microbial processes, this study investigated the effect of arsenate (As(V)) concentrations on the dissimilatory reduction of nitrate (NO_3^-), manganese oxides (MnO_2), and iron oxides ($Fe(OH)_3$) by different strains of the model metal reducing bacteria *Shewanella putrefaciens* 200, that carry both As(V) respiration (arr) and detoxification (dsr) genes, and *Shewanella oneidensis* MR-1 that is unable to respire on As(V) and lacks important components of the *ars* operon. As(V) toxicity was always observed in low cell densities or low orthophosphate conditions in the medium, suggesting inorganic phosphate transporter systems are involved in As(V) intracellular uptake. In general, NO_3^- reduction rates decreased, whereas MnO_2 and $Fe(OH)_3$ reduction rates increased in the presence of low but increasing As(V) concentrations. The highest As(V) concentrations (5-10 mM), however, were irreversibly toxic to both organisms.

Arsenite, (As(III)), the byproduct of As(V) reduction via detoxification or respiration, was rapidly produced when incubated on $Fe(OH)_3$, yet remained in relatively low concentrations in solution, unless As(III) concentrations exceeded the availability of adsorption sites on the remaining $Fe(OH)_3$. In turn, As(III) did not accumulate into solution until the complete reduction of MnO_2, likely due to the fast recycling of As(V) by MnO_2-driven abiotic oxidation of As(III). As(V) toxicity was enhanced in the presence of MnO_2 relative to $Fe(OH)_3$ by the apparent increase in As(V) exposure through this abiotic recycling mechanism and decrease in As(V) exposure as a result of the high As(V) scavenging onto $Fe(OH)_3$ surfaces at circumneutral pH. When As(V) concentrations were high enough to saturate the $Fe(OH)_3$ surface sites, however, As(V) toxicity resulted in a lag phase in $Fe(OH)_3$ reduction but respiration was restored once As(V) was completely reduced. Overall, these findings indicate As(V) is most toxic in the aqueous phase and As(V) toxicity results in enhanced respiration to compensate for cell stress and the energy required for detoxification. Thus, arsenic in sedimentary environments is not simply immobilized by adsorption. Instead, a suite of complex abiotic and microbial processes including adsorption, intracellular uptake, and redox reactions may affect the transport of arsenic in the environment, and ultimately the quality of drinking water resources.

4.2 Introduction

Arsenic may naturally accumulate above the World Health Organization guideline of 10 ppb (WHO, 2000) in aquifers around the world (Ahmed et al., 2004; Nickson et al., 2000)and therefore presents a global risk to human health (Nordstrom, 2002; Rasheed et al., 2017; Smith et al., 2000b). Arsenic is also introduced anthropogenically into the environment by mining, manufacturing, and agricultural practices (Bode and Dong, 2002;

Christen, 2001; Mukhopadhyay et al., 2002; Oremland and Stolz, 2003) and generally accumulates in low, yet detectable concentrations in aquatic environments (Chow and Taillefert, 2005; Donner et al., 2017; Smedley and Kinniburgh, 2002).

Arsenite (As(III)), under the form of the neutral H_3AsO_3 species across the pH of most aquatic environments (pKa values 9.2, 12.1, and 13.4), and arsenate (As(V)), under the form of the weak acid $H_2AsO_4^-$ at circumneutral pH (pKa of 2.24, 6.76, 11.6), represent the two most common oxidation states of arsenic in the environment (Stumm and Morgan, 1996). Given its neutral charge, As(III) represents the more mobile form of arsenic, whereas As(V) readily adsorbs to mineral surfaces such as clays and Fe(III), Al(III), and Mn(IV/III) oxides and, consequently, is less mobile (Amirbahman et al., 2006; Arai et al., 2001; Raven et al., 1998. As As(V) is only reduced abiotically by dissolved sulfide with a half-life of several months {Newman, 1997 #312; Rochette et al., 2000), and poorly reduced by structural S^{2-} from mackinawite (FeS) (Troyer et al., 2014), As(V) in aquatic systems is considered to be mainly reduced microbially via respiration (Krafft and Macy, 1998) or detoxification (Saltikov et al., 2005) processes. On the other hand, As(III) may be chemically oxidized to As(V) by dissolved oxygen (half-life of days) (Kim and Nriagu, 2000), Mn(IV) oxides (half-life of minutes to hours) (Kim and Nriagu, 2000; Oscarson et al., 1981b; Oscarson et al., 1981c; Oscarson et al., 1983; Owings et al., 2019), $Mn^{III}OOH$ (half-life of hours) (Chiu and Hering, 2000), and freshly formed iron oxyhydroxides (Amstaetter et al., 2010). These findings indicate that manganese oxides likely represent the main abiotic oxidant of As(III) in natural aquatic systems.

The arsenate molecule, $H_2AsO_4^-$, chemically resembles phosphate, $H_2PO_4^-$, with the main atom bound by four oxygens in a tetrahedral arrangement. The similarity of the two

molecules allows arsenate to enter cells via phosphate transporters (Rosenberg et al., 1977; Willsky and Malamy, 1980b). The two main inorganic phosphate (Pi) transport systems present in bacterial cells includes the high affinity phosphate specific transporter, Pst, and the low affinity inorganic phosphate transporter, Pit, systems (Willsky and Malamy, 1980a). In the more dominant Pst transport system, the *phoS* and *phoT* genes that are part of the *pho* operon are involved in the regulation and synthesis of the alkaline phosphatase (in low Pi conditions) (Willsky and Malamy, 1980a). The Pit system is a low affinity-high velocity system which favors arsenate uptake into the cell (at high Pi concentrations) (Willsky and Malamy, 1980b). Arsenite, $As(OH)_3$, toxicity derives from the fact it resembles glycerols, simple sugars also known as polyols, and enters prokaryotic cells via the glycerol facilitator, GlpF, as in yeast (Wysocki et al., 2001) and in a similar fashion as the trivalent antimonite, Sb_2O_3, which was recognized as a polyol in *E. Coli* (Sanders et al., 1997). Additionally, arsenite binds to sulfhydryl groups resulting in the deactivation of numerous enzymes once inside the cell.

4.2.1 Arsenic Detoxification

Once inorganic arsenic enters the bacterial cell, different detoxification pathways are activated. First, As(V) can be removed from the cell by methylation, a process that is well understood for fungi and eukaryotes, but not absolute in the prokaryotic world (Stolz et al., 2006). The Challenger pathway of methylation proceeds as sequential steps of oxidative addition of a methyl group from S-adenosylmethionine (SAM) metyltransferase to produce a methylated arsenate species, followed by the reduction to the methylated arsenite species (Bentley and Chasteen, 2002; Stolz et al., 2006). This series of oxidative additions and reductive elimination steps are repeated sequentially to form

monomethylarsonate (MMAs(V)), monomethylarsonite (MMAs(III)), dimethylarsinate(DMAs(V)), dimethylarsinite (DMAs(III)), trimethylarsine oxide (TMAO) and trimethylarsine (TMAs(III)), the final of which is volatile (Bentley and Chasteen, 2002; Stolz et al., 2006). This pathway is also proposed for bacteria, although arsine, Me_xAsH_{3-x} (where x=0-2), represents the most commonly formed by-product (Bentley and Chasteen, 2002). In addition to the Challenger mechanism, it has been proposed that substrate of the methytransferase is a glutathione conjugate $As(GS)_3$ that positions As on the cysteine groups of the protein via thiol exchange with glutathione. SAM is still involved in the methyl transfer reaction, however, instead of the oxidation of As(III), glutathione (GSH) is oxidized by SAM during the methylation process (Ajees and Rosen, 2015; Hayakawa et al., 2005). *Shewanella oneidensis* MR-1 methylates As species while reducing Fe(III) in laboratory conditions amended with SAM and SAM with GSH (Wang et al., 2016).

The better known detoxification mechanism involves the reduction of As(V) to As(III) followed by As(III) expulsion from the cell using the *ars* operons (Mukhopadhyay et al., 2002; Saltikov and Newman, 2003). The first reduction step is performed by the arsenate reductase ArsC, an enzymatic cytoplasmic protein encoded by the *arsC* gene (Ji and Silver, 1992). Prokaryotes remove the reduction product, As(III), from the cell using the As(III) sensitive repressor protein, ArsR, and the inducer-independent repressor, ArsD. ArsA, an ATPase structural subunit, and ArsB, together create a transmembrane oxyanion conducting channel, essentially acting as As(III) efflux pump (Rosen et al., 1995; Rosen, 2002). The percent amino acid identity and similarity of *arsB* and *arsC* are < 50% in *S. oneidensis* MR-1 relative to ANA3 (Jiang et al., 2013; Saltikov and Newman, 2003),

meaning MR-1 does not have the As(V) reductive and As(III) transport systems of the ars operon. In turn, the amino acid sequences of the *arsD*, *arsA*, *arsB*, and *arsC* putative genes were identified (>70%) in *Shewanella putrefaciens* 200 (Jiang et al., 2013). In addition to the As(III) efflux pump system, the arsenite oxidase enzyme, Aox, a molybdenum enzyme similar to the dimethylsulfoxide reductase family that consists of a large subunit with Mo and [3Fe-4S] clusters and a small subunit homologous to [2Fe-2S] proteins, is sometimes used for detoxification (Ellis et al., 2001; Hoke et al., 2004). Interestingly, some heterotrophic arsenite oxidizers (HAOs) express similar enzymes (vanden Hoven and Santini, 2004).

4.2.2 Arsenic Respiration

A variety of other prokaryotes gain energy during dissimilatory arsenate reduction using the respiratory arsenate reductase gene, *arr*. The Arr enzyme consists of a heterodimer with two subunits, ArrA and ArrB. The reductase is composed of molybdenum, iron, acid-labile sulfur, and zinc, leading to the conclusion that ArrA contains cysteine clusters and ArrB is made of iron-sulfur proteins (Krafft and Macy, 1998). Although the use of 'toxic' chemicals for growth is surprising, the redox potential of the As(V)/As(III) is +135 mV and heterotrophic arsenate reduction is thermodynamically favorable (Oremland and Stolz, 2003). Indeed, *Shewanella* species strain ANA-3 couples lactate oxidation to the reduction of As(V) (Saltikov et al., 2003). The presence of *arr*A and *arr*B putative genes and respiration activity were identified in *S. putrefaciens* strain 200 but no data was available to compare *arrA* and *arrB* similarity to *S. oneidensis* strain MR-1 (Jiang et al., 2013).

Previous studies demonstrated that dissolved arsenate (As(V)) diffuses out of Chattahoochee River (GA) sediments, suggesting active remobilization of As(V) into surface waters (Chow and Taillefert, 2005; Lesley and Froelich, 2003). Small As(V) concentrations ($\leq$ 1 μM) added to Chattahoochee River (GA) sediments increased microbial reduction rates of naturally-occurring Fe(III) oxides and remobilized arsenic trapped by adsorption onto the sediment into the pore waters (Chow and Taillefert, 2009). The rate increases could not simply be attributed to increased growth, suggesting that a change in mechanism of dissimilatory iron reduction was in effect. The effect of As(V) concentrations on dissimilatory nitrate, manganese oxides (MnO_2), and iron oxides ($Fe(OH)_3$) reduction by strains of the model metal reducing bacteria *Shewanella* that are capable of arsenic respiration or detoxification was investigated in laboratory incubations to elucidate the mechanisms involved in arsenic transformation in the environment. Incubations were monitored to detect As(V) reduction and methylation as detoxification pathways. In addition, incubations were performed with mutant strains of *S. oneidensis* MR-1 to determine the role of the Pst system in As(V) reduction.

4.3 Methods

4.3.1 Synthesis of vernadite and 2L ferrihydrite

Synthesis of vernadite (MnO_2) and 2L ferrihyride ($Fe(OH)_3$) took place under sterile lab conditions. Manganese oxides (50 mM MnO_2) was prepared by the drop wise (approx. 1 drop/sec) addition of a solution of $MnCl_2$ (0.3 M) to a basic solution (0.4M NaOH) of $KMnO_4$ (0.2 M) (Murray, 1973). The solution was stirred overnight with a magnetic stirrer and stir plate to allow the reaction to reach completion. The black precipitate formed from

the reaction was rinsed three times each with 0.1M $MgCl_2$ and DI water to remove excess Mn(II) ions. After rinsing, the oxides were dried at 50°C for 3-5 days. The dried birnessite was crushed with a mortar and pestle then analyzed. The surface area was determined to be 182 and 190 m^2/g by BET nitrogen adsorption experiments. The structure was verified as δ-MnO_2 according to X-Ray Diffraction (XRD) spectra and compared to literature (Manning et al., 2002; Villalobos et al., 2006). In some experiments the drying step was skipped, in this case the manganese oxides are referred to as hydrous manganese oxides (HMO). $Fe(OH)_3$ was prepared by the steady addition of a 10 N NaOH solution to a $FeCl_3$ solution (0.4 M) using a peristaltic pump until the final desired pH of 7 was reached. The resulting precipitate was rinsed 3x with water and stored until use. Concentration of the stock solution was determined by reducing an aliquot of stock with hydroxylamine to measure total Fe(II) by the ferrozine method (Stookey, 1970).

4.3.2 Stock solution preparation

Arsenate (As(V)) stock solutions were made by dissolving As_2O_5 (Alfa Aesar, 99.9%) into sterile water. Arsenite (As(III)) stock solutions were made by dissolved As_3O_5 (Alfa Aesar) into 0.1 M NaOH. Dimethylarsinate (DMA) standards were prepared by dissolving cacodylic acid (Sigma) in water, and monomethylarsonate (MMA) standards were prepared by dissolving methyl arsonic acid disodium salt (TRC Canada) in water. A 10 mM phosphate buffer stock solution was made using the appropriate proportions of HNa_2PO_4 and H_2NaPO_4 for the desired pH and filter sterilized. Final phosphate concentrations added to incubations were calculated from the volume of the stock solution and the desired volume of the incubation. The M1 medium used for incubations included 20 mM lactate (Fisher Sci) as electron donor, 15 mM PIPES (Fisher Sci.) as pH buffer, 2

µM Mn^{2+}, 240 µM Ca^{2+}, and 500 µM Mg^{2+} as chloride salts, and 35 µM EDTA to limit their removal by adsorption.

4.3.3 Cell cultures and incubation experiments

All microbial work was performed in sterile conditions by wiping down the bench top with ethanol, working under a flame, and degassing solutions with a 0.22 µm filter between the gas tank and the media. All glassware and solutions were either autoclaved or filter-sterilized. *S. putrefaciens* 200 and *S. oneidensis* MR1 were chosen based on their varying sensitivities to arsenic. *S. putrefaciens 200* encodes the *arr* respiratory and *ars* detoxification genes, whereas *S. oneidensis MR-1* carries neither *arr* nor *ars* genes (Jiang et al., 2013). Both strains were grown on agar plates from freezer stocks. After growth on agar, a single colony was incubated overnight in LB (NaCl, yeast extract, tryptone) in an automatic shaker at 30ºC. The resulting cell slurry was centrifuged and resuspended in M1 (pH 8, 100 µM $FeCl_3$, 42 mM lactate) after the supernatant was decanted (Myers and Nealson, 1988). Cell concentation was calculated using optical density at 600 nm (OD_{600}) and a conversion factor of $1x10^9$ and $2x10^9$ cell ml^{-1} abs. $unit^{-1}$ for *S. putrefaciens* 200 and *S. oneidensis* MR1 respectively. Next, cells were either grown on degassed M1 (pH 8, 0.1 mM $FeCl_3$) with 60 mM fumarate or aerated M1 until the desired cell density was reached. The M1 cell solution was washed with phosphate free medium (pH 7), and cell density was determined via OD_{600}. Incubations were conducted in sealed and crimped 20 mL hungate tubes or 100 mL serum bottles inoculated with terminal electron acceptor, lactate as electron donor, phosphate buffer aliquots required to reach the desired orthophosphate (P_i) concentration, and the appropriate cell slurry volume to reach the final desired cell concentration (10^5-10^7 cells mL^{-1}) under N_2 atmosphere in an anerobic chamber. Sealed

vials were either mixed continuously on a rotary wheel (Fisher Sci.) or stirred with a magnetic bar on a multi-position stir plate (Thermo).

4.3.4 Generation of mutant strains lacking phosphate transporters

The genome of *Shewanella oneidensis* encodes two families of Pst transporters, an indication that phosphate uptake systems are functionally redundant or that phosphate may be incorporated intracellularly by the two systems under different environmental conditions. Genome wide analyses indicated that the two phosphate uptake systems may operate under varying salinity and temperature conditions: the homologs of the first *S. oneidensis* Pst transporter (SO1724) are present in all *Shewanella* genomes (Table 4-1), while homologs of the second transporter (SO4290) are only present in the genomes of psychrophilic marine *Shewanella* (*S. piezotolerans* WP3, *S. halifaxensis* HAW-EB4, *S. pealeana* ATCC 700345, *S. waksmanii* ATCC BAA-643, *S. fidelis* ATCC BAA3-18, and *S. marina* JCM 15074) (Table 4-1).

Table 4-1: Similarity (E-value) and percent identity of SO1724 and SO4290 homologs of the two Pst transporters found in the *Shewanella* genome

***Shewanella* strain**	**E value**	**% Ident**	***Shewanella* strain**	**E value**	**% Ident**
SO1724					
S. oneidensis MR-1	0.0	100%	*Shewanella violaceas*	0.0	80%
Shewanella sp. W3-18-1	0.0	91%	*S. algae*	0.0	83%
Shewanella sp. MR-7	0.0	91%	*S. amazonensis*	0.0	84%
S. putrefaciens	0.0	91%	*S. benthica*	0.0	79%
Shewanella sp. MR-4	0.0	91%	*S. colwelliana*	0.0	82%
Shewanella sp. HN-41	0.0	91%	*S. denitrificans*	0.0	83%
S. putrefaciens	0.0	91%	*S. loihica*	0.0	82%
S. putrefaciens	0.0	89%	*S. fidelis* ATCC BAA-318	0.0	81%
S. baltica	0.0	89%	*Shewanella* sp. cp20	0.0	81%
S. baltica	0.0	89%	*Shewanella* sp. ECSMB14101	0.0	81%
S. baltica	0.0	89%	*S. pealeana* ATCC700345	0.0	80%
S. frigidimarina	0.0	86%	*S. piezotolerans* WP3	0.0	80%
S. woodyi	0.0	83%	*S. halifaxensis* HAW-EB4	0.0	78%
S. sediminis	0.0	83%	*S. waksmanii* ATCC BAA-643	0.0	79%
S. violacea DSS12	0.0	80%	*Shewanella* sp. YQH10	0.0	77%
Shewanella sp. ECSMB14102	0.0	84%	*S. marina* JCM15074	8E-33	40%
S. haliotis	0.0	84%			
SO4290					
S. fidelis ATCC BAA-318	1e-172	86%	*S. pealeana* ATCC700345	1e-164	87%
S. piezotolerans WP3	9e-169	85%	*S. waksmanii* ATCC BAA-643	2e-164	84%
S.halifaxensis HAW_EB4	1e-164	85%	*S. marina* JCM 15074	7e-134	67%

Genes encoding the Pst proteins required for phosphate transport (SO1724 and SO4290) were deleted in *Shewanella oneidensis* MR-1 using a suicide vector (designated pKO2.0) constructed for targeted in-frame deletion mutagenesis in *Shewanella* (Burns and DiChristina, 2009). Regions corresponding to ~750 bp upstream and downstream from the targeted gene were PCR-amplified from genomic DNA. The resulting PCR fragments were isolated and subsequently joined using overlap-extension PCR to generate a DNA fragment containing regions homologous to the flanking regions of the targeted gene, and an in-frame deletion. This region were cloned into pKO2.0, and the resulting plasmid (pKO2.0-Δgene) were electroporated into *E. coli* EC100D and screened on LB agar containing X-Gal. The recombinant plasmid was confirmed by noting the proper-sized insertion following digestion with BamHI. pKO2.0-Δgene were electroporated into *E. coli* β2155 λpir, and the resulting donor strain was mated into *Shewanella* on LB agar containing DAP. Recipient transconjugates were selected on LB-Gm agar. *Shewanella* colonies with pKO2.0-Δgene integrated into the genome were screened by PCR using primers flanking the recombination region. The resulting strain (Strain::pKO2.0-Δgene) was grown in LB medium with NaCl omitted and subsequently transferred to LB agar with NaCl omitted and containing 10% sucrose (w/v). Colonies were patched to LB-Gm agar to confirm loss of pKO2.0. Gm-sensitive colonies were tested by PCR using primers flanking the recombination region to confirm the targeted deletion. The resulting mutant strain (Strain::Δgene) was confirmed by DNA sequencing of the deleted region, and in-frame deletion was confirmed by RT-PCR of the flanking genes.

4.3.5 Measurement of reduced species

At each time point, aliquots were collected from the sealed incubation vials by piercing through the septa using a syringe and needle and immediately filtering through 0.2 micron nitrocellulose filters (Millapore) under N_2-atmosphere. Chemical constituents measured in the filtered samples were considered 'dissolved'. Reduced species (NO_2^-, Mn^{2+}, Fe^{2+}) were measured immediately, or stored at 4º C until analysis. NO_2^- was measured using sulfanilamide and N-1-napthyethylenediamine reagents (Bendschneider and Robinson, 1952). Total Fe(II) was measured in unfiltered samples by the ferrozine method (Stookey, 1970) after 1 M HCl extraction on a rotary wheel for 24 hours. Dissolved Mn (Mn_d) was measured by ICP-MS (Owings et al., 2019) or the porphyrin method (Madison et al., 2011b). Dissolved Mn^{2+} (Mn^{2+}) was measured voltammetrically using PEEK Hg/Au microelectrodes {Luther, 2008 #518}(Brendel and Luther, 1995). The adsorbed and carbonate bound manganese fractions were measured by extracting the 0.2 um nitrocellulose membrane used for filtration of the sample with $MgCl_2$ (0.5 M) and sodium acetate (1M, pH 5) for 5 hours (Tessier et al., 1979). Total Mn (Mn_t) represents the sum of the dissolved, adsorbed, and carbonate fractions.

4.3.6 Arsenic speciation

Dissolved As(III) concentrations were determined voltammetrically with a Metrohm VA 663 Hanging Mercury Drop Electrode coupled to an Ecochemie Autolab PGSTAT 12 potentiostat in a three electrode configuration, using a glassy carbon counter electrode and an Ag/AgCl/KCl (3M) reference electrode with a 2 M NaCl glass bridge. Samples were spiked to solutions pre-purged with N_2 gas that contained 0.8 mM $CuCl_2$, 2

M HCl, and 40 µM hydrazine (Chow and Taillefert, 2005; Li and Smart, 1996). A minimum of triplicate scans were performed per sample. Detection limits of 300 nM with typical relative standard deviations of 0.5-8.0% (n=3) were obtained using this procedure. Total dissolved arsenic concentrations were determined by an Agilent 7500a Inductively Coupled Plasma-Mass Spectrometer (ICP-MS). Standards and samples were prepared in 2% nitric acid (Trace Metal Grade, Fisher) and included Sc and Y internal standards (SPEX CertiPrep) to account for the drift of the instrument. Blanks were run every 10 samples, and calibration curves were run every 20 samples. Minimum detection limits (3σ of blank) for As was 0.3 nM. Dissolved As(V) was determined by difference between total dissolved arsenic and dissolved As(III).

For some incubations, a high performance liquid chromatograph (Shimadzu LC-20AT) was paired with the ICP-MS (HPLC-ICP-MS) to simultaneously detect inorganic As(V), As(III), MMA, and DMA after separation of 50 µL samples injected through a Hamilton PRP-X100 (10 µm, 4.1 x 250mm) anion exchange column with guard. The mobile phases consisted of 6 mM ammonium phosphate buffer (pH 6.2) in 0.1 mM EDTA and 1% methanol eluted at a flow rate of 1.0 mL min^{-1} (Fang et al., 2016). Indium was used to correct for the drift of the ICP-MS by normalizing the peaks of interest to the indium peak. Minimum detection limits (MDL) for As(III), DMA, MMA, and As(V) at three times the standard deviation of the blank was determined to be 78.0, 142, 71, and 56 nM, respectively.

4.4 Results

4.4.1 Effect of cell and orthophosphate concentration on anaerobic respiration of various terminal electron acceptors amended or not with As(V)

The effect of orthophosphate (P_i) concentrations on anaerobic respiration rates was examined in experiments with various terminal electron acceptors and low or high cell concentrations (10^5 and 10^7 cells mL^{-1}) of both *S. putrefaciens* 200 and *S. oneidensis* MR1. The effect of P_i and cell concentration was most prominent in experiments with NO_3^- as the electron acceptor and *S. putrefaciens* 200 (Figure 4-1). At high cell concentrations (10^7 cells mL^{-1}) NO_2^- production was similar in all P_i conditions (Figure 4-1a). In turn, after a phase lag, the rate of NO_2^- production increased with increasing P_i concentrations at low cell concentrations (10^5 cells mL^{-1}) (Figure 4-1b). Similarly, MnO_2 reduction observed visually was achieved much more rapidly at high cell concentrations than in incubations with 10^5 cells mL^{-1} (Figure C 1). Final Mn_d concentrations measured in these experiments were similar when porphyrin and microelectrodes measurements were compared, indicating Mn_d was mainly in the form of Mn^{2+} in these conditions (Figure C 2). $Fe(OH)_3$ reduction rates were low below 50 µM P_i in experiments with 10^5 cells mL^{-1} *S. putrefaciens* 200, but rates increased in conditions with ≥ 50 µM P_i (Figure C 3). Similarly, $Fe(OH)_3$ reduction rates with *S. oneidensis* MR1 were greater with ≥ 50 µM P_i in both cell concentrations (10^6 and 10^7 cells mL^{-1}) (Figure C 3).

NO_3^- reduction rates decreased with increased As(V) concentrations in incubations with 10^7 cells mL^{-1} *S. putrefaciens* 200 (Figure 4-1c) and NO_3^- reduction rates were not significantly different between the 0.1 or 1.0 µM P_i conditions (Figure 4-1c). As(III)

concentrations increased over time but remained below 10 µM (< 12% of total As added) regardless of the initial As(V) concentration added or orthophosphate concentrations in the medium, and As(V) predominantly remained in solution in these incubations (Table C 1). NO_3^- reduction rates with 10^5 cells mL^{-1} were one to two orders of magnitude lower than with 10^7 cells mL^{-1} (Figure 4-1d) and were higher with 1.0 µM P_i than 0.1 µM (arsenic speciation not determined). NO_3^- reduction rates decreased with increasing As(V) concentration in the presence of both 0.1 and 1.0 µM P_i but the impact of As(V) on the rate was much more significant at low P_i concentrations (Figure 4-1d).

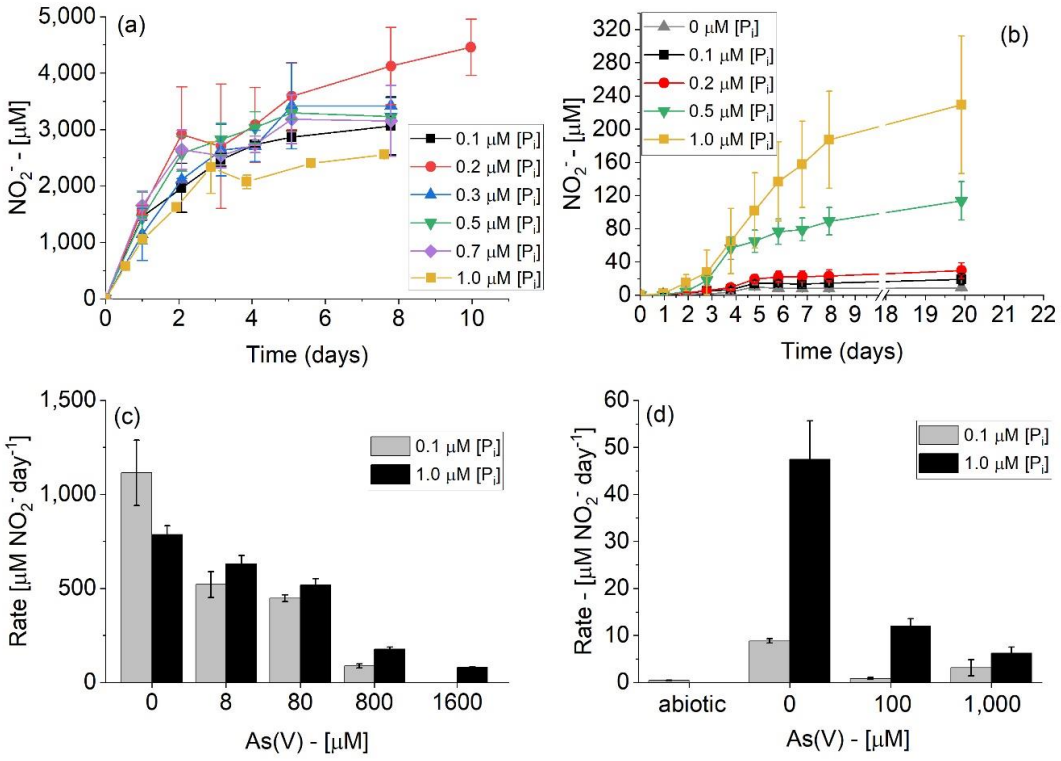

Figure 4-1: Effect of: (a, b) orthophosphate concentrations ([P_i]) on NO_3^- reduction measured as NO_2^- production over time; and (c, d) As(V) concentrations on NO_3^- reduction rates (µM day^{-1}) in incubations amended with 0.1 µM (gray bars) and 1.0 µM (black bars) [P_i]. All incubations were conducted with (a, c) 10^7 cells mL^{-1} and (b, d) 10^5 cells mL^{-1} of *S. putrefaciens* 200, 10 mM nitrate as terminal electron acceptor, and 20 mM lactate as electron donor in M1 medium at pH 7 (PIPES). Rates were based on the average of duplicate incubations in each condition except for abiotic controls which were based on single experiments.

Experiments were conducted with As(V) as the sole electron acceptor with *S. putrefaciens* 200 (10^5 and 10^7 cells mL^{-1}) to determine the extent of As(V) reduction by microbial respiration (Table S1). As(V) reduction was observed in all conditions tested with both 10^5 and 10^7 cells mL^{-1}. However, As(V) was only completely reduced after 28 days when initial As(V) concentrations of 1,000 µM were amended in the 10^7 cells mL^{-1}

incubations or when initial As(V) concentrations ranged between 500 and 5,000 µM in the 10^5 cells mL^{-1} incubations. Above 5,000 µM As(V), less than 1% of As(III) was detected in the 10^5 cells mL^{-1} incubations after the same time (Table C 1).

Orthophosphate concentrations influenced the effect of As(V) on MnO_2 reduction as measured by the production of Mn_d. A lag phase was observed in MnO_2 reduction between day 0 and 23 at both low and high P_i conditions (Figure 4-2a & b). After this lag phase, MnO_2 reduction took place in the presence of up to 1 mM As(V) in low P_i conditions and up to 5 mM As(V) in high P_i conditions between days 23-71. Longer lag phases existed in the incubations amended with 5 and 10 mM As(V) in low P_i and 10 mM As(V) in high P_i conditions, but MnO_2 reduction recovered even at the highest As(V) concentration. Mn_d concentrations decreased after reaching maximum Mn_d concentrations in incubations containing between 0-1 mM As(V) in the low P_i conditions and 0.1-5 mM As(V) in the high P_i conditions, likely due to precipitation of manganese carbonates with HCO_3^-, as observed by the formation of a cloudy precipitate in the serum bottles (Figure C 7). MnO_2 reduction rates were generally higher in high P_i conditions and increased as the concentration of As(V) amended to the incubations increased up to 1 mM As(V) in the presence of 10 µM P_i and 5 mM in the presence of 100 µM P_i (Figure 4-2c). Above these As(V) concentrations, MnO_2 reduction rates decreased until day 71 in which rates recovered to values similar to the As(V) free incubations (Figure 4-2a, b).

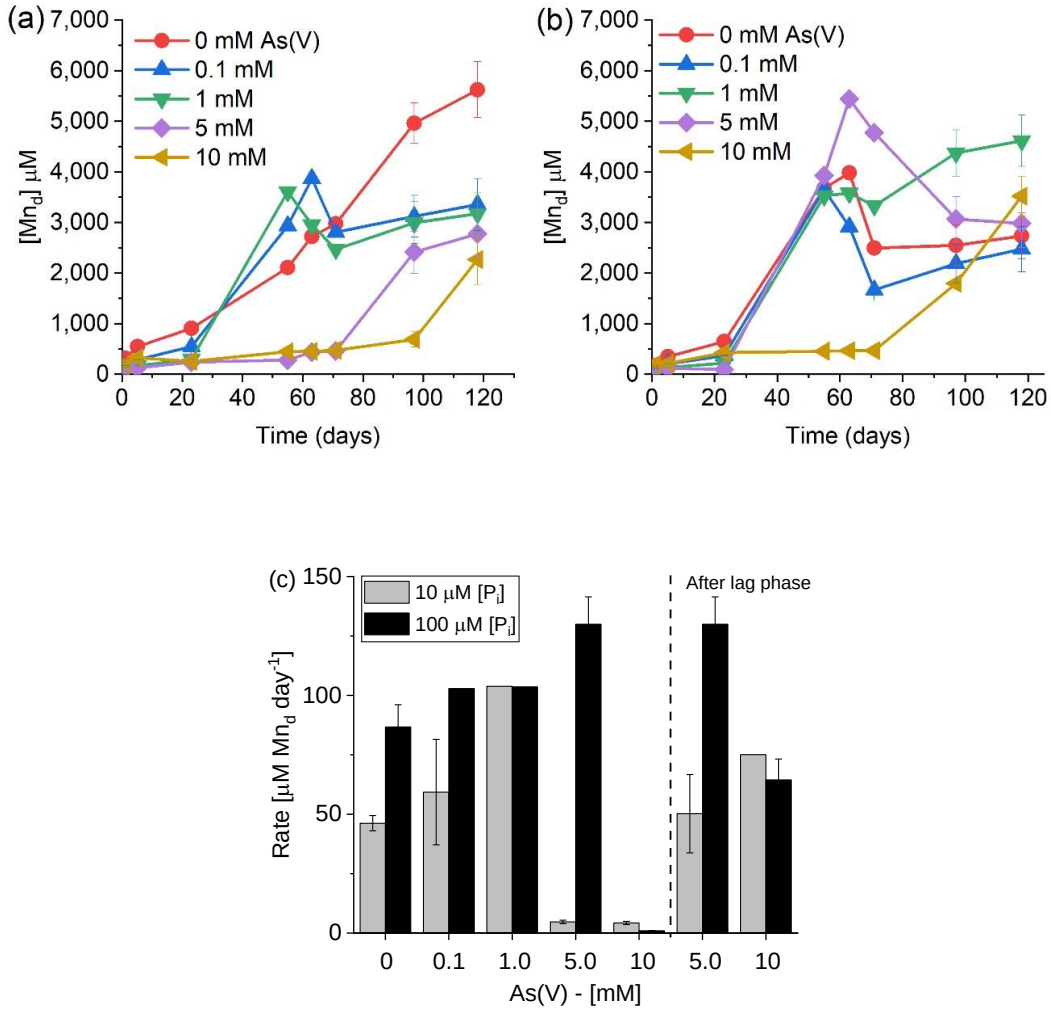

Figure 4-2: Effect of As(V) concentrations on: (a, b) MnO_2 reduction measured as Mn_d production over time and (c) MnO_2 reduction rates (µM day^{-1}) by $2x10^5$ cells mL^{-1} *S. putrefaciens* 200 in the presence of 5 mM MnO_2 (solid phase), 10 mM lactate in M1 medium at pH 7 (PIPES) amended with (a, c) 10 µM P_i and (b, c) 100 µM P_i. Error bars on Mn_d concentrations represent instrumental error (the same aliquot measured twice), whereas error bars on rates represent the standard deviation of the linear regression of the maximum slope of Mn_d production over time. For 5 and 10 mM As(V) conditions, rates were compared before and after lag phases (> 55 days). The abiotic control contained 1.0 mM As(V).

$As(III)_d$ and total As_d (to determine $As(V)_d$ concentrations) were measured over time in the incubations amended with 0.1 and 1.0 mM As(V) in the 10 µM P_i medium (Figure 4-3). Initially (days 0-23), $As(V)_d$ concentrations decreased while $As(III)_d$ concentrations remained below detection limit at both As(V) amendments (Figure 4-3). After 23 days, As(V) and As(III) in the 0.1 mM As(V) incubation were both produced in solution simultaneously with Mn_d, but As(V) was successively consumed while As(III) was continuously produced until the end of the experiment (Figure 4-3a). In the 1 mM As(V) incubation, As(III) was also produced simultaneously with Mn_d, but As(V) was removed from solution until the end of the experiment (Figure 4-3: Dissolved Mn (Mn_d, blue squares), dissolved As(III) ($As(III)_d$, red circles), and dissolved As(V) ($As(V)_d$, black triangles) concentrations produced over time in incubations of 10^5 cells mL^{-1} *S. putrefaciens* 200 in the presence of 5 mM MnO_2 (solid), 10 mM lactate, at pH 7 (PIPES) and (a) 0.1 mM As(V) and (b) 1.0 mM As(V). Error bars on Mn_d represent instrumental error and error bars for $As(III)_d$ represent variations from the mean of at least triplicate measurements of each sample measured by HMDE voltammetry. $As(V)_d$ represents the difference of total As_d measured by ICP-MS and $As(III)_d$.b). After 71 days, up to 70% of total As was reduced in the 10 µM P_i medium, while up to 100% of total As was reduced in the 100 µM P_i, although at the highest As(V) amendments total As was not reduced at all in both P_i concentrations (Figure C 2). Additionally, cell counts show low cell viability in all conditions except for exceptionally high cell counts in the 10 µM P_i conditions at 0.1 mM and 5 mM As(V) concentrations with $1.4 \pm 0.6 \times 10^6$ and $0.4 \pm 0.1 \times 10^{-6}$ colony forming units mL^{-1} respectively (Figure C 6).

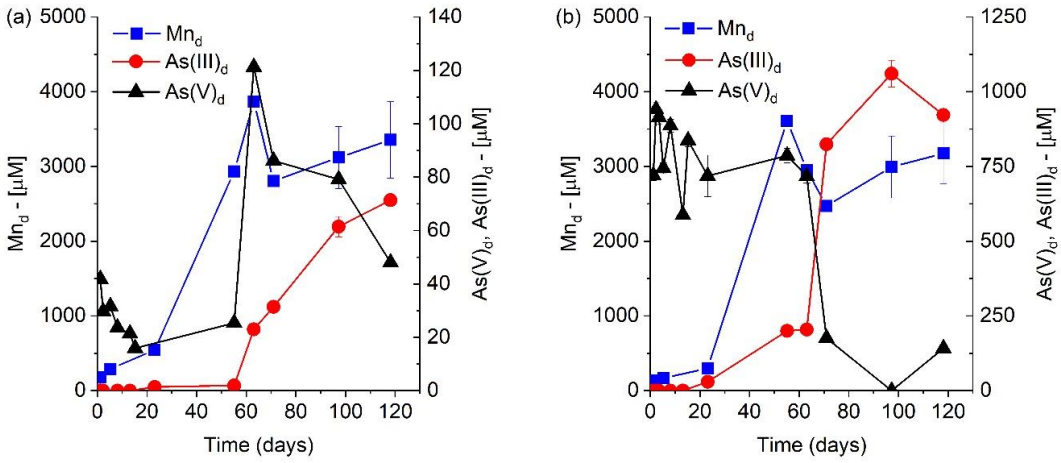

Figure 4-3: Dissolved Mn (Mn_d, blue squares), dissolved As(III) ($As(III)_d$, red circles), and dissolved As(V) ($As(V)_d$, black triangles) concentrations produced over time in incubations of 10^5 cells mL^{-1} *S. putrefaciens* 200 in the presence of 5 mM MnO_2 (solid), 10 mM lactate, at pH 7 (PIPES) and (a) 0.1 mM As(V) and (b) 1.0 mM As(V). Error bars on Mn_d represent instrumental error and error bars for $As(III)_d$ represent variations from the mean of at least triplicate measurements of each sample measured by HMDE voltammetry. $As(V)_d$ represents the difference of total As_d measured by ICP-MS and $As(III)_d$.

Additional incubations were conducted with *S. putrefaciens* 200 and *S. oneidensis* MR1 to compare the effect of As(V) on MnO_2 reduction (Figure 4-4, Figure C 8). Overall, MnO_2 reduction rates were faster with *S. oneidensis* MR1 than *S. putrefaciens* 200, and the arsenic free incubations with both strains displayed the fastest MnO_2 reduction rates (1,429 ± 0 *S.* µM Mn_t day^{-1} with *oneidensis* MR1 and 698 ± 229 µM Mn_t day^{-1} with *S. putrefaciens* 200) (Figure 4-4). More importantly, MnO_2 reduction rates increased slightly with increasing As(V) concentrations in the *S. putrefaciens* 200 incubations in contrast to the MnO_2 reduction rates with *S. oneidensis* MR1 which remained similar at all As(V) amendments (694-760 µM Mn_t day^{-1}) (Figure 4-4).

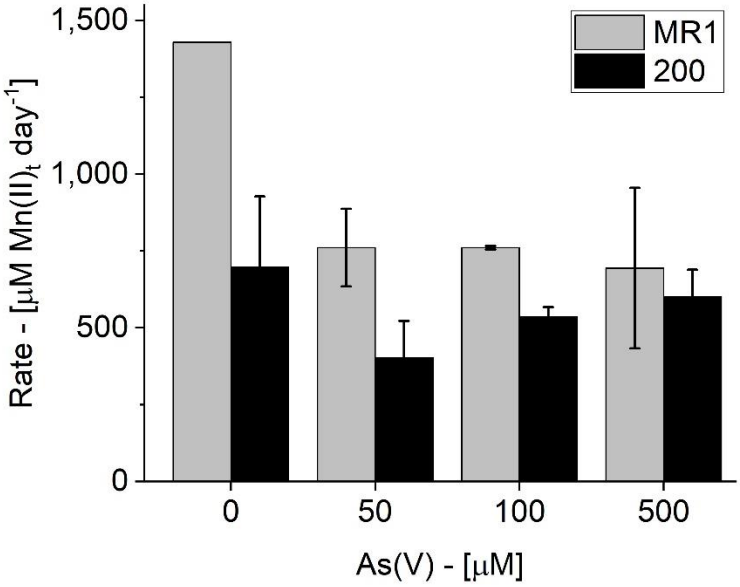

Figure 4-4: Effect of the increase in As(V) concentrations on hydrous manganese oxides (HMO) reduction (μM day^{-1}) by 2x10^{6} cells mL^{-1} *S. oneidensis* MR1 (gray) or *S. putrefaciens* 200 (black) incubated in the presence of 10 mM MnO_2, 20 mM lactate, and 50 μM P_i at pH 7 (PIPES). Rates were based on the average of duplicate incubations in each condition. Cells were grown in liquid cultures on O_2 (in the presence of fumarate) before inoculation.

4.4.2 Effect of As(V) on Fe(III) reduction rates by S. putrefaciens 200 and S. oneidensis MR1

$Fe(OH)_3$ reduction rates displayed similar trends in incubations with either *S. putrefaciens* 200 or *S. oneidensis* MR1 (Figure 4-5b and Figure 4-5). $Fe(OH)_3$ reduction rates in the arsenic free incubations were much higher with *S. oneidensis* MR1 (434 ± 0 μM Fe(II) day^{-1}) than with *S. putrefaciens* 200 (234 ± 50 μM Fe(II) day^{-1}). $Fe(OH)_3$ reduction rates increased relatively similarly with both strains as As(V) concentrations were raised from 50 to 100, to 500 μM (Figure 4-5), though rates with *S. oneidensis* MR-

1 remained below the As free condition. In turn, $Fe(OH)_3$ reduction rates with *S. putrefaciens* 200 in the 100 µM and 500 µM As(V) incubations were at least similar to or slightly higher than the arsenic free control (252 ± 48 and 298 ± 111 µM Fe(II) day^{-1} respectively) (Figure 4-5). When *S. oneidensis* cell concentrations were increased to 2x 10^7 cells mL^{-1}, iron reduction rates increased in the presence of 50, 100, and 500 µM As(V) in comparison to the unamended live control (Figure 4-4b). At As(V) concentrations greater than 1,000 µM, however, As(V) toxicity increased the lag phase and decreased iron reduction rates. Total As(III) was produced rapidly within the first 3 days of the experiments in concentrations that increased proportionally to the initial As(V) concentration, except in the presence of 50 µM As(V) (Figure 4-4c). Simultaneously, total As(III) produced did not exceed 2% of total arsenic concentrations (Figure 4-5b). In addition, dissolved As(III) concentrations were much lower than the As(V) decrease detected over the course of the incubations (Figure 4-5c and d), suggesting either that As(III) was methylated or removed by incorporation in the crystal lattice of $Fe(OH)_{3(s)}$. As MMA and DMA were never detected in any incubations (Figure C 5), the second option is likely.

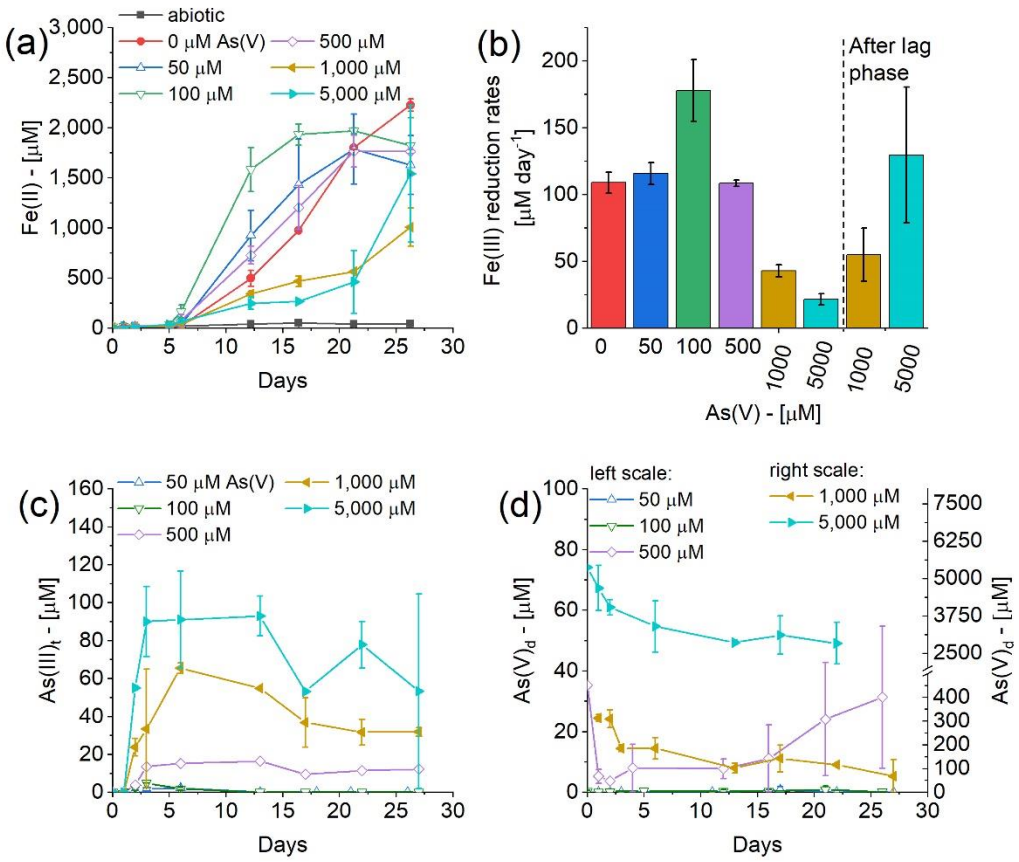

Figure 4-5: Effect of As(V) concentrations on the reduction of 5.8 mM 2L-ferrihydrite by 2 x 10^7 cells mL^{-1} of *S. oneidensis* MR1: (a) $Fe(OH)_3$ reduction as a function of time (b) Fe(III) reduction rates; (c) total As(III) production as a function of time; and (d) Dissolved As(V) as a function of time. Rates and standard deviations of the rates were based on the average of duplicate incubations and calculated before and after the lag phase (~16 days) for the 1,000 and 5,000 µM As(V) incubations. Error bars in the time series represent the standard deviation of the average of duplicate incubations. All incubations were conducted in the presence of 20 mM lactate as electron donor in M1 medium at pH 7 (PIPES) amended with 50 µM P_i

Table 4-2: Mass balance of total As (As(V), As(III), MMA, DMA) in percentage (%) in filtered and unfiltered samples from As(V) amended conditions (50, 100 and 500 µM). Error based on mass balance of duplicate experiments per condition.

[As(V)]:	50 µM	50 µM	100 µM	100 µM	500 µM	500 µM
Days	filtered	unfiltered	filtered	unfiltered	filtered	unfiltered
0.0		81 ± 27	0.3 ± 0.4	100 ± 0	7.1 ± --	94 ± --
1.0	3.7 ± 5.3	96 ± 3	0.0 ± --	79 ± 1	2.6 ± 1.8	91 ± 7.2
2.0	0.9 ± 1.3	110 ± 2	0.3 ± --	102 ± 2	3.7 ± --	157 ± 92
3.0	0.0 ± 0.0	141 ± 15				79 ± 12
4.0					2.7 ± 3.2	
5.0			0.9 ± --	116 ± 5		
6.0		102 ± 4				87 ± 4
11.0	0.0 ± 0.0					
12.0			0.7 ± 0.5	118 ± 12	2.7 ± 2.0	
13.0		117 ± 4				73 ± 4
16.0			1.5 ± 0.0	101 ± 16	4.2 ± 4.6	
17.0	2.0 ± 2.8	121 ± 3				80 ± 6
21.0			2.7 ± 0.8	118 ± 21	8.1 ± 7.6	
22.0	0.9 ± 1.2	118 ± 10				80 ± 18
26.0		99.9 ± --	1.0 ± 0.6	106 ± 26	9.3 ± 8.1	
27.0	1.5 ± 1.6	133 ± 34				88 ± 6

Table 4-3 Mass balance of total As (As(V), As(III), MMA, DMA) in percentage (%) in filtered and unfiltered samples from As(V) amended conditions (1,000 and 5,000 µM). Error based on mass balance of duplicate experiments per condition.

[As(V)]:	1000 µM	1000 µM	5000 µM	5000 µM
Days	filtered	unfiltered	filtered	unfiltered
0.0			107.7 ± --	86 ± 19
1.0	31 ± 2	94 ± 8	94± 16	94 ± 7
2.0	32 ± 4	91 ± 10	82 ± 5	90 ± 8
3.0	20 ± 2	67 ± 47		117 ± 49
4.0				
5.0			69 ± 17	
6.0	20 ± 5	100 ± 7		101 ± 6
11.0				
12.0			58 ± 2	
13.0	11 ± 2	120.1 ± --		87 ± 0.1
16.0			63 ± 13	
17.0	15 ± 6	75± 20		70 ± --
21.0				
22.0	12 ± 0.7	101 ± 11	58 ± 14	90 ± 6
26.0				
27.0	8.1 ± 7.0	96 ± 4		53 ± 46

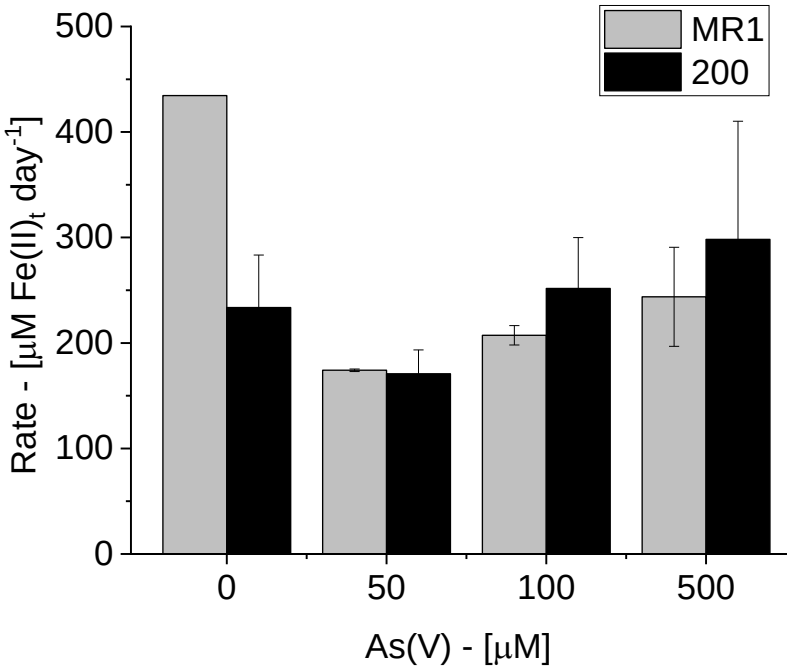

Figure 4-6: Effect of the increase in As(V) concentrations on Fe(III) reduction rates by $2x10^6$ cells mL^{-1} *S. oneidensis* MR1 (gray) or *S. putrefaciens* 200 (black) in the presence of 10 mM 2L-ferrihydrite, 20 mM lactate, and 50 µM P_i at pH 7 (PIPES). Rates were based on the average of duplicate incubations in each condition. Cells were grown in liquid cultures on O_2 (in the presence of fumarate) before inoculation.

4.4.3 Incubations with wild type and mutant strains of S. oneidensis MR1

MnO_2 reduction rates in incubations of both wild type and Pst-deficient mutant strains of *S. oneidensis* MR1 were highest without As(V) (76 ± 0 µmol Mn_d day^{-1}), more than 3-fold higher with the wild-type than the mutants, and decreased with increasing As(V) concentrations in otherwise identical conditions (Figure 4-7). Slight variations in MnO_2 reduction rates were observed between the Pst-deficient mutants, however, these variations were not significantly different from each other, except perhaps with mutant Δ90 and double-mutant DM10 which showed increases in MnO_2 reduction rates in the

incubations amended with both 1.0 and 5.0 mM As(V) (Figure 4-7). In parallel, As_d remained constant or slightly decreased at the end of the incubations with both wild type strain and the different mutants, while a corresponding increase in solid As was observed although the oxidation state of the solid fraction was not determined (Figure C 9).

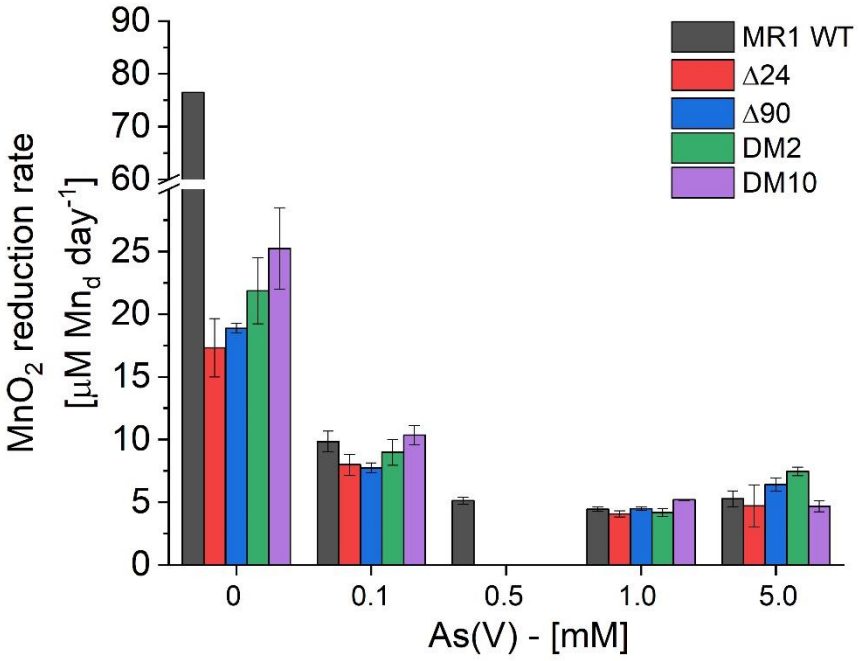

Figure 4-7: Effect of As(V) concentrations on MnO_2 reduction rates by $2x10^5$ cells mL^{-1} of *S. oneidensis* MR1 wild type (WT, black) and Pst mutants Δ24 (red), Δ90 (blue), DM2 (green), and DM10 (purple). All incubations were conducted with 0.5 g L^{-1} (6.1 mM) MnO_2 as terminal electron acceptor and 20 mM lactate as electron donor in M1 medium at pH 7 (PIPES) amended with 10 µM P_i. Mn_d, As_d and As_{ads} times series for each condition available in Figure C9.

4.5 Discussion

4.5.1 Role of phosphate in As(V) acquisition

Phosphate (P_i) and arsenate (As(V)) are intertwined during cell growth due to their physiochemical similarity which allows As(V) to enter cells via phosphate transporters with significant intoxication effects (Rosenberg et al., 1977; Willsky and Malamy, 1980b). P_i uptake by cells is controlled either by the high affinity phosphate specific transporter, Pst, or the low affinity inorganic phosphate transporter, Pit, systems (Willsky and Malamy, 1980a). The first objective of this study was to establish the P_i concentration threshold at which cells experienced toxicity as a result of the addition of As(V) to determine whether P_i transporter systems are involved in the As(V) toxicity of cells. As cells also scavenge phosphorus from other lysing cells, it was also necessary to determine whether cell density have a possible effect on As(V) toxicity. Results of experiments conducted with *S. putrefaciens* 200 demonstrated at high cell concentrations NO_3^- and MnO_2 reduction rates are not affected by varying P_i concentrations (Figure 4-1a, Figure C 1) because living cells likely use phosphorus from dead cells. However, at low cell concentrations, NO_3^- reduction rates increased with increasing P_i amended to the system (Figure 4-1b), likely because living cells were not receiving enough nutrients from dying cells. Similarly, cell-normalized $Fe(OH)_3$ reduction rates were enhanced much more significantly at lower cell concentrations when P_i concentrations were increased in the medium (Figure C 3e). However, cell-normalized $Fe(OH)_3$ reduction rates were in general much higher at low cell densities relative to high cell densities. These findings suggest that the availability of $Fe(OH)_3$ surface sites was limited at high cell density. In addition, $Fe(OH)_3$ reduction rates increased significantly after a threshold of 10 µM P_i irrespective of the cell concentration

(10^5-10^7 cells mL^{-1}) and the type of strain used, but did not change significantly above 10 µM P_i (Figure C 3d and e). Phosphate adsorbs to the surface of $Fe(OH)_3$ (Jain and Loeppert, 2000) removing phosphate from solution and decreasing P_i availability for cellular uptake. Increased $Fe(OH)_3$ reduction rates above the 10 µM P_i threshold indicates enough orthophosphate was available in solution for the bacteria to use as a nutrient at these concentrations.

4.5.2 Effect of As(V) on anaerobic respiration processes by the As(V)-respiring S. putrefaciens

Once the P_i concentration threshold and minimum cell densities required to promote respiration and growth were determined, incubations on each anaerobic terminal electron acceptor were conducted in the presence of As(V) to determine the effect of As(V) on anaerobic respiration processes. *S. putrefaciens* is known to carry the As(V) respiratory *arr* genes, raising the possibility that As(V) uptake in low P_i conditions may result in preferential respiration of As(V). Although As(V) was reduced in *S. putrefaciens* incubations without alternate terminal electron acceptor (Table C 1), thermodynamic calculations in the conditions of all experiments with alternate terminal electron acceptors (Table 4-4) indicated that the Gibbs free energy of the reaction was always more favorable to NO_3^-, MnO_2, and $Fe(OH)_3$ reduction initially or during the course of the reaction, even in the cases in which the terminal electron acceptor was almost completely depleted (e.g., Figure 4-2 and Figure 4-3). These findings therefore suggest that the respiration of As(V) did not significantly impact the results of the *S. putrefaciens* incubations.

In general, *S. putrefaciens* 200 displayed a high threshold for As(V) exposure at high cell concentrations or large P_i concentrations, indicating of active detoxification. Higher As(V) thresholds were evidenced by larger NO_3^- and MnO_2 reduction rates or little variation between phosphate conditions in the presence of As(V) at high cell densities (Figure 4-1c and d, Figure 4-4) relative to low cell densities. $Fe(OH)_3$ reduction for *S. putrefaciens* 200 was only tested at one cell concentration and phosphate condition (Figure 4-6), however, only a small difference in $Fe(OH)_3$ rates were observed amongst the 0-500 µM As(V) conditions, similar to MnO_2 reduction rates, suggesting *S. putrefaciens* 200 has an increased threshold for As(V) toxicity. This observation is not surprising as *S. putrefaciens* 200 was isolated from an oil-pipeline where it promoted corrosion by reducing $Fe(OH)_3$ (Arnold et al., 1988; Obuekwe et al., 1981). Indeed, *S. putrefaciens* 200 is more tolerant to organic contaminants (McKinzi and DiChristina, 1999; Picardal et al., 1993; Sekar and DiChristina, 2017; Sekar et al., 2016) and even able to gain energy from uranium (Dale et al., 2007; Lovley et al., 1991; Sanford et al., 2007; Wade and DiChristina, 2000). In turn, at low cell densities, *S. putrefaciens* 200 was more susceptible to As(V) toxicity, and this effect was exacerbated at low P_i concentration (Figure 4-1d, Figure 4-2). Although NO_3^- reduction rates decreased as As(V) additions were increased regardless of the cell density, conditions in the low cell density and low P_i concentrations (0.1 µM, Figure 4-1d) suffered the most to As(V) exposure. These findings suggest that the increased uptake of As(V) via phosphate transporters in low P_i conditions irreversibly affect cell growth at much lower concentrations that used in the present incubations. In turn, MnO_2 reduction rates increased as As(V) concentrations were increased with low cell densities ($2x10^5$ cells mL^{-1}), and this effect was exacerbated in low and P_i conditions (10 µM Pi, Figure 4-2c).

Once an As(V) threshold was exceeded, however, MnO_2 reduction was inhibited, although after a lag phase, MnO_2 reduction rates recovered at lower P_i concentrations and even exceeded As(V)-unamended rates at high P_i concentration (Figure 4-2c). These findings suggest that As(V) toxicity either affect ATP levels or stress the cells to ultimately increase MnO_2 reduction rates and overcome energy lost in the detoxification process.

S. putrefaciens responded to As(V) toxicity by reducing As(V) to As(III) irrespective of the terminal electron acceptor used (e.g., Figure C 4 with NO_3^- and Figure 4-3 with MnO_2). However, whereas As(V) reduction did not exceed a few percent with NO_3^- as terminal electron acceptor (Figure C 4), As(V) was almost completely reduced to As(III) with MnO_2 as terminal electron acceptor (Figure 4-3), likely because the rapid oxidation of As(III) by MnO_2 (Owings et al., 2019) masked the net production of As(III) until after all MnO_2 was reduced. As MnO_2 reduction was thermodynamically more favorable throughout the entire incubation (120 days, Table 4-4), As(V) reduction in these conditions was likely due to As(V) detoxification rather than arsenate respiration.

Table 4-4: Thermodynamic calculations

	ΔG^0 (kJ mol^{-1})[a]		ΔG_{rxn} (kJ mol^{-1})[b]	
Condition	MnO_2 reduction	As(V) reduction	MnO_2 reduction	As(V) reduction
S. putrefaciens 200, 5 mM MnO_2, 0.1 mM As(V)	-439	-305	-381 ± 51	-244±57
S. putrefaciens 200, 5 mM MnO_2, 1.0 mM As(V)	-439	-305	-387 ± 43	-262±63

[a]: calculated using initial experimental conditions
[b]:average and standard deviation of ΔG_{rxn} at each time point of the experiment

4.5.3 Differences in behavior between S. oneidensis and S. putrefaciens for same substrate

S. oneidensis MR1 displayed higher rates of MnO_2 and $Fe(OH)_3$ reduction in the arsenic free conditions compared to *S. putrefaciens* 200 in otherwise identical conditions (Figure 4-4, Figure 4-6). *S. oneidensis* MR1 was isolated from a pristine lake sediment (Lake Oneida, NY,(Myers and Nealson, 1988)) and is therefore expected to be adapted to respiration on manganese and iron oxides. In contrast to *S. putrefaciens*, however, As(V) decreased anaerobic respiration rates in *S. oneidensis* at low cell densities, regardless of the terminal electron acceptor (MnO_2 in Figure 4-4, 2L-ferrihydrite in Figure 4-6). Interestingly, low As(V) additions to high cell densities (10^7 cells mL^{-1}) apparently increased $Fe(OH)_3$ reduction rates compared to the As(V) free culture (Figure 4-5b). Above a As(V) threshold of 100 µM, however, $Fe(OH)_3$ reduction rates were severely impacted, but rates recovered after a lag phase to the levels of the As(V) free culture.

S. oneidensis was more sensitive to As(V) concentrations than *S. putrefaciens* as predicted by the absence of the As(V) reductase, ArsC, that is required to detoxify As(V) in the *ars* detoxification system (Jiang et al., 2013; Saltikov and Newman, 2003). As a result, total As(III) concentrations remained low in $Fe(OH)_3$ conditions (< 2% of total As(V) at steady-state, Figure 4-5c and Figure C 5). The production of low As(III) concentrations despite the inability of *S. oneidensis* to reduce As(V) suggests that *S. oneidensis* may detoxify As(V) by methylation (Wang et al., 2016). As a result, *S. oneidensis* was selected to investigate the potential of detoxification via methylation (*arsM*). Unfortunately, methylated species were not detected in this study (Figure C 5), although only monomethylarsonate (MMAs(V)) and dimethylarsinate (DMAs(V)) were

targeted for quantification but below detection limits. Mass balance on arsenic species was for the most part conserved (Table 4-2, Table 4-3), however, suggesting monomethylarsonite, dimethylarsinite, trimethylarsine oxide, or the gaseous species trimethylarsine (TMAs(III)) were not formed in significant concentrations.

Attempts to determine whether the orthophosphate uptake system *pst* is involved in As(V) uptake were not successful. MnO_2 reduction rates in *pst*A gene-deficient mutants of *S. oneidensis* were low across all As(V) conditions, including the As(V)-free incubations (Figure 4-7). These findings suggest the *pst*A-deficient mutant strains were unable to uptake phosphate and could not grow, regardless of the As(V) concentration added. The much lower MnO_2 reduction rates at increasing As(V) concentrations relative to the As(V)-free incubations may represent additional toxicity effects that have yet to be identified but could result from cell stress.

4.5.4 As(V) toxicity is related to its speciation

The pH_{pzc} of $Fe(OH)_3$ ranges between 7 and 9 (Anderson and Benjamin, 1990; Cismasu et al., 2013) whereas the pH_{pzc} of MnO_2 is reported as 1.85 to 3.1 (Jones et al., 2012; Morgan and Stumm, 1964; Murray, 1973; Scott and Morgan, 1995; Yao and Millero, 1993). These considerations indicate that, at the circumneutral pH of most aquatic systems, the surface of $Fe(OH)_3$ is slightly positive or neutral, whereas, that of Mn(IV) oxides is overall negative. In parallel, As(V) is negatively charged at circumneutral pH (approximately 45% as $H_2AsO_4^-$ and 55% as $HAsO_4^{2-}$ at pH 7) such that As(V), in the conditions of these incubations, was more likely to adsorb to $Fe(OH)_3$ surfaces than MnO_2 surfaces. Indeed, As(V) was mainly adsorbed to $Fe(OH)_{3(s)}$ until surface sites were

saturated ([As(V)] > 1 mM, Figure C 5). In addition, As(V) did not accumulate significantly in the dissolved phase during the reduction of $Fe(OH)_3$ below 500 µM initial As(V). Interestingly, dissolved and total As(III) accumulation in the *S. oneidensis* incubations coincided with the accumulation of As(V) in solution, and total As(III) concentrations produced increased proportionally to the initial As(V) concentration when that concentration exceeded 500 µM (Figure C 5). Finally, $Fe(OH)_3$ reduction rates only decreased significantly once dissolved As(V) was detected in solution ($\geq$ 500 µM initial As(V)) (Figure 4-5,d, Figure C 5). These findings indicate As(V) toxicity is related to the dissolved fraction of As(V). Similarly for MnO_2, initial As(V) adsorption varied between 60 and 80% at low As(V) addition ($\leq$ 100 µM, Figure 4-3), but by 500 µM initial As(V), most of the As(V) remained in solution (Figure C 9). MnO_2 reduction rates increased already in the 100 µM As(V) treatment (Figure 4-3c), suggesting again that As(V) susceptibility depends on its availability in solution. Corroborating this theory, *S. putrefaciens* was more susceptible to As(V) in incubations using NO_3^- as terminal electron acceptor (Figure 4-1d) than MnO_2 (Figure 4-2 or Figure 4-4) or $Fe(OH)_3$ (Figure 4-5b).

4.5.5 Working model on effect of As(V) on respiration by non-As(V) respiring microorganisms

Although NO_3^- reduction rates by *Shewanella* decreased rapidly at low but increasing As(V) amendments (Figure 4-1c), $Fe(OH)_3$ and MnO_2 reduction rates increased as As(V) concentrations were higher relative to the As(V)-free controls (Figure 4-2c and Figure 4-5b). The working model of this behavior includes that *S. putrefaciens* exposure to As(V) result in As(V) detoxification via the *ars* system which reduces and excretes As(III) from the cell via an efflux pump that requires ATP. The working model with *S. oneidensis,*

which does not carry important components of the *ars* detoxification operon, nor is able to respire on As(V), is that As(V) methylation and demethylation results in production of As(III) as proposed (Zhu et al., 2017). Regardless of the pathways, cells increase respiration rates to overcome the energy-consuming detoxification process, resulting in a lag phase. Once the lag phase was overcome, respiration occurred to a capacity comparable to the lower As(V) concentration conditions (Figure 4-2c and Figure 4-5b). If As(V) concentrations are too large, however, cells are not able to compensate for As(V) toxicity and do not recover. With $Fe(OH)_3$ as terminal electron acceptor, the tolerance of *Shewanella* to As(V) is enhanced by the scavenging of both As(III) and As(V) as long as the surface adsorption sites of $Fe(OH)_3$ are not saturated (Figure 4-5, Figure C 5). Once surface adsorption sites are saturated, As(V) is toxic and $Fe(OH)_3$ reduction rates increase. With MnO_2 as terminal electron acceptor, the increase in MnO_2 reduction rates was likely due to a catalytic cycle of continuous oxidation and reduction of arsenic. Dissolved As(III) accumulated in solution after complete reduction of MnO_2 only (Figure 4-3), indicating As(III) was likely formed via microbial detoxification during the earlier time frame of the incubation but went undetected due to rapid MnO_2 – dependent As(III) oxidation (Owings et al., 2019), which reintroduces As(V) back to the cell, thus exacerbating As(V) toxicity.

4.6 Environmental implications

This study demonstrated that As(V) toxicity is exacerbated when cells grow on low phosphate concentrations, likely due to active intracellular uptake of As(V) through phosphate transporters. Microorganisms in most sedimentary environments are typically exposed to low dissolved phosphate concentrations and adopt different strategies for phosphorus acquisition (Cleland and Hengge, 2006; White and Metcalf, 2007). One of

these strategies includes activating phosphate transporter systems to actively acquire dissolved orthophosphate. Given that As(V) and orthophosphate are physicochemically similar, microorganisms may be experiencing higher As(V) toxicity than previously considered in these environments. As As(V) is efficiently removed from solution by adsorption onto $Fe(OH)_3$ surfaces, however, As(V) toxicity may not be significant until the surface sites of sedimentary minerals are saturated and dissolved As(V) accumulates in pore waters. Dissolved As(V) concentrations (up to 200 nM) representing about a 10-fold increase in natural abundance are commonly detected in natural riverine sediments (Chow and Taillefert, 2005, 2009). $Fe(OH)_3$ reduction rates measured in sediment slurry incubations amended with as low as 1 μM As(V) were increased by 4-fold relative to unamended control sediment, providing direct evidence for the importance of this toxicity effect in a natural systems (Chow et al., 2009). The present study demonstrated that the presence of manganese oxides in iron-rich sedimentary environments should promote As(V) toxicity via a catalytic cycle in which arsenic is constantly reduced via microbial detoxification and re-oxidized by manganese oxides. As a result, low As(V) concentrations may have a dramatic impact on the anaerobic respiration of $Fe(OH)_3$, one of the main anaerobic terminal electron acceptor in freshwater sediments: The reductive dissolution of $Fe(OH)_3$ may promote the release of other adsorbed contaminants into the pore waters and eventually affect drinking water resources.

CHAPTER 5. WATER COLUMN AND SEDIMENT DEPTHS DRIVE SPATIAL DECOUPLING OF SEDIMENT MICROBIAL COMMUNITIES IN THE NORTHERN GULF OF MEXICO

This chapter is authored by Shannon Owings[1*], Ana Clavere-Graciette[2*], Anthony D. Bertagnolli[2], Eryn Eitel[1,3], Alex Price[2], Martial Taillefert[1], and Frank J. Stewart[2] ([*]co-first authors) to be submitted to *Limnology and Oceanography*

[1]School of Earth and Atmospheric Sciences, Georgia Institute of Technology [2]School of Biological Sciences, Georgia Institute of Technology [3]Geological and Planetary Science, California Institute of Technology

5.1 Abstract

Biogeographic surveys of sediment microbial communities and their link to geochemical parameters as a function of depth on broad spatial scales across a region are relatively scarce. In this study, sequencing of 16S rRNA gene amplicons from both *Bacteria* and *Archaea* was used alongside high resolution depth profiles of the main redox species involved in carbon remineralization processes and nutrients to explore microbial diversity patterns in sediment cores from the continental shelf to the slope of the northern Gulf of Mexico. Both shelf and slope sediments were deprived of dissolved oxygen within 7 mm from the sediment-water interface and were therefore mostly anoxic. The shelf sediments were characterized by geochemical indicators of sulfate reduction with either dissolved H_2S or FeS_{aq} proxies for iron sulfide mineral precipitation, whereas the slope sediments were characteristic of nitrate- and metal-reducing conditions with strong nitrate

gradients below the sediment-water interface and high dissolved manganese but relatively low dissolved iron concentrations. Multivariate analyses of 16S rRNA gene amplicons and geochemical signals provided strong evidence that the composition of both the sediment bacterial and archaeal communities was linked to the depth of the overlying water column and proximity to shore. Sediments from shallow waters that receive much higher organic matter inputs were clearly distinct from those of deeper offshore waters where the supply of organic matter is much lower. Canonical Correspondence Analysis (CCA) revealed that dissolved inorganic carbon, orthophosphate, and sulfide concentrations were the main drivers in shaping the microbial communities across the shelf communities, while NO_3^- appeared more important in shaping microbial communities along the slope (p-value $\leq$ 0.01). Vertical differences in composition were also observed at centimeter resolution along the sediment depth profiles and were most pronounced in continental shelf sediments. The representation of taxa associated with specific metabolisms varied significantly between continental shelf and slope sediment cores. Specifically, dissimilatory sulfur metabolizing (oxidizing and reducing) microbes were enriched in continental shelf sediments, consistent with elevated dissolved sulfide in these cores. In contrast, sediments from the continental slope were enriched in aerobic ammonia oxidizing *Thaumarchaeota* and *Bacteria*, as well as anaerobic ammonia oxidizing *Brocadiales*, suggesting ammonia consumption and nitrification as important microbial processes in slope sediments. Analysis of the *Archaea* community using domain-specific primers provided insight into diversity patterns not captured through the use of more conventional 16S rRNA gene survey primers. Estimates of Archaea diversity (based on 97% sequence similarity clusters) increased ~2-3X using the domain-specific primers. Overall, the data

support the hypothesis that high organic matter deposition to shelf sediments significantly differentiates the resident microbial communities from those in deeper, continental slope environments, and may stimulate taxa involved in sulfur and methane cycling. Such studies are useful to identify geochemical features associated with unique microbial assemblages and, therefore, help clarify the functional roles of microbes in the environment.

5.2 Introduction

Sedimentary processes in marine environments affect the overlying column and the global cycling of elements including carbon, nitrogen, iron, manganese, and sulfur (Snelgrove et al., 1997). Despite the importance of these environments, biogeographic surveys of sediment microbial communities and their link to geochemical parameters on broad spatial scales across a region are relatively scarce. This information is critical to better characterize sediment ecosystems and their impact on global processes such as nutrient cycling (Arrigo, 2005; Forsberg, 1989), ocean acidification (Cai et al., 2011), and primary production (Johnson et al., 1999). Although multiple geochemical parameters measured simultaneously may help infer part of the microbial activity in sediments, cryptic cycles that simultaneously produce and consume reaction products and reactants are left undiscovered by geochemical techniques alone. For example, active 'cryptic' sulfur cycles have been identified in which microbial communities of both sulfate reducing bacteria (SRB) and sulfur oxidizing bacteria (SOB) co-exist and therefore utilize the by-products of each reaction, creating an illusion of no change in concentrations with depth despite active cycling (Reese et al., 2013). In these cases, coupling DNA and RNA-based molecular techniques with geochemical tools may help characterize the main

biogeochemical processes of complex environments such as marine sediments (Reese et al., 2013; Reese et al., 2014a; Reese et al., 2018).

Sediment microbial communities are estimated to represent at least half of the Earth's microbial biomass (Whitman et al., 1998) but remain relatively under characterized. In addition to the lack of culturable representatives which can limit our understanding of microbial function, most studies have mainly focused on the bacterial fraction of the prokaryotic community. Archaea, however, also appear to be active, abundant, and widespread in marine sediments, particularly in the deep marine subsurface where they contribute to carbon degradation processes and nutrient cycling (Biddle et al., 2006; Schippers et al., 2005; Sturt et al., 2004). The limited number of studies of this group compared to their bacterial counterpart can be attributed to their relatively recent discovery, the fact that they are almost exclusively composed of uncultured microorganisms, and that most PCR 16S rRNA universal primers are predominantly designed to target the bacterial fraction, missing archaeal members (Raymann et al., 2017b; Teske and Sørensen, 2008). Therefore, better targeting this group may be particularly useful to better understand deep sedimentary processes, including the processes only conducted by archaea, such as the production and consumption of methane (Beulig et al., 2019; Hinrichs et al., 1999; Lloyd et al., 2011; McGlynn, 2017).

The amount of organic and inorganic material reaching sediments mostly depends on the intensity of primary production in the overlying water column, water column depth, distance from shore, and riverine inputs (Bienhold et al., 2016; Overholt et al., 2019; Wei et al., 2010; Zinger et al., 2011). Near shore sediments are associated with higher loads of organic material from surface primary production and riverine sources, and as a result

experience more biogeochemical variability than deep sea systems because of their stronger connection to terrestrial processes (Bauer et al., 2013). In organic matter rich sediments, oxygen is rapidly depleted through aerobic respiration and reoxidation of reduced metabolites (Glud, 2008), anaerobic processes are found closer to the sediment-water interface, and geochemical gradients are sharper (Burdige, 1993). Sulfate is the most abundant terminal electron acceptor in seawater and such a particularly efficient oxidant of natural organic matter that it is considered the primary terminal electron acceptor in anaerobic metabolism (Jørgensen, 1982). Thus, higher abundances of microbial species associated with sulfur cycling are present in organic-rich marine sediments, followed by a fast and sharp increase in methane- or hydrocarbon-related microbial species in the deeper layers (Beulig et al., 2018).

In contrast, the deep sea is largely oligotrophic, and temporally and spatially stable. Therefore, gradients of physical and geochemical parameters such as pressure, temperature, salinity, and pH, which control microbial community composition and function, remain mostly consistent (Bienhold et al., 2012; Lozupone and Knight, 2007). In these environments, the input flux of organic carbon is so low that oxygen penetration depth reaches several centimeters (Glud, 2008), and are dominated by aerobic respiration, denitrification and manganese reduction (Jahnke et al., 1990). In continental slope sediments, riverine dissolved and particulate material eventually delivered to the ocean flocculates and aggregates into fine-grained material that settles into the benthic boundary layer (BBL) 0.1-2 m above the seabed and forms mobile muds, an ephemeral layer that is often remobilized by physical mixing generated by tidal currents or storms (Aller, 1982, 1998; McKee et al., 2004). These mobile muds are eventually deposited on continental

shelves and slopes, with selective dispersal that depends on particle size, density, morphology, or composition (McKee et al., 2004), and enhance carbon remineralization by exposing sediment to oxygenated bottom waters (Aller, 1998; Blair and Aller, 2012; Hartnett et al., 1998) and co-metabolizing fresh, planktonic organic carbon (Canfield, 1994). As a result, sediment distribution across continental margins and their associated diagenetic processes may vary widely depending on the organic carbon and lithologic composition of the top sediment layers (Canfield, 1994; Grégoire and Friedrich, 2004; Taillefert et al., 2017). Subsequently, sulfur cycling processes are more prevalent deeper into the sediment in the anoxic zones as a result of the depletion of more energetically favorable electron acceptors ((Froelich et al., 1979)). Finally, the low concentration of organic material in open ocean environments limits microbial diversity, while in organic rich sediments, the unavailability of electron donors and acceptors deeper within the sediment control microbial abundance and richness (D'Hondt et al., 2004; D'Hondt et al., 2002).

The Louisiana continental shelf in the northern Gulf of Mexico is a dynamic system within close proximity of the Mississippi and Atchafalaya River system (MARS) which transports large amounts of freshwater and sediment material to the shelf (Dagg et al., 2004) and references therein). The high discharge of nutrients to the nGoM creates a seasonal hypoxic zone in the water column during the summer (May-August) (Rabalais et al., 2007). Hypoxic zone sediments can be classified in three geochemically distinct zones influenced by the sedimentology resulting from MARS discharge including regions where (1) metal oxide cycling dominates, (2) oxygen delivery into sediments exist due to bioturbation, and (3) iron oxide limited sulfate reduction dominates (Devereux et al., 2019).

Additionally, the continental slope and Mississippi canyon receive terrestrial inputs from the shelf region, including organic (Bianchi et al., 2006) and inorganic material (Trefry and Presley, 1982) (Owings et al., 2020) that influence microbial respiration processes. Therefore, continental slope sediments (>1,000 m water depth) of the nGoM could potentially be more microbially active than previously considered. The nGoM is a unique environment to study sediment microbial communities linked to geochemical parameters due to the proximity of geochemically distinct sedimentary regions corresponding to a range of bottom water oxygen concentrations as well as a range of organic carbon inputs due to the influence of the Mississippi River on the region. This study combined molecular and geochemical investigations to characterize the effect of a dominant riverine system (MARS) on the surrounding shelf and slope ecosystems during the hypoxic season and provide insights into the potential influence of sediment carbon remineralization pathways on the overlying water column.

5.3 Methods

5.3.1 Station locations and core descriptions

Sediments were collected for coupled molecular and geochemical analyses across the Louisiana continental shelf (LCS) in the northern Gulf of Mexico (nGoM) at stations across two transects (Figure 5-1) during July-August 2016 onboard the *R/V Pelican*. The first transect, referred to as the shelf transect, investigated geochemical and microbial processes across the hypoxic continental shelf. The shelf transect began at St. 6 (15 m water depth, located outside of Vermilion Bay, LA) and continued east toward the Mississippi River delta (St. 2, 67 m), including stations 5B, C6C, and MK (Figure 5-1, Table 5-1). The

second transect, referred to as the slope transect, examined the molecular and geochemical differences in the underlying sediment at four stations ranging in depths from 67 m (St. 2) on the hypoxic shelf to 1,230 m (St. 10) in the oxygenated waters of the continental slope (Figure 5-1, Table 5-1). At most stations, dissolved oxygen, conductivity, and temperature were measured as a function of depth in the water column with a Conductivity, Temperature and Depth (CTD) rosette (Sea-bird) equipped with oxygen sensor. To avoid disturbing the sediment, the rosette was lowered to about 1-2 m above the seafloor. CTD casts were not conducted at St. 5B, St. 2, and St. 3.

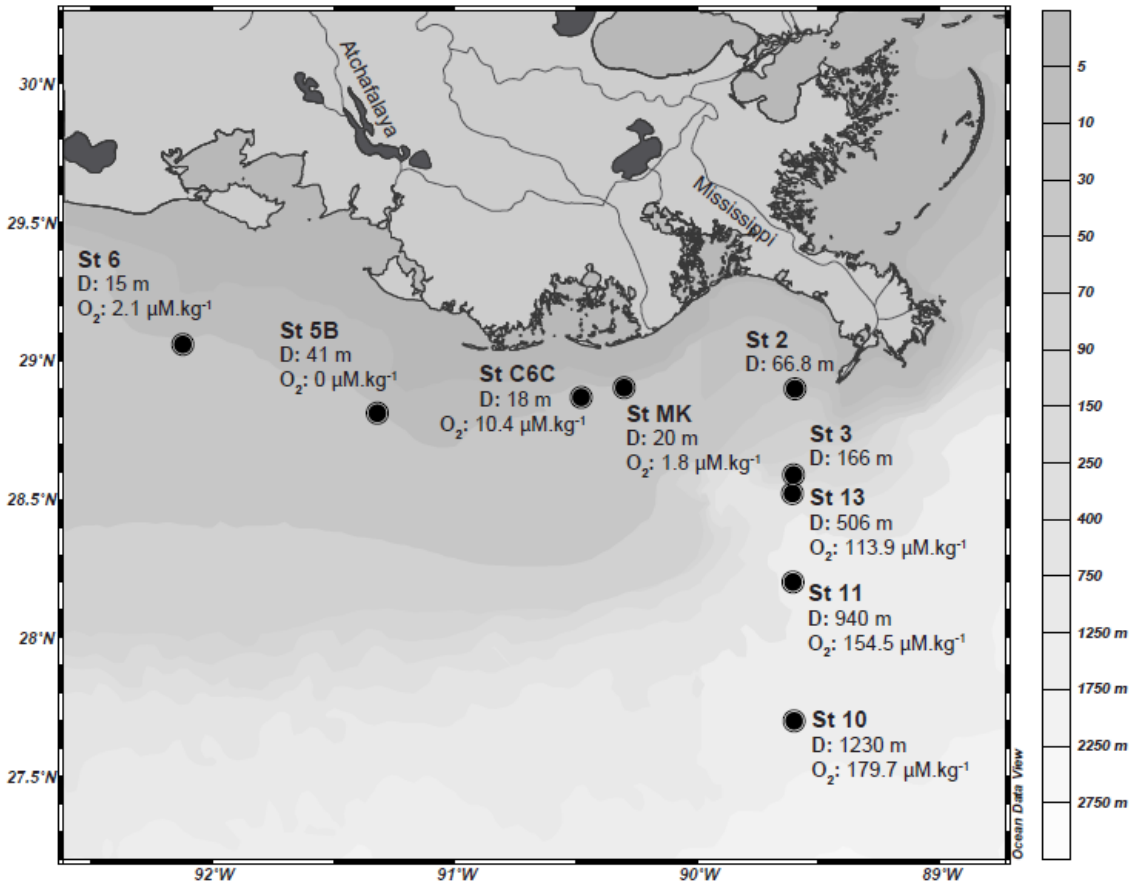

Figure 5-1 Map of the locations across the Louisiana shelf and slope in the northern Gulf of Mexico where sediment cores were collected during a research cruise in late July- early August of 2016. Water depths (D, m) and bottom water oxygen concentrations measured from CTD profiles (O_2, µM kg^{-1}) are provided for reference. Depth contours (m) indicate ocean bathymetry. Mississippi and Atchafalaya Rivers are labeled.

Table 5-1: Station location, depth and corresponding bottom water oxygen concentrations, salinities and temperatures

Transect	St..	Lat. (deg)	Long. (deg)	Depth (m)	Oxygen, (µmol/kg)[a]	Sal. (PSU)[b]	Temp. (°C)[b]
Shelf	6	29.060	-92.120	15	2.1	36	26.8
	5B	28.484	-91.199	41	< 63 µM[c]	36	27.1
	C6C	28.868	-90.478	18	10.43	37	27.4
	MK	28.903	-90.301	20	3.26	37.5	27.6
	2	28.899	-89.595	66.8	114[d]	38	22.6
Slope	3	28.590	-89.603	166	168[e]	38	28.6
	13	28.308	-89.358	506	113.91	35	13.3
	11	28.121	-89.358	940	154.52	35	9.0
	10	27.420	-89.360	1230	179.68	38	13.4

[a]: Oxygen concentrations measured by CTD rosette
[b]: Salinity and temperature of overlying waters measured onboard with refractometer and thermocouple
[c]: averaged from 2015 and 2017 NOAA dead zone data at a nearby location (Rabalais and Turner, 2015, 2017)
[d]: data from Taillefert cruise 2017 (Owings et al., submitted)
[e]: data from June 2006 at a nearby station (Devereux et al., 2015)

5.3.2 Sediment collection, voltammetric profiling, and pore water analysis

Sediment cores of approximately 20 cm in length and 9.6 cm inner diameter were collected using a MC-800 Multi-Corer (Ocean Instruments). After collection, the temperature and salinity of the overlying water of the core were measured using a thermocouple and refractometer. All cores were voltammetrically profiled immediately after collection except in the case of the sediment core from St. 3, which was collected in the evening, sealed, stored on deck, and analyzed 12 hours later. Voltammetric profiles were used to measured redox active species, including oxygen ($O_{2(aq)}$), manganese(II)(Mn^{2+}), iron (II) (Fe^{2+}), organic-Fe(III) complexes (org-Fe(III)), FeS_{aq}, and ΣH_2S (Luther et al., 2008; Taillefert et al., 2000b), using a three-electrode configuration

including a silver/silver chloride (Ag/AgCl) reference electrode, a platinum (Pt) counter electrode, and a gold/mercury (Au/Hg) working electrode (Beckler et al., 2016; Brendel and Luther, 1995; Luther et al., 1999). Profiles were conducted with less than 1 mm resolution using minimally invasive Au/Hg voltammetric microelectrodes connected to a computer-controlled Analytical Instrument Systems, Inc. (AIS, Inc.) MAN-1 micromanipulator and measured with an AIS, Inc. DLK-70 potentiostat. A combination potentiometric minielectrode (1.6 mm diameter, Microelectrodes, Inc.) was used to measure pH at each depth along the profile. The pH minielectrode electrode was connected to the potentiostat and pH was calibrated externally using TRIS buffer in synthetic seawater (Dickson, 1993). Dissolved oxygen was measured by linear sweep voltammetry (LSV) between -0.1 and -1.8 V including a preconditioning period of 10 s at -0.1 V and calibrated assuming the maximum peak amplitude measured in the overlying water corresponded to the bottom water oxygen concentration detected using the CTD oxygen sensors. Mn^{2+} and all other redox species were measured by cathodic square wave voltammetry (CSW) using at 200 mV s^{-1} scan rate, and a preconditioning step of 10 s at -0.1 V. An additional preconditioning step consisting of 10 seconds at -0.9 V was added before the aforementioned -0.1 V conditioning step if organic-Fe(III) complexes or dissolved sulfide signals were detected to clean the electrode surface (Tercier-Waeber and Taillefert, 2008). The resulting scans of current versus potential were analyzed to quantify peak height and surface area using a semi-automated VOLTINT software package (Bristow and Taillefert, 2008). The working electrodes were calibrated with a $MnCl_2$ solution (0-400 µM) in 0.54 M NaCl before profiling. Fe^{2+} and ΣH_2S concentrations in the pore waters were quantified using the pilot ion method with Mn^{2+} as pilot ion (Luther et al., 2008). As the exact

structures of the organic-Fe(III) and FeS_{aq} complexes are unknown, voltammetric signals are reported in peak current intensities normalized to the sensitivity of the manganese calibration for the respective core (Taillefert et al., 2000b).

After voltammetric microprofiles were completed, the sediment cores were sectioned in approximately twenty 7-10 mm sections and pore waters extracted under N_2 atmosphere in a glove bag (Sigma-Aldrich). A pellet of less than 0.5 g of sediment from the top 2 sections and every other section afterward was added to RNAlater, flash frozen on dry ice, and stored at -20°C for 16s rRNA extraction at Georgia Tech. The sediment sections were then centrifuged for 10 minutes at 3000 rpm and the pore waters were filtered through 0.22 µm PES Puradisc syringe filters (Whatman) into polypropylene Falcon tubes (Nalgene). To minimize oxidation of the sample, pore waters were then immediately transferred to a secondary glove bag under N_2 atmosphere and split for subsequent analyses of dissolved Fe(II) (Fe^{2+}_d) by the Ferrozine method (Stookey, 1970), orthophosphates (ΣPO_4^{3-}) by the methylene blue method (Murphy and Riley, 1962), and dissolved inorganic carbon (DIC) via a flow-injection analysis (Hall and Aller, 1992). Aliquots of pore water samples were also added to 0.2 M hydroxylamine at pH 1.0 and stored in the dark for 24 hours to quantify total dissolved iron (Fe_{tot}) by the Ferrozine method and dissolved Fe(III) ($Fe(III)_d$) by difference between Fe_{tot} and Fe^{2+} (Stookey, 1970). Finally, aliquots were analyzed onboard for dissolved Mn (Mn_d) by ligand exchange reaction with a porphyrin molecule [(α,β,γ,δ-tetrakis(4-carboxyphenyl)porphine (T(4-CP)P)] and absorbance measurement at 468 nm (Madison et al., 2011a) after correction for Fe^{2+} interference by dilution (Owings et al., submitted). The leftover pore waters were frozen at -20°C until analysis of ammonium (NH_4^+) by the indophenol blue method (Strickland and Parsons,

1972) and anions by high performance liquid chromatography (HPLC) without suppression at Georgia Tech. Anion separation was achieved with a Waters 1525 pump and a 4.0 mm x 150 mm Metrosep Supp 5 anion exchange column (Metrohm) using either 3.2 mM $NaCO_3$ / 1.0 mM $NaHCO_3$ buffer bicarbonate (Cl^-, Br^-, SO_4^{2-} in 30-fold diluted samples) or 54 mM sodium chloride (NO_2^-, and NO_3^- in undiluted samples) as mobile phase. The mobile phase was eluted through the column at a flow rate of 0.75 ml min^{-1} and absorbance was measured at 210 nm with a Waters 2487 photodiode array detector (Beckler et al., 2014). Error for dissolved components analysis was propagated from the calibration curves.

5.3.3 Nucleic Acids Extraction and Illumina Sequencing

Microbial communities were characterized at every station. In order to relate chemical changes within the sediment with potential changes in microbial community composition, 10 samples were taken from every core, down to about 135 mm, with a separation of 5 to about 20 mm between each sample. DNA was extracted using the MoBio Power Soil Kit™. Approximately 0.3 grams of sediment was used for extraction, yielding approximately 20 ng/µL (in 50 µL) DNA. For Bacteria, 16S rRNA genes were amplified using primer pairs 505F and 806R, with PCR primers harboring sample specific adapters for de-multiplexing as described previously (Kozich et al., 2013). PCR reactions were carried out in 25 µL total volume with 0.5µL of each forward and reverse primer at (0.2 µM final concentration) with GoTaq green master mix (12.5 µL per reaction), 1 µL of template, and 9.5 µL PCR-grade water. PCR reactions consisted of an initial denaturation step of 95 degrees C for 5 minutes, followed by 28 cycles of 95 degrees C for 1 minute, 55 degrees C annealing for 1 minute, 72 degrees C extention for 2 minutes, followed by a final

5 minute extension of 72 degrees. PCR products (5uL) were visualized by gel electrophoresis (1% agarose, 1% Gel Red). The remainder of the products (20 µL) were cleaned using the QIAQuick PCR clean-up kit, and eluted in 30 µL elution buffer. Cleaned PCR products were quantified using the broad range double stranded DNA quantification kit (Thermo Scientific). PCR products were pooled, with each sample-PCR product representing 10ng. This pooled mixture was then diluted to 1.2 ng/µL and used for further sequencing analyses on an Illumina MiSeq, using a V2 500 cycle paired end mode kit.

Archaeal 16S rRNA gene amplifications were carried out using the same PCR-recipe as above, with PCR primers Arch516F (TGYCAGCCGCCGCGGTAAHACCVGC) and 915R (GTGCTCCCCCGCCAATTCCT) (Raymann et al., 2017a). These primers were amended with Illumina adapters specific for the forward and reverse primers, barcodes, primer pad, and primer linkers. The thermocycler protocol was similar, with one exception, 30 cycles were utilized rather than 28.

5.3.4 Quality Sequence Processing and Analyses

Amplicon sequences from both Bacterial and Archaeal data sets were analyzed essentially the same, using the DADA2 pipeline. Taxonomy was assigned to the representative ASVs from this pipeline using were compared to the SILVA rRNA gene database (version 132) at 99% identity level . Sample-taxonomy tables were generated by 'adding' the taxonomy information for each representative ASV to sample-ASV tables in Qiime-2019.4. Sequences classified as chloroplasts or Eukaryota were removed from the final tables. Amplicons obtained using universal prokaryotic primers were rarefied to a depth of 50000 reads, while those obtained using the archaea specific primer set were

rarefied to 1200 reads. Further diversity analyses including phylogenetic tree construction, and alpha and beta diversity metrics were conducted using Qiime-2019.4.

5.3.5 Phylogenetic Inference

In order to better characterize the *Bathyarcheaia* group in our dataset, phylogenetic approximation of bathyarcheaial ASVs was inferred by comparing those sequences to the *Bathyarchaeota* database from Zhou et al. (2018) using BLASTN (97% similarity cutoff).

5.3.6 Multivariate Analyses

Canonical correspondence analyses (CCA) were performed in R (version 3.6) using the vegan package. Rarefied sample-ASV matrices, and the associated metadata (environmental parameters) were used. ASV relative abundances were square root transformed while sediment chemistry measurements were log transformed. To identify which environmental variables were significant, an ANOVA test was performed on those terms of the CCA.

Co-occurrence network analysis was performed following the pipeline established by (Pylro et al., 2014), which used SparCC to determine correlations between ASVs. This analysis was performed on the ASVs with a relative abundance ≥ 0.002% from the ASV table obtained using the universal primer set. Only strong correlations with a p-value ≤ 0.01, and imported into Cytoscape where and Markov clustering method (MCL) was applied based on betweenness centrality.

The *Bathyarchaeia* heatmap was realized using R (version 3.6), package Heatplus. Only *Bathyarchaeia* ASVs retrieved from the ASV table obtained using the archaea

specific primer set. For clarity and visibility, only ASVs with a relative abundance ≥ 1.5% are presented.

5.4 Results

5.4.1 Mississippi River discharge and visual sediment characteristics

The Mississippi River discharge from Belle Chasse, LA monitoring station (29°51'25", 89°58'40") was 418,556 ± 22,875 cm^3 s^{-1} during this study (Figure D 1). Overall, the discharge pattern was transitioning from high discharge (1,330,000 cm^3 s^{-1} between January and March 2016) to low discharge (229,000 cm^3 s^{-1} in December 2016) (Figure D 1, USGS). Sediment cores collected varied in color depending on station location (Figure D 2). Across the shelf (St. 6, 5B, C6C and MK), sediments were a mix of gray to dark gray with patches of black (Figure D 2). A worm (approx. 6.5 cm long) was discovered while sectioning St. 6 sediment core, indicative of active bioturbation (not pictured). Interestingly, at St. MK a floc of black sediment was present in the top 7 cm (Figure D 2). Sediments from St. 2 and St. 3 were similar with a small band of brown sediments in the top few centimeters, followed by dark gray/black sediments to depth. At St. 11, sediments contained a thicker layer of brown sediments in the top 4 cm that was distinct from the remaining gray sediment below the brown layer (Figure D 2). The sediment core from St. 10 appeared to be homogenously distributed as brown/gray sediment throughout the core (Figure D 2). Station 6, Station 2 and station 10 were chosen as representative stations of the shelf, shelf-slope transition, and slope regions (Figure 5-3). These the sediment biogeochemistry at these three stations are discussed in detail (Figure 5-3) in the results,

however, the remainder of the stations are briefly discussed and figures for each data set at each station are found in the supplemental material.

5.4.2 Bottom water oxygen concentrations and oxygen penetration depths in the sediment:

Bottom water oxygen concentrations along the shelf transect ranged from 2 to 11 µM (Table 5-1), therefore falling under the defined conditions of hypoxic (< 63 µM) (Rabalais et al., 2010). Although not measured in the present study, St. 5B was in the hypoxic zone according to 2015 and 2017 historical data (Rabalais and Turner, 2015, 2017). In turn, bottom water oxygen concentrations at St. 2 were slightly below saturation at114 µM during the summer of 2017 (Owings et al., submitted) and close to saturation at 168 µM in 2006 at a station (St. z01 29º0.117" N, 89º 32.258"W) near St. 2 and 3 was (Devereux et al., 2015), suggesting that the hypoxic zone did not extend over the shelf. Indeed, bottom waters of the slope stations were oxic and fully saturated (Table 5-1). Correlating bottom oxygen concentrations, dissolved oxygen concentrations in the sediment core overlying waters were below detection limit of the voltammetric microelectrodes (Minimum Detection Limit: MDL ~ 3 µM (Luther et al., 2008)) across the hypoxic shelf. In turn, overlying waters of the continental shelf ranged between 113 and 180 µM kg^{-1} (Table 5-1) , while oxygen penetration depths (OPDs) increased from 4 mm (St.2) to >10 mm across the slope.

5.4.3 DIC, NH_4^+, ΣPO_4^{3-} and pH profiles

Pore water DIC concentrations were generally higher across the hypoxic shelf than across the continental slope (Figure 5-2) and more elevated on the western and eastern ends

of the hypoxic zone. Bottom water DIC concentrations at the shelf stations were between 2-2.8 mM and pore water DIC concentrations increased to maximum concentrations of 4.3-5.5 mM at St. C6C (Figure D 4), St. 6 (Figure 5-3), and St. 5B (Figure D 3) around 50 mm below the sediment water, however the peak at St. MK was more shallow at 13 mm (Figure D 5). Deeper, DIC concentrations generally decreased to 4.2, 3.0 or 2.3 mM at stations 6, 5B and MK respectively. DIC at St. 2 (closest to the Mississippi River delta) increased from 3.0 mM at 3 mm to 7.1 mM at 148 mm (Figure 5-3b). On the other hand, no variations in DIC concentrations (2.3-3.8 mM) were observed in the slope sediments (Figure 5-2). Simultaneously, NH_4^+ concentrations increased constantly with depth from the SWI to maximum concentrations at the bottom of the sediment cores and, similarly to DIC, reached higher maximum concentrations at the shelf stations (210-440 µM) than slope stations (113-160 µM) (Figure 5-2). A few stations displayed linear trends of about 200 µM with slight oscillations at depth (St. MK, St. 13, St. 10). St. 11 maintained low concentrations (11-34 µM) until 51 mm, followed by higher concentrations of 93-149 µM until depth (143 mm), with a peak to 360 µM at 86 mm (Figure 5-3). Similarly, St. 10 maintained low concentrations of NH_4^+ within the first 48 mm (20-78 µM) followed by peaks in concentrations at 71 and 95 mm of 896 and 1,023 µM, respectively before a return to concentrations between 144-444 µM between depths 103-151 mm (Figure D 8). NH_4^+ concentrations for St. C6C and ΣPO_4^{3-} concentrations for St. 5B were not analyzed due to limited sample size. ΣPO_4^{3-} concentrations in shelf sediments were low near the SWI (<30 µM) and peaked to about 40-80 µM around 20-40 mm and remained elevated through the remainder of the core (Figure 5-2, Figure 5-3a, Figure D 4, Figure D 5, Figure 5-3b). In contrast, the ΣPO_4^{3-} concentrations in the slope stations increased continuously with depth

to maximum concentrations around 25 µM (Figure 5-2, Figure D 6, Figure D 7, and Figure D 8).

The overlying water pH ranged between a minimum of 7.5 (St. 6, Figure 5-3a) and a maximum of 8.1 (St. C6C, Figure D 4) across the shelf stations and reached a maximum (approx. 0.1 units higher than overlying waters) around 3-5 mm below the SWI (Figure 5-3a,b Figure D 3, Figure D 4, Figure D 5). Deeper, the pH decreased by about 0.5-0.7 units and remained constant between 7.2 (St. 6, Figure 5-3a) and 7.3 (St. C6C, Figure D 4) at depth. The overlying water pH of the continental slope stations was generally higher, ranging from 7.4 at St. 13 (Figure D 7) to 7.7-7.9 at St. 3, 11, and 10 (Figure D 6, Figure 5-3c, Figure D 8). pH data were not collected at St. 2. Interestingly, the pH of the continental slope stations did not produce a maximum below the SWI, instead the pH decreased moderately in comparison to the shelf stations from approximately 3-10 mm below the SWI to a pH minimum ranging between 7.1 and 7.6 (Figure D 6, Figure 5-3c, and Figure D 8).

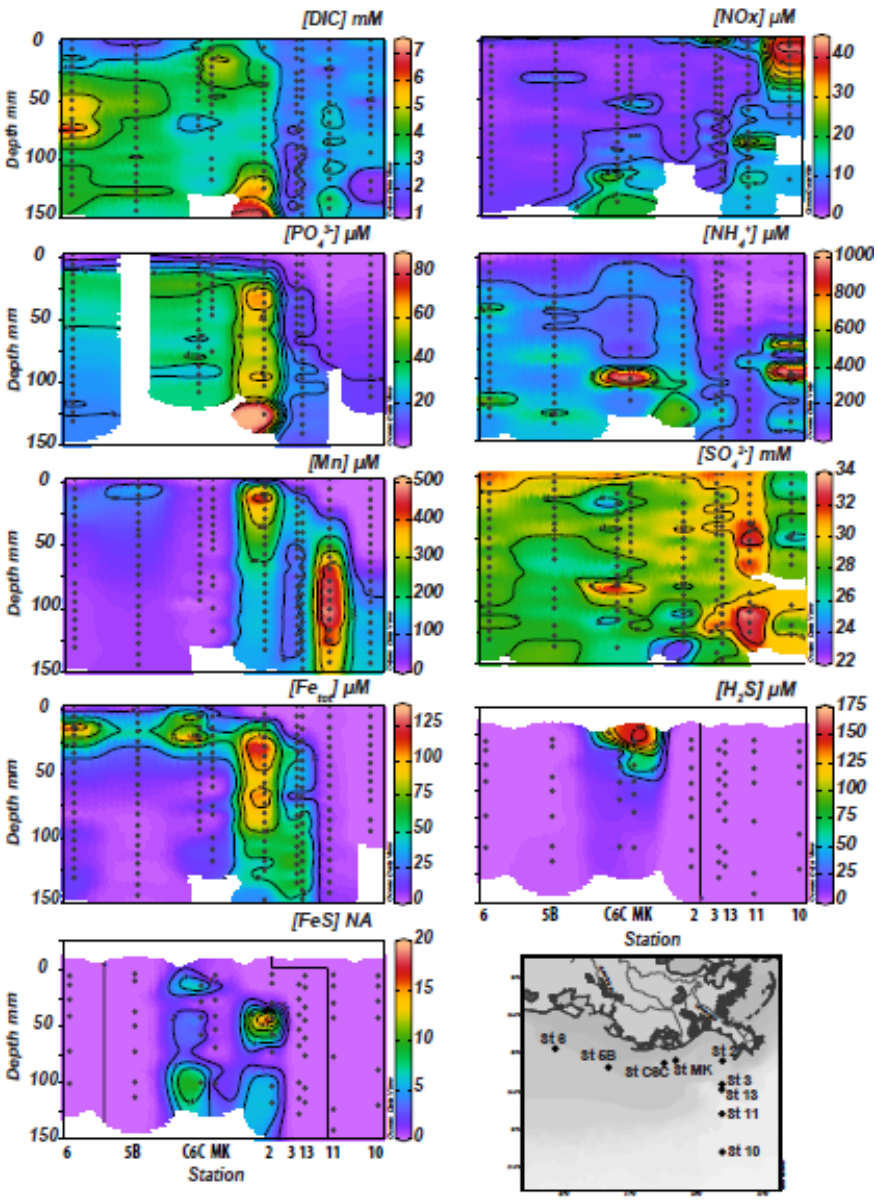

Figure 5-2 Dissolved inorganic carbon (DIC, mM), NO_x=NO_2^- + NO_3^- (µM), orthophosphate (PO_4^{3-}, µM), ammonium (NH_4^+, µM), total dissolved Mn (Mn_d, µM), sulfate (SO_4^{2-}, mM), and total dissolved Fe (Fe_d, µM) measured in the pore waters along with dissolved sulfide (ΣH_2S, µM) and aqueous FeS (FeS, nA) measured by voltammetric microelectrodes as a function of depth at each station using a heat map. The map of station locations is included for reference (bottom right). Black dots on each plot represent actual measurement locations. Color contours from red to purple represent high to low concentrations indicated by the scale to the right of each panel. Plots created in Ocean Data View (ODV) software.

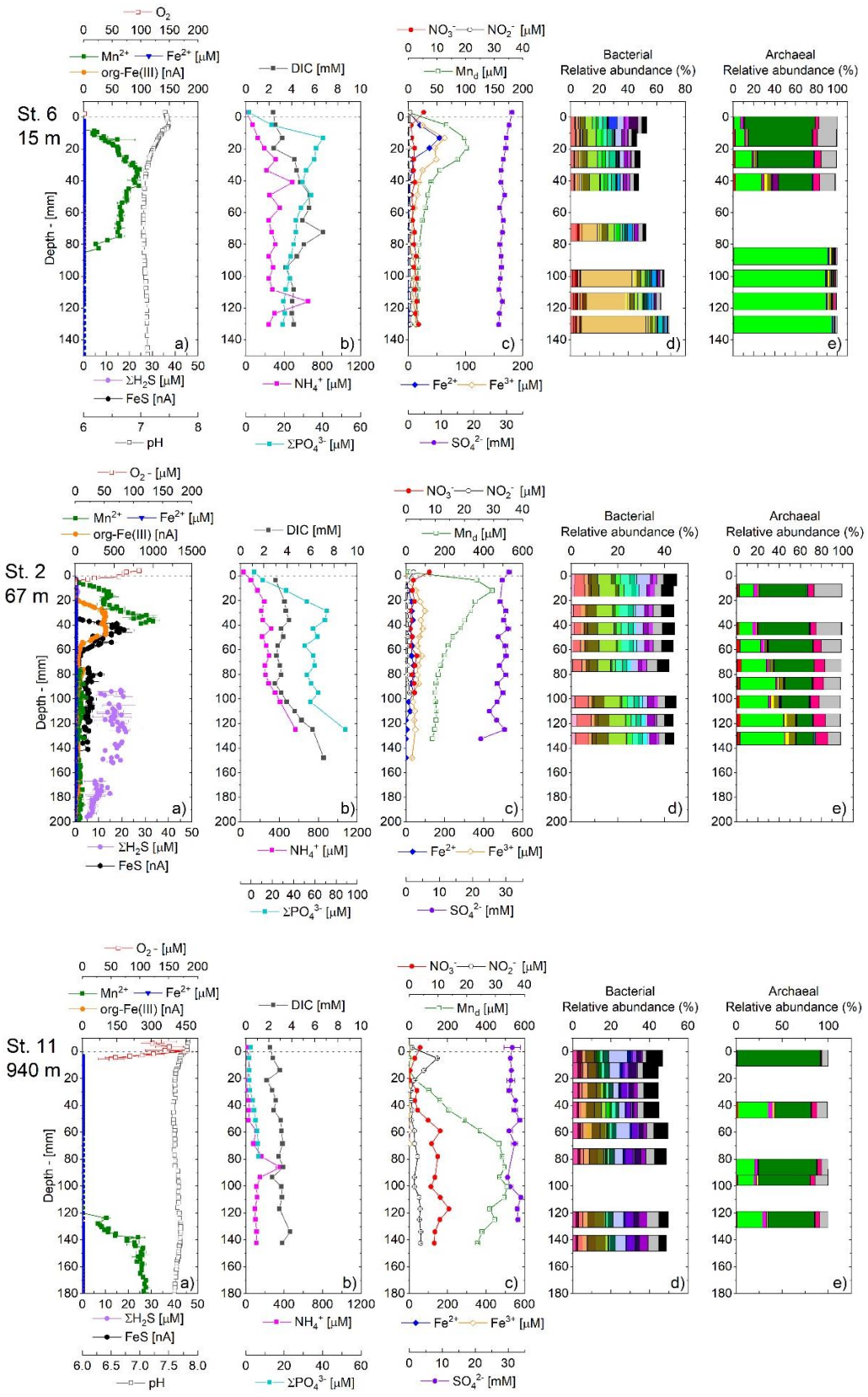
St. 6
15 m
St. 2
67 m
St. 11
940 m
Depth - [mm]
O2 [µM]
Mn2+ Fe2+ [µM]
org-Fe(III) [nA]
ΣH2S [µM]
FeS [nA]
pH
DIC [mM]
NH4+ [µM]
ΣPO43- [µM]
NO3- NO2- [µM]
Mnd [µM]
Fe2+ Fe3+ [µM]
SO42- [mM]
Bacterial
Relative abundance (%)
Archaeal
Relative abundance (%)
a)
b)
c)
d)
e)

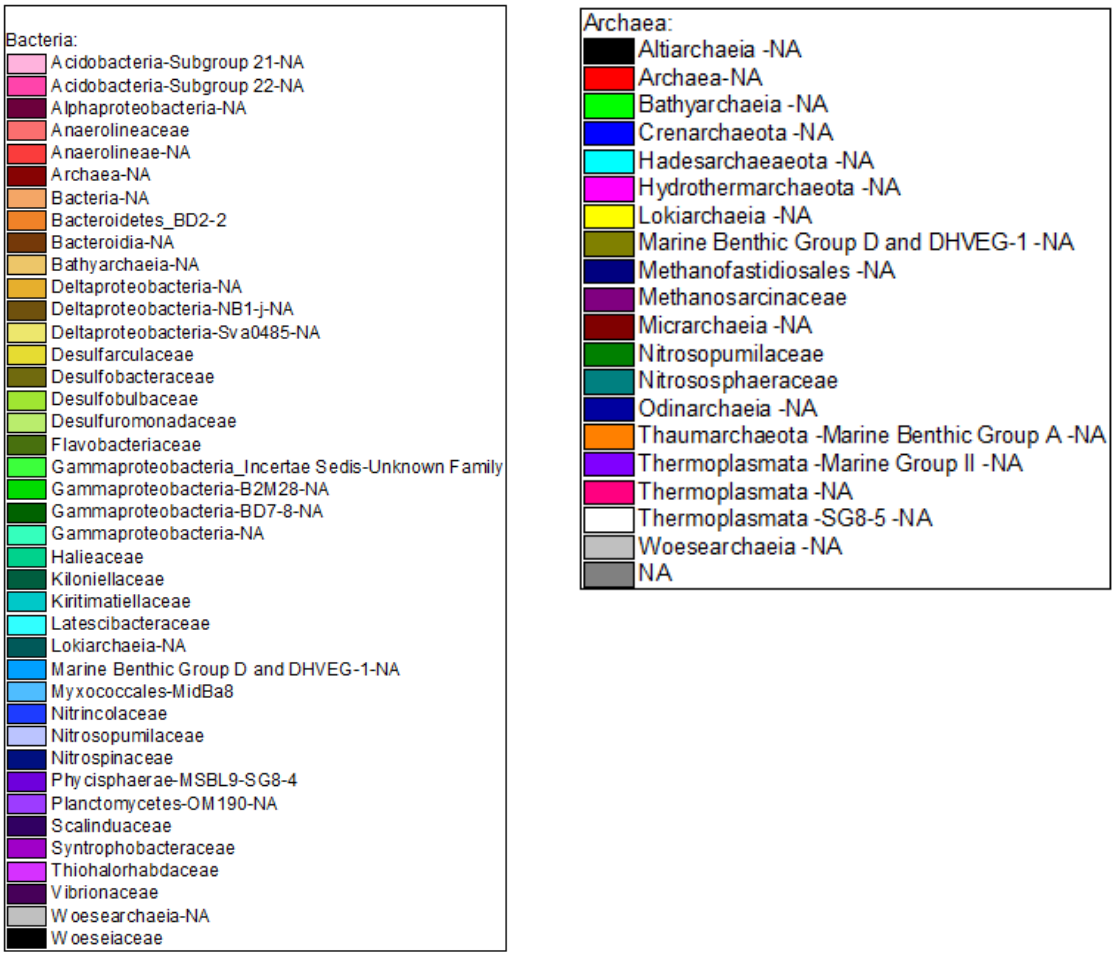

Figure 5-3 Pore water geochemistry (a-c) and bacterial (d) and archaeal (e) populations at the family level (including the 10 most abundant families of each sample) at: a) St. 6; b) St. 2; and c) St. 11. Sediment-water interface (SWI) indicated by the dashed line. The pH data were not available at St. 2. Mn and Fe signals overloaded between 40 and 80 mm at St. 2 and are not provided. Note the change in scale for voltammetric Mn^{2+}, Fe^{2+} and org-Fe(III) measurements, as well as Mn_d, Fe^{2+} (St. 6), and ΣPO_4^{3-} (St. 2) concentrations to better display trends at each station.

5.4.4 Main sedimentary redox processes in the LCS

NO_2^- and NO_3^- concentrations (presented as NO_x=NO_2^- + NO_3^- in Figure 5-2 were generally low in most shelf and slope sediments with some subsurface maxima found in the middle of the shelf (St. C6C and MK) and at St. 3, 10, and 11 on the slope (Figure 5-2). In contrast, NO_x concentrations were high at the sediment surface of most of the slope stations (St. 3, 13, and 10). At most stations (St.6, 5B, 2, and 13), NO_x decreased rapidly with depth and remained below 5 µM and 1.8 µM respectively within 20 mm from the SWI (Figure 5-3a, Figure D 3, and Figure D 7). The profiles of the easternmost shelf stations, St. C6C and St. MK, however, revealed that both NO_2^- and NO_3^- concentrations increased at depth to maximums of 23 µM NO_3^- and 6.3 µM NO_2^- at 115 mm at station C6C (Figure D 4), and 11 µM NO_3^- and 3.9 µM NO_2^- at 108 mm at station MK (Figure D 5). Although NO_2^- concentrations remained constant below 2.3 µM throughout the core at St. 3 (Figure D 6) and 11 (Figure 5-3), NO_3^- concentrations decreased from 19 µM at St. 3 and 3.8 µM at St. 11 in the overlying waters to approx. 2 µM at 20 mm, followed by a rebound to 12 µM at 67 mm at St. 3 and between 8 and 13 µM with depth at St. 11. In turn, St.10 displayed a broad subsurface NO_2^- peak of 23 µM centered at 20 mm, while NO_3^- concentrations decreased from 37 µM in the overlying waters to 9.8 µM at 27 mm and remained stable around this concentration deeper in the sediment (Figure D 8).

Most stations on the shelf displayed generally low dissolved Mn and dissolved Fe concentrations with small peaks at shallow depths in the profiles (Figure 5-2). At St. 6, Mn_d, Fe^{2+} and $Fe(III)_d$ peaked at 20 mm to concentrations of 102, 36, and 46 µM respectively (Figure 5-3a). Although slightly offset with depth, a broad Mn^{2+} peak (max. concentration of 98 µM at 32 mm) was also observed in the voltammetric profile at St. 6,

while all other redox species remained below detection limit (Figure 5-3a). Such differences between voltammetric and pore water measurements likely reflect the fact that voltammetric measurements are obtained at one point at each depth in the sediment, compared to the pore water measurements that are integrated over the entire slice of sediment from which they are extracted. At St. 5B, a peak in Mn_d concentrations (145 µM) occurred immediately below the SWI (3.5 mm), followed by a peak in Fe^{2+} and $Fe(III)_d$ (11 and 40 µM respectively) at 17 mm. A Fe^{2+} peak in the voltammetry profile also mirrored the $Fe^{2+}{}_d$ peak in the pore waters (Figure D 3). The pore water profile of St. C6C displayed a peak in Fe^{2+} and $Fe(III)_d$ of equal concentrations (67-71 µM) at 21 mm and low Mn_d (< 35 µM) concentrations throughout the core (Figure D 4). The voltammetry profile at St. C6C detected Fe^{2+} throughout the core, except between 33 and 82 mm where Mn^{2+} was detected. Additionally, org-Fe(III) complexes were detected around 30 nA between 26-84 mm and at depth between 150-197 nA. At St. MK, Mn_d in the pore waters remained around 4-14 µM throughout the core, and $Fe(III)_d$ peaked at 20 mm (36 µM). Dissolved Mn and Fe species were below detection limit of the voltammetric measurements at St. MK.

In contrast, dissolved Mn and dissolved Fe concentrations were much higher in the slope station sediments (Figure 5-2), although the onset depth of these species in the pore waters increased progressively with water depth. As a result, dissolved metals were the most abundant at St. 2 compared to the other shelf stations: A broad Mn_d peak of 445 µM centered at 12 mm that progressively decreased in concentration to 136 µM at 132 mm (Figure 5-3b) was accompanied by a modest increase in Fe^{2+} (to 41 µM at depth) and a broad peak in organic-Fe(III) voltammetric signals (between 20-70 mm) that was mirrored

by the $Fe(III)_d$ pore water measurements (Figure 5-3b). The Mn_d peak migrated progressively deeper in the sediment across the continental slope, whereas Fe_d concentrations generally decreased in the pore waters (Figure 5-2). At St. 3, Mn_d concentrations peaked to 181 µM at 13 mm, decreased to 51 µM at 75 mm, and remained constant deeper in the sediment (Figure D 6). Fe^{2+} and $Fe(III)_d$ species appeared around 26 mm and hovered around 9-40 µM and 34- 62 µM deeper, respectively (Figure D 6). Although slightly offset with depth and concentrations, the voltammetric profiles at St. 3 also revealed a Mn^{2+} peak (203 µM) at 31 mm before coinciding Fe^{2+} (433 µM) and org-Fe(III) complexes (78 nA) peaks around 50 mm. At St. 13, Mn_d increased to a maximum concentration of 190 µM at 32 mm, dipped to around 100 µM at 60 mm, and remained constant deeper in the sediment. Mn^{2+} was not detected by voltammetry until 75 mm and remained relatively low around 25-63 µM deeper in the same sediment. At St. 13, the onset of Fe^{2+} and $Fe(III)_d$ production occurred simultaneously around 32 mm, and Fe^{2+} and $Fe(III)_d$ concentrations increased up to 21 and 51 µM with depth, although voltammetric Fe^{2+} remained below detection limit and org-Fe(III) signals were small (Figure D 7). Mn_d concentrations at St. 11 increased from below detection limit at 20 mm to 600 µM at 70 mm and remained elevated deeper (Figure 5-3c), whereas pore water Fe^{2+} remained below detection limit and $Fe(III)_d$ concentrations were around 2 µM (Figure 5-3). In turn, the voltammetry profile only showed Mn^{2+} production at 120 mm to a maximum concentration around 307 µM Mn(II) at 140 mm that remained constant deeper, whereas Fe^{2+} and org-Fe(III) were not detected throughout the profile (Figure 5-3). Finally, Mn_d concentrations at St. 10 were below detection limit until 55 mm below the SWI and gradually increased

with depth to 170 µM at 151 mm, whereas pore water Fe^{2+} and Fe(III)d remained below detection limit and Mn2+ and Fe species were not detected by voltammetry (Figure D 8).

SO_4^{2-} concentrations across the shelf and slope ranged from 25-32 mM, with no significant decrease with depth at all stations (Figure 5-2), except at St. 2 where SO_4^{2-} decreased to 22.5 mM at 133 mm (Figure 5-3b). Despite no significant decrease in SO_4^{2-} concentrations, ΣH_2S was detected in all shelf station sediments (Figure 5-2) except for the westernmost St. 6 (Figure 5-3a). ΣH_2S concentrations were low (< 5 µM) but present consistently below 25 mm at St. 5B (Figure D 3). ΣH_2S was detected in the overlying waters (26-31 µM) at St. MK (Figure D 5), formed a sharp peak around 181 µM at 15 mm, and decreased progressively deeper (Figure D 5). A similarly sharp ΣH_2S peak was found below the SWI at St. C6C (41 µM at 18mm) that was followed by another broader peak reaching 20 µM between 74 and 116 mm that progressively decreased with depth (Figure D 4). Finally, the onset of sulfate reduction as revealed by the ΣH_2S depth profile, where ΣH_2S concentrations increased to approximately 20 µM at 113 mm, remained constant until 170 mm, then progressively decreased in concentration with depth (Figure 5-3b). In contrast, ΣH_2S was detected generally in much lower levels at the slope stations (Figure 5-2), but decreased from the mid-slope stations (5-10 µM) at depth (> 80mm) at St. 3 and St. 13 (Figure D 6 and Figure D 7) to below detection limit at the deep St. 11 and St.10 (Figure 5-3c and Figure D 8). Finally, FeS_{aq} was below detection limits at most stations, except on the eastern shelf and on the shelf break (Figure 5-2). Although detected in low current intensities (< 5 nA) throughout most of the profile at St. 6C6, FeS_{aq} formed a subsurface peak (2-20 nA) between 35-142 mm and hovered around 5 nA deeper at St. 2

(Figure 5-3b). Similarly, FeS_{aq} was produced below 80 mm at St. 3 and reached current intensities oscillating between 5 and 17 nA deeper (Figure 5-2).

5.4.5 Abiotic factors influencing microbial community structure in the Northern GoM

Beta and alpha diversity analyses indicated that microbial communities varied with both water column and sediment core depth. Canonical correspondence analysis (CCA) on both prokaryotic and archaea datasets separated microbial communities from shelf stations from those from slope stations (Figure 5-4). Except for NO_2^- and org-Fe(III), most chemical species appeared to be significantly related to microbial community structure in the prokaryotic dataset (Table D1a), whereas only DIC, NH_4^+, SO_4^{2-}, and ΣH_2S appeared significantly related to the archaeal dataset (Table D1b). Despite these features, the same trend appeared for both datasets with DIC, ΣPO_4^{3-}, and ΣH_2S as the main variables related to shelf microbial structure (p-value $\leq$ 0.01), whereas NO_3^- was the most related species to slope microbial assemblages (p-value $\leq$ 0.01) (Figure 5-4). Moreover, sediment core depth also appeared as a principal variable related to the microbial community composition of both datasets (p-value $\leq$ 0.01) (Figure 5-4). Interestingly, differences in alpha diversity were also observed with water column depth, as well as within the sediment in both shelf and slope samples (Figure D 9). Richness measured by Faith-phylogenetic diversity index (Faith-pd) decreased between shelf and slope in both the prokaryotic (p-value = 0.006) and archaea (p-value = 9.00E-07) datasets, while diversity (Shannon index) did not appear to significantly change. On the shelf, richness (Faith- pd) of both the prokaryotic (p-value = 0.007) and archaea (p-value = 0.0008) showed an overall decrease with sediment core

depth, whereas diversity (Shannon index) of both shelf (p-value = 0.0058) and slope (p-value = 0.05) stations increased with sediment core depth only for the archaea dataset.

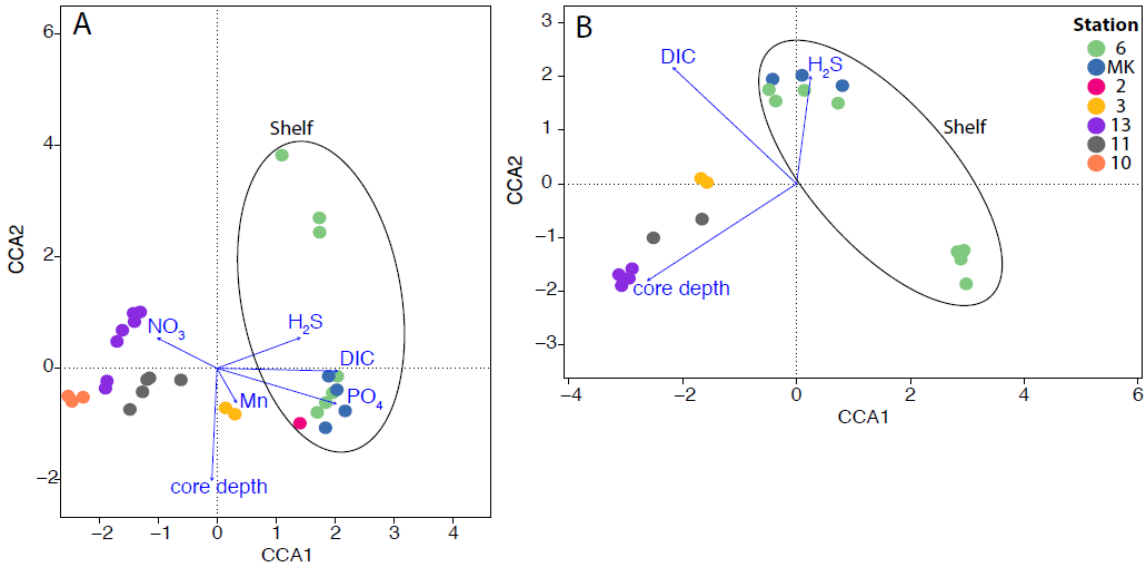

Figure 5-4 Ordination plots of Canonical Correspondence Analysis (CCA) obtained with: a) universal primers; and b) archaeal specific primers to explore the relationship between prokaryotic communities at each station and significant environmental variables (p-value<0.01). Only samples with measurements of all geochemical parameters were included in analysis (i.e. NH_4^+ data not available for C6C and ΣPO_4^{3-} data not available for 5B).

5.4.6 Microbial community composition along the nGoM shelf and slope

Sediment samples used for microbial characterization were collected at all stations along with geochemical data. Microbial community composition in sediments was evaluated by sequencing 16S rRNA gene amplicons generated using both non-domain-specific primers that amplify all bacterial and some archaeal groups (Earth Microbiome Primers 505F and 806R; "bacterial" amplicons hereafter) as well as Archaea domain-specific primers that amplify the V4-V5 region of the 16S rRNA gene (516F/915R;

"archaeal" amplicons hereafter). These primers were developed to better target the archaeal community, which appeared to be largely under characterized using universal prokaryotic primers due to their low specificity to this specific microbial group (Raymann et al., 2017b). Initial analyses were performed on sequence data partitioned at the level of amplicon sequence variant (ASVs) using DADA2. ASVs from the bacterial and archaeal datasets were compared against the SILVA rRNA gene database (version 132). Sequence counts corresponding to ASVs sharing identical taxonomic hierarchies were summed and the rank abundance of ASVs was compared among sites. 76 prokaryotic amplicon datasets were rarefied to 50000 sequences, yielding a total of 70332 ASVs, and 58 archaeal amplicon datasets were rarefied to 1200 sequences each, yielding 3999 ASVs.

The entire prokaryotic dataset was dominated by *Gammaproteobacteria* (19.4%), and Deltaproteobacteria (18.5%). *Nitrosphaeria* was the third most abundant class (5.3%), followed by *Anaerolineae* (4.8%) *Phycisphaerae* (4.2%), *Bathyarchaeia* (3. 4%), *Alphaproteobacteria* (3.5%), *Bacteroidia* (2.9%), *Woesearchaeia* (2. 4%), and *Acidobacteria-Subgroup22* (1.8%) (Table D 4). Interestingly, most of these groups varied strongly in relative abundance and microbial composition at finer taxonomic resolution between shelf and slope stations. While samples for microbial and biochemical profiling were collected at every station and at different depths within the sediment core, 3 stations including St 6, St 2, and St 10 were chosen to represent the general trends observed on the shelf (St 6), on the slope (St 10), and on the transition between the two (St. 2) (Figure 5-3). Among the groups that showed the largest differences between shelf and slope, *Bathyarchaeia* were 17 times more abundant on the shelf (Figure 5-3, Table D 4, Table D 5). Other classes that were among the 10 most abundant at shelf stations, such as

Thermoplasmata (~ 3.5 times more abundant on the shelf) dominated by *Marine Benthic Group D* and *DHVEG-1*, and *Anaerolineae* (~ 2 times more abundant on the shelf) dominated by *Anaerolineaceae*, also showed higher relative abundances on the shelf compared to the slope (Figure 5-3, Table D 4, Table D 5). In contrast, *Brocadiae* dominated by *Scalinduaceae*, *Nitrososphaeria* dominated by *Nitrosopumilaceae*, *Alphaproteobacteria* dominated by *Kiloniellacea*, and *Phycisphaerae* dominated by *MSBL9-SG8-4* were 38, 6, 4 and 2 times more abundant on the slope, respectively (Figure 5-3, Table D 4). Moreover, a microbial network analysis conducted on the prokaryotic dataset (relative abundances > 0.0002) was able to partition the microbial diversity into several clusters which were composed by ASVs that were differentially abundant following water column or sediment depth gradients (Figure 5-5). Families including *Bathyarchaeia-NA*, *Desulfobacteraceae*, *Desulfobulbaceae*, *Anaerolineaceae*, *Halieaceae*, *Marine Benthic group D* and *DHVEG-1*, *Thiohalorhabdaceae*, *Thioalkalispiraceae*, *Ectothiorhodospiraceae*, *Lokiarchaeia-NA*, *4572-13 (Phycisphaerae-MSBL9)*, *Thiotrichaceae*, *Fusobacteriaceae*, *Methanofastidiosales-NA*, and *Methanosarcinacea*, were part of a single cluster (cluster 2), which was primarily composed of microorganisms that showed higher relative abundances on the shelf (Figure 5-3, Figure 5-5, Table D 4). These particular groups represented about ~ 30% of the microbial community on the shelf compared to ~ 8% on the slope, and potentially play an important role in microbial community composition and function in shelf sediments based on network analysis (Figure 5-5, Table D 2). On the other hand, the slope was characterized by higher relative abundances of *Nitrosopumilaceae*, *Woeseiaceae*, *NB1-J-NA (Deltaproteobacteria)*, *Kiloniellaceae*, *Acidobacteria (Subgroup 21, 22)*, P*hycisphaerae-MSBL9 (L21-RPul-D3,*

SG8-4), Scalinduaceae, Nitrosococcaceae, NC10 (Methylomirabilaceae), Nitrospinaceae, Rhodobacteraceae, Methyloligellaceae, Nitrospiraceae, and which also appeared as important nodes of a separate cluster (cluster 1) on the network analysis, representing slope microbial communities (Figure 5-3, Figure 5-5, Table D 2). These groups represented about 35% of the microbial community on the slope, compared to ~ 11% on the shelf (Figure 5-3, Table D 4).

Microbial community composition also varied with sediment core depth. On the shelf, *Bathyarchaeia* dramatically increased in relative abundance below ~ 10 cm, as it represented an average of ~5% of the community on upper layers compared to ~53% in sediments below 10 cm (Figure 5-3, Table D4, and Table D5). A heat map of the most abundant *Bathyarchaeia* ASVs (> 1.5% of the archaea dataset) revealed that this group presented strong spatial clustering between shelf and slope at the ASV level (Figure D 10). To better characterize the bathyarhaeal diversity in the present samples, bathyarchaeal sequences were compared to another bathyarchaeal database using BLASTN (Zhou et al. (2018). This analysis showed that subgroup 8 dominated shelf communities, followed by subgroup 15, 12, 13, and 17, while subgroup 15 dominated slope communities followed by subgroup 2, 13, and 6 (Figure D 10, Table D 3). Other microbial groups such as *Anaerolineae-NA, Woesearchaeia, Sva0485 (Deltaproteobacteria),SG8-4 (Phycisphaerae-MSBL9), H3.93 (Dehalococcoida), Aminicenantales, Desulfatiglans, Methanofastidiosales, Methanosarcinales, Methanocellales, ANME-1*(a, b), and *Methanomicrobiales* also increased with sediment core depth on the shelf and, by forming clusters 3 and 4 in the network analysis (Figure 5-5, Table D 2), appeared important players in deeper layers of these sediments. Although less striking than shelf sediments, differences

in microbial diversity associated with sediment core depth were also observed on the slope. For example, *NC10, Woesarchaeia*, and *Scalinduaceae* increased in relative abundance with sediment core depth (Figure 5-3, Table D 4, and Table D 5).

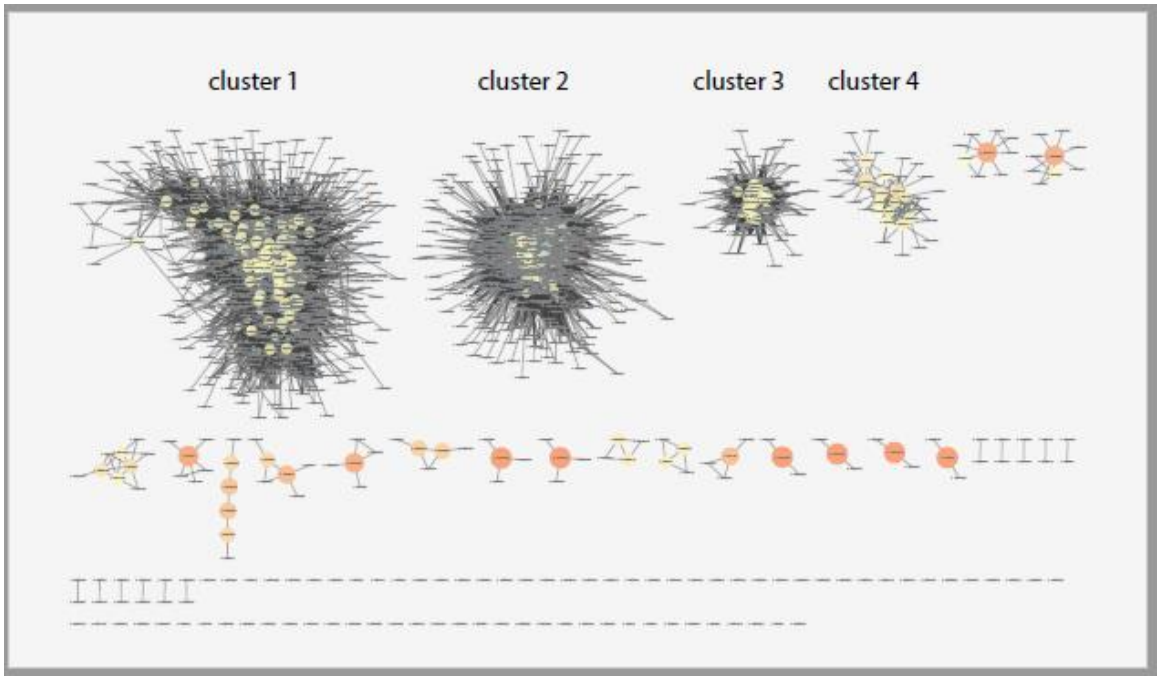

Figure 5-5 Interaction networks of sediment microbial community members. ASVs are depicted as circles, and sized and colored based on betweenness centrality values (the larger this value, the larger the size of the circle, and the warmer the color). Cluster 1 is composed by ASVs with higher relative abundances on the slope, cluster 2 is composed by ASVs with higher relative abundances on the shelf, and clusters 3 and 4 are composed by ASVs particularly abundant in deeper layers of the sediment. For this analysis, only ASVs with a relative abundance ≥ 0.0002%, and only interactions with a p-value ≤ 0.01 were included. Associated data can be found in Table D 4.

5.4.7 Universal prokaryotic primers versus Archaea specific primers

The initial microbial composition using universal prokaryotic primers revealed that a significant portion of the community was represented by archaea (15%) (Table D 4). Moreover, in accordance with previous research, *MG-I Thaumarcaheota* was the second

most abundant class in our dataset (Learman et al., 2016; Overholt et al., 2019), and earlier studies have shown that due to the larger proportion of bacteria compared to archaea in many environments, the use of universal primers is not enough to accurately capture the entire archaeal diversity (Raymann et al., 2017b; Teske and Sørensen, 2008). In an attempt to better characterize this archaeal diversity, archaea specific primers were used which had showed that over 90% of the archaeal gut diversity in humans and apes was not captured using universal prokaryotic primers (Raymann et al., 2017b). In order to compare the specificity of both the universal and archaea specific primers in targeting the archaeal community, the bacterial reads from the prokaryotic dataset were removed, and all samples were rarefied to 1200 sequences. This new archaeal dataset derived from the prokaryotic dataset obtained using universal primers, yielded 77 samples with a total of 8053 ASVs. For comparison, the dataset obtained using archaeal specific primers yielded 58 samples with a total of 3999 ASVs. In order to see if the extra ASVs obtained using the universal primer set were due to the extra number of samples retrieved (77 vs 58), both the dataset obtained using universal primers and the one obtained using archaea specific primers were filtered to keep the exact same samples. The final archaea datasets contained 49 samples, and 6127 ASVs using the universal primer set versus 3922 ASVs using the archaea specific pair. Despite this difference in number of ASVs retrieved using either the universal primer pair or the archaea specific one, the overall trends remained unchanged. Therefore, the use of these primers in this specific system was not particularly useful in better characterizing this portion of the prokaryotic community. Indeed, patterns of diversity remained relatively unchanged using either universal or archaea specific primers, and the number of samples and archaea ASVs recovered was actually higher using the universal primer pair (77

samples versus 58, and 8053 versus 3999 ASVs). This result suggests that the effectiveness of this primer may be related to the environment studied and may not be particularly useful when characterizing sediment communities.

5.5 Discussion

5.5.1 Water column depth and sediment core depth represent major drivers of microbial community composition.

Both prokaryotic and archaeal datasets were primarily structured by water column depth and sediment core depth (Figure 5-3, Figure 5-4). Sediment communities from samples along the shelf (St 6 to St 2, < 100 m water column depth) were significantly different from sediment communities on the slope (St. 3 to St. 10, >100 m water column depth). In addition, alpha diversity decreased between shelf and slope stations, which appeared stronger in the archaeal dataset (Figure D 9). This decrease in microbial diversity may be related to a decrease in organic carbon availability at deep sea stations where inputs from both primary production and terrestrial sources may not be as strong compared to shelf stations. Interestingly, this result was significant using the Faith-pd index (Figure D 9a) but not the Shannon index (Figure D 9c) for the prokaryotic dataset, which indicates a decrease in richness but not specifically in diversity. Richness (Faith-pd) decreased with sediment core depth on the shelf but appeared to stay constant or even increase in deeper layers of slope sediments, particularly for the archaea dataset (Figure D 9a,b). On the shelf, this result suggests a more constraining environment in deeper layers of the sediment, probably related to a lack of electron donors and acceptors, which may limit microbial development (D'Hondt et al., 2004; D'Hondt et al., 2002). The fact that diversity remained

unchanged or showed a slight increase with sediment core depth in slope sediments, suggests that in contrast to other deep sea sediments, organic carbon may still be sufficient available in the deeper layers (between 66 mm and 130 mm) of these sediments to sustain a level of microbial diversity similar to the one observed in the upper layers. This result may in part be explained by the strong influence of the Atchafalaya and Mississippi rivers in this region (Owings et al., 2020), which could transport enough organic matter on the slope to maintain microbial diversity throughout the sediment. Interestingly, whereas archaeal richness (Faith-pd) decreased with sediment core depth on the shelf (Figure D 9), archaeal diversity (Shannon index) increased. In addition to the differentiation between shelf and slope stations, beta diversity analysis also revealed differences in microbial community structure with sediment core depth in accordance to previous studies (Durbin and Teske, 2011; Hunter et al., 2006; Overholt et al., 2019). This pattern had already been observed in the GoM (Overholt et al., 2019) where these factors not only stratified sediment microbial communities but also influenced niche diversification across geographically distant regions. In turn, alpha diversity in this past study appeared to be lower in shallower samples (<100 m water column depth) compared to deeper samples (> 400 m), whereas the opposite trend was observed in the present study (Figure 5-3).

Similarly, to other sediment studies in the GoM (Overholt et al., 2019; Reese et al., 2013), Proteobacteria dominated the entire prokaryotic dataset with an average relative abundance of about 42% at both shelf and slope stations. This phylum was largely dominated by *Gammaproteobacteria* (19.4%) and *Deltaproteobacteria* (18.5%) throughout both shelf and slope stations. Some archaeal classes were also particularly

abundant including *Nitrososphaeria* (5.3%), *Bathyarchaeia* (4%), *Woesearchaeia* (2. 4%), and *Thermoplasmata* (1.8%).

5.5.2 Shelf sediments are characterized by carbon remineralization and sulfur cycling

The analysis of microbial community composition relative to the sediment geochemistry using Canonical Correspondence Analysis (CCA) revealed that DIC, ΣPO_4^{3-}, and ΣH_2S were the main variables controlling shelf communities (p-value ≤ 0.01) (Figure 5-4). Indeed, DIC, NH_4^+, and ΣPO_4^{3-} concentration increased with depth in the pore waters on the shelf, indicating that carbon remineralization processes were intensified with depth. However, overall concentrations of these species generally decreased eastward from St 6 to St C6C before increasing again, along with ΣH_2S and FeS_{aq}, across the eastern side of the shelf (St. MK to St. 2) (Figure 5-2). These two compounds are main indicators of SO_4^{2-} reduction and suggest increase in SO_4^{2-} reduction on the eastern shelf, despite undetectable SO_4^{2-} loss. In addition, ΣH_2S rapidly reduces organic-Fe(III) complexes (Taillefert et al., 2002), Mn(IV/III) oxides, and Fe(III) oxides, and precipitates rapidly with Fe^{2+} to form $FeS_{(s)}$ (Pyzik and Sommer, 1981) but does not precipitate easily with Mn^{2+} (Luther, 2005). Therefore, low dissolved Fe^{2+} and $Fe(III)_d$ concentrations, lack of org-Fe(III) complexes, and the relatively high Mn_d concentrations (Figure 5-3a, Figure D 3, Figure D 4, and Figure D 5), along with the dark color of the sediment typical of $FeS_{(s)}$ (Figure D 2) are all indicative of active SO_4^{2-} reduction on the continental shelf. In accordance with the geochemical data, microbes that are implicated in organic matter degradation, sulfur, and methane cycling were enriched at shelf stations. In order of relative contribution on the shelf, families such as *Bathyarchaeia-NA* (~7%), *Desulfobulbaceae* (~5%), *Desulfobacteraceae* (~5%), *Anaerolineaceae* (~3. 5%), *Woeseiaceae* (~3%), *Halieaceae*

(~2%), *Marine Benthic group D* and *DHVEG-1* (~1%), *Thiohalorhabdaceae* (~1%), *Thioalkalispiraceae* (~1%), *Lokiarchaea-NA* (~0.7%), *Thiotrichaceae* (~0.6%), *Methanofastidiosales-NA* (~0.1%), and *Methanosarcinaceae* (~0.03%), among others, represented important members of the shelf microbial community (Figure 5-3, Figure 5-5, Table D 2). Following changes in redox potential and decreases in pH with increasing sediment core depth, shifts in shelf microbial community were also observed (Figure 5-3). Upper sediment layers were dominated by SRB including *Desulfobacteraceae*, and *Desulfobulbaceae* (Bahr et al., 2005; Kümmel et al., 2015). Despite having relative abundances below 1. 5%, several members of the families *Thioalkalispiraceae*, *Ectothiorhodospiraceae*, *Rhodobacteraceae*, *Thiotrichaceae*, *Hyphomicrobiaceae*, *Chromatiaceae*, *Burkholderiaceae*, and *Rhodospirillaceae*, which have been related to sulfide oxidation (Cytryn et al., 2005; Devereux et al., 2015; Franz et al., 2009; Lipsewers, 2017; Montoya et al., 2011; Mori et al., 2011; Sakurai et al., 2010; Xu, 2014) were generally more abundant in the upper layers of the sediment. Similarly, *Lokiarchaea* which are capable of homoacetogenesis in sulfidic marine sediments (Orsi et al., 2019), and *Halioglobus* and *Parahaliea* (*Halieaceae*) which are both aerobic bacteria implicated in denitrification processes (Jung et al., 2017; Kim et al., 2017) (Table D 4) were also more abundant in surficial sediments. Finally, *Woeseiaceae* also appeared as important contributor to the surface sediment structure on the shelf (Figure 5-3, Figure 5-5,Table D 2). This family seems to possess an incomplete denitrification pathway and be able to reduce nitrite and NO and produce N_2O (Hinger et al., 2019), underlining that denitrification is a potentially significant process in these sediments.

In contrast, deeper sediment layers (below ~ 10 cm) harbored increasing proportions of microbes such as *Bathyarchaeia*, *Marine Benthic group D* and *DHVEG-1*, *Thermoplasmata*, *Desulfarculaceae*, *Syntrophobacteraceae*, and *Dehalococcoidia* (Figure 5-3, Table D 4,Table D 5). Although some of these microorganisms are also members of the SRB, including *Syntrophobacteraceae* and *Desulfarculaceae* (Julies Elsabé et al., 2012; Liu and Conrad, 2017), *Thermoplasmata* contain uncultured members present in anoxic sediments (Lloyd et al., 2013) and co-occur with *Bathyarchaeia* (Bukin et al., 2016). In turn, *Marine Benthic group D* and *DHVEG-1* are usually found in anoxic, organic and sulfide rich environments and some of their members are capable of conducting assimilatory sulfate reduction (Lazar et al., 2017), whereas *Dehalococcoidia* respires on organohalide (Wasmund et al., 2014). More importantly represented deep in these sediments, *Bathyarchaeia* have been linked to acetogenesis and sulfur and nitrogen reduction and appear to play a role in methane cycling, as they metabolize methane and interact with anaerobic methane-oxidizing archaea, acetoclastic methanogens, and heterotrophic bacteria (Zhou et al., 2018). This group showed the largest increases, particularly at St 6 and St MK where it went from < 0.5% to representing about 50% of the total microbial community, and showed micro diversity at the ASV level with a clear differentiation between ASVs present on the shelf relative to the slope, as well as with sediment core depth (Figure D 10). Interestingly, communities more closely related to members of subgroup 8 were the most frequent among the most abundant ASVs (>1.5% from the archaea specific primer dataset) in the deep layers of the shelf stations. This subgroup has been implicated in methylotrophic methanogenesis and the degradation of lignin and aromatics (Evans et al., 2015), which suggests that methane cycling may be

important in the deep sediment layers. Finally, several additional archaeal groups implicated in methane metabolism, including *Methanosarcinales, Methanofastidiosales, Methanocellales, ANME-1*(a, b), and *Methanomicrobiales* (Chen et al., 2020), while in low relative abundances (from $5x10^{-5}$ to 0.03% on the shelf), were also more abundant in shelf sediments and increased with sediment depth (Table D 4,Table D 5). Other more abundant microbial groups linked to hydrocarbons, such as *Anaerolineaceae* (McIlroy et al., 2017), or associated with high organic matter content, a potentially symbiotic lifestyle, and methane cycling, such as *Woesarchaeia* (Castelle et al., 2015; Fan and Xing, 2016; Liu et al., 2018) tended to increase with sediment core depth (Figure 5-3, Table D 4,Table D 5). In particular, *Woesearchaeia* which did not show strong changes in relative abundance between shelf and slope, increased with sediment core depth in both these regions. Based on network analysis, a subset of ASVs from these groups that were more abundant in shelf stations appeared as significant taxa structuring the microbial community in this region (Figure 5-5, Table D 2). Together with the higher abundance of methanogens, this observation reinforces the possibility of methane cycling taking place in the deep sediment layers of the shelf.

5.5.3 Slope sediments are characterized by metal reduction and nitrogen-related microbial processes

Overall increases in dissolved Mn and Fe concentrations with depth, and below detection limit concentrations of FeS and ΣH_2S, suggest a transition from SO_4^{2-} reduction in shelf sediments to metal reduction in slope sediments (Figure 5-2) even though CCA revealed that NO_3^- appeared more important in shaping the microbial communities along the slope (Figure 5-4, Table D 1). Indeed, NO_x concentrations were much higher in

continental slope sediments and generally decreased with depth (Figure 5-2), except at St. 11 where an increase in NO_x was evident (Figure 5-3c). These geochemical changes were accompanied by an increase in nitrogen cycling microbes. In order of relative contribution on the slope, these groups included *Nitrosopumilaceae* (~10%), *Woeseiaceae* (~5%), *NB1-J-NA* (*Deltaproteobacteria*) (~ 4%), *Kiloniellaceae* (~3%), *Scalinduaceae* (~2%), *Acidobacteria* (Subgroup 21, 22) (~2%), *Nitrosococcaceae* (~1%), NC10 (~0.8%), *Nitrospinaceae* (~0.6%), *Nitrospiraceae* (~0.4%) (Figure 5-3, Table D 4). Based on network analysis, these microbes also appeared as important members of the slope microbial community, with potentially important functions (Figure 5-5, Figure D 2). In accordance with previous studies in the GoM, *Nitrosopumilaceae* was the most abundant family in the dataset, particularly in surficial sediments where it reached up to 34% (Learman et al., 2016; Overholt et al., 2019). As part of the *Thaumarchaeota* phylum, these organisms are known ammonia oxidizers that usually occupy oxic or suboxic sediment layers where either the quality or quantity of organic carbon has decreased (Danovaro et al., 2016; Durbin and Teske, 2011; Durbin and Teske, 2012; Learman et al., 2016). *Nitrospiraceae* was dominated by *Nitrospira*, and *Nitrospinaceae* was dominated by *Nitrospina*. Although these groups are usually affiliated with nitrite oxidation, certain cultivated *Nitrospira* strains have recently been implicated in complete ammonia oxidation to nitrite and then to nitrate, so-called 'comammox' (Daims et al., 2015; van Kessel et al., 2015). Whereas *Nitrospira* showed microdiversity at the ASV level between shelf and slope stations, the majority of *Nitrospira* ASVs from either shelf or slope sediments were not closely related with any of the subgroups or sublineages of previously reported comammox or nitrite-oxidizing organisms. In much lower abundance, *Nitrosococcaceae*

are capable of ammonia oxidation (Ward et al., 2019), *Acidobacteria* (Subgroup 21,22) are typical of sedimentary environments, have been correlated with higher nitrogen concentrations (Chaves et al., 2019), and are capable of both nitrite and nitrate reduction (Ward et al., 2009), whereas *Scalinduaceae* are usually related to anammox (van de Vossenberg et al., 2013) (Table D 4). Finally, Woeseiaceae possess an incomplete denitrification pathway and reduce nitrite and NO to produce N_2O (Hinger et al., 2019), whereas Kiloniellaceae conduct denitrification (Imhoff and Wiese, 2014). On the other hand, members of the NC10 group, which was dominated by Methylomirabilaceae (wb1-A12) are known to carry out nitrite dependent methane oxidation (He et al., 2015).

Similar to shelf stations, changes in microbial community composition were observed with changes in redox potential associated with sediment core depth in the slope stations (Figure 5-3, Table D 4). In particular, *NC10*, *Woesarchaeia*, and *Scalinduaceae*, which was only represented by *Candidatus-Scalindua* increased in relative abundance. Interestingly, these changes were accompanied by a shift in the trend in Mn_d distributions from the behavior of a sub-surface peak, to the rise to a maximum concentration at depth (Figure 5-2). This behavior could be due to reaching super saturation with respect to carbonate minerals in shelf-break and mid-slope sediments (Owings et al., 2020), or possibly a link between the nitrogen and manganese cycles at depth (Luther et al., 1997). Moreover, NO_2^- and NO_3^- were produced at depth in slope sediments at St. 3, 11, and possibly 10 (Figure 5-3, Figure D 6, and Figure D 8) and, coincidentally, at two shelf stations (St. C6C and MK). Anaerobic ammonium oxidation (anammox) to NO_2^- or NO_3^- linked to $Mn(IV/III)O_2$ reduction has been demonstrated in anoxic sediments (Anschutz et al., 2000; Bartlett et al., 2008; Bartlett et al., 2007; Lin and Taillefert, 2014). Although

Scalinduaceae (Candidatus Scalindua) are usually linked to anammox using nitrite as electron acceptor (van de Vossenberg et al., 2013), members of this particular genus are able to use Fe(III) and Mn(IV/III) oxides as terminal electron acceptors (Bertrand et al., 2018; van Niftrik and Jetten, 2012). Their increase in abundance in deeper layers of these sediments therefore suggests that they might be related to subsurface maxima in both NO_x and dissolved Mn (Figure 5-3, Figure D 6, and Figure D 8). The high relative abundances of microbes related to nitrogen cycling on the slope including nitrifying, denitrifying, and anammox bacteria, supports previous work showing that inorganic nitrogen species are an important source of electron acceptors and donors in these sediments (Danovaro et al., 2016; Glud et al., 2009; Overholt et al., 2019; Swan et al., 2011), which can ultimately affect global nitrogen budgets.

5.5.4 Possible cryptic sulfur cycling in shelf and slope sediments

As described above, sulfur cycling was observed in both the geochemistry and microbial data on shelf stations. However, the sediment pore water geochemistry showed a transition from SO_4^{2-} to metal reduction from the continental shelf to the slope, microbes potentially implicated in sulfur cycling persisted on the slope. Both SRB and SOB groups generally decreased in relative abundance moving from shelf to slope but remained relatively abundant on the slope, with SRB representing over 5% of the microbial community in 55% of slope samples (Figure 5-3, Table D 4). Deltaproteobacteria and *Gammaproteobacteria* dominated at all stations and included microbes that play an important role in SO_4^{2-} reduction (Figure 5-3, Table D 4). These organisms included *Desulfobacteraceae*, *Desulfobulbaceae*, *Desulfarculaceae*, and *Syntrophobacteraceae*, known SRB which were among the most abundant families of *Deltaproteobacteria*. While in lower relative

abundance (from ~0.003% to ~0.07%) SOB including *Thioalkalispiraceae*, *Ectothiorhodospiraceae*, *Rhodobacteraceae*, *Thiotrichaceae*, *Hyphomicrobiaceae*, *Chromatiaceae*, *Burkholderiaceae*, and *Rhodospirillaceae*, (Cytryn et al., 2005; Devereux et al., 2015; Franz et al., 2009; Lipsewers, 2017; Montoya et al., 2011; Mori et al., 2011; Sakurai et al., 2010; Xu, 2014), were also present throughout both shelf and slope sediments. The high relative abundance and distribution of these taxa along the whole dataset indicate that sulfur cycling is a potentially important process in both shelf and slope stations, despite the lack of geochemical evidence of these processes occurring on the slope (Figure 5-3, Table D 4).

Interestingly, the fact that neither SO_4^{2-} loss nor dissolved sulfide production were clearly observed in the geochemical profiles at most stations suggests the existence of either a biological cryptic sulfur cycle, in which SRB and SOB are metabolically active, resulting in no dissolved sulfide accumulation, nor SO_4^{2-} loss, or a geochemical cryptic cycle, in which SRB produces ΣH_2S but abiotic or biotic reduction of Fe(III) oxides simultaneously promotes the removal of ΣH_2S by precipitation of $FeS_{(s)}$ (Reese et al., 2013; Reese et al., 2014b). In the present study, iron-reducing bacteria (FeRB) including *Geobacteraceae* (~0.05%), *Shewanellaceae* (~ 0.02%), and *Pseudomonadaceae* (~ 0.006%) (Balashova and Zavarzin, 1979; Fredrickson and Gorby, 1996; Hersman et al., 1996; Lin et al., 2005) were present in both shelf and slope samples. However, FeRB showed low relative abundances compared to SOB, which were on average 10 times higher (Table D 4). Moreover, dissolved Fe^{2+} concentrations remained low throughout the transect, and the cores did not appear particularly black which would indicate the presence of FeS. These observations suggest that a biological rather than geochemical cryptic sulfur cycle may be

going on in these sediments. Nevertheless, actual SO_4^{2-} reduction measurements, metagenomics or other analysis looking at microbial function should be performed to confirm and better characterize the presence of the sulfur cryptic cycle.

5.6 Conclusions

This study reports extensive geochemical, bacterial, and archaeal data sets to characterize the main biogeochemical cycles in sediments of the northern Gulf of Mexico and understand the interplay between geochemical and microbial pathways in nutrient and carbon cycling. Results indicate different geochemical characteristics paired with distinct microbial communities across the shelf and slope. Shelf sediments provide geochemical evidence of sulfate reduction via detection of ΣH_2S and elevated DIC, NH_4^+, and PO_4^{3-} concentrations in the pore waters. In parallel, the dominant microbial communities across the shelf included sulfate-reducing bacteria and sulfur-oxidizing bacteria. In addition, slope sediments display geochemical proxies indicative of increased nitrogen and metal cycling. In agreement, the dominant microbial communities include species affiliated with nitrogen cycling (including co-annamox) as well as communities capable of using iron and manganese as electron acceptors. In addition, indications of cryptic sulfur cycling were apparent in the slope sediments in the microbial populations despite the lack of sulfur cycling observed in the geochemical proxies. Both the shelf and slope sediment communities contained changes in microbial community composition with respect to depth, indicative of the change in community due to organic carbon source and availabilities of terminal electron acceptors. This study illustrates the importance of pairing microbial and geochemical techniques to characterize the relative importance of biogeochemical and abiotic pathways involved in carbon and nutrient cycling in sediments.

CHAPTER 6. DIFFERENTIAL MANGANESE AND IRON RECYCLING AND TRANSPORT IN CONTINENTAL MARGIN SEDIMENTS OF THE NORTHERN GULF OF MEXICO

This chapter is a manuscript, authored by Shannon M. Owings[1], Laurie Bréthous[2], Eryn M. Eitel[1,3], Benjamin P. Fields[1], Anthony Boever[1], Jordon S. Beckler[4], Bruno Bombled[2], Bruno Lansard[2], Edouard Metzger[5], Christophe Rabouille[2], and Martial Taillefert[1],

currently under review in *Marine Chemistry*

[1]School of Earth and Atmospheric Sciences, Georgia Institute of Technology, Atlanta GA 30332 [2] Laboratoire des Sciences du Climat et de l'Environnement (LSCE), UMR 8212, IPSL-CEA-CNRS-UVSQ-Université Paris Saclay, 91198 Gif-sur-Yvette, France [3]Geological and Planetary Science, California Institute of Technology, Pasadena, CA 91125, United States of America [4]Florida Atlantic University, Harbor Branch Oceanographic Institute, Boca Raton, FL 33431 [5]UMR CNRS 6112 LPG-BIAF, Université d'Angers, 49045 Angers Cedex, France

6.1 Abstract

Manganese and iron cycling and their role in carbon remineralization processes are poorly characterized in continental margin sediments world-wide. River-dominated ocean margins (RiOMars) receive large amounts of Mn(III/IV) and Fe (III) oxides that settle to the shelf and neighboring slope sediments, suggesting that dissimilatory metal reduction may be an important diagenetic pathway and compete with sulfate reduction in these

sediments. In this study, sediment cores were collected along one transect in the northern Gulf of Mexico near the mouth of the Mississippi River from the Louisiana shelf to the continental slope (60-1,000 m water depth) and an additional transect to the east of the Mississippi River mouth to determine the role of manganese and iron in the remineralization of carbon. Sediment cores were profiled using potentiometric, amperometric, and voltammetric microelectrodes and sectioned to quantify pore water DIC, TA, NH_4^+, NO_x^-, SO_4^{2-}, and the speciation of sedimentary manganese and iron. Results indicate that sedimentation rates control the extent of anaerobic carbon remineralization and select for the dominant anaerobic carbon remineralization pathways. Although sulfate reduction dominates the shelf station (65 m water depth), denitrification and microbial manganese reduction appear equally significant anaerobic respiration processes along the continental slope the closest to the Mississippi River. At water depths >200 m, dissolved sulfides were never detected and dissolved Fe^{2+} remained relatively low in the pore waters compared to dissolved Mn^{2+} which formed distinct peaks below the sediment-water interface. In turn, large concentrations of poorly crystalline and crystalline Fe(III) oxides and correspondingly low acid volatile sulfide (AVS) were found throughout the sediment column along the continental slope, whereas manganese accumulated under the form of reactive manganese oxides and carbonate minerals at deeper depth in the sediment column as water depth increased along the continental slope. These findings suggest that the differential kinetics of manganese and iron redox transformations, in addition to the variations in organic carbon and mineral delivery modulated by Mississippi River discharge variations, influence carbon remineralization processes on the continental slope. The fast kinetics of Fe^{2+} oxygenation near the sediment-water interface and high

sedimentation maintain Fe under the form of Fe(III) oxides and thermodynamically prevent sulfate reduction from dominating carbon remineralization processes on the slope, whereas the much slower Mn^{2+} oxygenation kinetics allows diffusion of Mn^{2+} across the sediment-water interface. Exposure to oxygenated bottom waters and entrainment within mobile muds typical of deltaic sediments during high riverine discharge likely promote the formation and downslope transport of Mn(III/IV) oxides within the nepheloid layer, forming a manganese 'conveyor belt' that selectively enriches Mn(III/IV) oxides relative to Fe(III) oxides in the sediment compared to the source material from the river. In contrast, the extent of anaerobic carbon remineralization processes along the eastern continental slope the farthest from the Mississippi River plume is much lower due to the low organic and lithogenic inputs, and denitrification dominates anaerobic respiration. Overall, these findings suggest manganese cycling and role in carbon remineralization processes in continental slope sediments exposed to large riverine inputs may be more important than previously considered.

6.2 Introduction

Riverine-dominated continental margins (RiOMars) represent carbon remineralization hot spots as a result of the significant input of natural organic matter and inorganic particulate material from terrestrial origin (Bianchi et al., 2018). In addition, the nutrient supply from the underlying sediment (Aller et al., 1996; Grégoire and Friedrich, 2004; Morse and Rowe, 1999) or riverine inputs (Turner et al., 2007) promotes primary production on continental shelves that may enhance the overall input of natural organic matter to the seafloor (Aller et al., 1996; Waterson and Canuel, 2008) and increase diagenetic reactivity by a priming effect (Bianchi, 2011). The supply of organic matter and

lithogenic material to continental shelves depends on the intensity of riverine discharge, which typically varies seasonally (Bianchi et al., 2007; Mossa, 1996). At low discharge, the density difference between freshwater and seawater impedes the seaward transport of freshwater and its particulate load such that freshwater and sediment are both trapped in the estuary or backwater reach of rivers (Allison et al., 2012; Geyer et al., 2004). In contrast, the momentum of the river outflow at high discharge is strong enough to overcome this effect and export water and sediment offshore. As a result, sediment trapped in estuaries or backwater reach during low discharge seasons is biogeochemically processed until the next high discharge, such that the inorganic (Allison and Pratt, 2017; Meiggs and Taillefert, 2011; Sutula et al., 2004) and organic (Cowie and Hedges, 1984, 1992; Sampere et al., 2011) content of surrounding shelf sediments is seasonally altered. In turn, the lithologic input to continental shelves is greater during high discharge as a result of increased weathering upstream (Meiggs and Taillefert, 2011). Riverine dissolved and particulate material eventually delivered to the ocean flocculates and aggregates into fine-grained material that settles into the benthic boundary layer (BBL) 0.1-2 m above the seabed and forms mobile muds, an ephemeral layer that is often remobilized by physical mixing generated by tidal currents or storms (Aller, 1982, 1998; McKee et al., 2004). These mobile muds are eventually deposited on continental shelves and slopes, with selective dispersal that depends on particle size, density, morphology, or composition (McKee et al., 2004), and enhance carbon remineralization by exposing sediment to oxygenated bottom waters (Aller, 1998; Blair and Aller, 2012; Hartnett et al., 1998) and co-metabolizing fresh, planktonic organic carbon (Canfield, 1994). As a result, sediment distribution across continental margins and their associated diagenetic processes may vary widely depending

on the organic carbon and lithologic composition of the top sediment layers (Canfield, 1994; Grégoire and Friedrich, 2004; Taillefert et al., 2017).

The complex interplay between abiotic and biotic processes influences the availability of electron acceptors and efficiency of carbon remineralization processes. After aerobic respiration, sulfate reduction often plays a large role in marine sediments exposed to significant inputs of natural organic matter (Bowles et al., 2014; Ferdelman et al., 1999; Jørgensen, 1982; Lee et al., 2008; Lin et al., 2002) mainly due to the high concentration of sulfate in seawater and the efficient carbon remineralization yield of this process (i.e., 2 mole of carbon per mole of sulfate reduced). In RiOMars and shelf to slope transition zones of passive continental margins, however, manganese (Mn) and iron (Fe) reduction may contribute to a large fraction of carbon remineralization processes (Aller et al., 1990; Beckler et al., 2016; Canfield et al., 1993a; Canfield et al., 1993b; Devereux et al., 2015; Hyun et al., 2017; Law et al., 2009; Oldham et al., 2019; Sørensen and Jeørgensen, 1987; Thamdrup et al., 2000). The differential kinetics of manganese and iron transformations also separates Mn^{2+} and Fe^{2+} vertically in the sediment column, as microbial Mn(III/IV) oxide reduction is thermodynamically more favorable and much faster than microbial Fe(III) reduction (Arnold et al., 1988; Dollhopf et al., 2000; Larsen et al., 1998; Lovley and Phillips, 1988; Myers and Nealson, 1988) and abiotic Mn^{2+} oxidation is much slower than Fe^{2+} oxidation (Stumm and Morgan, 1996). As a result, Mn^{2+} diffuses out of the sediment and is slowly reoxidized either close to the sediment surface (Mouret et al., 2009) or in the overlying waters (Trefry and Presley, 1982), whereas Fe^{2+} is oxidized immediately at the oxic-anoxic transition (Millero et al., 1987). Simultaneously, Fe^{2+} is less mobile in comparison to Mn^{2+} due to rapid precipitation with H_2S (Pyzik and Sommer, 1981). Mn(III,

IV) oxides are therefore dispersed and redeposited in surface sediments where they become important electron acceptors for organic carbon oxidation (Hyun et al., 2017; Law et al., 2009), whereas Fe(III) oxides are typically immobilized below the oxygen penetration depth in the sediment. Differentiating these processes in RiOMar sediments may help quantify anaerobic carbon remineralization processes more accurately.

This study investigated the main redox processes involved in the transformation of natural organic matter in continental shelf and slope sediments of the northern Gulf of Mexico (NGoM). Two cross slope transects were studied to examine the effect of lithogenic and organic carbon inputs on diagenetic processes. One transect is influenced by inputs from the Mississippi River and the other, to the east of the Mississippi River plume, is not exposed to significant inputs. At each station, depth profiles with potentiometric, amperometric, and voltammetric microelectrodes in intact sediment cores were combined with conventional pore water analyses and solid phase chemical extractions of the same sediment cores. Finally, a one-dimensional transient reactive transport model ran to steady-state was also used to estimate carbon remineralization rates and identify the role of lithogenic inputs on microbial metal reduction.

6.3 Methods

6.3.1 Field site and sediment sampling

The continental margin of the NGoM is well known for its seasonal hypoxic zone (defined as < 63 µM $O_{2(aq)}$) as a result of the high input of nutrients from the Mississippi-Atchafalaya River System (MARS) (Rabalais et al., 2007). In addition, the continental margin of the NGoM is a unique region to study the effect of riverine inputs on diagenetic

processes in RiOMar sediments as it receives approximately 2.1 x10^8 tons of sediment per year (Milliman and Meade, 1983) and an annual mass load of 7.38 x10^7 tons of metals (Reiman et al., 2018) from the MARS under the form of a particulate plume (Xu et al., 2014). The transport of material extends beyond the hypoxic region and can be transferred to the nearby Mississippi canyon (Bianchi et al., 2006) via lateral down-slope accretion of material from the margins and/or mass wasting (Rowe et al., 2008).

Sediment cores (9.6 cm inner diameter x 70 cm) were collected using a multi-corer (MC 800, Ocean Instruments) onboard the R/V Savannah along the Louisiana shelf and slope during an oceanographic cruise from July 25 to August 6, 2017 (

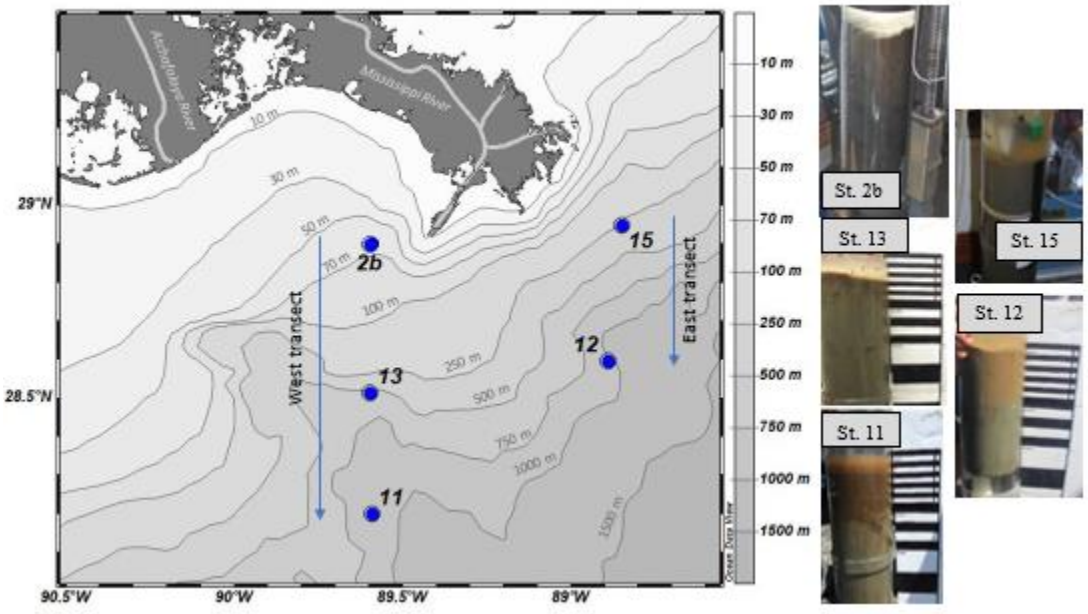

Figure 6-1 and Table 6-1). Station locations were selected along a transect near the outlet of the Mississippi River across the slope and toward the Mississippi canyon stations referred to as the ‘western transect’ with respect to positioning of the Mississippi River: St.

2b (65 m), St. 13 (510 m), and St. 11 (925 m) (Table 6-1 and

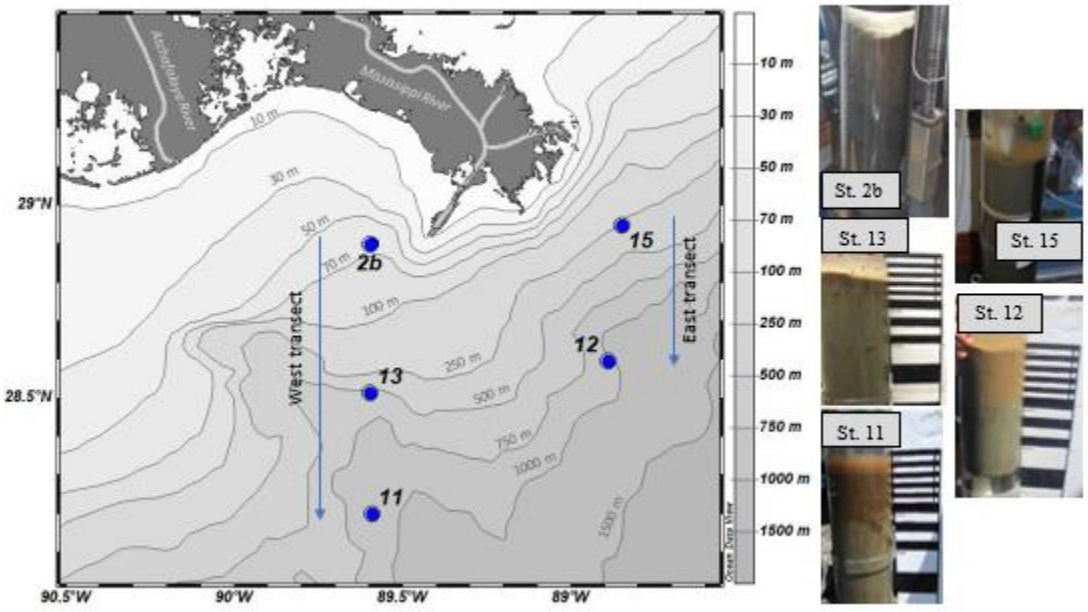

Figure 6-1). Two additional stations were selected to the east of the Mississippi River along a transect across the continental slope which is referred to as the ‘eastern transect’:

St. 15 (274 m) and St. 12 (989 m) (Table 6-1 and

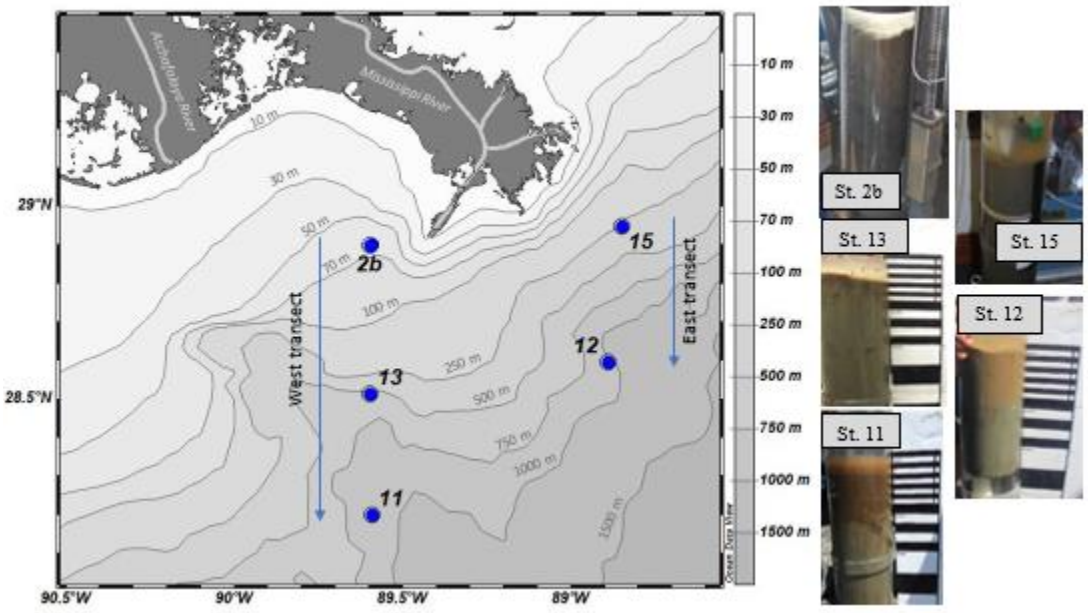

Figure 6-1). Stations were named based on the labelling of stations from previous expeditions (Beckler et al. 2016).

6.3.2 O_2 and pH microprofiles and porosity profiles

Bottom water samples were collected as close to the seafloor as possible (i.e. 2 meters) using the rosette of 12L Niskin bottles (OceanTest Equipment, Inc). Bottom water pH was measured using the m-cresol purple spectrophotometric method (Clayton and Byrne, 1993; Dickson et al., 2007; Rassmann et al., 2016) and recalculated at in situ temperature using salinity and total alkalinity (TA). Bottom water O_2 concentrations were determined by Winkler titration (Grasshoff et al., 1983) and oxygen saturation levels related to maximum oxygen concentrations (100% saturation) determined at the measured

temperature and salinity with USGS DO tables (https://water.usgs.gov/software/DOTABLES/).

In situ oxygen and pH profiles were collected at St. 2b in 100 µm increments using an autonomous benthic lander with a high resolution micromanipulator (Unisense®) equipped with a resistivity probe (Revsbech, 1989) and O_2 (Andrews and Bennett, 1981) and pH microsensors. For all other stations, ex situ O_2 and pH microprofiles were obtained with a 200 µm resolution in the same core using the same microsensors deployed on a laboratory micromanipulator (Unisense®). During ex situ profiling, overlying water temperature, oxygen concentrations, and pH were maintained by bubbling a mixture of air, N_2, and CO_2. The pH probes were practically calibrated with NBS buffers at pH 4, 7, and 10, but the pH profiles were adjusted using the spectrophotometrically measured bottom water pH at the in situ temperature (Rassmann et al., 2016). All pH values are reported on the total proton scale (pH_T). Oxygen sensors were calibrated using oxygen concentrations determined in bottom waters and their responses in the anoxic zone (Cai and Sayles, 1996). Two pH and two oxygen profiles were obtained successively in most of the sediment cores. After completion of the pH and O_2 microprofiles, the same core was sectioned in 3-60 mm sections with lower resolution at the surface of the core porosity. Sediment samples were frozen (-20°C) and porosity measured back at the LSCE by determining the difference between wet and dry sediment weight after heating at 60°C for 10 days using a sediment density of 2.65 g cm^{-3}.

6.3.3 Voltammetric ex situ profiling

A replicate core collected from the same MC800 deployment was profiled in millimeter increments with 100 µm gold/mercury (Au/Hg) voltammetric microelectrodes deployed on a computer-controlled micromanipulator with DLK 70 or 100 potentiostat (Analytical Instrument Systems, Inc.) in a three-electrode system (Ag/AgCl reference, Pt counter, and Au/Hg working electrodes). Au/Hg microelectrodes were fabricated as previously reported (Luther et al. 2008) and prepared daily by electrodeposition of mercury (Brendel and Luther, 1995). Dissolved oxygen was measured using linear sweep scans from -0.1 to -1.8V and a scan rate of 200 mV s^{-1} after a conditioning step at -0.1 V for 10 seconds (Minimum Detection Limit: MDL ~ 5 µM) (Luther et al., 2008). At each depth, cathodic square wave scans with a preconditioning step at -0.1 V for 10 seconds were run in at least triplicate from -0.1 to -1.8 V with a scan rate of 200 mV s^{-1} to quantify dissolved manganese(II) (Mn^{2+}, MDL ~ 15 µM), dissolved iron(II) (Fe^{2+}, MDL ~ 25 µM), thiosulfate ($S_2O_3^{2-}$, MDL ~ 10 µM), and total dissolved sulfide ($\Sigma H_2S=H_2S+HS^- + S^0 + S_x^{2-}$, MDL ~ 0.2 µM) in addition to qualitatively detect organic complexes of Fe(III) (org-Fe(III) (Taillefert et al., 2000a) and aqueous iron sulfide clusters ($FeS_{(aq)}$) (Theberge and Luther, 1997). When ΣH_2S or org-Fe(III) species were present, an additional preconditioning step was applied at -0.9 V for 10 seconds before each scan to avoid memory effects. Voltammetric signals were integrated using a semi-automated VOLTINT software package (Bristow and Taillefert, 2008). Before profiling, working electrodes were calibrated in a cell stand with $MnCl_2$ (0-400 µM Mn^{2+}), and Fe^{2+}, ΣH_2S, and $S_2O_3^{2-}$ were quantified from the pilot ion method with Mn^{2+} as pilot ion (Brendel and Luther, 1995). Oxygen concentrations in the overlying waters were calibrated using the bottom water oxygen concentrations determined by Winkler titration. As the chemical composition of

org-Fe(III) complexes and $FeS_{(aq)}$ is unknown, these species cannot be quantified (Taillefert et al., 2000a; Theberge and Luther, 1997) and are reported in normalized current intensities (Meiggs and Taillefert, 2011).

6.3.4 Pore water extraction and analyses

After voltammetric profiles were completed, the same core was immediately transferred to a glove bag (Sigma Aldrich) with a N_2 atmosphere for sectioning in 7-10, 20, 50, and 100 mm increment depending on core depth. Sediment sections were partitioned into 50 mL falcon tubes, centrifuged for 10 minutes at 3000 rpm under N_2 atmosphere to extract pore waters, and the leftover sediment sections were frozen at -20°C. Extracted pore waters were then filtered through 0.2-micron Whatman® nitrocellulose Puradisc syringe filters into 15 mL falcon tubes under N_2 atmosphere and immediately split for onboard analyses (dissolved iron and manganese speciation, dissolved orthophosphate, dissolved inorganic carbon, and total alkalinity). The leftover was preserved at 4°C after acidification (HCl 0.1 N) or at -20°C until analysis at Georgia Tech (dissolved ammonium, chloride, bromide, sulfate, nitrate, nitrite).

Total alkalinity (TA) measurements were conducted according to Dickson et al., 2007, but with a 3 mL open-cell potentiometric titration (Rassmann et al., 2016) using 0.01 M HCl, which was calibrated every day using Dickson standard batch #150 (Rassmann et al., 2016). Error in this analysis represents the standard deviation from the mean of duplicate samples if available or propagation of analytical error for single samples (1%). Dissolved inorganic carbon (DIC) was determined by flow injection analysis, if necessary after 5 mM $ZnCl_2$ amendment to avoid dissolved sulfide interference (Hall and Aller,

1992). Dissolved Mn(III) (Mn^{3+}) and total dissolved Mn (Mn_d) were determined in duplicate using the porphyrin kinetic spectrophotometric method (Madison et al., 2011a) modified to account for dissolved Fe^{2+} interferences. Mn_d was quantified by converting the final absorbance to concentration using the molar absorptivity ($\varepsilon = 91.2 \pm 0.4 \times 10^{-3}$ μM cm^{-1}) determined from external calibration curves with Mn^{2+} (MDL: 0.11 μM, 3σ of blanks, n=24). Mn^{3+} was quantified by fitting the spectrophotometric kinetic curve as an exponential rise to a maximum curve but was below detection limit (MDL < 1.5 μM) in the majority of pore water samples. Dissolved orthophosphates (ΣPO_4^{3-}) were quantified with the methylene blue method after correction for silica interference (Murphy and Riley, 1962). Finally, dissolved Fe^{2+} was quantified using the ferrozine method without hydroxylamine while total dissolved Fe (Fe_d) was determined by reacting a separate aliquot with hydroxylamine hydrochloride (0.2 M) in the dark for 24 hours. Dissolved Fe(III) ($Fe(III)_d$) was obtained by subtracting the dissolved Fe^{2+} concentration from total dissolved Fe (Stookey, 1970; Viollier et al., 2000). At Georgia Tech, NH_4^+ was quantified by the indophenol blue method (Strickland and Parsons, 1972) and anions via HPLC with UV detection using a 3.2 mM $NaCO_3$ / 1.0 mM $NaHCO_3$ buffer (SO_4^{2-}, Cl^-, Br^-; MDL: 218, 422, 114 μM respectively) and 54 mM NaCl (NO_2^- NO_3^-, MDL = 0.12 and 0.11 μM) eluents (Beckler et al., 2014). All standard deviations reported for pore water measurements represent analytical error propagated from calibration curves except for SO_4^{2-} at St. 13, St. 11, and St. 12 which represent the standard deviations from duplicate measurements.

6.3.5 Solid phase analysis

Solid phase manganese and iron were extracted in duplicate from sediments following classical sequential and parallel extraction protocols (Anschutz et al., 2000; Hyacinthe et al., 2001; Kostka and Luther, 1994; Tessier et al., 1979). A 0.2-0.5 g pellet of wet sediment was added to a 15 mL falcon tube, and the adsorbed fraction (absorbed Fe^{2+}, absorbed Mn^{2+}) was first extracted for 2 hours on a rotary wheel using 8 mL $MgCl_2$ (0.5 M, pH 7) (Tessier et al., 1979). The supernatant was removed for analysis and replaced by a 8 ml sodium acetate solution (0.5 M adjusted to pH 5 with acetic acid) to extract Fe^{2+} and Mn^{2+} bound in the carbonate phases (carbonate-bound Fe^{2+}, carbonate-bound Mn^{2+}) on a rotary wheel for 5 hours (Tessier et al., 1979). Finally, the supernatant was replaced by 8 ml of an ascorbate solution (pH 7.4) consisting of sodium citrate (0.2 M), sodium bicarbonate (0.6 M), and 0.1 M L-ascorbic acid for the extraction of poorly crystalline Fe(III) and Mn(III/IV) phases on the rotary wheel for 24 hours (Hyacinthe et al., 2001; Kostka and Luther, 1994). The ascorbate fraction reductively dissolves poorly crystalline Fe(III) oxides (i.e., ferrihydrite) and total Mn(III/IV) oxides (Anschutz et al., 2005) but not crystalline iron oxides (e.g., hematite, goethite, magnetite) or $FeS_{(s)}$ (Kostka and Luther, 1994). In parallel, total solid Fe (i.e., siderite, poorly crystalline Fe(III), crystalline Fe(III) oxides, and $FeS_{(s)}$) was extracted in duplicate sediment pellets with a dithionite reagent (0.35 M ammonium acetate, 0.2 M sodium citrate, 0.03 M sodium dithionite, pH 5) at 60°C in a water bath for 4 hours (Kostka and Luther, 1994). The carbonate and ascorbate concentrations were subtracted from the dithionite fraction to quantify crystalline Fe(III) + $FeS_{(s)}$. Between each extraction step, the sediment slurry was centrifuged for 10 min at 3000 rpm and the supernatant was stored in a separate falcon tube at 4°C until analysis the

same day. In addition, two sediment samples were dried at 50°C for 3-5 days, allowed to cool in the oven, and weighed to normalize concentrations to the weight of dry sediment in grams (gdw). Total extracted Fe^{2+} was measured in each fraction using the ferrozine method (Stookey, 1970), whereas total dissolved manganese (Mn_d) from the extractions were measured by Inductively Coupled Plasma – Mass Spectrophotometer (ICP-MS) using appropriate analytical procedures (Owings et al., 2019). All errors reported represent the standard deviation of the average of duplicate extractions. Finally, the acid volatile sulfides (AVS) fraction was extracted in triplicate by cold distillation of wet sediment (0.5-0.7 grams) with 5 ml of 3M HCl and entrainment of the H_2S gas product by a pre-purified (using a Cu trap heated at 400°C to remove O_2 traces) ultra-high purity (UHP) N_2 stream into a 1 M NaOH solution trap at low flow rate (Henneke et al., 1991). Total dissolved sulfide trapped after 4 hours was quantified by absorbance at 230 nm using NaS_2 standards dissolved daily in degassed 1 M NaOH (Ellis and Golding, 1959).

6.3.6 Calculations

6.3.6.1 Flux calculations

Dissolved oxygen uptake (DOU) rates and the diffusive fluxes of DIC, NH_4^+, and ΣPO_4^{3-}, were calculated from their concentration gradients across the sediment-water interface (SWI) using Fick's first law (Eq. 1), assuming diffusion mainly controlled transport.

$$F_i = -\varphi D_s \frac{dC_i}{dz} \qquad 1$$

In these calculations, φ represents the average porosity of the sediment layers where the diffusive flux was determined, D_s is the apparent diffusion coefficient after correcting for

tortuosity, and $\frac{dC_i}{dz}$ is the concentration gradient of species i as a function of depth z. For DOU, $D_s = \frac{D_0}{1+3(1-\varphi)}$ where D_0 is the diffusion coefficient of dissolved oxygen in free water (Broecker and Peng, 1974). For all other species $D_s = \frac{D_0}{\theta^2}$, where tortuosity $\theta^2 = 1 - \ln(\varphi^2)$ and $D_0 = (m_0 + m_1 T)\ 10^{-6}\ cm^2\ s^{-1}$ in which m_0 and m_1 are empirically derived constants (Boudreau, 1997). The diffusion coefficients for HCO_3^- and HPO_4^{2-} were used for the calculations of the diffusive fluxes of DIC and ΣPO_4^{3-} as these species constituted the majority of the carbonate and phosphate speciation in representative solutions for each station modeled using Visual MINTEQ version 3.1 (Gustafsson, 2019). Positive fluxes in these calculations represent downward fluxes into the sediment, whereas negative fluxes represent upward fluxes across the SWI.

6.3.7 Diagenetic modeling

The Matlab^{TM}-based one-dimensional reactive transport model MATSEDLAB (Couture et al., 2010; Pastor et al., 2011) was used to quantify the depth-integrated rates of aerobic and anaerobic respiration at each of the station investigated. In this model, the transport parameters reflect conventional bioturbation, irrigation, sedimentation, compaction, and diffusion in sediments (Boudreau, 1997; Wang and Van Cappellen, 1996). Porosity was assumed constant at the mean porosity determined in each core (Figure E 5), sedimentation rates were fixed at each station with values from the literature (Corbett et al., 2006; Yeager et al., 2004). Diffusion was assumed molecular and modified to account for salinity, temperature, and tortuosity (Boudreau, 1997). Finally, biorrigation and bioturbation were considered in the model and assumed similar at each station with an exponential decrease in bioturbation diffusion coefficient with depth in the sediment.

Organic carbon degradation that produces NH_4^+ and DIC as by-product is described by Michaelis-Menten rate laws with respiratory inhibition (Soetaert et al., 1996; Wang and Van Cappellen, 1996) using C:N ratios from the literature (Sampere et al., 2011; Waterson and Canuel, 2008). Reduced compounds produced during remineralization (i.e., NH_4^+, M(II), Fe^{2+}, ΣH_2S) are partly removed from the system by precipitation of sulfide (FeS) or carbonate minerals ($MnCO_3$, $FeCO_3$) and oxidation in the presence of $O_{2(aq)}$ or other oxidants (MnO_2, $Fe(OH)_3$) using explicit kinetic formulations (Wang and Van Cappellen, 1996). The whole suite of reactions and rate laws included in the model are provided in the appendix (Table E 1Table E 1: Respiration reactions involved in the remineralization of natural organic matter used in the 1D transient reactive transport model MATSEDLAB (R1 = aerobic respiration; R2 = denitrification; R3 = dissimilatory manganese reduction; R4 = dissimilatory iron reduction; and R5 = sulfate reduction). The C:N ratio is used to set up the stoichiometric coefficients x and y in the model-Table E 4). Boundary conditions included Dirichlet conditions at the sediment surface, using either bottom water concentrations of each dissolved constituent or optimized concentrations of particulate material (i.e. organic carbon, Mn(III/IV) oxides, or Fe(III) oxides), and zero flux (Neumann) conditions at the bottom of the domain. As kinetic parameters and rate laws of most abiotic processes are relatively well characterized, they were fixed in the model (Table E 5). In turn, microbial respiration rate constants (Table E 6) and other important parameters (Table E 7) were optimized to fit depth profiles of the main redox species measured in a self-consistent manner at each station.

6.4 Results

The stations investigated in this study (Table 6-1) include St. 2b located in the zone of highest sediment accumulation rate (>2.5 cm yr^{-1}, (Corbett et al., 2006)), while the other stations display relatively low sedimentation rates (<0.1 cm yr^{-1}, (Corbett et al., 2006; Yeager et al., 2004). Percentage of organic carbon content varies between 1.0 and 1.5%, with the highest percentages found at the shallowest stations of each transect (St. 2b, St. 15) (Table 6-2). The sediment texture and color reflected the different geochemical conditions at each station. St. 2b consisted mainly of dark gray/black mud (

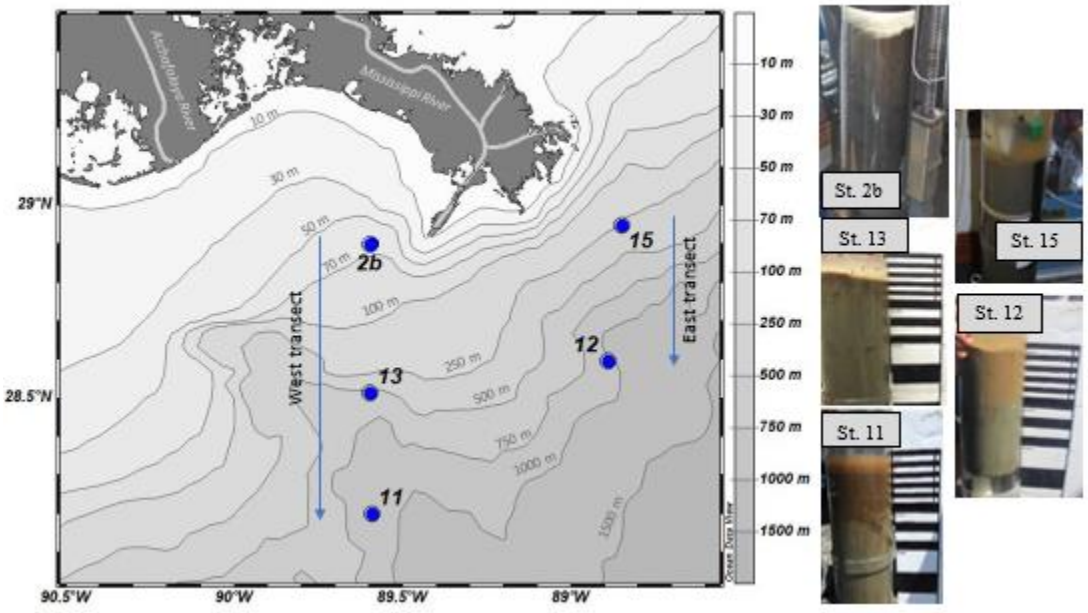

Figure 6-1) with a band of black sediment below 45 cm (not pictured). St. 13 and St. 11 cores contained light gray muds with flocculant rust and brown colored sediments

present in the top 5 and 10 cm, respectively (

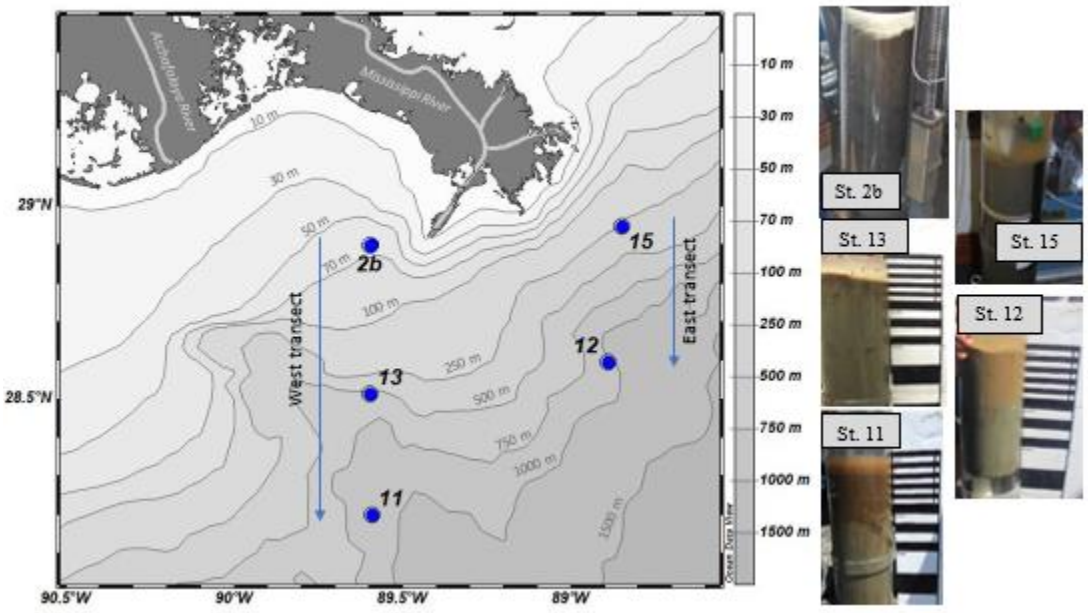

Figure 6-1). The sediments at St. 12 displayed a light orange/brown color in the top 10 cm that transitioned rapidly to gray sediments with black patches after 10 cm (

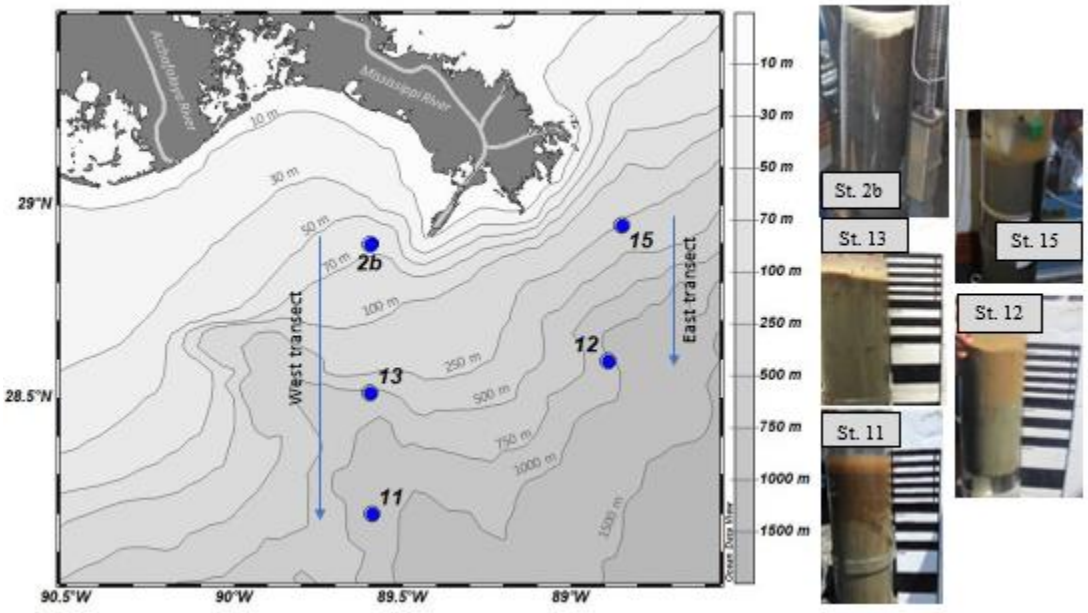

Figure 6-1). St. 15 was made of gray mud with rust colored patches.

Cores were also collected across the shelf during this cruise. The results of those analyzes will be included in the upcoming manuscript Rabouille et al., 2020, and provided in Appendix E (Figure E 1-Figure E 4).

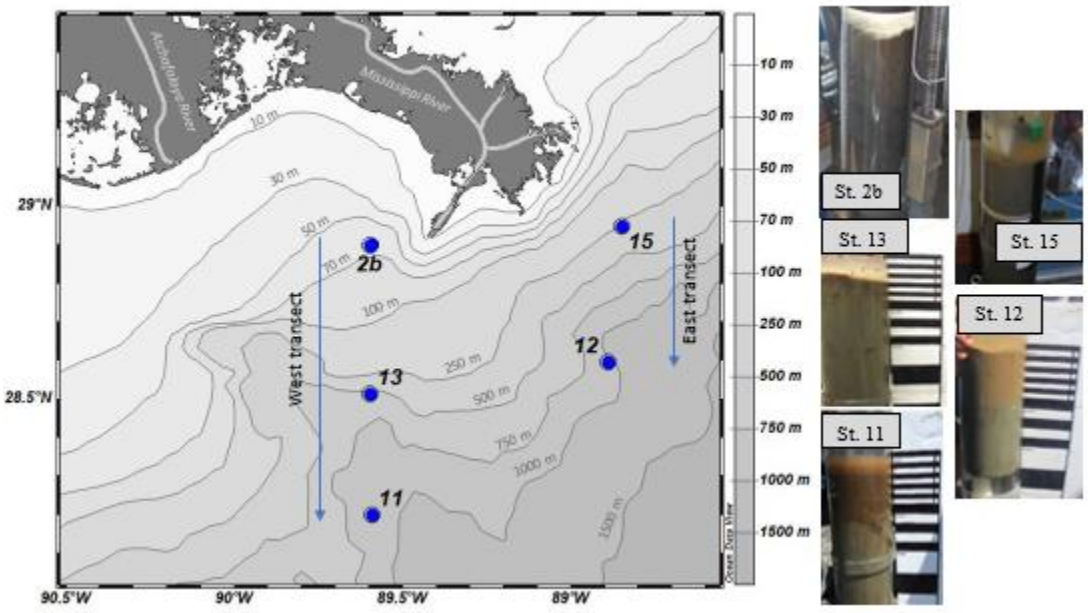

Figure 6-1 a) Map of the stations across the Louisiana shelf and slope in the northern Gulf of Mexico where benthic landers were deployed and sediment cores collected during a research cruise in July and August of 2017. The two transects, east and west, are labeled with arrows. Depth contours (m) indicate ocean bathymetry; b) pictures of the cores showing contrasting sediment colors at the different sampling locations and color variations with depth in each core. Thin, medium, and thick white and black lines represent depth intervals of 1, 2 and 5 cm respectively.

Table 6-1**:** Station location, water column depth, and corresponding bottom water parameters (temperature, salinity, oxygen concentration, pH) along the western (St.2b, 13, 11) and eastern (St. 15 and 12) transects.

Station	**Latitude (N)**	**Longitude (W)**	**Depth (m)**	**Temp (°C)**	**Salinity**	**O_2 [µM] (% sat)**	**pH**
St. 2b	28°54.033	89°35.417	65	22.5	36.3	114.7 (48%)	7.86
St. 13	28°30.721	89°35.730	510	9.4	34.9	126.4 (44%)	7.80
St. 11	28°12.043	89°35.486	925	11.5	33.4	130.0 (47%)	7.78
St. 15	28°56.855	88°50.903	274	13.2	35.4	122.5 (47%)	7.86
St. 12	28°35.896	88°53.435	989	13.9	34.7	186.3 (72%)	7.76

O_2 % sat calculated relative to saturated O_2 estimated from in situ temperature and salinity

6.4.1 Bottom water parameters and oxygen, pH, and porosity microprofiles

Bottom waters, though oxic (Table 6-1) and outside the hypoxic zone for that season (Rabalais and Turner, 2017), were significantly undersaturated (44-72%) along the continental slope. Dissolved oxygen concentrations decreased exponentially from the SWI to below detection limit at depth. The oxygen penetration depth (OPD) increased across the shelf to slope transects from 1.6 mm at St. 2b to 8.3 and 14.0 mm at St. 13 and 11 along the western transect, and to 7.4 and 9.0 mm at St. 15 and 12 along the eastern transect (Table 6-2). At St. 15, a pocket of oxygen was detected below the OPD (Figure 6-2) likely due to bioturbation. Bottom water pH_T collected from overlying waters of the core varied between 7.76 and 7.86 (Table 6-1), reflecting the widespread acidification of sediment overlying waters in this environment (Cai et al., 2011). The pH microprofiles collected over the first 5-8 cm at St. 13, 11, 15 and 12 displayed the same trend with an abrupt decrease in pH within the first 1-1.5 cm below the SWI to minimum pH values ranging from 7.0-7.3 followed by a rebound to relatively constant values between 7.0-7.8 at depth (Figure 6-2). At St. 2b, the pH profile followed a similar trend, however, the pH decrease occurred within a few millimeters (versus centimeters at the other stations) from the SWI. Furthermore, the pH decreased again after the initial rebound in pH around 10 mm and remained at its lowest value (i.e., pH 7.2) below 30 mm in the profile (Figure 6-2). Little to no differences were observed between ex situ and in situ oxygen and pH microprofiles (Figure 6-2), confirming the integrity of the sediment cores collected during this study. Sediment porosity ranged from 0.86 to 0.95 in surface sediments, decreased by 0.1-0.15 units within the top 50-100 mm, and remained relatively constant at depth (Figure E 5) with average values ranging from 0.75 to 0.87 (Table 6-2). Overall, stations along the eastern transect displayed lower porosities and steeper decreases in porosity with depth

compared to the western transect (Figure E 5), indicative of more significant inputs of fine grained sediments along the western transect. At each station, the water content of the different sections decreased with depth, suggestive of increased compaction.

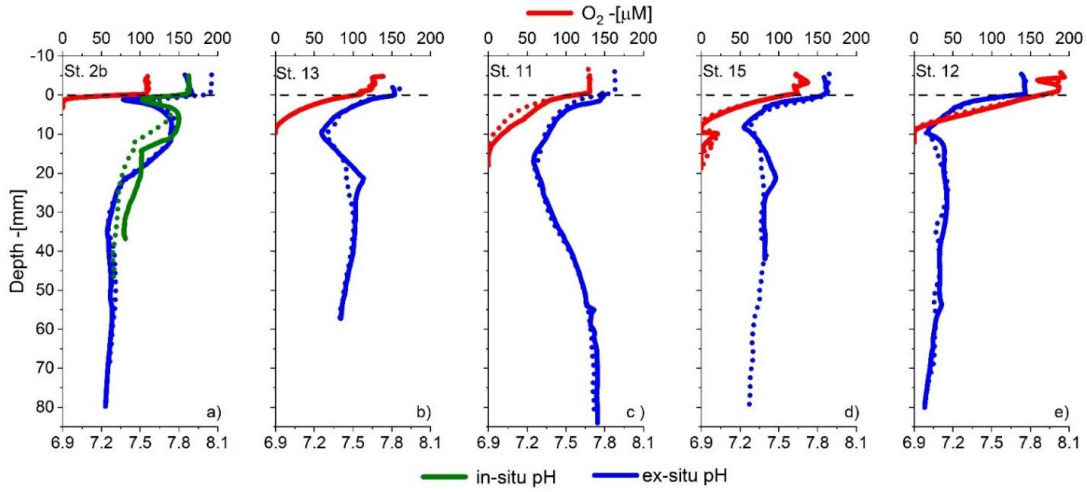

Figure 6-2 O_2 (red) and pH (green and blue) microprofiles in sediment cores along the western (St. 2, St. 13 and St. 11) and eastern transects (St. 15, St. 12). Replicate

profiles are indicated by solid and dotted lines. Oxygen profiles at St. 2b were collected in situ, while all others were collected ex situ after core collection. The pH profiles at St. 2b were collected both in-situ with a benthic lander (pH-green) and ex situ in sediment cores (blue). The sediment water interface (depth = 0 mm) is indicated by the dashed horizontal line.

Table 6-2: Sedimentation rate and Organic Carbon (OC) content obtained from the literature and average porosity, oxygen penetration depth (OPD), and diffusive oxygen uptake rate (DOU) determined along the western (St. 2b, 13, 11) and eastern (St. 15 and 12) transects.

Station	Sed Rate (cm/year)	OC (%)	Average porosity[g]	OPD (mm)[‡]	DOU ($mmol/m^2/d$)
St. 2b	>2.5[a]	1.5[d]	0.85 ± 0.04	1.6	13.8
St. 13	<0.7[b]	1.1 [d]	0.87 ± 0.04	8.3	3.6
St. 11	0.07±0.06[c]	1.2[e]	0.85 ± 0.05	14.0 ± 1.1	3.9 ± 0.3
St. 15		1.5 [f]	0.80 ± 0.05	7.4 ± 0.6	2.6 ± 0.1
St. 12	0.09±0.05[c]	1.0[e]	0.75 ± 0.05	9.0 ± 0.3	2.3 ± 0.2

[‡]OPD and DOU represent mean values from two ex situ profiles, except for St. 2 and 13 which were profiled once and St 2b which consisted of two in situ profiles

*see methods section for calculations

[a]Proximal (Type 1) sediment accumulation rates using ^{210}Pb from Corbett et al., 2006

[b] Distal (Type 3) sediment accumulation rates using ^{210}Pb from Corbett et al., 2006

[c] from ^{210}Pb measurements from Yeager et al., 2004 (stations MT3 and S36)
[d] TOC% St. 2 and St. 13 values from Waterson and Canuel 2008 (stations 80m and H9)
[e] % OC from Morse and Beazley, 2008 (stations MT3 and HiPro)
[f] %POC from Zhuang et al 2018 (Taylor Energy Site)
[g] Average porosity and standard deviation over entire core, porosity profiles in supplemental material

6.4.2 Voltammetric depth profiles of redox species

Dissolved oxygen measured by Au/Hg microelectrodes also decreased rapidly with depth (Figure 6-3) but OPDs, although increasing with water depth, were 3-6 mm shallower than detected with the amperometric microelectrodes. At St. 2b, pore water Mn^{2+} concentrations uniformly increased immediately below the sediment water interface (SWI) to a maximum concentration of 1,039 ± 96 µM at 56 mm. Mn^{2+} concentrations then rapidly decreased to below detection limits at 62 mm, and reappeared below 165 mm albeit in lower concentrations (ranging from 141-351 µM). Although Mn^{2+} concentrations also increased with depth to concentrations ranging between 295 and 347 µM at St. 13, 11, 15, and 12, the onset of Mn^{2+} production was detected much deeper at 103, 65, 82, and 150 mm below the SWI, respectively (Figure 6-3). In comparison, Fe^{2+} concentrations remained below detection limits throughout each core, even though org-Fe(III) was

detected in all cores except at St. 11. At St. 2b, a strong peak in org-Fe(III) was observed (372 ± 14 nA maximum) that coincided with the Mn^{2+} peak and progressively decreased to below detection limit at 150 mm. At St. 13, org-Fe(III) was produced between 110 and 146 mm to approximately 20 nA and abruptly increased to 96 ± 5 nA at 156 mm followed by a decrease to below detection limit within 30 mm. Across the eastern transect, org-Fe(III) was detected in much lower current intensities. At Station 15, org-Fe(III) was produced at 82 mm in low current intensities (ca. 5 nA) and increased to a maximum of 37 ± 6 nA at depth, whereas org-Fe(III) appeared at 151 mm at St. 12 and remained low deeper (9-12 nA). Dissolved ΣH_2S was only detected at St. 2b, where it was produced below 49 mm and reached a maximum of 219 ± 14 µM at 67 mm before decreasing regularly to below detection limit at 214 mm. Molecular clusters of FeS ($FeS_{(aq)}$) were also detected just above the onset of ΣH_2S production (50 mm) at St. 2b, although their current intensities remained relatively low (3-38 nA) across the profiles and decreased to below detection limit at 178 mm. Finally, $FeS_{(aq)}$ was also detected in low current intensities (max 10 ± 2 nA) below 150 mm at St. 13, but remained below detection limit at all other stations (Figure 6-3).

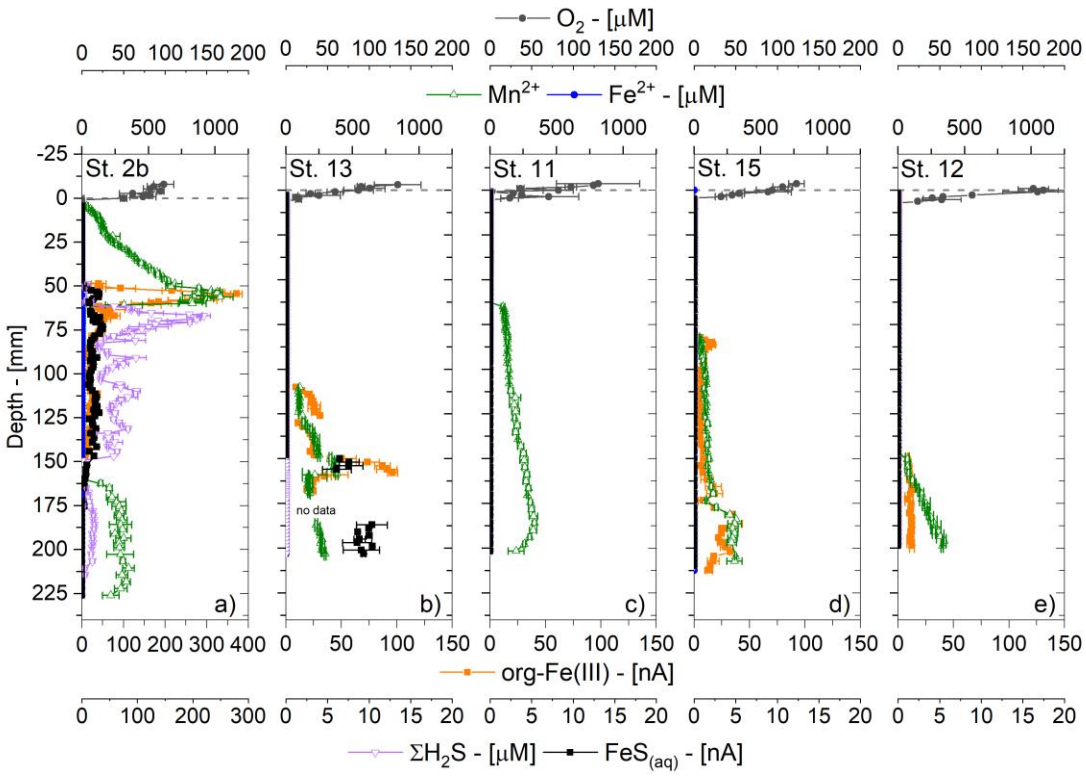

Figure 6-3: Depth profiles of dissolved oxygen (O_2) (gray circles), Mn(II) (green triangles), Fe(II) (blue circles), organic Fe(III)-L complexes (orange squares), ΣH_2S (purple down triangles) and FeS_{aq} (black squares) detected voltammetrically in the sediments of: St. 2b (a, b); St. 13 (c, d); St. 11 (e, f); St. 15 (g, h); and St. 12 (i, j). The sediment water interface is indicated by the dashed horizontal line. Note the different scales at St. 2b where concentrations and current intensities were much higher compared to the other stations. Error bars represent the standard deviations of at least triplicate voltammetric measurements at the same location.

6.4.3 Pore water profiles of carbon respiratory products, sulfate, and dissolved metals

Depth profiles of the main redox species reflected the intensity of respiratory processes as revealed by DIC, TA, ΣPO_4^{3-}, and NH_4^+ profiles. DIC, TA, ΣPO_4^{3-}, and NH_4^+ concentrations increased from the SWI to maxima at depth at all stations, but maximum

concentrations decreased with increasing water depth in the order St. 2b (Figure 6-4a_1) >> St. 13 (Figure 6-4b_1) > St. 11 (Figure 6-4c_1). In the eastern transect, DIC, ΣPO_4^{3-}, and TA did not vary throughout the core at St. 15 (Figure 6-4d_1), indicating little respiratory activity relative to the other stations. In turn, slight increases in DIC, TA, ΣPO_4^{3-}, and NH_4^+ concentrations with depth were observed at St. 12 (Figure 6-4e_1). Sulfate concentrations decreased regularly from 29.9 ± 0.5 to 21.3 mM at 500 mm at St. 2b (Figure 6-4a_2), only slightly to 26.7±1.13 mM between 365 and 525 mm at St. 13 (Figure 6-4b_2), and remained relatively constant throughout the profiles at the other stations (Figure 6-4c_2, d_2, and e_2). With respect to the dissolved nitrogen species, NO_3^- concentrations were highest in the bottom waters (ranging between 12 and 31 µM), decreased rapidly within the first 10-20 mm to approximately 1-5 µM, and remained relatively constant around these values at depth (Figure 6-4a_2, c_2, d_2, and e_2) as observed previously (Zhuang et al., 2019). In turn, NO_2^- concentrations remained below 5 µM throughout each core (Figure 6-4).

St. 2b displayed the highest Mn_d concentration in the overlying water (12.2 ± 0.2 µM) of all stations (1.7 ± 0.4 µM at St. 13 and < MDL at St. 11, St. 15, and St. 12) (Figure 6-4a_3, b_2, c_3, d_3, e_3), indicative of a benthic flux as observed by the voltammetric measurements (Figure 6-3a). At each western transect station, Mn_d was produced immediately below the SWI and generally displayed a subsurface peak with a maximum concentration ranging between 239 and 400 µM, the position of which increased with depth across the continental slope (10 mm at St. 2b, 43 mm at St. 13, and 127 mm at St. 11) (Figure 6-4a_3, b_3, c_3). Below this peak, Mn_d concentrations decreased to a minimum of approximately 100 µM at 600 mm at St. 2b, whereas it rebounded below 108 mm to a maximum of 277 ± 6 µM at depth at St. 13 and slightly decreased to a minimum of 191±

2 µM at depth at St. 11. The Mn_d profile at the deepest station of the eastern transect (St. 12), displayed a similar profile as the deepest station of the western transect (St. 11), with increase in Mn_d to a maximum of 317 ± 1 µM at 75 mm but only a slight decrease in concentration with depth (Figure 6-4d_3). Atypical to all other stations, Mn_d concentrations at St. 15 did not display a peak, rather concentrations remained relatively low and gradually increased to 73 ± 2 µM at 215 mm followed by a decrease in concentration deeper (Figure 6-4e_3).

Overall, pore water Fe^{2+} concentrations were lower than pore water Mn_d and $Fe(III)_d$ concentrations in all cores, suggesting sediments across the continental slopes were suboxic. Although a shallow Fe^{2+} peak (max. 62 ±0.6 µM at 90 mm) was present at St. 2b (Figure 6-4a_3), pore water Fe^{2+} was present in low concentrations (0-15 µM) throughout the cores of all other stations (Figure 6-4b_3, c_3, d_3, e_3), reflecting what was found with Au/Hg voltammetric microelectrodes (Figure 6-3). Station 2b displayed a large $Fe(III)_d$ peak (253 ± 1.3 µM) over the first 100 mm of sediment that coincided with the org-Fe(III) peak measured by voltammetry (Figure 6-3a) and was accompanied by small increases in Fe^{2+} measured voltammetrically (Figure 6-3a) and pore water Fe^{2+} (Figure 6-4a_3). In the deeper stations along the western transect, the onset of $Fe(III)_d$ production was located at greater depths of 34 and 144 mm at St. 13 and St. 11, and concentrations increased gradually with depth to concentrations of 128 ± 1.0 and 92 ± 1.5 µM respectively (Figure 6-4b_3, c_3). Although org-Fe(III) voltammetric signals did not match the $Fe(III)_d$ profiles at St. 13 and 11, likely due to the highly localized voltammetric measurements compared to the longitudinally-averaged pore water $Fe(III)_d$ concentrations in heterogeneous sediments, org-Fe(III) current intensities were similarly higher at St. 13 compared to St. 11. Along

the eastern transect, two subsurface peaks in Fe^{3+} with maximum concentration of 129 ± 2.1 and 398 ± 6.3 µM were found over the first 50 mm and between 200 and 300 mm at St. 15 (Figure 6-4d_3) that generally matched the org-Fe(III) voltammetric profile (Figure 6-3d). A gradual increase in Fe^{3+} concentration with depth to 90 ± 0.6 µM was observed at St. 12 (Figure 6-4e_3) that was reflected by the general increase in org-Fe(III) below 150 mm (Figure 6-3e).

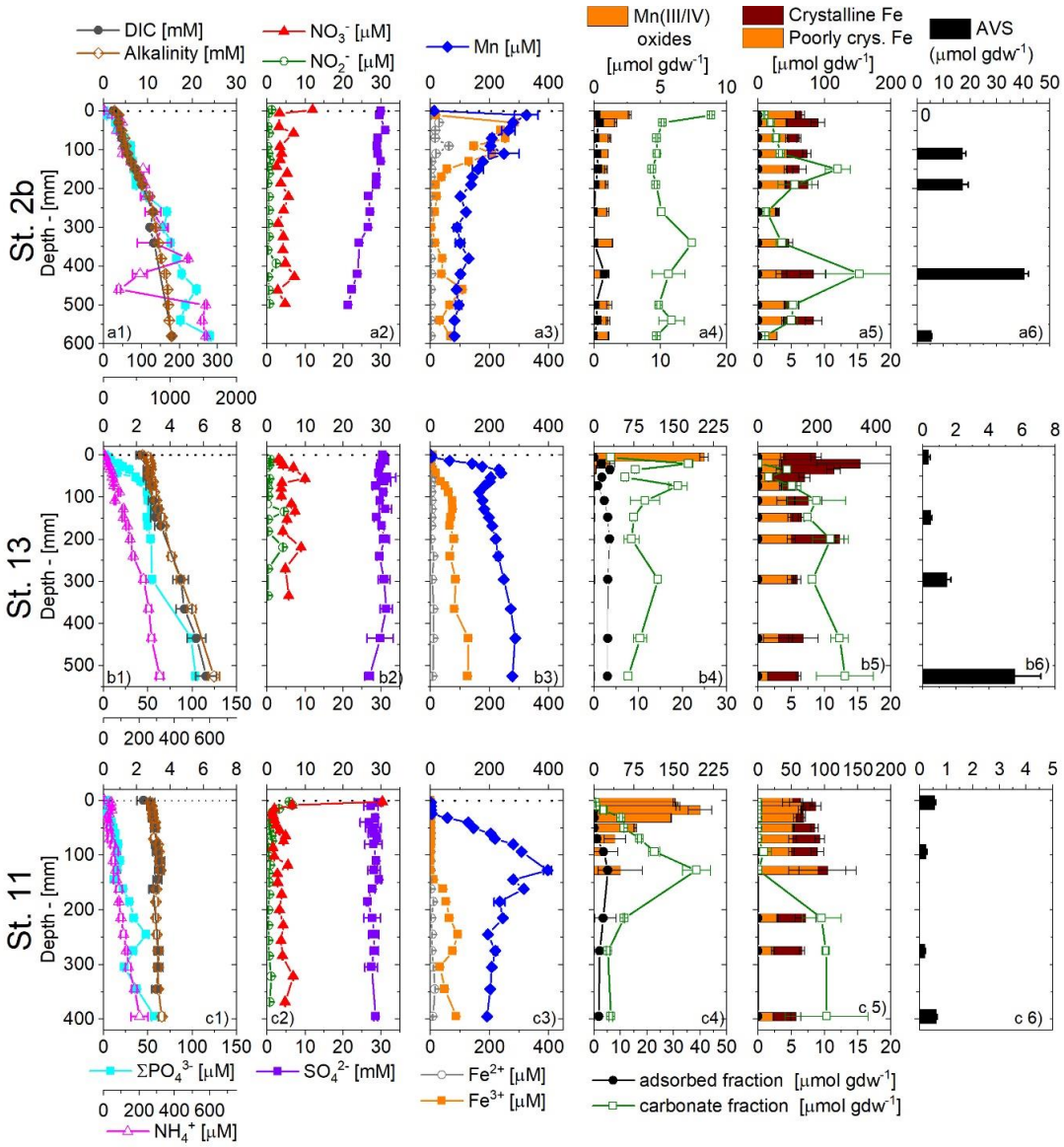
DIC [mM]
Alkalinity [mM]
NO3- [µM]
NO2- [µM]
Mn [µM]
Mn(III/IV) oxides [µmol gdw-1]
Crystalline Fe
Poorly crys. Fe
[µmol gdw-1]
AVS (µmol gdw-1)
St. 2b
St. 13
St. 11
Depth - [mm]
a1)
a2)
a3)
a4)
a5)
a6)
b1)
b2)
b3)
b4)
b5)
b6)
c1)
c2)
c3)
c4)
c 5)
c 6)
ΣPO43- [µM]
SO42- [mM]
Fe2+ [µM]
Fe3+ [µM]
NH4+ [µM]
adsorbed fraction [µmol gdw-1]
carbonate fraction [µmol gdw-1]

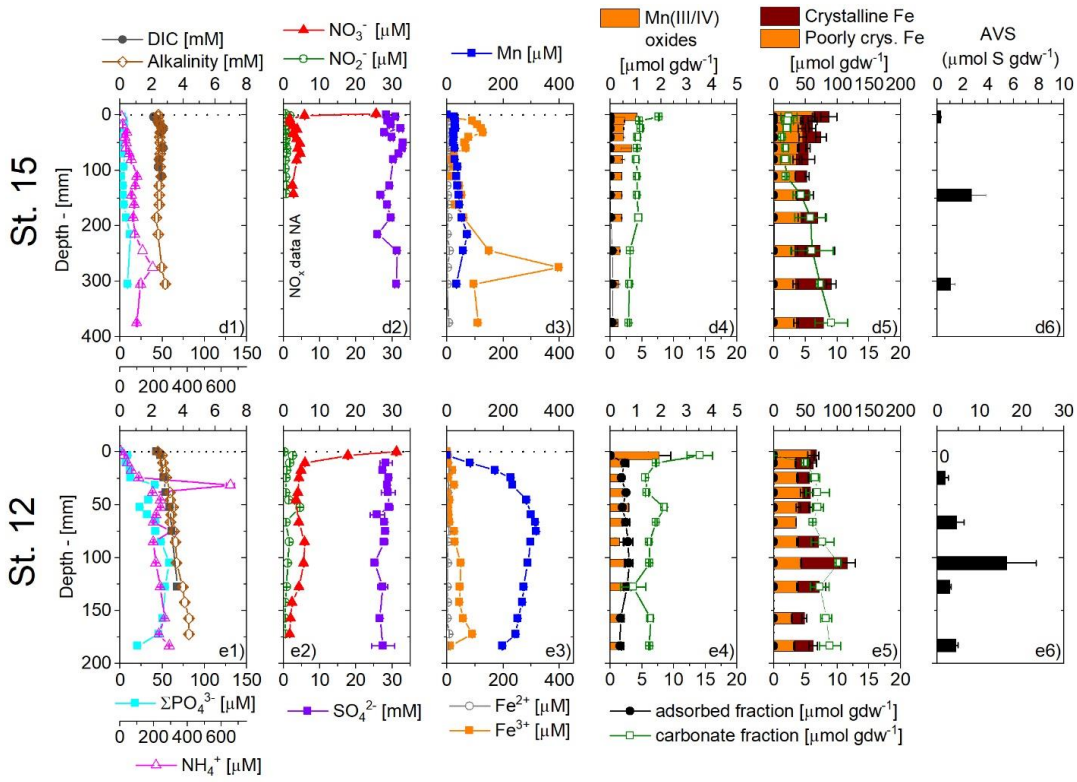

Figure 6-4: Depth profiles of DIC, total alkalinity (TA), ΣPO_4^{3-}, and NH_4^+ (first panel), NO_3^-, NO_2^-, and SO_4^{2-} (second panel), dissolved Mn(II), Mn(III), Fe(II), and $Fe(III)_d$ (third panel), total solid Mn and Fe partitioned as adsorbed, carbonate, non-crystalline, and crystalline phases (fourth and fifth panels), and 'acid volatile sulfides' (sixth panel) at: St. 2b (a_1-a_6); St. 13 (b_1-b_6); and St. 11 (c_1-c_6) along the western transect and at: St. 15 (d_1-d_6); and St. 12 (e_1-e_6) along the eastern transect. The sediment water interface is indicated by the dashed horizontal line. Note the change in scale of alkalinity, DIC, ΣPO_4^{3-}, and NH_4^+ at St. 2b in comparison with the other stations as well as the change in scale of Mn and Fe solid phase speciation and AVS between each station to observe general trends. '0's in the sixth panels represent AVS analyses of surface sediments that were below detection limit.

6.4.4 Solid manganese, iron, and sulfur profiles

At St. 2b, the highest total Mn concentration in the solid phase (20.7 ± 0.4 µmol gdw^{-1}) was present within the first 7 mm of the sediment and included 2.7 ± 0.1 µmol gdw^{-1} of Mn(III/IV) oxides (Figure 6-4a_4). The remainder of the core consisted of total Mn concentrations ranging between 10 and 16 µmol gdw^{-1}, the majority of which (8-14 µmol gdw^{-1}) was in carbonate-bound Mn^{2+} (80-91%), a smaller fraction (0.9-1.6 µmol gdw^{-1}, 6-12%) as Mn(III/IV) oxides, and a much smaller adsorbed Mn^{2+} fraction (0-1.6 µmol gdw^{-1}, 0-11%). The distribution of solid phase Mn was typically similar at stations St.13 and St. 11, with an enrichment of Mn(III/IV) oxides at the surface (207 ± 8.0 and 151 ± 1.9 µmol gdw^{-1}, respectively) that rapidly decreased to 1.2 ± 0.2 µmol gdw^{-1} at 53 mm at St. 13 but only progressively to 1.3 ± 0.2 µmol gdw^{-1} at 215 mm at St. 11 (Figure 6-4b_4, c_4). At both stations, carbonate-bound Mn^{2+} represented the dominant fraction (56-86% at St. 13 and 0.5-71.3% at St. 11) across the sediment column (Figure E 6) and increased in concentrations below the Mn(III/IV) oxide maximum. This increase, however, was much more rapid at St. 13 (approx. 1.3 µmol gdw^{-1} per mm on average between 7-20 mm) than at St. 11 (approx. 0.3 µmol gdw^{-1} per mm on average between 3-127 mm). Adsorbed Mn^{2+}, which was rapidly produced below 20 mm at St. 13 and much more progressively below 70 mm at St. 11 (Figure 6-4b_4 and c_4), remained relatively low in concentration at both stations (0.9-3.7 µmol gdw^{-1} at St. 13 and 1.2-5.2 µmol gdw^{-1} at St. 11), not exceeding 30% of total Mn (Figure E 6). Along the eastern transect, Mn(III/IV) oxides and carbonate Mn^{2+} displayed similar trends with the highest Mn(III/IV) oxide concentrations found at the sediment surface (1.1 ± 0.1 µmol gdw^{-1} at St. 15, 1.9 ± 0.5 µmol gdw^{-1} at St. 12) but < 1 µmol gdw^{-1} Mn(III/IV) oxides across the rest of the sediment column. Similarly, the

carbonate Mn^{2+} fraction, though dominating the solid phase speciation at both St. 15 and St. 12 (Figure E 6), was highest at the surface (7.63 ± 0.09 at St. 15, 14.12 ± 2.03 at St. 12) and below 5 and 8 μmol gdw^{-1}, respectively, across the remainder of the sediment column (Figure 6-4d_4, e_4). Interestingly, the difference in Mn solid phase speciation between St. 15 and St. 12 manifested in the adsorbed fraction which increased only to 0.3 μmol gdw^{-1} at 245 mm at St. 15, in contrast to St. 12 where adsorbed Mn^{2+} was detected as high as 1.5-3.0 μmol gdw^{-1} between 10 and 183 mm (Figure 6-4d_4,e_4, Figure E 6).

The distribution of total solid Fe in St. 2b sediment was relatively homogeneous with depth and included relatively high concentrations of poorly crystalline (30-55 μmol gdw^{-1} or 40-100% of total solid Fe) and crystalline (0-47.7 μmol gdw^{-1} or 0-51% of total solid Fe) Fe(III) (Figure 6-4a_6, Figure E 6), and generally low carbonate-bound Fe^{2+} (< 10%) (Figure 6-4a_5, Figure E 6). The distribution of total solid Fe was more variable at St. 13 (Figure 6-4b_5, Figure E 6), where the surface sediment (0-53 mm) was depleted in poorly crystalline Fe(III) oxides (36-83 μmol gdw^{-1} or 29 ± 10% of total solid Fe) and enriched in crystalline Fe(III) oxides (112-269 μmol gdw^{-1} or 57-77%), and the deep sediment was enriched in poorly crystalline Fe(III) oxides (μmol gdw^{-1} or %) and depleted in crystalline Fe(III) oxides (34-112 μmol gdw^{-1} or 22-79%). Although low at the surface (0-4.4 μmol gdw^{-1} or 0-1.6%), carbonate-bound Fe^{2+} concentrations increased at 73 mm to reach 5-13 μmol gdw^{-1} or 3.8-8.7% of total solid Fe between 73 and 525 mm (Figure 6-4b_5, Figure E 6). The inverse trend was apparent at St. 11 (Figure 6-4c_5), where poorly crystalline Fe(III) oxides rapidly increased below the SWI to 90 μmol gdw^{-1} at 20 mm and constituted the majority of total solid Fe (80-93%, Figure E 6), then decreased progressively to 22.8±2.5 μmol gdw^{-1} at depth. Although generally low at St. 11 (34-43

μmol gdw^{-1}, Figure 6-4c_5), crystalline Fe(III) oxides were proportionally lower than the poorly crystalline Fe(III) oxides fraction in surficial sediment (< 20%) but represented the dominant fraction of total solid Fe in the deep sediment (50-56%) with a small contribution from the carbonate fraction (9.6-10.4 μmol gdw^{-1} or ~12%) between 215 and 395 mm (Figure 6-4c_5, Figure E 6). On the eastern transect, poorly crystalline and crystalline Fe(III) oxide distributions were similar at both stations: The first 4 mm consisted mainly of poorly crystalline Fe(III) oxides (63.1 ± 2.0 and 58.5 ± 4.8 μmol gdw^{-1} at St. 15 and St. 12) (Figure 6-4d_5, e_5). Below the first section, poorly crystalline Fe(III) oxides constituted slightly more than half (58 ± 37% at St. 15 and 55 ± 15% at St. 12) of total solid Fe (Figure 6-4d_5,e_5, Figure E 6). On the other hand, differences in the carbonate fraction were evident along the eastern transect, where carbonate-bound Fe^{2+} concentrations increased from 2.4 ± 1.2 at the surface to 9.03 ± 2.6 μmol gdw^{-1} at depth at St. 15, whereas the carbonate fraction averaged 7.4 ± 1.5 μmol gdw^{-1} below the first 7 mm at St. 12 (Figure 6-4d_5,e_5).

At all stations, AVS concentrations were low in the top 3-10 mm of sediment, ranging from below detection limit to the highest value of 0.56 ± 0.05 μmol S gdw^{-1} at St. 11 (Figure 6-4a_6, b_6, c_6, d_6 and e_6). The highest AVS concentrations throughout the core were found in St. 2b, with a peak in concentration of 40.3 ± 1.7 μmol S gdw^{-1} at 42 mm, followed by the lowest concentration measured in the core of 5.3 ± 0.4 μmol S gdw^{-1} at 580 mm (Figure 6-4a_6). AVS concentrations at St. 13 were generally low but increased from 0.35 ± 0.12 μmol S gdw^{-1} at the surface to 5.6 ± 1.6 μmol S gdw^{-1} at the bottom of the core (525 mm) (Figure 6-4b_6). AVS concentrations were even much lower at Station 11, remaining below 1 μmol S gdw^{-1} throughout the core (Figure 6-4c_6). Along the eastern transect, AVS concentrations were also low at St. 15, with a maximum concentration of

2.7 ± 1.13 µmol S gdw^{-1} at 145 mm, whereas AVS concentrations were generally higher and ranged between 1.8 and 4.6 µmol S gdw^{-1} at St. 12, with a maximum concentration of 16.4 ± 7.0 µmol S gdw^{-1} at 105 mm (Figure 6-4d_6 and e_6).

6.5 Discussion

6.5.1 Carbon remineralization and main diagenetic pathways from the continental shelf to the slope

Although bottom waters were oxygenated, St. 2b, 13, 11, and 15 displayed lower percent saturations (44-48%) in comparison to those previously found (55-100%) in the same region during a similar season (Hu et al., 2011). Low oxygen saturation in the bottom waters could be caused by upwelling of O_2-depleted waters, respiration in the water column, or O_2 consumption by the sediments along with low vertical mixing rate due to limited winds or absence of storm events. As the surface area of the hypoxic zone during the present study was the largest ever recorded in the northern Gulf of Mexico (22,720 km^2) (Rabalais and Turner, 2017), it is likely that strong respiration in the water column and low vertical mixing conditions were responsible for the depleted O_2 levels in the overlying waters. The highest DOU rate was measured on the western transect and decreased from 13.8 mmol m^{-2} d^{-1} on the shelf (St. 2b) to 3.6 on the slope (St. 13) and 3.9 mmol m^{-2} d^{-1} at the bottom of the slope (St. 11) (Table 6-2). DOU rates along the eastern transect also decreased with distance from the shelf but were about 17 and 42% lower on the slope and bottom of the slope, respectively, than along the western transect (Table 6-2). These DOU rates are comparable to sediment community oxygen consumption (Rowe et al., 2008) and DOU rates measured at the deep stations along the continental shelf and

slope (Hu et al., 2011). In turn, DOU appears to vary seasonally on the shelf near St. 2b (Lehrter et al., 2012; Rowe et al., 2002). The higher DOU rates and compressed pH profile at St.2b are indicative of high carbon remineralization and re-oxidation in a thin sediment section near the SWI due to large labile organic carbon deposition from MARS (Table 6-2). The reactive transport model that optimized respiration rates to reproduce the experimental depth profiles (Figure 6-5 and Figure E 7- Figure E 10) confirms that aerobic respiration represents the main O_2 consumption process along these continental shelf and slope sediments and that the contribution of reduced metabolites reoxidation to O_2 removal is negligible at most station except at St. 13, where it reaches around 20% (Table 6-3). Except for St. 2b, where high Mn^{2+} fluxes were observed (-1,325 ± 70 μmol m^{-2} d^{-1}), Fe^{2+} and Mn^{2+} fluxes across the SWI were either absent (St. 11, St. 12) or low (-5.4 ± 0.2 μmol m^{-2} d^{-1} at St. 13, -191 ± 12 at St. 15) (Figure 6-3- Figure 6-4), suggesting most of the reduced metabolites produced during anaerobic respiration processes were buried under the form of sulfide or carbonate minerals (Figure 6-4). In contrast, DIC, NH_4^+, and even ΣPO_4^{3-} diffused across the SWI (Figure 6-4, Figure 6-6), demonstrating input of nutrients into the overlying waters that may help fuel new primary production (Figure 6-6). The trends in flux values indicate a decrease in overall anaerobic carbon remineralization rates from the shelf to the continental slope in agreement with respiration measurements in incubations of Louisiana shelf and slope sediments (Lin and Morse, 1991) and integrated carbon remineralization rates calculated with the reactive transport model (Table 6-3). Interestingly, the stations in the middle of the slope (i.e., St. 13 for the eastern transect and St. 15 for the western transect) also showed much lower DIC and NH_4^+ diffusive fluxes (Figure 6-6) and integrated carbon remineralization rates (Table 6-3) than the deepest

stations (i.e., St. 11 and St. 12), suggesting the accumulation of particulate material may be transient along the steepest part of the slope (

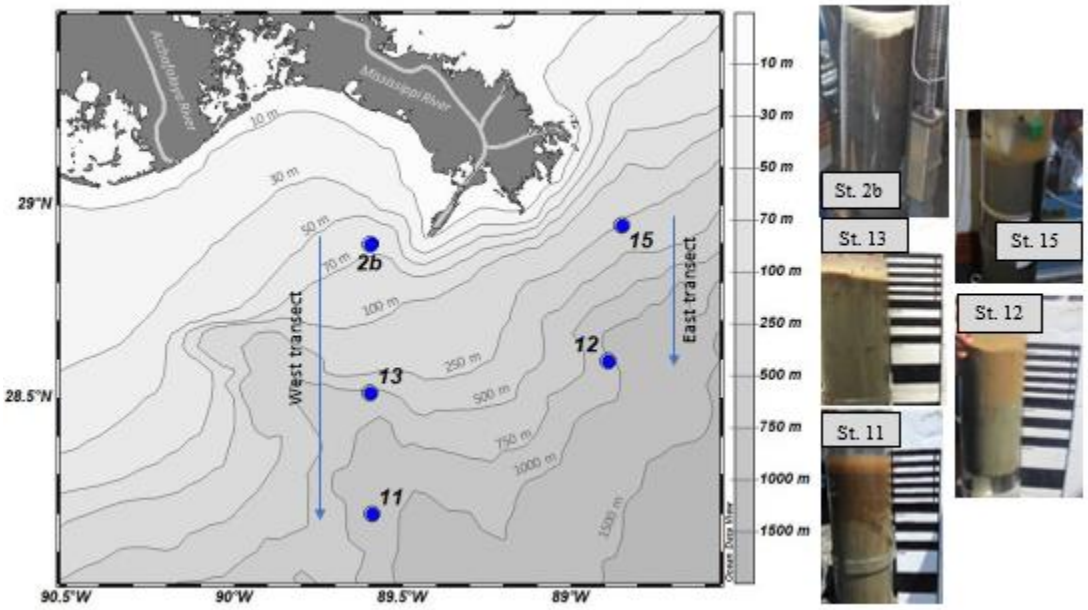

Figure 6-1). Differences between integrated carbon remineralization rates calculated with the model and the 7-50 lower DIC fluxes measured at the SWI may be explained by the significant precipitation of carbonate minerals in the sediment, including calcium-magnesium (not determined), iron (Figure 6-4a_4-e_4), and manganese (Figure 6-4a_5-e_5) carbonates.

Table 6-3: Percent O_2 consumption by reoxidation of reduced metabolites and relative importance of aerobic respiration, denitrification, Mn(III/IV) oxide reduction, Fe(III) oxide reduction, and sulfate reduction on carbon remineralization processes calculated by the MATSEDLAB reactive transport model at steady-state

Stat.	O_2 Consump. by Reduced	Aerobic Resp. (%)	Denitri. (%)	Mn red. (%)	Fe red. (%)	SO_4^{2-} red. (%)	Rate Cox (mmo

	Metabolites (%)						l m^{-2} d^{-1})
2b	1.9	11.5	15.4	6.7	4.9	61.5	171
13	21.2	15.6	25.0	24.8	6.0	28.6	36.4
11	0.1	63.8	15.3	10.2	0.4	10.3	49.7
15	0.3	72.2	19.1	3.1	5.3	0.3	19.3
12	3.7	16	6.3	1.3	0.1	76.3	107

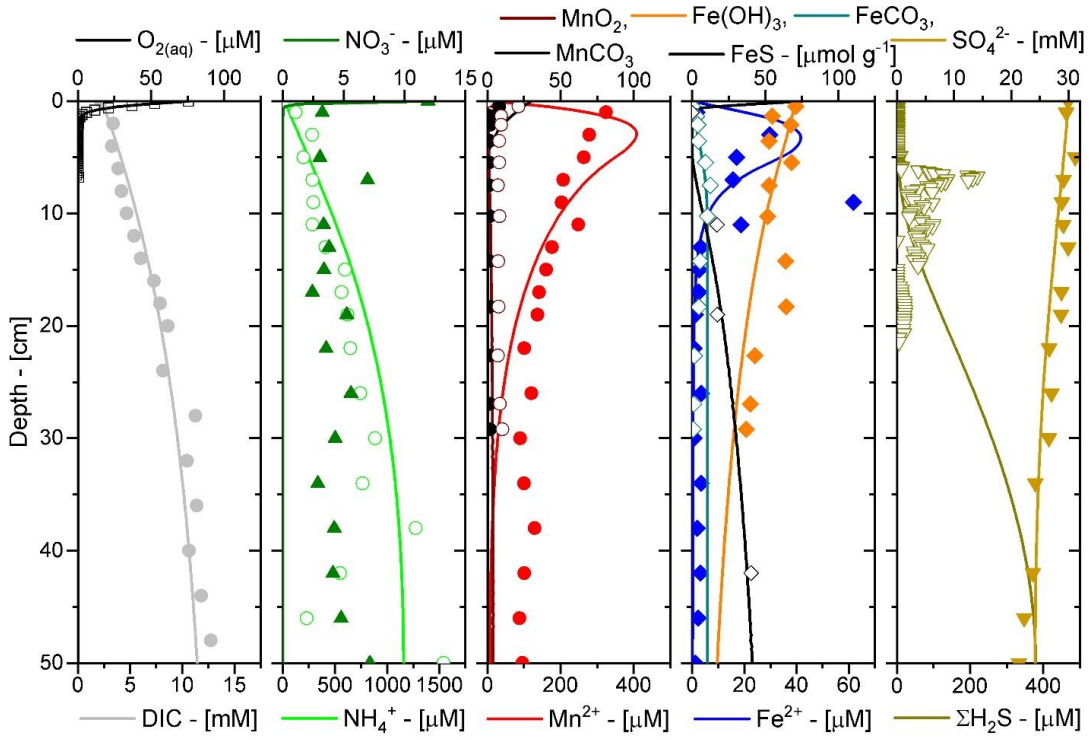

Figure 6-5: Example of modeled depth profiles of the main species involved in diagenetic processes at St. 2b (plain lines) compared to experimental depth profiles (scatter points). Only respiration rates (aerobic, denitrification, Mn reduction, Fe

reduction, and SO_4^{2-} reduction) were optimized to fit the experimental data at steady-state. Rate constants of abiotic processes and biological oxidation of NH_4^+, ΣH_2S, and Mn^{2+} by $O_{2(aq)}$ were fixed at each station.

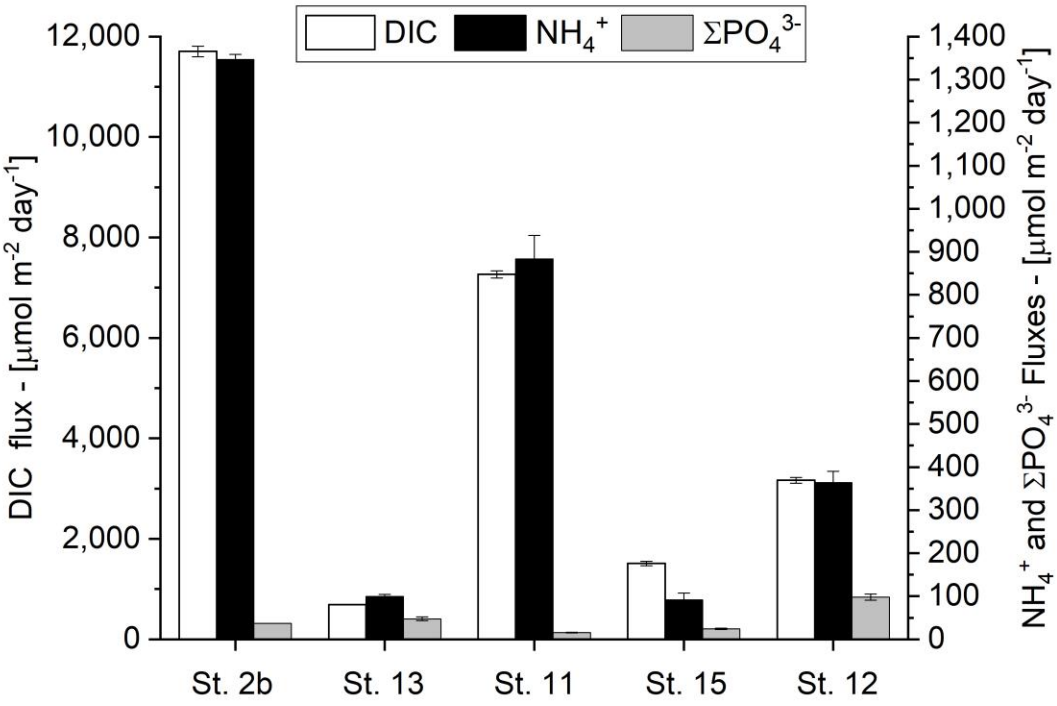

Figure 6-6 Diffusive fluxes of DIC, NH_4^+, ΣPO_4^{3-}, and SO_4^{2-} across the sediment-water interface. Error bars represent the standard deviation extrapolated from porosity.

The rapid decrease in NO_3^- concentrations below the SWI is attributed to high denitrification in Gulf of Mexico sediments (McCarthy et al., 2015). Denitrification plays

a significant role in the top 2 cm of sediment, suggesting its effect on carbon remineralization processes may be important. Indeed, the reactive transport model ran at steady-state reveals that denitrification constitutes between 6 and 25% of carbon remineralization rates and is more prominent in mid-slope sediments (St. 13 and St. 15) where bottom water NO_3^- concentrations are larger (Table 6-3). However, these calculations do not account for anaerobic nitrification processes that may explain the low, yet above detection limit, NO_3^- concentrations below the apparent denitrification zone (< 2 cm) which would enhance overall denitrification even more. In turn, multiple proxies suggest sulfate reduction is most active on the shelf of the western transect (St. 2b) and decreases in intensity with water depth. First, a significant decrease in sulfate concentrations on the shelf (St. 2b) and mid-slope (St. 13) that was not observed at the bottom of the slope (St. 11), and the detection of ΣH_2S at St. 2b only, provide evidence for sulfate reduction on the upper slope but not in deep sediments. Second, AVS was present throughout the sediment at St. 2b and deep in the sediment at St. 13, and the simultaneous detection of $FeS_{(aq)}$ at these stations indicates active precipitation of FeS (Beckler et al., 2016; Rickard and Luther, 1997; Theberge and Luther, 1997). In contrast, AVS was only observed in small concentrations and $FeS_{(aq)}$ was not detected at St. 11 (Figure 6-3). Finally, the low Mn(III/IV) oxide concentrations below 5 cm (St. 2b and 13), generally low $Fe(III)_d$ concentrations and org-Fe(III) current intensities below 10 cm (St. 2b) and 20 cm (St. 13), and decreasing Fe^{2+} concentrations with depth (St. 2b) by precipitation with ΣH_2S (Taillefert et al., 2000a) (Figure 6-3 and Figure 6-4) present additional evidence that sulfate reduction is most active in shelf and upper slope sediments of the western transect. Comparatively, $Fe(III)_d$ concentrations and org-Fe(III) current intensities were much lower

or below detection limit at St. 11, whereas Mn(III/IV) oxides and Fe^{2+} concentrations declined at deeper depths in the sediment, suggesting that sulfate reduction is much less significant deeper along the slope. In contrast to the western transect, sulfate reduction appears insignificant along the eastern transect mid-slope sediment (St. 15) as sulfate concentrations did not decrease significantly (Figure 6-4d_2), in agreement with previous studies on the Louisiana shelf (Zhuang et al. 2018) and slope (Lin and Morse, 1991). Neither $FeS_{(aq)}$ nor ΣH_2S were detected (Figure 6-3d), org-Fe(III) (Figure 6-3) and/or Fe^{3+} (Figure 6-4d_3) were observed at depth, and AVS concentrations were much lower (Figure 6-4d_6), in agreement with visual inspection of the cores which did not reveal any black $FeS_{(s)}$ in sediments at St. 15. In turn, sulfate reduction appeared much more important in the deep sediments of the eastern transect (St. 12). Although $FeS_{(aq)}$ and ΣH_2S (Figure 6-3e), indicative of active bacterial activity, were not detected, sulfate decreased noticeably in the first 12 cm (Figure 6-4e_2), $Fe(III)_d$ concentrations remained low, Fe^{2+} decreased deep in the sediment (Figure 6-4e_3), and AVS concentrations were much higher than in the mid-

slope sediments (Figure 6-4e$_6$) as corroborated by visual FeS patches at St. 12 (

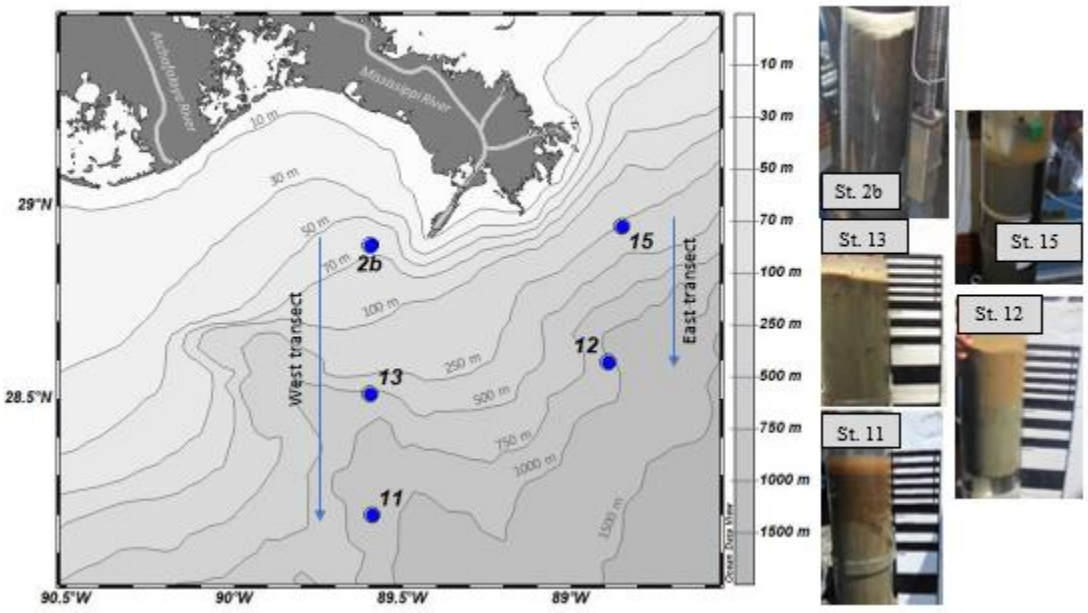

Figure 6-1). The reactive transport model confirms that the contribution of sulfate reduction to carbon remineralization rates (Table 6-3) is highest on the shelf of the western transect (62% at St. 2b) and decreases as water depth increases (28.6% at St. 13 and 10.3% at St. 11). These calculations also demonstrate that the contribution of sulfate reduction to carbon remineralization processes is low along the slope of the eastern transect (0.3% at St. 15) but much higher in the deep sediments (76.3% at St. 12).

Simultaneously, geochemical evidence suggests microbial Mn(III/IV) and Fe(III) oxide reduction are active in the surface sediments of St. 2b and 13 and relatively important across the sediment column at St. 11 and 15, but much less at St. 12 (Figure 6-3, Figure 6-4). The presence of org-Fe(III) and Fe(III)$_d$ indicates ΣH_2S was not produced significantly in the top 5 cm at St. 2b (Figure 6-3a and Figure 6-4c), top 15 cm at St. 13

(Figure 6-3b and Figure 6-4h), and across the profiles at St. 11 and 15 (Figure 6-3c and d, Figure 6-4c_3-d_3). The formation of org-Fe(III) at depths much deeper than oxygen penetration and the build-up of Fe^{2+} in the pore waters (Figure 6-4a_3-c_3 and e_3) before the decrease in sulfate concentration also suggests microbial $Fe(OH)_3$ reduction was active at depth in these sediments (Beckler et al., 2016; Taillefert et al., 2017). In turn, the absence of org-Fe(III), much lower $Fe(III)_d$ concentrations, and decrease in Fe^{2+} with depth below 80 mm at St. 12 suggest that sulfate reduction was more prominent at the deepest station of the eastern transect. Although the reactive transport model indicates that Mn(III/IV) oxide reduction contributes between 6.7 and 24.8% of carbon remineralization rates at St. 2b and 13 compared to 10.2% at St. 11 (Table 6-3), the contribution of microbial Fe(III) oxide reduction is much smaller at these stations (< 6% of carbon remineralization rates). These findings are explained by the shallow location of the sulfate reduction zone on the shelf at St. 2b (Figure 6-5), mid-slope at St. 13 (Figure E 7), and bottom of the slope at St. 11 (Figure E 8) that compresses the microbial metal reduction zone against the SWI and therefore favors microbial Mn(IV/III) reduction and abiotic Fe(III) oxides reduction by ΣH_2S with eventual precipitation of $MnCO_3$ and FeS minerals. Significant contributions of manganese reduction to carbon remineralization have also been quantified in the Canadian continental margin (Boudreau et al., 1998). The increase in pH in these sediments may be indicative of Mn reduction, whereas carbonate precipitation may cause the subsequent decrease in pH as observed and attributed to these processes previously (Luther et al., 1999). Along the eastern transect, microbial metal reduction rates are much lower, and the anaerobic respiration of carbon is mainly driven by denitrification (19.1% at St. 15 and 6.3% at St. 12) with minor contribution by microbial Mn(III/IV) oxide reduction (< 3%).

These findings are in agreement with the generally low sediment deposition rates predicted across the slope at this location (Xu et al., 2011).

6.5.2 Dissolved metal transport mechanism and enrichment of Mn(III/IV) oxides on the Louisiana Slope

The Mississippi River supplies a large load of particulate material during its high discharge period from the winter to early spring that is eventually deposited on the Louisiana shelf (Corbett et al., 2006; Corbett et al., 2004; Devereux et al., 2019). These sediments form mobile muds that are often remobilized by physical mixing generated by tidal currents or storms (Sampere et al., 2011). This process eventually sorts material by size, morphology, or composition (McKee et al., 2004), transports terrestrial organic carbon (Waterson and Canuel, 2008) and inorganic material (Trefry and Presley, 1982) to the deep sediment, and increase diagenetic reactivity by a priming effect (Bianchi, 2011). An enrichment of Mn(III/IV) oxides is observed at the sediment surface of St. 13 and more particularly St. 11, but not St. 2b, nor along the eastern transect (St. 15 and 12) where Mn(III/IV) concentrations remain low across the sediment (Figure 6-4a_4-e_4). The reactive Mn:Fe ratios (log of the ratio of Mn(IV)oxides to poorly crystalline Fe(III) oxides) in the top 5 cm of St. 13 and in the top 25 cm of St. 11 are far greater (log (Mn:Fe) ratio > -1.5) (Figure 6-7) than the Mn:Fe ratio obtained from the annual mass load of metals (128 $x10^3$ tons of Mn and 3934 $x10^3$ tons of Fe) from the MARS (Reiman et al., 2018), confirming previous reports of Mn enrichment in surface sediments in deep Gulf of Mexico sediments (Wade et al., 2008). In turn, the reactive Mn:Fe ratio is roughly conserved at St. 2b (Figure 6-7), likely due to the high sedimentation rate (> 2.5 cm yr^{-1}, Table 6-1) that constantly incorporates source material delivered by the Mississippi River, and is slightly lower than

the source material ratio at St. 15 and 12, likely due to the enhanced variability associated with the low Mn(III/IV) oxide concentrations along the eastern transect. Surface enrichment in Mn(III/IV) oxides is commonly reported in marine sediments along water depth gradients (Aller, 1994; Law et al., 2009; Mouret et al., 2009; Sundby et al., 1981; Trefry and Presley, 1982) and attributed to the diffusive flux of Mn^{2+} formed at depth in reduced conditions to the oxic zone and eventual heterogeneous reoxidation by oxygen (Sundby and Silverberg, 1985; Trefry and Presley, 1982). In the shelf and mid-slope sediments of the western transect (St. 2b and St. 13), microbial Mn(IV/III) reduction and reduction of Mn(IV) oxides by ΣH_2S generate a high upward flux of Mn^{2+} to the sediment surface (Figure 6-4a_3-b_3), even though a significant fraction of Mn^{2+} is immobilized under the form of carbonate minerals (Figure 6-4a_4-b_4 and Figure E 6). Mn^{2+} oxidation rates are enhanced by bioirrigation which increases the penetration of dissolved oxygen into the sediment (Aller and Aller, 1998) and decreased by the precipitation of $MnCO_3$ minerals in pore waters (Duckworth and Martin, 2004). Evidence of bioturbation exists in the oxygen profile at St. 15, where a pocket of oxygen was detected below the OPD (Figure 6-2) and has been documented in the vicinity of the slope stations (Xu et al., 2014). Low adsorbed Mn^{2+} concentrations were observed at depth in cores along both transects (Figure 6-4a_4-e_4, Figure E 6). Additionally, adsorbed Mn^{2+} was absent in the surface sediments, likely due to enhanced Mn^{2+} oxidation in the oxic zone by surface catalyzed reactions on Fe(III), Al, and Si oxide surfaces (Davies and Morgan, 1989; Lan et al., 2017). As the abiotic oxidation of Mn^{2+} by dissolved oxygen is slow in sediments, Mn(III/IV) oxides are not recycled efficiently (Richard et al., 2013). Compounded by the low dissolved O_2 concentrations of the overlying waters (Table 6-1), Mn_d is able to reach the bottom waters, where it is

removed by particle adsorption (Trefry and Presley, 1982), oxidized heterogeneously (Davies and Morgan, 1989), then eventually transported by mobile muds and deposited in continental slope sediments (St. 11), generating a Mn 'conveyor belt' from the shelf to the bottom of the slope. Although the upward diffusive flux of Mn^{2+} was not significantly lower at this station (136 ± 10 µmol m^{-2} d^{-1}) than the mid-slope sediment (172 ± 17 µmole m^{-2} d^{-1} at St. 13), the enhanced thickness of the Mn^{2+} oxidation zone, as evidenced by the deeper OPD, pH minimum (Figure 6-2), and position of the dissolved Mn peak (Figure 6-4b_3-c_3), likely prevented Mn^{2+} to reach the SWI (Figure 6-4c_3).

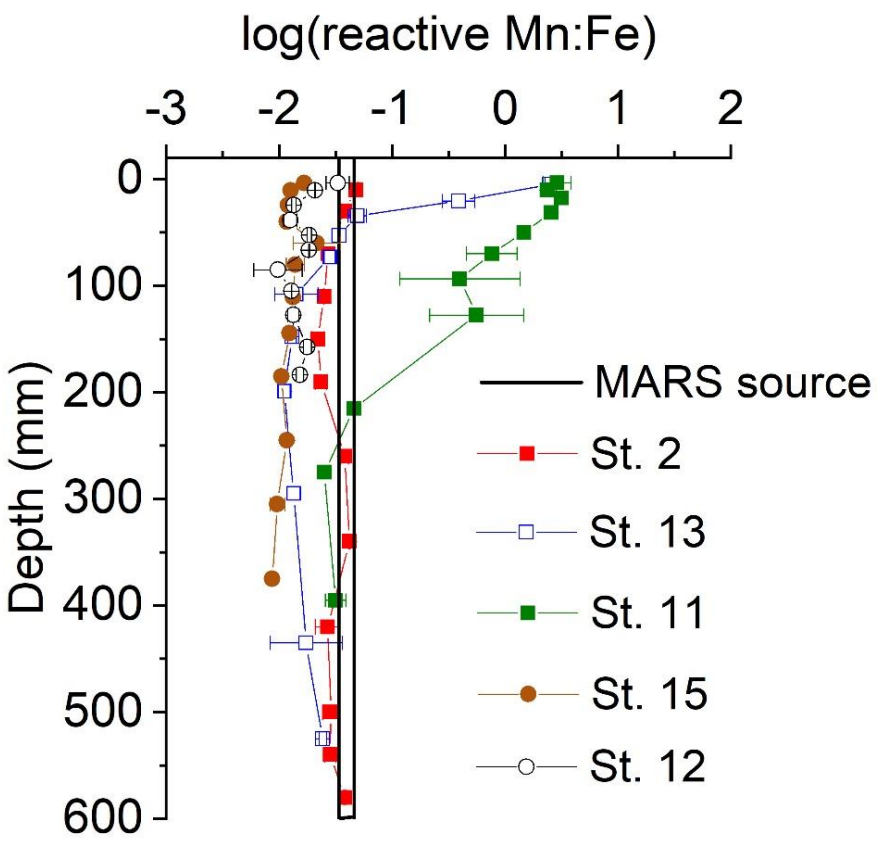

Figure 6-7 Depth profiles of total solid Mn to Fe ratios (logarithmic scale) at St. 2 (red), St. 13 (blue), and St. 11 (green) along the western transect. The source of Mn and Fe in the particulate phase from the Mississippi Atchafalaya River System (MARS) is indicated by the box (Trefry and Presley, 1982; Reiman et al. 2018).

6.5.3 Differential Iron and Mn Cycling

The pore water and solid phase speciation of Mn and Fe as a function of depth in these sediments is consistent with the predictions of the thermodynamic redox ladder regarding the dynamics of Fe and Mn redox cycling (Froelich et al., 1979). Whereas Mn^{2+} concentrations were greater than Fe^{2+} in most sediment pore waters studied, the inverse is true in the solid phase (Figure 6-4), except for a few depths near the sediment surface at St. 11 where Mn(III/IV) oxides were enriched relative to Fe(III) oxides (Figure 6-4c_4-c_5). Abiotic and biotic Mn(III/IV) oxides reduction are typically faster than Fe(III) oxide reduction (Arnold et al., 1988; Dollhopf et al., 2000; Larsen et al., 1998; Lovley and Phillips, 1988; Myers and Nealson, 1988), while Mn^{2+} oxidation is much slower than Fe^{2+} oxidation (Stumm and Morgan, 1996). The large abundance of poorly crystalline (51 ± 21 μmol gdw^{-1}) and crystalline Fe(III) oxides (46 ± 45 μmol gdw^{-1}) throughout each profile, representing about 94 ± 5% of total solid Fe in these sediments (Figure E 6) and the low AVS concentrations in all sediments except St. 2b and the deep layers of St. 13 (Figure 6-4a_6-e_6) suggest that these sediments have been exposed to dissolved oxygen during resuspension as mobile muds prior to eventual deposition and accumulation. In contrast to Mn^{2+}, however, Fe^{2+} is mostly retained in the sediment either by oxidation near the SWI or precipitation under the form of carbonate or sulfide minerals.

The data collected in this study immediately at the end of the high discharge period confirm that sedimentary material is transported all the way to the bottom of the slope (St. 11) during the high discharge period and preferentially enriched in Mn(III/IV) oxides relative to the input material from the MARS. Whereas Mn(III/IV) oxide reduction was active in these sediments, the reduction of Fe(III) oxides was apparently not significant

(i.e., low Fe^{2+}, $FeCO_3$ minerals, and $FeS_{(s)}$), providing evidence for the differential kinetics of microbial Mn and Fe reduction in a natural setting. The reactive transport model confirms these findings by demonstrating that metal respiration processes on the slope during that time period were mainly controlled by microbial Mn reduction and not microbial Fe reduction (Table 6-3). As suggested by thermodynamic calculations (SI section 1, Figure E 11), microbial Fe(III) oxide reduction likely dominates after depletion of the Mn(IV) oxides, which would explain the high concentrations of reduced Fe^{2+} previously observed near St. 12 (Beckler et al., 2016). However, it is not clear whether the stock of Fe(III) oxides is large enough to prevent sulfate reduction from dominating anaerobic respiration processes during the rest of the summer and fall. The enhanced production of carbonates under sulfate reducing conditions should at least shut down the Mn conveyor belt and efficiently bury this important terminal electron acceptor at the end of the high discharge period. Overall, these findings indicate continental slope sediments exposed to large riverine inputs are highly dynamic systems that may remineralize natural organic matter using different terminal electron accepting processes depending on riverine discharge intensity.

6.5.4 Conclusions

The main redox processes involved in the transformation of natural organic matter in RiOMars sediments were investigated along two transects in the northern Gulf of Mexico to examine the effect of particulate material inputs from the Mississippi River plume on diagenetic processes after a high riverine discharge period. Results suggest organic carbon deposition control the extent of anaerobic carbon remineralization processes and select the dominant anaerobic carbon remineralization pathways. Although

sulfate reduction is significant at the shelf station (65 m water depth), microbial Mn reduction appears to represent the dominant anaerobic respiration process along the continental slope closest to the Mississippi River plume whereas iron mainly remains under the form of Fe(III) oxides and does not play a major role in carbon remineralization. These findings suggest the differential kinetics of Mn and Fe redox transformations coupled with the high discharge of the Mississippi River during the winter and spring influence carbon remineralization processes on the continental slope. The fast Fe^{2+} oxygenation kinetics near the sediment-water interface and high sedimentation rates maintain iron under the form of Fe(III) oxides and prevent sulfate reduction from being significant, whereas the much slower kinetics of oxygenic oxidation allows diffusion of Mn^{2+} across the sediment-water interface. Exposure to bottom water oxygen and mobile muds typical of deltaic sediments during high riverine discharge likely promote the formation and downslope transport of Mn(III/IV) oxides, forming a Mn 'conveyor belt' that selectively enriches Mn(III/IV) oxides relative to Fe(III) oxides in the deep slope sediment compared to the source material from the river. Although it is not clear whether the stock of Fe(III) oxides is large enough to prevent sulfate reduction from dominating anaerobic respiration processes over time, the enhanced production of carbonates under sulfate reducing conditions should at least shut down the Mn conveyor belt and efficiently bury this important terminal electron acceptor during the low riverine discharge period. In contrast, the strength of carbon remineralization processes along the eastern continental slope the farthest from the Mississippi River plume is much lower due to the low organic and lithogenic inputs, and denitrification dominates anaerobic respiration. Overall, these findings suggest Mn cycling in continental slope sediments exposed to large riverine inputs may be more important than

previously considered, and carbon remineralization via Mn reduction could contribute significantly to benthic DIC and alkalinity production.

6.5.5 Acknowledgements

We would like to thank the captain and crew of the RV Savannah as well as Emily Buckley, Julien Richirt, and Andrew Stancil for help with the collection and/or analysis of samples. This research was supported by the National Science Foundation (OCE-1438648) to M. Taillefert, EC2CO-DRIL MissRhoDia project to C. Rabouille, National Academies of Science, Engineering, and Medicine Gulf Research Program (Early Career Grant 2000007281) to J. Beckler, and the Chateaubriand Fellowship of the Office for Science & Technology of the Embassy of France in the United States awarded to S. Owings.

CHAPTER 7. CONCLUSIONS

Manganese oxides are important oxidants in the environment and play an important role in the global biogeochemical cycling of elements, including metal contaminants and carbon. In this dissertation, the mechanism of abiotic As(III) oxidation by manganese oxides was characterized in a thorough kinetic study, and the effect of As(V) concentrations on metal reducing microorganisms was investigated to examine the complexity involved in As(V) toxicity in natural sediments. In parallel studies, the role of manganese oxides on the biogeochemical cycling of carbon in marine sediments that receive large terrigenous inputs from a large river was determined using a combination of state-of-the-art manganese speciation measurements and diagenetic modeling.

In Chapter 3, the kinetics of As(III) oxidation by manganese oxides was systematically quantified and compared to existing literature to explore the reaction mechanism and the effect of pH on the reaction. The initial concentrations of As(III) and effective surface sites of MnO_2 were the main variables affecting the rate of reaction while pH did not vary the rate of the reaction in the conditions studied. Given the high rate of these reactions, a two-electron transfer reaction may be likely, especially if vacancy sites are available to catalyze the electron transfer. Two steps of one-electron transfer, however, may be possible although it is likely that both Mn(IV) and Mn(III) species are ultimately reduced to produce Mn^{2+}. As Mn(IV) oxides are the most efficient oxidants of As(III), the findings of this study have important environmental implications. First, the second order rate law developed in this study should be able to predict the fate of As(III) in a variety of geochemical conditions with different Mn(IV) minerals, including biogenic manganese

oxides which are most prevalent in sedimentary environments. Second, As(III) introduced to a Mn(IV)-rich sedimentary environment should be efficiently oxidized to the less toxic and less mobile As(V), although at Mn:As molar ratios below 60, the overall adsorption of As(V) may be controlled by the concentration of the Mn^{2+} product or any other divalent cation in solution. Finally, the mobility of As(III) may be enhanced in the presence of more crystalline MnO_2 phases or large As(III) concentrations which decrease the rate of As(III) oxidation.

In Chapter 4, results from the abiotic study of As(III) oxidation by MnO_2 were expanded to determine the effect of As(V) on anaerobic microbial respiration by two strains of the model metal-reducing bacteria *Shewanella* that have the ability to reduce or methylate As(V) through either detoxification or respiration pathways. These studies demonstrated that As(V) intracellular uptake is associated with inorganic phosphate uptake systems and that As(V) toxicity results in the production of As(III) by a mechanism that has yet to be completely identified. In addition, these studies demonstrated that cells exposed to As(V) respond to this stress by increasing anaerobic respiration rates, likely to compensate for the energy spent for detoxification. In the presence of iron oxides as terminal electron acceptor, cells tolerate high As(V) concentrations as As(V) is rapidly adsorbed to the mineral surface. In contrast, As(V) stress is exacerbated with nitrate as terminal electron acceptor, demonstrating that the toxicity of As(V) is only efficient when As(V) is in solution. Finally, the fast reoxidation of As(V) in experiments conducted with manganese oxides as terminal electron acceptor appears to increase cell susceptibility to As(V). Interestingly, the toxicity effect of As(V) on *Shewanella* species appears reversible, as respiration rates recovered after a lag phase that coincided with the As(V) reduction

process. Although these studies were conducted in the laboratory, they have important environmental implications. Freshwater environments typically display low dissolved inorganic phosphate concentrations, suggesting that microorganisms may experience higher As(V) toxicity than previously considered. The simultaneous presence of both iron and manganese oxides may also amplify the toxicity effect of As(V) on microbial communities, as As(V) detoxified by reduction may be recycled efficiently by manganese oxides, in a catalytic cycle that could be detrimental to microbial communities. Finally, if metal reduction is enhanced as a result of this complex interplay additional contaminants absorbed to the mineral surfaces maybe be released into solution (Stuckey et al., 2016; Wielinga et al., 2000). Thus, arsenic in sedimentary environments is not simply immobilized by adsorption. Instead, a suite of complex abiotic and microbial processes including adsorption, intracellular uptake, and redox reactions may affect the transport of arsenic in the environment and ultimately the quality of drinking water resources. Furthermore, cryptic cycles involving manganese oxides may be underestimated in the environment as, for example, the recently characterized fungal-mediated cryptic selenium cycle involving the bioreduction of Se(VI) and eventual abiotic reoxidation of Se(IV) by manganese oxides (Rosenfeld et al., 2020).

In Chapters 5 and 6, the focus of this dissertation changed to investigating manganese redox cycling in marine sediments. Sediments were collected across the hypoxic shelf and oxygenated continental slope in the northern Gulf of Mexico during the summer of 2016 and 2017 to understand how inputs from the Mississippi River influence sediment diagenesis. Geochemical results from the 2016 expedition indicated that shelf sediments were dominated by sulfate reduction (i.e., dissolved H_2S or FeS_{aq} proxies for iron sulfide

mineral precipitation and low dissolved nutrients), whereas slope sediments were characteristic of nitrate- and metal-reducing conditions with strong nitrate gradients below the sediment-water interface and high dissolved manganese, but relatively low dissolved iron concentrations. In parallel, and molecular microbial markers (16S rRNA) revealed that dissolved inorganic carbon, orthophosphate, and sulfide concentrations were the main drivers in shaping the microbial communities across the shelf communities, while NO_3^- appeared more important in shaping microbial communities along the slope (p-value ≤ 0.01). Although geochemical indicators for sulfur cycling were not evident along the slope, microbial evidence suggests a cryptic sulfur cycle is established in these sediments based on the presence of both sulfate reducing and sulfide oxidizing bacteria. In 2017, sediments collected along two transects across the continental slope near the Mississippi River delta demonstrated that sulfate reduction was significant on the shelf near the Mississippi delta (65 m water depth). In turn, microbial Mn reduction represented the dominant anaerobic respiration process along the continental slope closest to the Mississippi River plume whereas iron mainly remained under the form of Fe(III) oxides and did not play a major role in carbon remineralization processes. The fast kinetics of Fe^{2+} oxygenation near the sediment-water interface and high sedimentation across the continental slope appears to maintain Fe under the form of Fe(III) oxides and thermodynamically prevent sulfate reduction from dominating carbon remineralization processes on the slope, whereas the much slower Mn^{2+} oxygenation kinetics allows diffusion of Mn^{2+} across the sediment-water interface. Exposure to oxygenated bottom waters and entrainment within mobile muds typical of deltaic sediments during high riverine discharge likely promote the formation and downslope transport of Mn(III/IV) oxides forming a manganese ‘conveyor

belt' that selectively enriches Mn(III/IV) oxides relative to Fe(III) oxides in the sediment compared to the source material from the river. The differential oxidation kinetics of Mn^{2+} and Fe^{2+} as well as transport of Mn(III/IV) oxides allows for Mn(III/IV) reduction to dominate over iron and sulfate reduction on the continental slope and canyon. Overall, these findings suggest Mn cycling in continental slope sediments exposed to large riverine inputs may be more important than previously considered, and carbon remineralization via Mn reduction could contribute significantly to benthic DIC and alkalinity production.

7.1 Recommendations for future work

The microbial incubations conducted in this study (Chapter 4) were amended using one terminal electron acceptor at a time. Eventually, a mix of electron acceptors should be used in the incubations to more accurately represent, model and track the fate of arsenic in conditions that resemble natural environments. This is especially important considering the possible interplay between iron and manganese reduction in the presence of arsenic. This study revealed the oxidation state of arsenic was important to describe the impact of arsenic on microbial functions. Arsenic speciation using voltammetric techniques was a time-consuming analysis to conduct and assumes that the speciation of arsenic is dominated by arsenate and arsenite. Now that a HPLC-ICP-MS method has been developed in our laboratory, a more efficient and complete analysis of inorganic and organic arsenic speciation may provide more insights into some of these processes. For future experiments it is recommended that complete speciation is measured for each sample. Furthermore, it is recommended that total arsenic be measured as well as arsenic found in all phases including the solid, adsorbed, and dissolved phases to elucidate the fate and transport of As. The experimental conditions of this study used pure strains of bacteria, therefore,

As(V) amendments to these systems were higher than concentrations found in the environment. In future work, lower As(V) concentrations should be used to more accurately reflect As concentrations in the environment. After incubations are complete it would be insightful to compare data to model simulations of As in the environment to validate our understanding of these processes. Results from experimental and theoretical work could have far reaching implications including influencing policies related to the management of coal fly ash ponds which are known sources of As and other contaminants to waterways, including the Chattahoochee River in Georgia.

In order to create a full picture of sediment biogeochemistry from the existing parameters quantified in this study, it would be powerful to measure organic carbon concentrations and characterize the organic source material to understand the composition of carbon in these distinct regions of the Gulf of Mexico. In particular, it would be interesting to determine whether carbon sources to this region are of terrestrial or marine origin, and how the partitioning of available carbon changes with sediment depth. Sedimentation rates should be investigated using multiple isotope tracers including ^{210}Pb, ^{137}Cs, ^{7}Be and ^{234}Th (Corbett et al., 2004). Currently the benthic fluxes (measured) and carbon oxidation rates (calculated using MATSEDLAB) contain discrepancies although the values should match. In order to compare these values to a better degree of accuracy it would be beneficial to measure rates of sulfate reduction using sediment incubations (Devereux et al., 2015). The evidence of cryptic sulfur cycling could be further investigated and parameterized by quantifying elemental sulfur (S0) as well in these sediments. Bioturbation may also play a role in benthic fluxes by bringing DIC to the sediment water interface and should, therefore, be investigated using three dimensional imaging techniques

(Devereux et al., 2019). Currently, studies exist to quantify these parameters in surface sediments, however, it would be insightful to understand how the seasonal contributions of inputs from the Mississippi influence or do not influence the stratification of sediment layers. Finally, it would be important to study the role of sediments in shaping the geochemistry of the overlying water column by studying in situ benthic fluxes of metals, nutrients, and alkalinity in these regions.

APPENDIX A. SUPPLEMENTAL INFORMATION FOR CHAPTER 2

A1. MATLAB Porphyrin speciation code

A.1.1 BeginMnpor.m

This is the gui that begins the user-interaction for 'Mnporphyrin'. It calls 'getporphyrinfile.m' from the pushdone button ("Done")

```
clear all
close all
clc

%GUI COLORS
global bcolor           %button color
bcolor = [.64 .7 .7];
global activbcolor;     % active button color
activbcolor = [0.722 0.733 0.671];%.9 .8 .7];
global backcolor        %backgrd color
backcolor = [0 0 0];
global axcolor%axes color
axcolor = [0.66274509803922   0.73725490196078   0.43921568627451];
global textcolor   %Color for text messages
textcolor = [1 1 1];
global noisecolor%  Line color for plots of noise (raw data)
noisecolor = [.5 .5 .5];
global smoothcolor;%Line color for plots of smooth data
smoothcolor = [.5 .2 .2];
%global filenames;
scrsize = get(0,'Screensize');
global specialbuttoncolor;
specialbuttoncolor = [ 0.75294117647059   0.75294117647059
0.75294117647059];
global typecalc

typecalc = [];
beginfig = figure(1);
coordplot = zeros(2,1);
set(beginfig,'MenuBar','figure','NumberTitle','off','Color',[0 0
0],'Position',[(scrsize(3)/10) (scrsize(4)/6) (scrsize(3)*4/5)
(scrsize(4)*2/3)]);
choice =
uicontrol(gcf,'Tag','choice','Style','Text','Units','normalized','Posit
ion',[.209 .762 .145
.045],'BackGroundColor',[0,0,0],'ForeGroundColor',[1 1
1],'String','Smoothing Average');
smoothing =
uicontrol(gcf,'Style','popupmenu','Units','normalized','Position',[.209
```

```
.739 .145
.034],'String','3|5|7|9|11|13|15|17|19|21|23|25|27|29','Tag','sman','Va
lue',6);
%
% Pulling files from directory listing (dir) that are not .m and
displaying them
% so that user may choose files to run through voltint.
d = dir;
files = {d.name};
files = shiftdim(cellstr(sortrows(char(files{:}))),1);
files = char(files);
f = zeros(size(files,1));
for   i = 1: size(files);
    i = i';
    f(i) = isempty((findstr(files(i,:),'.m')));
end
f = find(f);
files = files(f,:);
for i = 1: size(files);                % Updated by MT on 4/6/16
    f(i) = isempty((findstr(files(i,:),'.txt')));  % to avoid text
files
end
% f = find(f);
% files = files(f,:);
% for i = 1: size(files);
%     f(i) = isempty((findstr(files(i,:),'.csv')));  % to avoid files
from ISEAIV
% end
% f = find(f);
% files = files(f,:);
% for i = 1: size(files);
%     f(i) = isempty((findstr(files(i,:),'.xml')));  % to avoid files
from ISLC
% end
% f = find(f);
% files = files(f,:);
% for i = 1: size(files);
%     f(i) = isempty((findstr(files(i,:),'.XML')));  % to avoid files
from ISLC
% end
f = find(f);
files = files(f,:);                    % End of update
files = cellstr(files);

pushdone =
uicontrol(gcf,'Style','pushbutton','Units','normalized','Position',[.62
5 .295 .08
.056],'String','OK','BackgroundColor',bcolor,'Callback','getporphyrinfi
le','Enable','off');
listchoice =
uicontrol(gcf,'Style','listbox','Units','normalized','Position',[.522
.4 .3
.45],'String',files,'Max',10,'Tag','listchoice','CallBack','set(pushdon
e,''Enable'',''on'')');
askuser1 =
uicontrol(gcf,'Style','checkbox','Units','normalized','Position',[.743
0.951 0.161
```

```
0.024],'String','hello','BackgroundColor',backcolor,'ForegroundColor',[
1 1 1],'Tag','askuser1','CallBack','uiresume');
askuser2 =
uicontrol(gcf,'Style','checkbox','Units','normalized','Position',[.743
0.921 0.161
0.024],'String','hello','BackgroundColor',backcolor,'ForegroundColor',[
1 1 1],'Tag','askuser2','CallBack','uiresume');
askuser3 =
uicontrol(gcf,'Style','checkbox','Units','normalized','Position',[.743
0.891 0.161
0.024],'String','hello','BackgroundColor',backcolor,'ForegroundColor',[
1 1 1],'Tag','askuser3','CallBack','uiresume');
askusertext1 = findobj('Tag','askuser1');
set(askusertext1,'Enable','on');
askusertext2 = findobj('Tag','askuser2');
askusertext3 = findobj('Tag','askuser3');
set(askusertext1,'Visible','on','String','Calibration','Value',0,'Enabl
e','on','Callback','uiresume;typecalc =
1;set(askusertext1,''Enable'',''inactive'');set(askusertext2,''Enable''
,''inactive'');set(askusertext3,''Enable'',''inactive'')');%calibration
will be called from here
set(askusertext2,'Visible','on','String','Mn Speciation 3-
param','Value',0,'Enable','on','Callback','uiresume;typecalc =
2;set(askusertext2,''Enable'',''inactive'');set(askusertext1,''Enable''
,''inactive'');set(askusertext3,''Enable'',''inactive'')');%Mn
speciation with 4-parameters will be called from here
set(askusertext3,'Visible','on','String','Mn Speciation 4-
param','Value',0,'Enable','on','Callback','uiresume;typecalc =
3;set(askusertext3,''Enable'',''inactive'');set(askusertext1,''Enable''
,''inactive'');set(askusertext2,''Enable'',''inactive'')');%Mn
speciation with 3-parameters will be called from here
uiwait
```

A.1.2 Getporphyrinfile.m

'Getporphyrinfile.m' is a script that intercepts the name of the file chosen by the user. It then launches 'Mnporphyrin.m' 'getporphyrinfile.m' is called by the callback of the "Done" button created by 'Introgui.m'

```
global filenames;

a = findobj('Tag','listchoice');
filechoice = get(a,'Value');
filename = (files(filechoice));% This is a cell array of the filenames
(chosen by the user).

for i = 1: length(filename),
   filenames(i).name =  filename{i};% Accesses the contents of the
```

```
   %cells in filename and converts each to strings which it then
   %stores in a structure:  filenames(i)
end
filenames.name;

%y = 1;
%Launch Integration routine:
Mnporphyrin;
```

A.1.3 Mnporphyrin.m

This program fits the concentrations of Mn(II) and Mn(III) as well as their rate constant of complexation from the total Manganese data measured by the porphyrin method of Madison et al. 2011

```
tic
format long
extplot = 0;

%figure and button colors:
global backcolor specialbuttoncolor axcolor textcolor;
global filenames typecalc
global Mn20
global k1

skipp = 0;
nothing = 0;
clear filename;
%
% Read the names of the input files called by BeginMnpor.m
%
a = struct2cell(filenames);
a = char(a);
bb = size(a);
gw = findstr('.',a(1,:));          % Finds at which index (left to
right) the dot is.
if max(bb) > 12
    filenumstr = a(:,[gw-1:gw]);   % The file numbers are >9
else
    filenumstr = a(:,gw-1);        % The file numbers are < 10
end
filenum = str2num(filenumstr);     % Now they are numbers
%
% Creating figure for plotting:
%
fig2 = figure(2);
```

```
theplot = axes;
set(theplot,'Position',[0.103 0.085 0.799
0.800],'Color',axcolor,'Xcolor',[1 1 1],'Ycolor',[1 1 1]);
set(fig2,'MenuBar','none','NumberTitle','off','Color',backcolor);
informtext =
uicontrol(gcf,'Style','text','Units','normalized','Position',[0.089
.905 0.536
0.06],'FontSize',14,'Visible','off','String','','BackGroundColor',backc
olor,'ForegroundColor',textcolor,'Tag','informtext');
informbox1 =
uicontrol(gcf,'Style','checkbox','Units','normalized','Position',[0.636
.951 0.088
0.024],'Visible','off','String','','BackGroundColor',backcolor,'Foregro
undColor',[1 1 1],'Tag','informbox1');
informbox2 =
uicontrol(gcf,'Style','checkbox','Visible','off','Units','normalized','
Position',[0.636 .912 0.088
0.024],'String','','BackGroundColor',backcolor,'ForegroundColor',[1 1
1],'Tag','informbox2');
ok =
uicontrol(gcf,'Style','Pushbutton','Visible','off','Enable','off');
exxit =
uicontrol(gcf,'Style','Pushbutton','Visible','on','Units','normalized',
'Position',[.913 .100 0.08
0.056],'String','EXIT','BackgroundColor',specialbuttoncolor,'Foreground
Color',[0 0 1],'Tag','exxit','Callback','terminate =
1;uiclearmode(gcf);uiresume');
%
% The smoothing average number entered by the user (from the gui) is
used
% to smooth the data
%
smaverage = findobj('Tag','sman');
n = get(smaverage,'Value');
nstring = get(smaverage,'String');
n = str2num(nstring(n,:));
close(figure(1))
%
% If a calibration is requested
%
if typecalc == 1;      % calibration is requested
    Abstot = [];
    for m = 1:length(filenames)
        set(ok,'Visible','off','Enable','off');
        set(exxit,'Enable','on');
       %
       % Read the data through the file line
       %
        file = filenames(m).name;
        [D,S] = xlsread(file);
        data = cellfun(@(x)str2double(regexp(x, ',', 'split')),
S(9:end), 'Uni',0);
        data1 = cell2mat(data);
       %
       % Determine the maximum total Mn concentration of each file and
store in a matrix
       %
```

```
        dF = gradient(data1(:,2));      % gradient of the absorbance
data
        maxAbstot = mean(data1(dF<0.001,2));
        sdAbstot = std(data1(dF<0.001,2));
       %
       % plot the findings
       %
        figure(2);
        plot1 = plot(data1(:,1),data1(:,2),'o');                        %
Rawdata
        set(plot1,'Color',noisecolor);
        hold on
        plotx=plot(data1(:,1),maxAbstot*ones(length(data1),1),'b');
% Total data
        set(plotx,'Color',smoothcolor,'LineWidth',1);
        xlabel('time - [min]'); ylabel('Absorbance');
       %
       % Store the data and the max absorbance of each standard curve
into a matrix to determine slope of calibration
       %
        eval(['data' num2str(m) '= data1;']);
        Abstot = [Abstot;maxAbstot];
    end
    uiwait
    close(figure(2))
   %
   % Ask the user to provide the concentrations of each Mn standard
   %
    for i = 1:length(filenames)
        Mnstd(i,1) = input('What is the concentration of the Mn
standards used (in the order of the file numbers)');
    end
   %
   % Calculate the slope and standard deviation of the slope after
subtracting
   % the blank values to all standards and plot the calibration curve
   %
    Absblk = Abstot(1);
    Abstot = Abstot - Absblk;
% Subtract the blank from the standards
    LM = fitlm(Mnstd,Abstot,'intercept', false);
% Calculate the linear regression to the data
    LMdata = [Absblk LM.Coefficients.Estimate LM.Coefficients.SE];  %
Store the blank absorbance, slope and standard deviation in a matrix
    disp(LM)
    figure(2)
    plot(LM)
    title('Calibration Curve for Total Mn')
    xlabel('Mntot - [uM]')
    ylabel('Absorbance')
   %
   % k1 is determined from calibration data with Mn(II) standards in
case the user wants to run
   % a 3-parameters optimization of the Mn speciation
   %
    k1all = [];
    for i = 1:length(Mnstd)
```

```
        Mn20 = Mnstd(i);                    % Initial concentration of
standard is known
       %
       % Calculate the concentration of total dissolved Mn from
absorbance values after subtracting the initial
       % absorbance (t = 0) using the slope calculated above
       %
        eval(['Mnexp = (data' num2str(i) '(:,2) -
LMdata(1))/LMdata(2);']);  % LMdata(1) = blank absorbance; LMdata(2) =
slope of the calibration
       %
       % Smooth the data. n points are used to calculate each averaged
result. The smoothed value at index i is
       % the average of the data points in the interval [l -(n-1)/2,
l+(n-1)/2], inclusive.
       %
        if exist('smooth','file')==2
        eval(['t = data' num2str(i) '(:,1);']);
        ts = smooth(t,n,'sgolay');
        Mnexps = smooth(Mnexp,n,'sgolay');
        else
            for l= 1:n:length(t)-n;
                if exist('ts')==0
                    ts = mean(t([l:l+(n-1)]));
                elseif exist('ts')==1 && isempty(ts) == 1,
                    ts = mean(t([l:l+(n-1)]));
                else
                    ts = [ts;mean(t([l:l+(n-1)]))];
                end
%                if exist('Mnexps')==0
                    Mnexps = mean(Mnexp([l:l+(n-1)]));
%                else
%                    Mnexps = [Mnexps;mean(Mnexp([l:l+(n-1)]))];
%                end
            end
        end
        figure(3)
        plot1 = plot(t,Mnexp,'ob');                                  %
Rawdata
        set(plot1,'Color',noisecolor);
        hold on
        plotx=plot(ts,Mnexps,'b');                                   %
Smoothed data
        set(plotx,'Color',smoothcolor,'LineWidth',1);          %Smooth
Data
        xlabel('time - [min]'); ylabel('Absorbance');
       %
       % Optimize the rate constant k1 to fit the total dissolved Mn
curve
       %
        X0 = 0.09;
        LB = 0;
        UB = 10;
        [X,RESNORM,RESIDUAL,EXITFLAG,OUTPUT,LAMBDA] =
lsqnonlin('optim_Mn2',X0,LB,UB,[],ts,Mnexps);
        k1 = X(1);                          % Rate constant for
oxidation of Mn(II) by porphyrin
```

```
        Mn2 = Mn20*exp(-k1*ts);            % Calculate the
disappearance of Mn(II)
        Mntot = Mn20*(1-exp(-k1*ts));      % Calculate Mntot from the
disappearance of Mn(II)
       %
       % Plot the data and output of the calculations
       %
        figure(3)
        extplot2 = plot(ts,Mn2,'r',ts,Mntot,'b');
        xlabel('Time - [min]');
        ylabel('Concentration - [uM]');
        legend('Exp Mn','smoothed Exp Mn','Mn(II)','Calc Mntot')
       %
       % Store the parameter k1 in a matrix
       %
        k1all = [k1all;k1];        % save each k1 optimized for each
standard
        pause(5)
        hold off
    end
   %
   % Save the matrix of data in an output file in the order: blank
absorbance, calibration slope, standard deviation of calibration
   %
    k1all(Mnstd == 0) = [];        % Make sure to remove the k1
calculated for the blank, as it is meaningless
    mk1 = mean(k1all);
    sdk1 = std(k1all);
    LMdata = [LMdata mk1 sdk1];
    filename = ['Mncal' num2str(min(filenum)) '_' num2str(max(filenum))
'.txt'];
    eval(['save ' filename ' LMdata -ascii']);

   %
else       % If the speciation of Manganese is investigated only
   %


   %
   % Ask the user to provide the name of the Mn calibration file (in
quotes and .txt)
   %
    file = input('What is the name of the Mn calibration file (between
single quotes and .txt)?');
    fid = fopen(file);
    C = fscanf(fid,'%f%f%f');
    fclose(fid);
   %
   % Ask the user to provide the concentration of the interfering
Fe(II)
   %
    Feint = input('What is the absorbance of the Fe interference?');
   %
   % The data are extracted from the input files and parameters
optinmized to
   % fit the total Mn data with Mn(II) and Mn(III)
   %
```

```
    RLS1 = [];
    for m = 1:length(filenames)
        set(ok,'Visible','off','Enable','off');
        set(exxit,'Enable','on');
       %
       % Read the data through the file line
       %
        file = filenames(m).name;
        [D,S] = xlsread(file);
        data = cellfun(@(x)str2double(regexp(x, ',', 'split')),
S(9:end), 'Uni',0);
        data1 = cell2mat(data);
       %
       % Calculate the concentration of total dissolved Mn from
absorbance values after subtracting the initial
       % absorbance (t = 0) using the slope entered by the user and
accounting for the Fe interference
       %
        Mnexp = (data1(:,2) - C(1) - Feint)/C(2);  % C(1) = absorbance
of the blank; C(2) = slope of the calibration
       %
        % Smooth the data. n points are used to calculate each averaged
result. The smoothed value at index i is
        % the average of the data points in the interval [l -(n-1)/2,
l+(n-1)/2], inclusive.
        %
        if exist('smooth','file')==2
        t = data1(:,1);
        ts = smooth(t,n,'sgolay');
        Mnexps = smooth(Mnexp,n,'sgolay');
        else
            for l= 1:n:length(t)-n;
                if exist('ts')==0
                    ts = mean(t([l:l+(n-1)]));
                elseif exist('ts')==1 && isempty(ts) == 1,
                    ts = mean(t([l:l+(n-1)]));
                else
                    ts = [ts;mean(t([l:l+(n-1)]))];
                end
                if exist('Mnexps')==0
                    Mnexps = mean(Mnexp([l:l+(n-1)]));
                else
                    Mnexps = [Mnexps;mean(Mnexp([l:l+(n-1)]))];
                end
            end
        end
        %
        % Plot raw and smoothed data Raw,'color',smooth,'color'
        %
        %figure(2);
        set(fig2,'Name',file);
        plot1 = plot(t,Mnexp,'ob');                                    %
Rawdata
        set(plot1,'Color',noisecolor);
        hold on
        plotx=plot(ts,Mnexps,'b');                                     %
Smoothed data
```

```
        set(plotx,'Color',smoothcolor,'LineWidth',1);%Smooth Data
        set(theplot,'Position',[0.103 0.085 0.799
0.815],'Color',axcolor,'Xcolor',[1 1 1],'Ycolor',[1 1 1]);
        xlabel('time - [min]'); ylabel('Absorbance');
        %
        % If the speciation of Mn is calculated using 3 adjustable
parameters (k2, [Mn(II)], and [Mn(III)])
        % and k1 is fixed from calibration data.
        %
        if typecalc == 2
        %
        % Optimize the rate constants k2 as well as the initial
concentrations of Mn(II) and Mn(III) to fit
        % the total dissolved Mn curve
        %
            k1 = C(4);      % Rate constant calculated from Mn(II)
calibration data
            X0 = [0.03;10;2];
            LB = [0;0;0];
            UB = [0.5*C(4);20;10];
%            [X,RESNORM,RESIDUAL,EXITFLAG,OUTPUT,LAMBDA] =
lsqnonlin('optim_Mn233',X0,LB,UB,[],ts,Mnexps);
            [X,RESNORM,RESIDUAL,EXITFLAG,OUTPUT,LAMBDA,J] =
lsqnonlin('optim_Mn233',X0,LB,UB,[],ts,Mnexps);
            ci = nlparci(X,RESIDUAL,'JACOBIAN',J);      % function that
calculates the lower and upper boundaries on each parameter (i.e.
standard deviation)
%             k2 = X(1);
%             Mn20 = X(2);
%             Mn30 = X(3);
            k2 = [X(1) ci(1,:)];            % Report the value and its
lower and upper boundaries
            Mn20 = [X(2) ci(2,:)];
            Mn30 = [X(3) ci(3,:)];
        %
        % If the speciation of Mn is calculated using 4 adjustable
parameters (k1, k2, [Mn(II)], and [Mn(III)])
        %
        elseif typecalc == 3    % calculation of Mn speciation is
requested
        %
        % Optimize the rate constants k1 and k2 as well as the initial
concentrations of Mn(II) and Mn(III) to fit
        % the total dissolved Mn curve

        %[SMO notes: Madison et al 2013 Science supplemental material
states rate of
        %Mn(II) complexation was 0.025 sec-1 and Mn(III) complexation
was 3.37-6.15 x10^-3
        %converted to min-1 is Mn(II) 1.5 min-1, and about 0.2-0.4 min-
1 for
        %Mn(III)]
            X0 = [0.09;0.03;10;2];
            LB = [0;0;0;0];
            UB = [(2*C(4));(0.5*C(4));12;12];
            [X,RESNORM,RESIDUAL,EXITFLAG,OUTPUT,LAMBDA,J] =
lsqnonlin('optim_Mn234',X0,LB,UB,[],ts,Mnexps);
```

```
            ci = nlparci(X,RESIDUAL,'JACOBIAN',J);      % function that
calculates the lower and upper boundaries on each parameter (i.e.
standard deviation)
%             k1 = X(1);
%             k2 = X(2);
%             Mn20 = X(3);
%             Mn30 = X(4);
            k1 = [X(1) ci(1,:)];            % Report the value and its
lower and upper boundaries
            k2 = [X(2) ci(2,:)];
            Mn20 = [X(3) ci(3,:)];
            Mn30 = [X(4) ci(4,:)];
        end
        %
        % Calculate the temporal evolution of Mn(II) and Mn(III) as a
result of the reaction with the porphyrin
        %
        Mn2 = Mn20(1)*exp(-k1(1)*ts);
        Mn3TCPP2 = Mn20(1)*(1-exp(-k1(1)*ts));

        Mn3 = Mn30(1)*exp(-k2(1)*ts);
        Mn3TCPP3 = Mn30(1)*(1-exp(-k2(1)*ts));

        Mntot = Mn3TCPP2 + Mn3TCPP3;
        %
        % Plot the data and output of the calculations
        %
        figure(2)
        hold on
        extplot2 = plot(ts,Mn2,'r',ts,Mn3,'g',ts,Mntot,'b');
        xlabel('Time - [min]');
        ylabel('Concentration - [uM]');
        legend('Exp Mn','smoothed Exp Mn','Mn(II)','Mn(III)','Calc
Mntot')
        %
        % Store the four parameters and their lower and upper
boundaries in a matrix
        %
        RLS = [eval([int2str(filenum(m))]) k1 k2 Mn20 Mn30];
        RLS1 = [RLS1;RLS];
        pause(5)
        hold off
    end
    uiwait
    close(figure(2))
    %
    % Save the matrix of data in an output file in the order: file
number
    % k1 k2 Mn20 Mn30 but, each of the k1 k2 Mn20 and Mn30 parameters
also include  next to them the two
    % boundaries (lower and upper) defined by ci that report their
incertitude
    %
    filename = ['Mnspec_results' num2str(min(RLS1(:,1))) '_'
num2str((max(RLS1(:,1)))) '.txt'];
    eval(['save ' filename ' RLS1 -ascii']);
```

```
end % end of calibration or Mn speciation loop
```

A.1.4. optim_Mn2.m

This subroutine fits the initial concentration of Mn(II) and Mn(III) in a natural sample as well as their respective rate constants (k_1 and k_2) with a porphyrin competitive ligand to the data. It uses a non-linear least square optimization procedure.

```
function [rsOutput] = optim_Mn2(X,ts,Mnexps)

global Mn20

rss1 = Mn20*(1-exp(-X(1)*ts)) - Mnexps;

rsOutput = [rss1];
```

A.1.5. optim_Mn233.m

This subroutine fits the initial concentration of Mn(II) and Mn(III) in a natural sample as well as the rate constant k2 for the reaction of Mn(III)with a porphyrin competitive ligand to the data. The rate constant k1 is fixed and calculated from Mn(II) calibration data. The routine uses a non-linear least square optimization procedure.

```
function [rsOutput] = optim_Mn233(X,ts,Mnexps)

global k1

% rss1 = X(3)*(1-exp(-X(1)*ts)) - Mnexps;
% rss2 = X(4)*(1-exp(-X(2)*ts)) - Mnexps;
rss1 = X(2)*(1-exp(-k1*ts)) + X(3)*(1-exp(-X(1)*ts)) - Mnexps;

% Mn3TCPP2 = X(3) - Mn2;
% Mn3TCPP3 = X(4) - Mn3;
%
% Mntot = Mn3TCPP2 + Mn3TCPP3;

% rsOutput = [rss1;rss2];
rsOutput = [rss1];
%F= norm((Mntot-Mnexps))*1e6;
```

A.1.6 optimMn234.m

This subroutine fits the initial concentration of Mn(II) and Mn(III) in a natural sample as well as their respective rate constants (k1 and k2) with a porphyrin competitive ligand to the data. It uses a non-linear least square optimization procedure.

```
function [rsOutput] = optim_Mn234(X,ts,Mnexps)

% rss1 = X(3)*(1-exp(-X(1)*ts)) - Mnexps;
% rss2 = X(4)*(1-exp(-X(2)*ts)) - Mnexps;
rss1 = X(3)*(1-exp(-X(1)*ts)) + X(4)*(1-exp(-X(2)*ts)) - Mnexps;

% Mn3TCPP2 = X(3) - Mn2;
% Mn3TCPP3 = X(4) - Mn3;
%
% Mntot = Mn3TCPP2 + Mn3TCPP3;

% rsOutput = [rss1;rss2];
rsOutput = [rss1];
%F= norm((Mntot-Mnexps))*1e6;
```

APPENDIX B. SUPPLEMENTAL INFORMATION FOR CHAPTER 3

B.1 Thermodynamic Calculations

The Gibbs free energy of formation at standard state was calculated for the overall reaction of arsenite oxidation by MnO_2 using Equations B1-B3 and Table B1. Subsequently, the Gibbs free energy of the reaction (ΔG_r) was calculated using to demonstrate the favorability of the oxidation of As(III) by MnO_2 in the conditions of this study (Equation B4-B5).

$$MnO_2 + H_3AsO_3^0 + H^+ \rightarrow Mn^{2+} + H_2AsO_4^- + H_2O \quad \text{(B1)}$$

$$\Delta G_f^0 = \sum \Delta G_{f,products}^0 - \sum \Delta G_{f,reactants}^0 \quad \text{(B2)}$$

Table B 1: Thermodynamic constants

Species	ΔG_f^0 (KJ mol^{-1})	Reference
MnO_2	-466.41	1
$H_3AsO_3^0$	-646.0	2
H^+	0	3
Mn^{2+}	-228.0	3
$H_2AsO_4^-$	-748.5	3
H_2O	-237.18	3

$$\Delta G_f^0 = -1213.68\,\frac{KJ}{mol} - \left(-112.405\,\frac{KJ}{mol}\right) = -101.275 \quad \text{(B3)}$$

$$\Delta G_r = \Delta G_f^0 + RTlnQ \quad \text{(B4)}$$

$$where, R = 0.008314 \frac{KJ}{K * mol}, T = 298\ K, Q = \frac{\{H_2AsO_4^-\}\{Mn^{2+}\}}{\{H_3AsO_3^0\}\{H^+\}} \quad \text{(B5)}$$

ΔG_r was calculated at the beginning of the experiment using activities (denoted by '{}', Eq. S5) calculated with an ionic strength of 0.01 M (Stumm and Morgan, 1996). Experimental values were used for arsenite and proton concentrations, [H_3AsO_3] and [H^+], whereas the concentrations arsenite and dissolved manganese, [$H_2AsO_4^-$] and [Mn^{2+}], at the beginning of the experiment were assumed to be 1 μM. ΔG_r for all conditions ranged between -99 and -122 KJ mol^{-1}.

B.2 Calculation of precursor species

It is valuable to calculate the distribution of the precursor complex over pH to predict how the reaction mechanism may affect the mechanism or reaction rate. The precursor complex was calculated by multiplying the fraction of the surface species, α_{MnOH2+}, α_{MnOH} & α_{MnO-}, by the fraction of the arsenic species, α_{H3AsO3} & α_{H2AsO3}- α_{HAsO32}- α_{AsO33}-. The reactions, equations, and calculations necessary to determine the alpha species are listed below (Eqns B6-B23)

Calculation of the different fractions of Mn surface species:

$$> Mn - OH_2^+ \rightarrow\ > Mn - OH + H^+ \quad pK_{a1} = -1.6 \quad \text{(B6)}$$

$$K_{a1} = \frac{[MnOH_2^+][H^+]}{[MnOH]} \quad \text{(B7)}$$

$$> Mn - OH \rightarrow\ > MnO^- + H^+ \quad pK_{a2} = 4.6 \quad \text{(B8)}$$

$$K_{a2} = \frac{[MnO^-]H^+}{[MnOH]} \quad \text{(B9)}$$

$$Mn_T = > MnOH_2^+ + > Mn - O^- + > Mn - OH$$
$$= MnOH_2^+ + MnOH + MnO^- \quad \text{(B10)}$$

At pH << pKa_2, MnO^- species is ignored from Eq. B10 because of its negligible concentration

$$Mn_T = [MnOH_2^+] + [MnOH] + [\cancel{MnO^-}]$$
$$Mn_T = [MnOH_2^+] + \frac{K_{a1}[MnOH_2^+]}{[H^+]}$$
$$Mn_T = [MnOH_2^+]\left(1 + \frac{K_{a1}}{[H^+]}\right)$$
$$\frac{1}{\alpha_{MnOH2+}} = 1 + \frac{K_{a1}}{[H^+]}$$
$$\boxed{\alpha_{MnOH2+} = \frac{[H^+]}{[H^+] + K_{a1}}} \quad \text{(B11)}$$

At pKa_1 < pH < pKa_2, all species are considered to exist

$$Mn_T = [MnOH_2^+] + [MnOH] + [MnO^-]$$
$$Mn_T = \frac{[MnOH][H^+]}{K_{a1}} + [MnOH] + \frac{[MnOH]K_{a2}}{[H^+]}$$
$$Mn_T = [MnOH]\left(\frac{[H^+]}{K_{a1}} + 1 + \frac{K_{a2}}{[H^+]}\right)$$
$$Mn_T = [MnOH]\left(\frac{[H^+]^2}{K_{a1}[H^+]} + \frac{K_{a1}[H^+]}{K_{a1}[H^+]} + \frac{K_{a1}K_{a2}}{K_{a1}[H^+]}\right)$$
$$\frac{1}{\alpha_{MnOH}} = \left(\frac{[H^+]^2 + K_{a1}[H^+] + K_{a1}K_{a2}}{K_{a1}[H^+]}\right)$$
$$\boxed{\alpha_{MnOH} = \left(\frac{K_{a1}[H^+]}{[H^+]^2 + K_{a1}[H^+] + K_{a1}K_{a2}}\right)} \quad \text{(B12)}$$

At pH > pKa_2, $MnOH_2^+$ species is ignored because of its negligible concentration

$$Mn_T = \cancel{MnOH_2^+} + [MnOH] + [MnO^-]$$

$$Mn_T = \frac{[MnO^-][H^+]}{K_{a2}} + [MnO^-]$$

$$Mn_T = [MnO^-]\left(\frac{[H^+]}{K_{a2}} + 1\right)$$

$$\frac{1}{\alpha_{MnO-}} = \frac{[H^+] + K_{a2}}{K_{a2}}$$

$$\boxed{\alpha_{MnO-} = \frac{K_{a2}}{[H^+] + K_{a2}}} \quad \text{(B13)}$$

Calculation of the different fractions of arsenite species:

$$H_3AsO_3 \rightarrow H^+ + H_2AsO_3^- \quad pK_{a1} = 9.2 \quad \text{(B14)}$$

$$H_2AsO_3^- \rightarrow H^+ + HAsO_3^{2-} \quad pK_{a2} = 12.1 \quad \text{(B15)}$$

$$HAsO_3^{2-} \rightarrow AsO_3^{3-} + H^+ \quad pK_{a3} = 13.4 \quad \text{(B16)}$$

$$K_{a1} = \frac{[H^+][H_2AsO_3^-]}{[H_3AsO_3]} \quad \text{(B17)}$$

$$K_{a2} = \frac{[H^+][HAsO_3^{2-}]}{[H_2AsO_3^-]} \quad \text{(B18)}$$

$$K_{a3} = \frac{[H^+][AsO_3^{3-}]}{[HAsO_3^{2-}]} \quad \text{(B19)}$$

$$As_T = [H_3AsO_3] + [H_2AsO_3^-] + [HAsO_3^{2-}] + [AsO_3^{3-}] \quad \text{(B20)}$$

At pH < pKa_1, both the $HAsO_3^-$ and AsO_3^{3-} species are ignored from Equation B20 because of their negligible concentrations

$$As_T = [H_3AsO_3] + [H_2AsO_3^-] + \cancel{[HAsO_3^{2-}] + [AsO_3^{3-}]}$$

$$As_T = [H_3AsO_3] + \frac{[H_3AsO_3]K_{a1}}{[H^+]}$$

$$As_T = [H_3AsO_3]\left(1 + \frac{K_{a1}}{[H^+]}\right)$$

$$\frac{1}{\alpha_{H3AsO3}} = \left(1 + \frac{K_{a1}}{[H^+]}\right)$$

$$\boxed{\alpha_{H3AsO3} = \frac{[H^+]}{[H^+] + K_{a1}}} \quad \text{(B21)}$$

At $pK_{a1} < pH < pK_{a2}$, the AsO_3^{3-} species is ignored because of its negligible concentration

$$As_T = [H_3AsO_3] + [H_2AsO_3^-] + [HAsO_3^{2-}] + \cancel{[AsO_3^{3-}]}$$

$$As_T = \frac{[H^+][H_2AsO_3^-]}{K_{a1}} + [H_2AsO_3^-] + \frac{[H_2AsO_3^-]K_{a2}}{[H^+]}$$

$$As_T = [H_2AsO_3^-]\left(\frac{[H^+]}{K_{a1}} + 1 + \frac{K_{a2}}{[H^+]}\right)$$

$$As_T = [H_2AsO_3^-]\left(\frac{[H^+]^2 + K_{a2}K_{a1}}{K_{a1}[H^+]} + 1\right)$$

$$\frac{1}{\alpha_{H2AsO3-}} = \left(\frac{[H^+]^2 + K_{a2}K_{a1}}{K_{a1}[H^+]} + 1\right)$$

$$\frac{1}{\alpha_{H2AsO3-}} = \left(\frac{[H^+]^2 + K_{a2}K_{a1}}{K_{a1}[H^+]} + \frac{K_{a1}[H^+]}{K_{a1}[H^+]}\right)$$

$$\frac{1}{\alpha_{H2AsO3-}} = \left(\frac{[H^+]^2 + K_{a2}K_{a1} + K_{a1}[H^+]}{K_{a1}[H^+]}\right)$$

$$\boxed{\alpha_{H2AsO3-} = \frac{K_{a1}[H^+]}{[H^+]^2 + K_{a2}K_{a1} + K_{a1}[H^+]}} \quad \text{(B22)}$$

At $pKa_2 < pH < pKa_3$, the H_3AsO_3 species is ignored because of its negligible concentration

$$As_T = \cancel{[H_3AsO_3]} + [H_2AsO_3^-] + [HAsO_3^{2-}] + [AsO_3^{3-}]$$

$$As_T = \frac{[H^+][HAsO_3^{2-}]}{K_{a2}} + [HAsO_3^{2-}] + \frac{[HAsO_3^{2-}]K_{a3}}{[H^+]}$$

$$As_T = [HAsO_3^{2-}]\left(\frac{[H^+]}{K_{a2}} + 1 + \frac{K_{a3}}{[H^+]}\right)$$

$$As_T = [HAsO_3^{2-}]\left(\frac{[H^+]^2 + K_{a2}K_{a1}}{K_{a1}[H^+]} + 1\right)$$

$$\frac{1}{\alpha_{HAsO32-}} = \left(\frac{[H^+]^2 + K_{a2}K_{a3}}{K_{a2}[H^+]} + \frac{K_{a2}[H^+]}{K_{a2}[H^+]}\right)$$

$$\frac{1}{\alpha_{HAsO32-}} = \left(\frac{[H^+]^2 + K_{a2}K_{a3} + K_{a2}[H^+]}{K_{a2}[H^+]}\right)$$

$$\boxed{\alpha_{HAsO32-} = \frac{K_{a2}[H^+]}{[H^+]^2 + K_{a2}K_{a3} + K_{a2}[H^+]}} \quad \text{(B23)}$$

At pH > pKa_3, both the H_3AsO_3 and the $H_2AsO_3^-$ species are ignored because of their negligible concentrations

$$As_T = \cancel{[H_3AsO_3]} + \cancel{[H_2AsO_3^-]} + [HAsO_3^{2-}] + [AsO_3^{3-}]$$

$$As_T = \frac{[H^+][AsO_3^{3-}]}{K_{a3}} + [AsO_3^{3-}]$$

$$As_T = [AsO_3^{3-}]\left(\frac{[H^+]}{K_{a3}} + 1\right)$$

$$\frac{1}{\alpha_{AsO33-}} = \left(\frac{[H^+] + K_{a3}}{K_{a3}}\right)$$

$$\boxed{\alpha_{AsO33-} = \left(\frac{K_{a3}}{K_{a3} + [H^+]}\right)} \quad \text{(B24)}$$

The fraction of the precursor complexes were then calculated and represented in Fig. B 1 as a function of pH using the following equations (B25-B34):

$$MnOH_2^+ \cdot As(OH)_3 = \alpha_{MnOH2+} * \alpha_{H3AsO3} \quad \text{(B25)}$$

$$MnOH_2^+ \cdot H_2AsO_3^- = \alpha_{MnOH2+} * \alpha_{H2AsO3-} \quad \text{(B26)}$$

$$MnOH \cdot As(OH)_3 = \alpha_{MnOH} * \alpha_{H3AsO3} \quad \text{(B27)}$$

$$MnOH \cdot H_2AsO_3^- = \alpha_{MnOH} * \alpha_{H2AsO3-} \quad \text{(B28)}$$

$$MnOH \cdot HAsO_3^{2-} = \alpha_{MnOH} * \alpha_{HAsO32-} \quad \text{(B29)}$$

$$MnOH \cdot AsO_3^{3-} = \alpha_{MnOH} * \alpha_{AsO33-} \quad \text{(B30)}$$

$$MnO^- \cdot As(OH)_3 = \alpha_{MnO-} * \alpha_{H3AsO3} \quad \text{(B31)}$$

$$MnO^- \cdot H_2AsO_3^- = \alpha_{MnO-} * \alpha_{H2AsO3-} \quad \text{(B32)}$$

$$MnO^- \cdot HAsO_3^{2-} = \alpha_{MnO-} * \alpha_{HAsO32-} \quad \text{(B33)}$$

$$MnO^- \cdot AsO_3^{3-} = \alpha_{MnO-} * \alpha_{AsO33-} \quad \text{(B34)}$$

These calculations revealed the most common precursor species are the species $MnOH \cdot As(OH)_3$, $MnO^- \cdot As(OH)_3$, and $MnO^- \cdot H_2AsO_3^-$ (Equations B35-B37, Figure B 1). When the surface species react with arsenite to form arsenate, the following reactions illustrate the reaction sequence including the precursor complexes between pH 3 and 10, the conditions of most environments.

$$> Mn - OH + H_3AsO_3 \rightarrow > MnOH \cdot As(OH)_3 \rightarrow Mn - OAsO_3H + 2H^+ \quad \text{(B35)}$$

$$> Mn - O^- + H_3AsO_3 \rightarrow > MnO^- \cdot As(OH)_3 \rightarrow Mn - OAsO_3H + 2H^+ \quad \text{(B36)}$$

$$> Mn - O^- + H_2AsO_3^- \rightarrow > MnO^- \cdot H_2AsO_3^- \rightarrow Mn - OAsO_3H + H^+ \quad \text{(B37)}$$

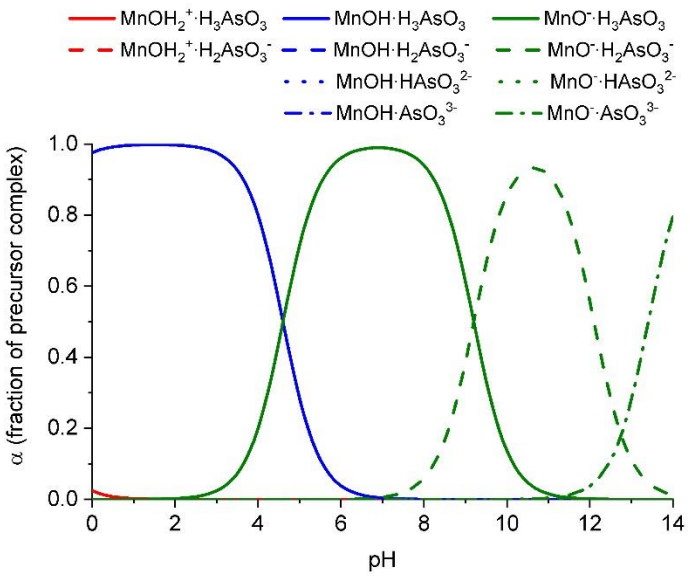

Figure B 1 Distribution of precursor species across pH values. $MnOH_2^+$ (red), MnOH (blue) and MnO^- (green) surface species paired with the respective arsenite species H_3AsO_3 (solid), $H_2AsO_3^-$ (dashed), $HAsO_3^{2-}$ (dotted) and AsO_3^{3-} (dashed dotted) are plotted versus pH (Eqns 25-34). pKa values for the deprotination of the Mn surface are -1.6 and 4.6. pKa values for H_3AsO_3 deprotination are 9.2, 12.1 and 13.4.

APPENDIX C. SUPPLEMENTAL INFORMATION FOR CHAPTER 4

Table C 1: As(III) concentrations from incubations with *Shewanella* 200 with As(V) as the sole electron acceptor after 28 days in M1 media (15 mM lactate, 100 µM phosphate).

Condition	As(V) added (µM)	% As(V) reduced
10^5 cells mL^{-1} (duplicate)	0	na
	10	37 ± 40
	50	50 ± 67
	500	78 ± 23
	1,000	150 ± 2
	2,000	105 ± 13
	5,000	135 ± 5
	10,000	0.9 ± 1.2
	20,000	0.1 ± 0.00
10^7 cells mL^{-1} (single)	0	na
	10	36 ± 1
	500	11.9 ± 0.3
	1,000	132 ± 1.1
Abiotic (single)	0	na
	10	na
	500	na
	1000	na

Table C 2: As(III) concentrations detected in solution and relative proportion of As(V) reduced (%) at day 71 during the reduction of MnO_2 by 10^5 cells ml^{-1} *S. putrefaciens* in the presence of increasing initial As(V) concentrations. All incubations were conducted with 5 mM MnO_2 as terminal electron acceptor and 10 mM lactate as electron donor in M1 medium at pH 7.0 amended either with 10 or 100 µM orthophosphate. Standard deviations represent instrumental error based on triplicate scans of the same sample).

	10 µM P_i		100 µM P_i	
Condition	**As(III) (µM)**	**% As(V) reduced**	**As(III) (µM)**	**% As(V) reduced**
Abiotic (1 mM As(V))	19.95 ± 0.77	2.0	452.8 ± 40.7	45.3
0 mM As(V)	0.00 ± 0.00	na	na	na
0.1 mM As(V)	68.5 ± 2.3	68.5	113.4 ± 1.1	113.4
1.0 mM As(V)	628.1 ± 4.51	62.8	532.3 ± 50.8	53.2
5.0 mM As(V)	0.05 ± 0.01	0	4,778.1 ± 175.7	95.6
10 mM As(V)	0.08 ± 0.02	0	1.3 ± 0.0	0.01

Figure C 1: Qualitative observations of the effect of cell and phosphate concentrations on MnO_2 reduction after: (a) Day 6 of incubations with 10^7 cells/mL; and (b) Day 20 of incubations with 10^5 cells/mL of *S. putrefaciens* 200 on 5 mM MnO_2 (0.5 g/L) as terminal electron acceptor and 15 mM lactate as electron donor in M1 medium at pH 7 (HEPES) in the presence of increasing P_i concentrations from (0-1,000 uM) from left to right. The clear solutions indicate complete reduction of solid MnO_2, whereas dark suspensions indicate low to no reduction of MnO_2 at that time point in the incubations.

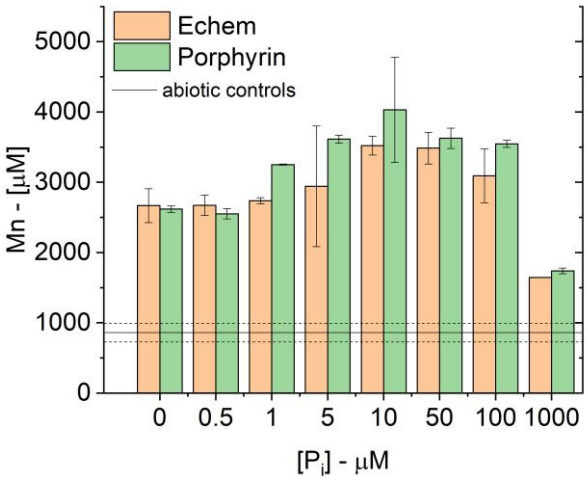

Figure C 2 Mn^{2+} detected voltammetrically (orange) compared to Mn_d quantified by the porphyrin method (green) in: (a) *S. putrefaciens* 200 incubations (10^7 cells mL^{-1}); and (b) abiotic controls in the presence of different phosphate concentrations [P_i] after day 6 of the incubations shown in Figure C 1. Abiotic controls averaged 860 ± 132 µM Mn^{2+} measured by voltammetry (shown in black solid and dashed lines.

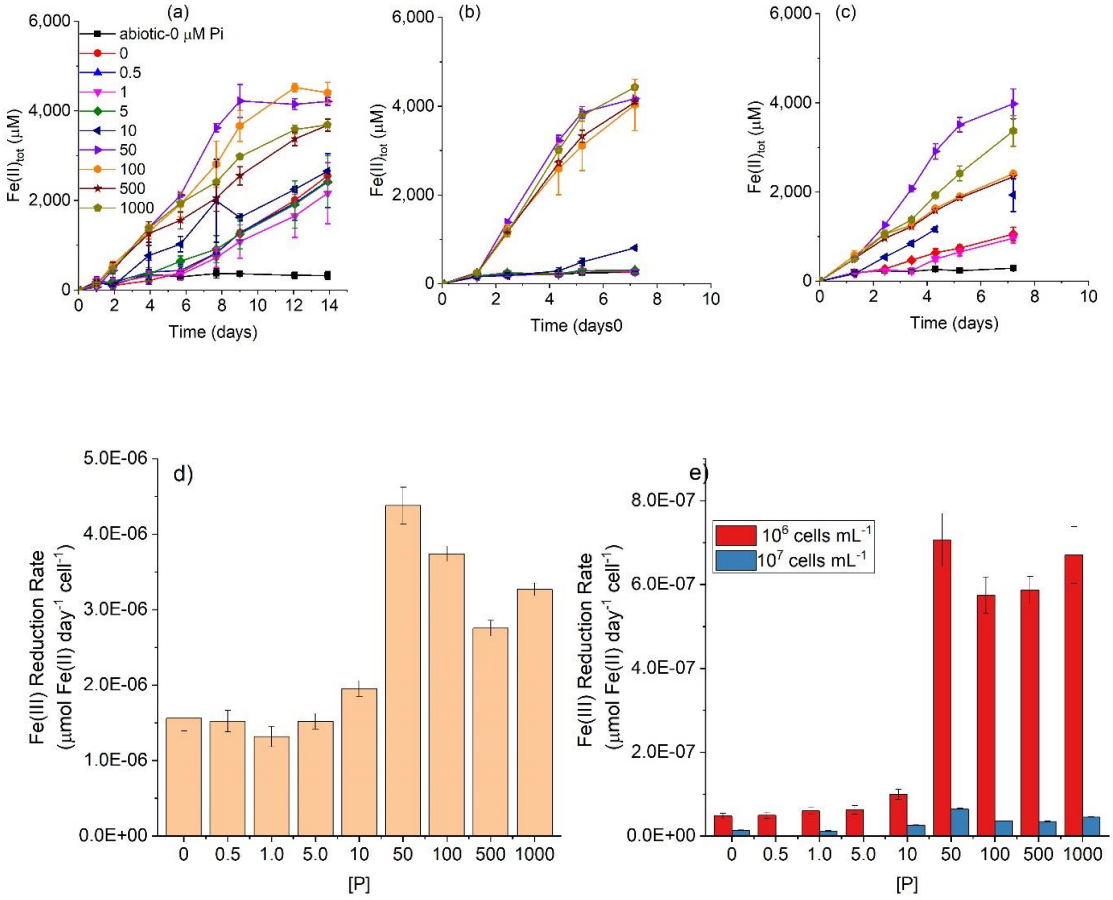

Figure C 3 Effect of P_i concentration on the reduction of 2L-ferrihydrite by different *S. putrefaciens* and *S. oneidensis* cell densities. Total Fe(II) produced as a function of time with: (a) 10^5 cells mL^{-1} *S. putrefaciens* 200; (b) 10^6 cells mL^{-1} *S. oneidensis* MR1; and (c) 10^5 cells mL^{-1} *S. oneidensis* MR1. Corresponding Fe(II) production rates normalized to cell concentration (μmol Fe(II) day^{-1} $cell^{-1}$) are shown for: (d) *S. putrefaciens* 200; and (e) the low and high cell concentrations of *S. oneidensis* MR1. All incubations were conducted with 10 mM 2L-ferrihydrite ($Fe(OH)_3$) as terminal electron acceptor and 15 mM lactate as electron donor in M1 medium at pH 7 (PIPES) amended with various orthophosphate concentrations.

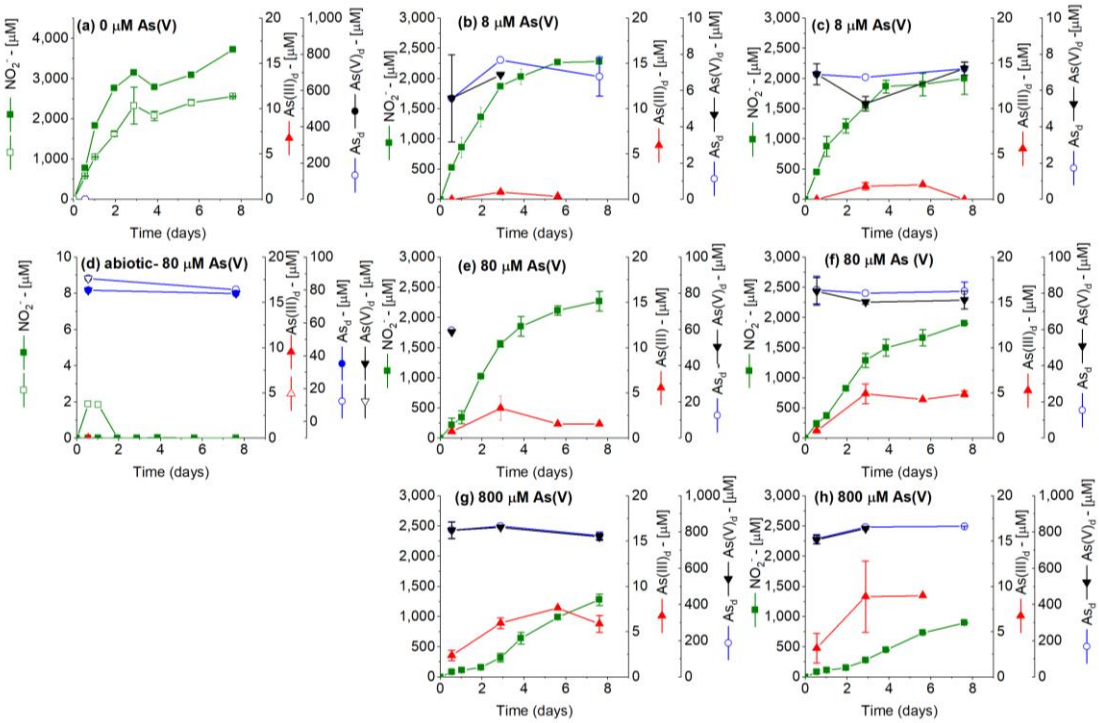

Figure C 4 Effect of increasing As(V) concentrations on NO_3^- reduction by *S. putrefaciens* and the speciation of dissolved arsenic: NO_2^- (green squares), As(III) (red triangles), As(V) (black inverse triangles), and total dissolved As (blue open circles) concentrations as a function of time in incubations of 10^7 cells mL^{-1} *S. putrefaciens* 200 on 10 mM nitrate as terminal electron acceptor and 20 mM lactate as electron donor in M1 medium at pH 7 (PIPES) amended with 0 µM As(V) (a), 8 µM As(V) (b,c), or 800 µM As(V) (g, h) and either 0.1 (right column c, f ,h) or 1 (middle column b, e, g) µM P_i . Abiotic control (d, 80 µM As(V)) contained the same conditions with 0.1 (closed symbols) or 1 (open symbols) µM P_i. NO_2^- error bars represent standard deviation of duplicate incubations. Dissolved As(V) calculations were calculated by the difference between dissolved As measured by ICP-MS (As_d) and dissolved As(III) quantified by voltammetry (HMDE). As(III) and As_d error based on duplicate incubations when available. Conditions: These experiments were used to calculate the rates shown in Figure 4-1c.

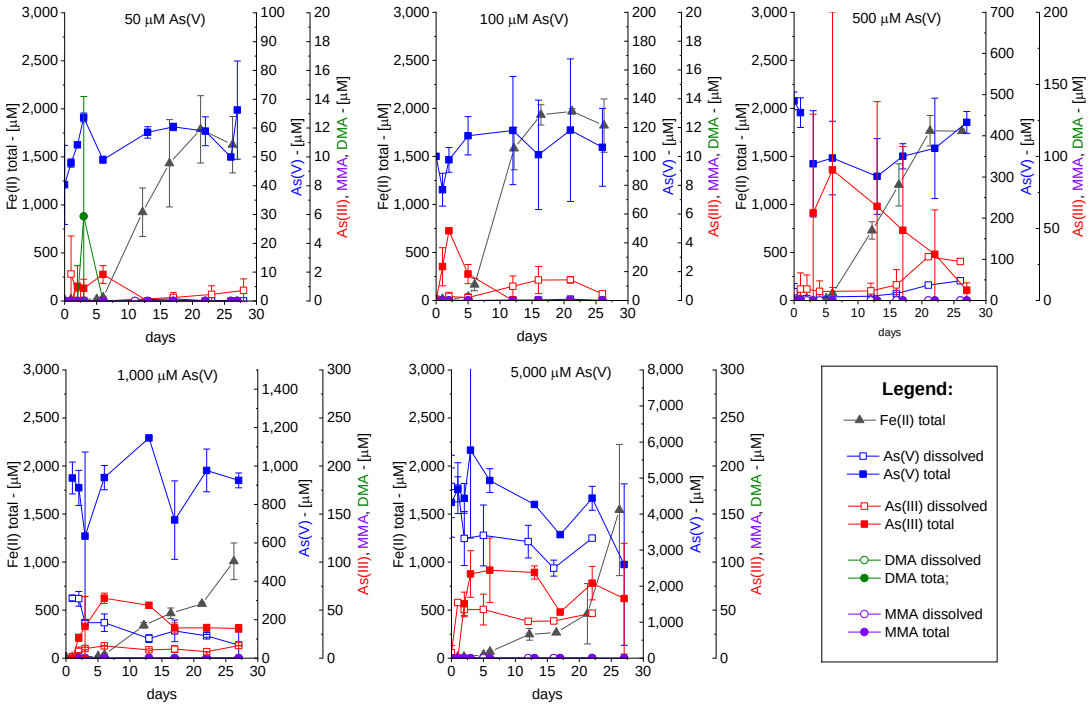

Figure C 5: Effect of increasing As(V) concentrations on the reduction of $Fe(OH)_{3(s)}$ by *S. putrefaciens* and the speciation of arsenic: Total Fe(II), As(V), As(III), MMA, and DMA as a function of time. All incubations were conducted with10^7 cells mL^{-1} *S. oneidensis* MR1, 5.8 mM 2L-ferrihydrite, and 20 mM lactate as electron donor in M1 medium at pH 7 (PIPES buffer) amended with 50 µM [Pi]. Error bars represent the standard deviation of the average of duplicate incubations in each condition.

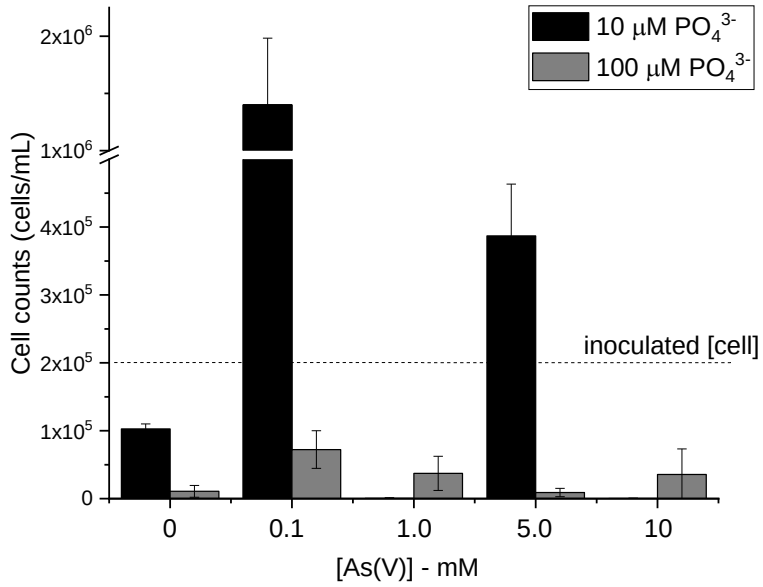

Figure C 6 Colony forming units (CFUs) obtained at day 71 in incubations of $2x10^5$ cells *S. putrefaciens* 200 on 5 mM MnO_2 as electron acceptor and 10 mM lactate as electron donor in the presence of 0, 0.1, 1, 5, and 10 mM As(V) in M1 media at pH 7 (PIPES) amended with10 and 100 µM P_i. Initial cell concentration based on OD_{600} of stock bacteria calculated as 10^5 cells mL^{-1}.

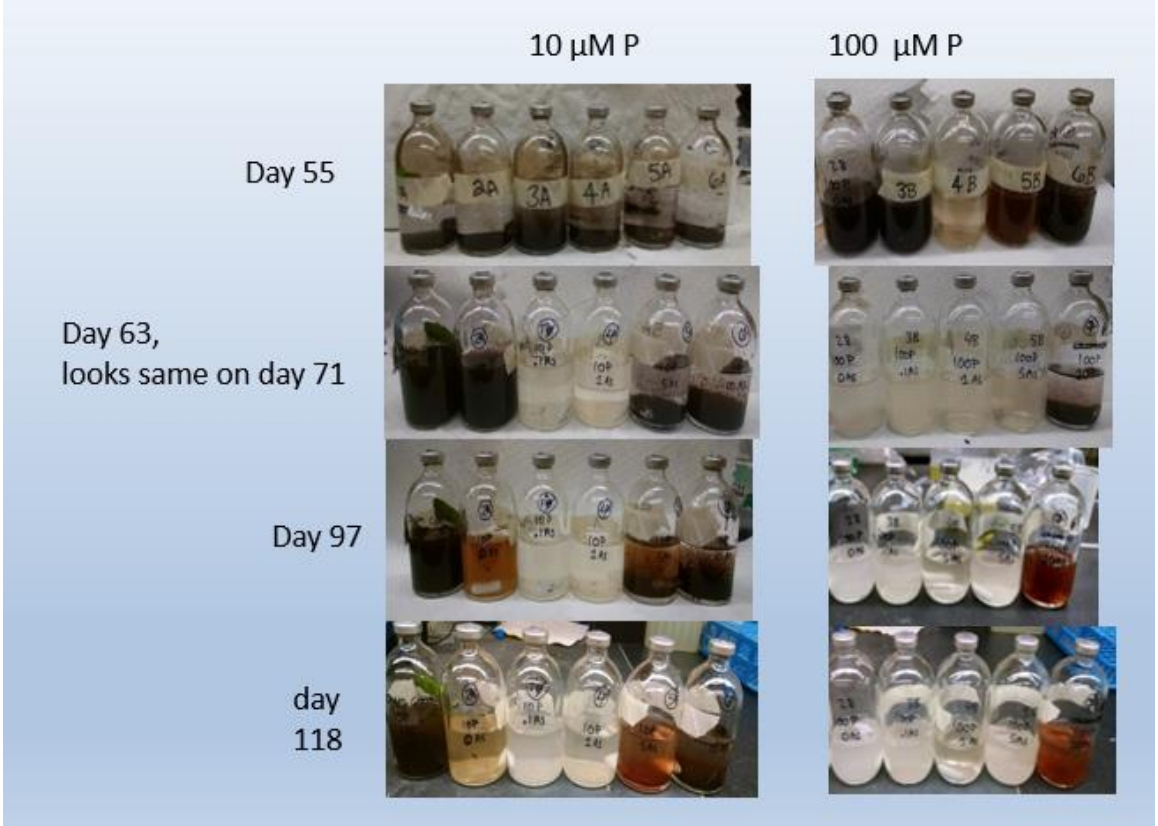

Figure C 7: Photographs taken at different time points during the reduction of MnO_2 in (from left to right in each photograph): the abiotic control and incubations of *S. putrefaciens* 200 with 0, 0.1, 1, 5, and 10 mM As(V) in the presence of 10 (left) and 100 (right) µM P_i. All incubations were conducted with $2x10^5$ cells, 5 mM MnO_2 as terminal electron acceptor, and 10 mM lactate as electron donor in M1 medium at pH 7 (PIPES). The 100 µM abiotic condition is not available. These photos match the experiments used for the time series shown in Figure 4-2 and Figure 4-3.

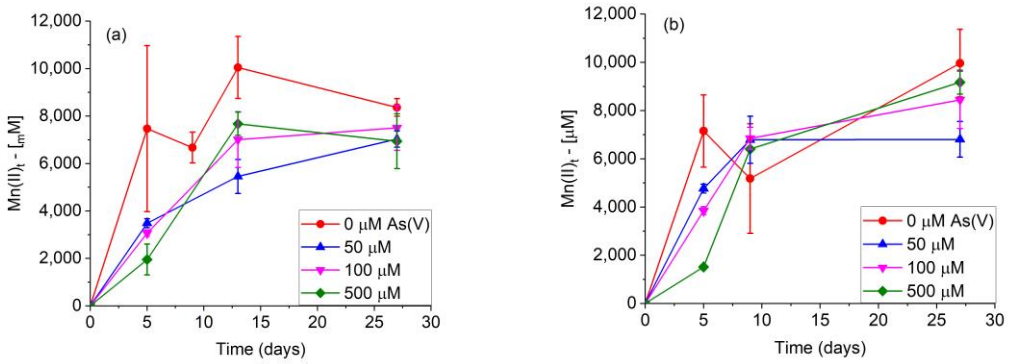

Figure C 8 Effect of As(V) concentrations on the reduction of 10 mM MnO_2 by: (a) *S. putrefaciens* 200 or (b) *S. oneidensis* MR-1 with 20 mM lactate as electron donor in M1 medium at pH 7 (15 mM PIPES) amended with 50 µM P_i. Cells were grown at pH 8 on fumarate/O2. Errors based on duplicate incubations.

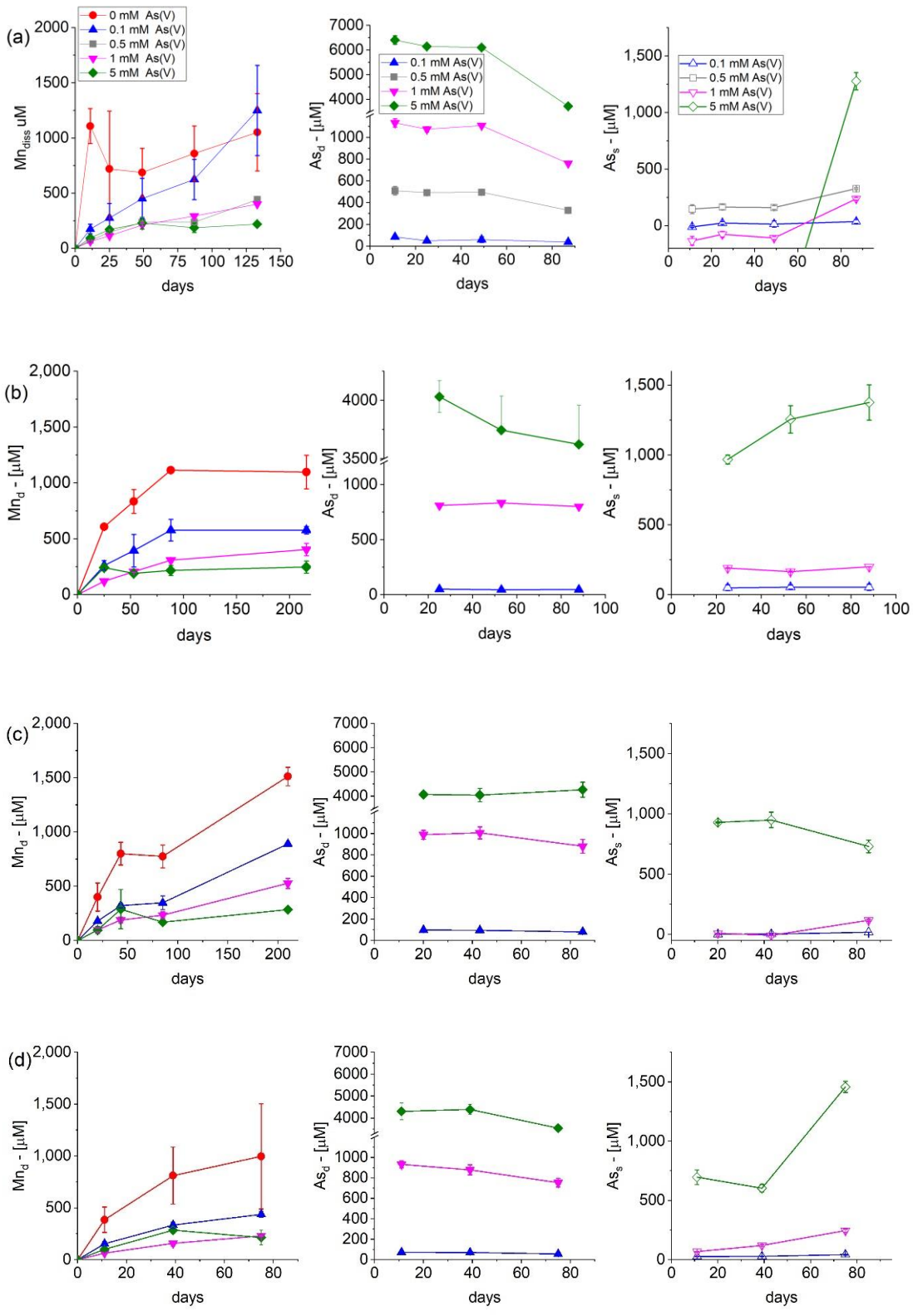
(a)
0 mM As(V)
0.1 mM As(V)
0.5 mM As(V)
1 mM As(V)
5 mM As(V)
Mn$_{diss}$ uM
As$_d$ - [µM]
As$_s$ - [µM]
days
(b)
Mn$_d$ - [µM]
(c)
(d)

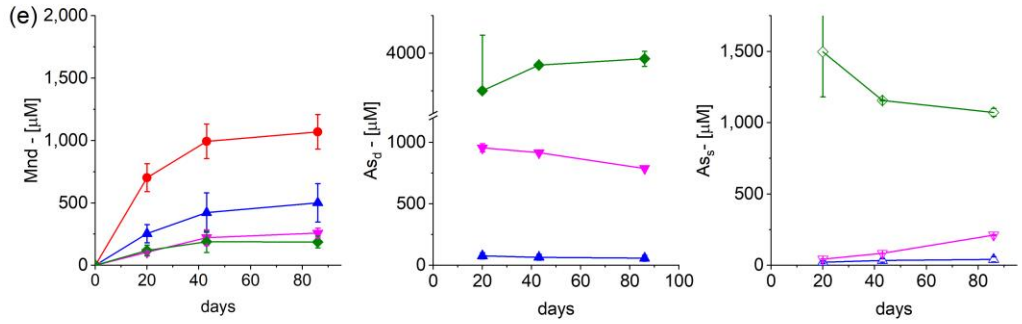

Figure C 9 Effect of increasing As(V) concentrations on MnO_2 reduction and the speciation of arsenic by: (a) *S. oneidensis* MR1; and the Pst mutants (b) Δ24; (c) Δ90; (d) DM2; and (e) DM10: Total dissolved Mn (left column), total dissolved As (middle column), and solid As (right column) as a function of time. Solid As was calculated from the difference of total As added and measured dissolved As.

APPENDIX D. SUPPLEMENTAL INFORMATION FOR CHAPTER 5

Table D 1a: The level of significance (ANOVA results) of environmental variables of the Canonical Correspondence Analysis for both the a) Prokaryotic dataset, and the b) archaeal dataset. Significance codes correspond to the associated p-value.

Parameter	DF	ChiSquare	F	Pr(>F)	Significance codes
DIC (mM)	1	0.55665	3.2303	0.001	0
ΣPO_4^{3-} (µM)	1	0.38015	2.2061	0.001	0
Mn_{tot} (µM)	1	0.29782	1.7283	0.006	0.001
Fe_{tot} (µM)	1	0.26754	1.5526	0.014	0.01
NH_4^+ (µM)	1	0.24267	1.4082	0.039	0.001
NO_3^- (µM)	1	0.29921	1.7363	0.002	0.001
NO_2^- (µM)	1	0.2058	1.1943	0.144	0.1
SO_4^{2-} (µM)	1	0.24744	1.4359	0.035	0.01
ΣH_2S (µM)	1	0.31874	1.8497	0.005	0.001
Org-Fe(III) (nA)	1	0.21791	1.2646	0.123	0.1
depth (mm)	1	0.40724	2.3633	0.001	0
Residual 17	17	2.92948			

Table D 1b: The level of significance (ANOVA results) of environmental variables of the Canonical Correspondence Analysis for both the a) Prokaryotic dataset, and the b) archaeal dataset. Significance codes correspond to the associated p-value.

Parameter	Df	ChiSquare	F	Pr(>F)	Significance codes
DIC (mM)	1	0.66877	2.4499	0.001	0
ΣPO_4^{3-} (µM)	1	0.34374	1.2592	0.088	0.5
Mn_{tot} (µM)	1	0.30454	1.1156	0.244	0.1
Fe_{tot} (µM)	1	0.32692	1.1976	0.137	0.1
NH_4^+ (µM)	1	0.38342	1.4046	0.021	0.01
NO_3^- (µM)	1	0.35358	1.2953	0.066	0.05
NO_2^- (µM)	1	0.30607	1.1212	0.187	0.1
SO_4^{2-} (µM)	1	0.40013	1.4658	0.019	0.01
ΣH_2S (µM)	1	0.41242	1.5108	0.01	0.001
Org-Fe(III) (nA)	1	0.3166	1.1598	0.176	0.1
depth (mm)	1	0.44848	1.6429	0.009	0.001
Residual	7	1.91084			

Table D 2: Network Table (too large for this document, in separate document available on request)

Table D 3: The correspondence between Bathyarchaeal ASVs and Bathyarcheial species from Zhou et al. (2018) using BLASTN (97 % similarity cutoff), and their associated subgroup.

In_Off	Order_HM	Bathy_Nb	Ref_Name	Subgroup
shelf	1	Bathy_356	MCG-15_FR695318.1	15
shelf	2	Bathy_27	KC925875.1.915_1	15
shelf	3	Bathy_396	MCG-15_AB301865.1	15
shelf	4	Bathy_397	MCG-15_AB301865.1	15
shelf	5	Bathy_1190	KC925912.1.915_1	8
shelf	6	Bathy_40	KC925875.1.915_1	15
shelf	7	Bathy_1059	MCG-8_DQ363807.1	8
shelf	8	Bathy_1230	KC003572.1.884_1	1
shelf	9	Bathy_319	MCG-15_DQ641883.1	15
shelf	10	Bathy_661	MCG-12_GQ848385.1	12
shelf	11	Bathy_574	EF203596.1.898_1	13
shelf	12	Bathy_937	MCG-12_GQ848385.1	12
shelf	13	Bathy_20	KC925875.1.915_1	15
shelf	14	Bathy_938	MCG-12_GQ848385.1	12
shelf	15	Bathy_901	MCG-8_DQ363807.1	8
shelf	16	Bathy_196	MCG-17_FJ404037.1	17
shelf	17	Bathy_1012	KX077312.1.914_1	8
shelf	18	Bathy_943	MCG-12_GQ848385.1	12
shelf	18	Bathy_943	MCG-12_GQ848385.1	12
shelf	19	Bathy_1011	MCG-8_DQ363807.1	8
shelf	20	Bathy_823	AB213058.1.1549_1	8

Table D 3 cont: The correspondence between Bathyarchaeal ASVs and Bathyarcheial species from Zhou et al. (2018) using BLASTN (97 % similarity cutoff), and their associated subgroup.

In_Off	Order_HM	Bathy_Nb	Ref_Name	Subgroup
shelf	21	Bathy_930	***	8
shelf	22	Bathy_1213	KC925912.1.915_1	8
shelf	23	Bathy_825	AB213058.1.1549_1	8
shelf	24	Bathy_1211	KC925912.1.915_1	8
shelf	25	Bathy_720	JX492958.1.890_1	13
shelf	26	Bathy_941	MCG-12_GQ848385.1	12
shelf	27	Bathy_1055	MCG-8_DQ363807.1	8
shelf	28	Bathy_751	GQ927628.1.918_1	8
shelf	29	Bathy_757	GQ927628.1.918_1	8
shelf	30	Bathy_848	MCG-12_GQ848385.1	12
slope	31	Bathy_209	MCG-17_FJ264803.1	17
slope	32	Bathy_334	AB797651.1.1428_1	15
slope	33	Bathy_355	MCG-15_FR695318.1	15
slope	34	Bathy_414	MCG-15_EU385859.1	15
slope	35	Bathy_1253	DQ302018.1.863_1	13
slope	36	Bathy_795	MCG-6_FJ264555.1	6
slope	37	Bathy_202	MCG-17_FJ264803.1	17
slope	38	Bathy_345	MCG-15_EU385859.1	15

***:Archaea_TACK_group_Candidatus_Bathyarchaeota_Candidatus_Bathyarchaeota_archaeon_BA2_GCA_001399795.1_16S_1

Table D 4 Universal OTU table (too large for this document, in separate document available on request

Table D 5 Archaea OTU table (too large for this document, in separate document available on request)

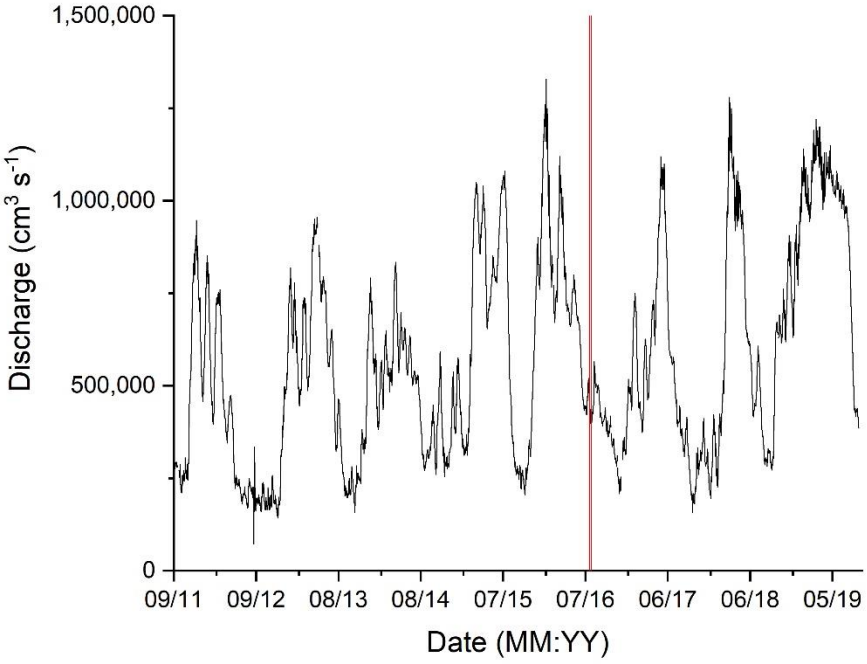

Figure D 1: Mississippi River Discharge data ($cm^3\ s^{-1}$) at the Belle Chasse, LA monitoring station (USGS Station #07374525). Date in Month: Year format (MM:YY).

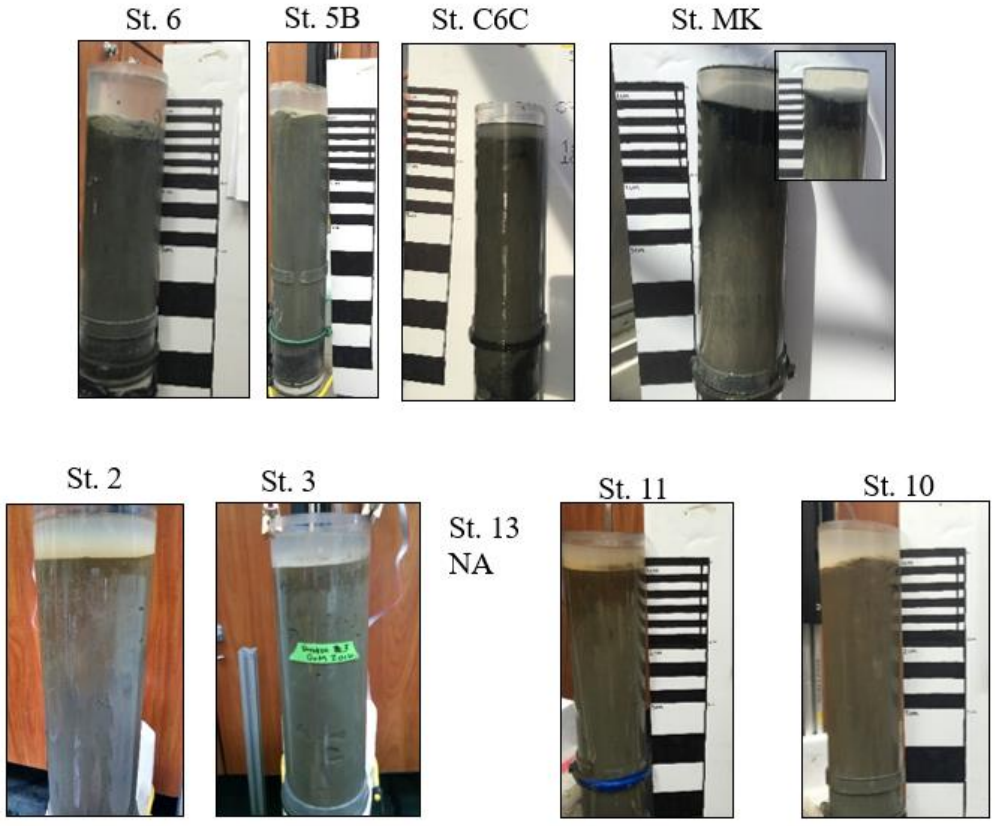

Figure D 2: Pictures of the cores showing variations in sediment color and stratification at the different locations. Thin, medium, and thick white and black lines represent depth intervals of 1, 2, and 5 cm respectively. The inset picture of the St. MK sediment core provides a better contrast of the top 14 cm. A picture of the sediment core from St. 13 was not available (NA).

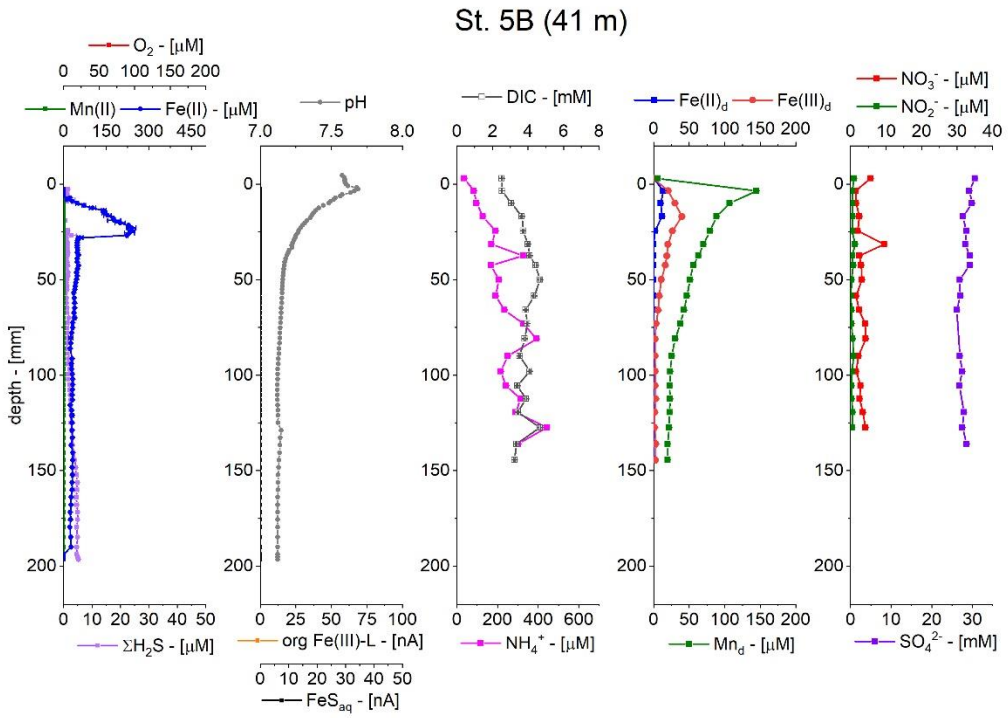

Figure D 3: Depth microprofiles at St. 5B of O_2, Mn^{2+}, Fe^{2+}, H_2S, org-Fe(III) complexes and FeS_{aq} (first and second panel) as well as pH (second panel) obtained with voltammetric and potentiometric microelectrodes. Depth profiles of pore water species DIC, NH_4^+(third panel), Fe^{2+}, $Fe(III)_d$, Mn_d (fourth panel), NO_3^-, NO_2^-, and SO_4^{2-} (fifth panel). ΣPO_4^{3-} data were not available (NA).

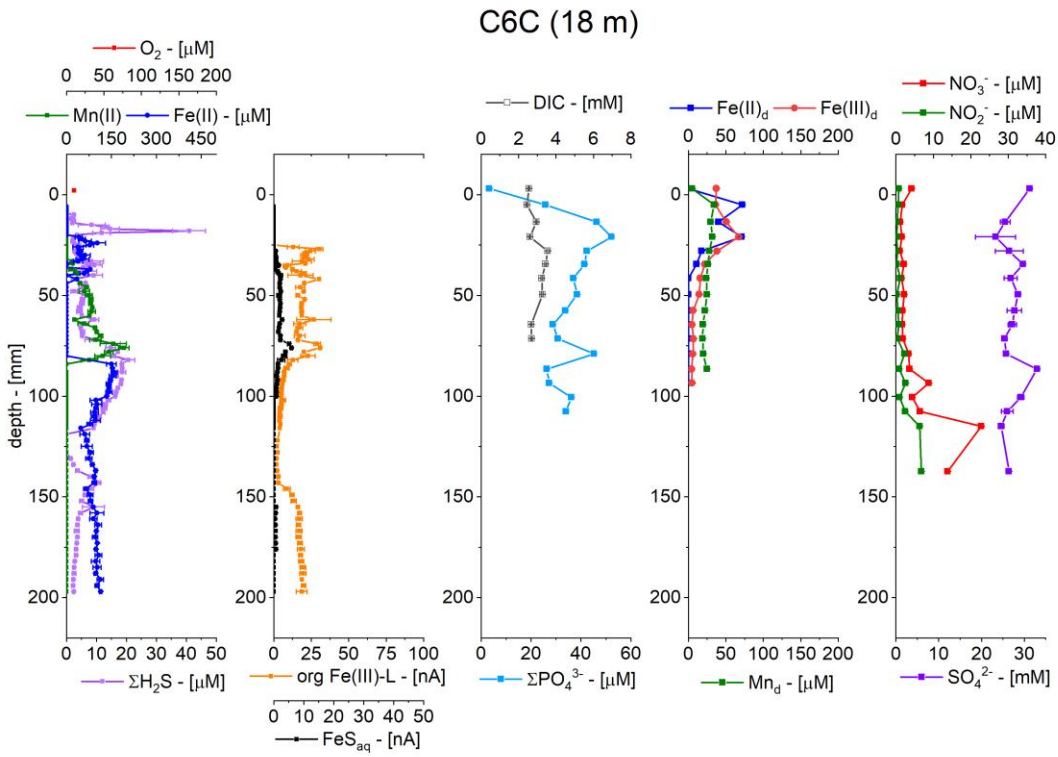

Figure D 4 Depth microprofiles at St. C6C of O_2, Mn^{2+}, Fe^{2+}, H_2S, org-Fe(III) complexes and FeS_{aq} (first and second panel) as well as pH (second panel) obtained with voltammetric and potentiometric microelectrodes. Depth profiles of pore water species DIC, NH_4^+(third panel), Fe^{2+}, $Fe(III)_d$, Mn_d (fourth panel), NO_3^-, NO_2^-, and SO_4^{2-} (fifth panel). pH and NH4+ data were not available (NA). Enlarged picture of sediment core provided (right) including scale for reference. Thin, medium, and thick white and black lines represent depth intervals of 1, 2, and 5 cm respectively.

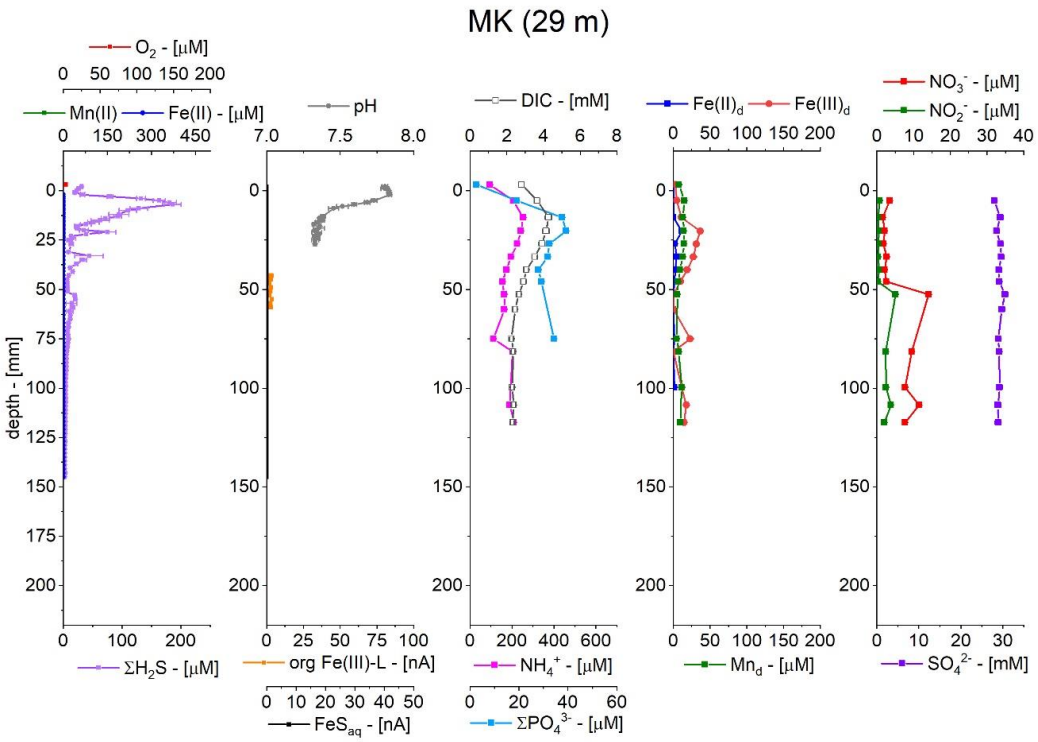

Figure D 5: Depth microprofiles at St. MK of O2, Mn^{2+}, Fe^{2+}, H_2S, org-Fe(III) complexes and FeS_{aq} (first and second panel) as well as pH (second panel) obtained with voltammetric and potentiometric microelectrodes. Depth profiles of pore water species DIC, NH_4^+(third panel), Fe^{2+}, $Fe(III)_d$, Mn_d (fourth panel), NO_3^-, NO_2^-, and SO_4^{2-} (fifth panel).

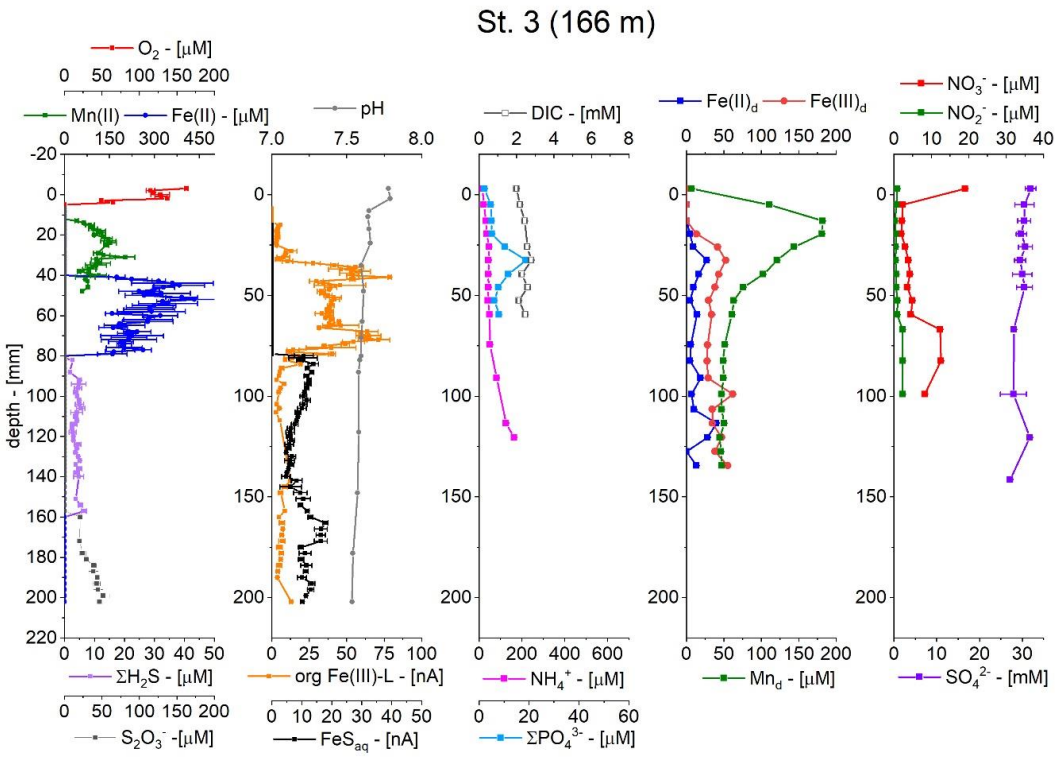

Figure D 6: Depth microprofiles at St. 3 of O_2, Mn^{2+}, Fe^{2+}, H_2S, org-Fe(III) complexes and FeS_{aq} (first and second panel) as well as pH (second panel) obtained with voltammetric and potentiometric microelectrodes. Depth profiles of pore water species DIC, NH_4^+(third panel), Fe^{2+}, $Fe(III)_d$, Mn_d (fourth panel), NO_3^-, NO_2^-, and SO_4^{2-} (fifth panel).

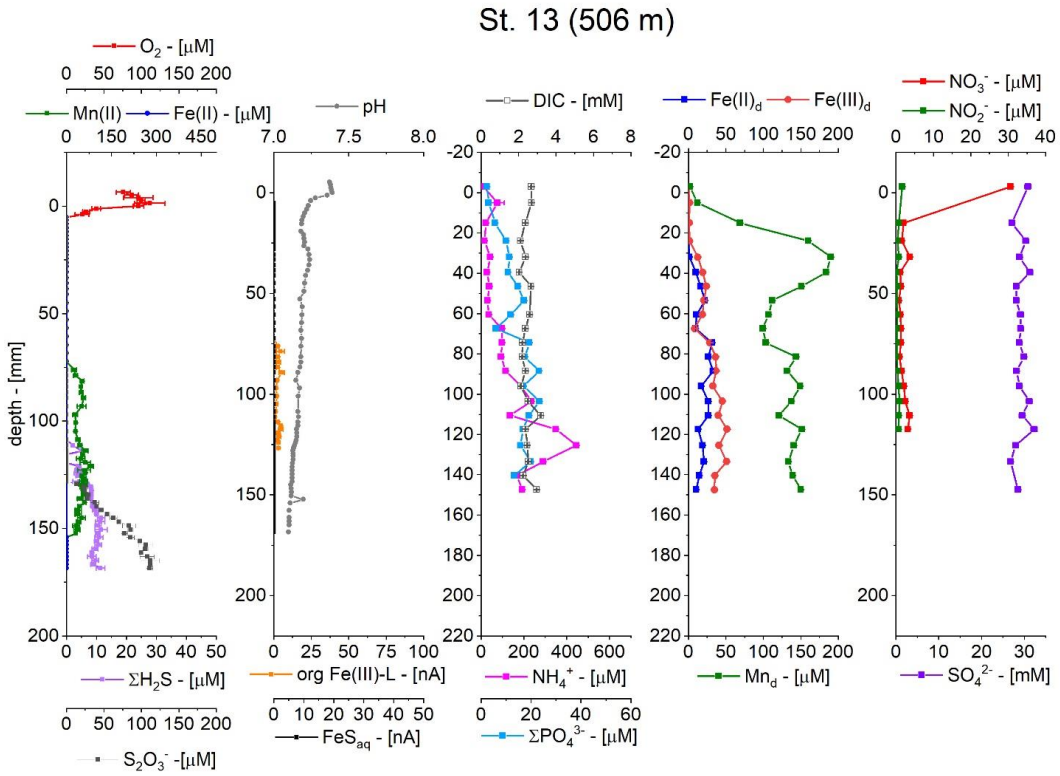

Figure D 7: Depth microprofiles at St. 13 of O_2, Mn^{2+}, Fe^{2+}, H_2S, $S_2O_3^-$, org-Fe(III) complexes and FeS_{aq} (first and second panel) as well as pH (second panel) obtained with voltammetric and potentiometric microelectrodes. Depth profiles of pore water species DIC, NH_4^+(third panel), Fe^{2+}, $Fe(III)_d$, Mn_d (fourth panel), NO_3^-, NO_2^-, and SO_4^{2-} (fifth panel). ΣPO_4^{3-} data were not available (NA).

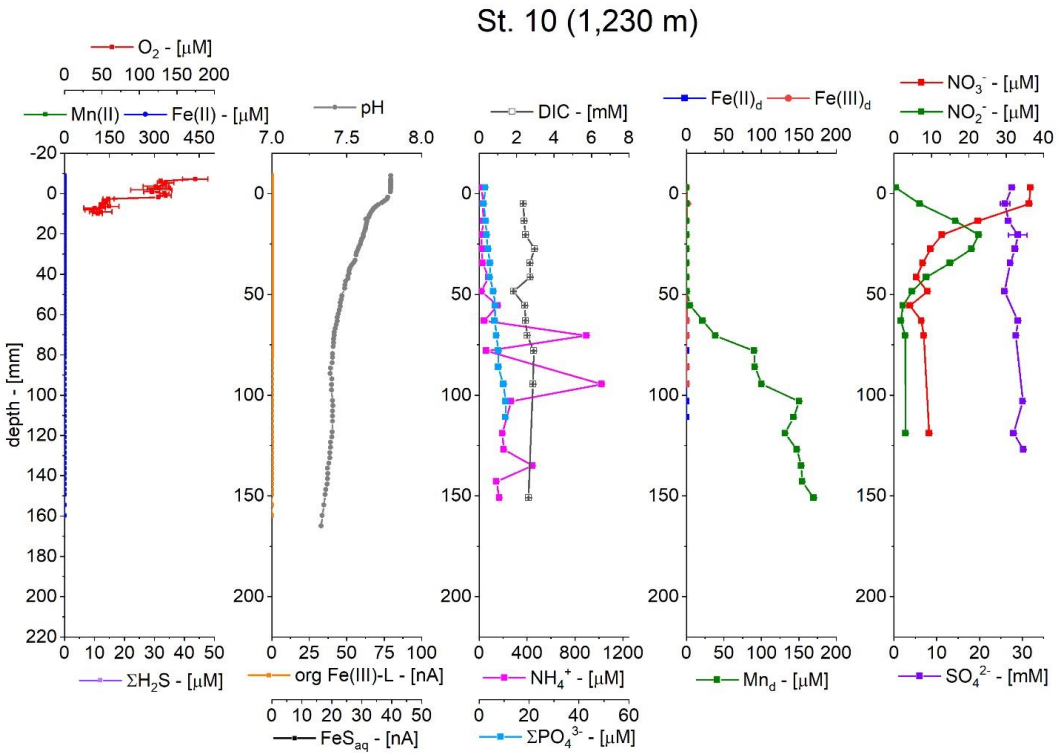

Figure D 8: Depth microprofiles at St. 10 of Mn^{2+}, Fe^{2+}, H_2S, $S_2O_3^-$, org-Fe(III) complexes and FeS_{aq} (first and second panel) as well as pH (second panel) obtained with voltammetric and potentiometric microelectrodes. Depth profiles of pore water species DIC, NH_4^+(third panel), Fe^{2+}, $Fe(III)_d$, Mn_d (fourth panel), NO_3^-, NO_2^-, and SO_4^{2-} (fifth panel). Voltammetric O_2 profiles were not available (NA).

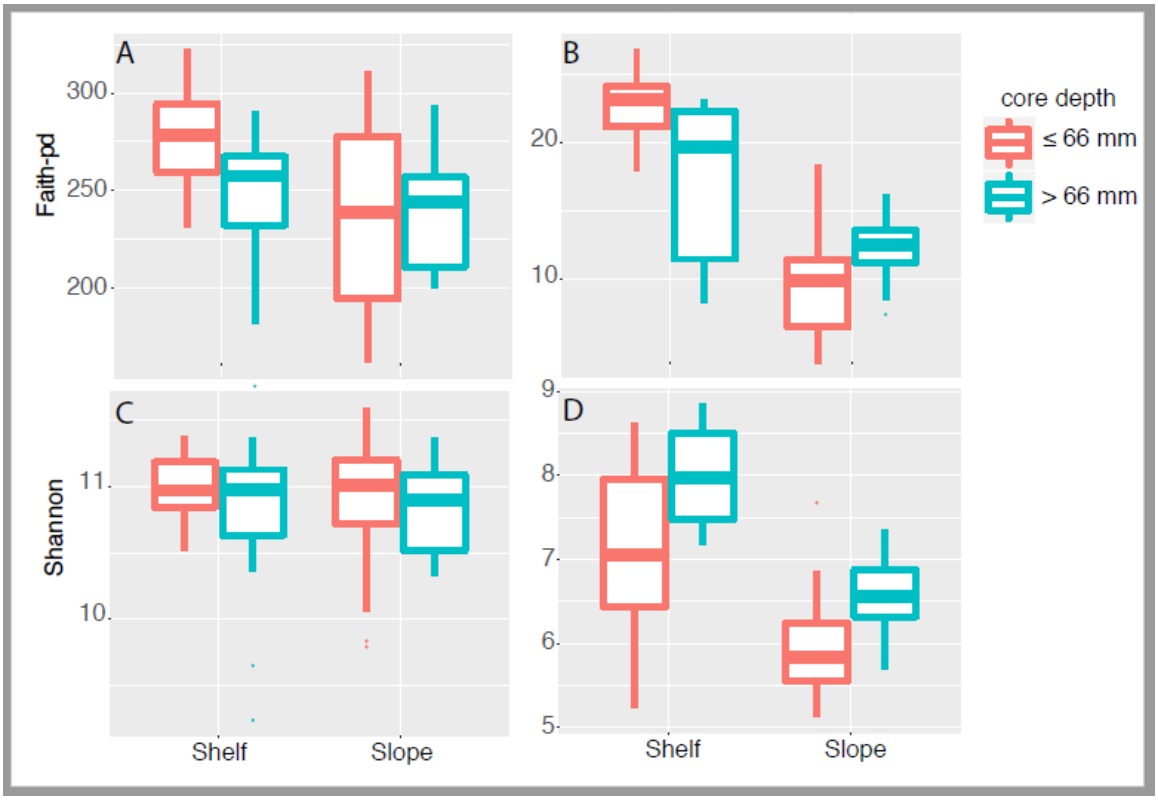

Figure D 9: Changes in alpha diversity between shelf and slope, and between sediment samples above (red) and below (blue) 66 mm sediment core depth. These analysis were performed using Faith phylogenetic diversity (A and B), and Shannon diversity (C and D) metrics for both the prokaryotic (A and C) and archaea specific (B and D) datasets.

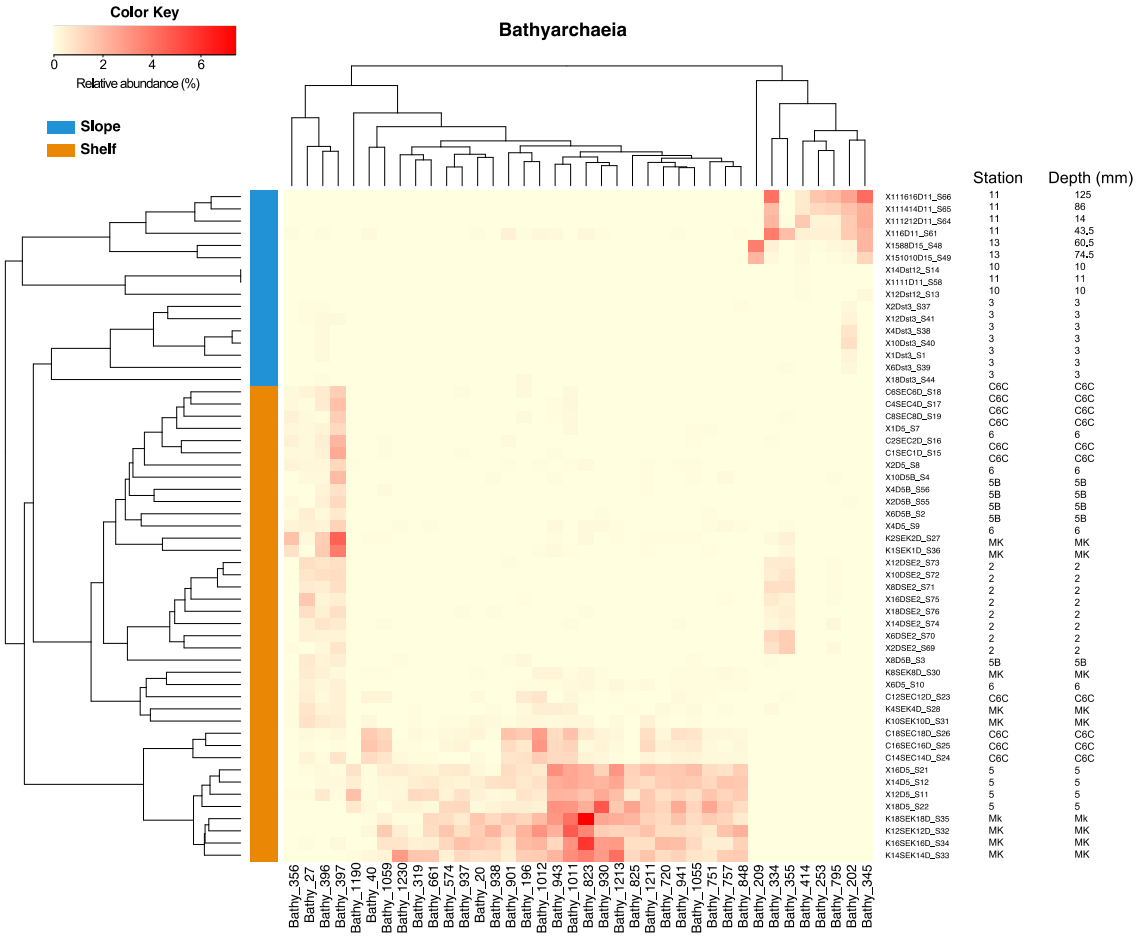

Figure D 10: Heatmap representing Bathyarchaeia ASVs from the archaea specific dataset with a relative abundance >1.5 %. heat map showing changes in relative abundance of ASVs in this group between shelf (orange) and slope (blue) samples.

APPENDIX E. SUPPLEMENTAL INFORMATION FOR CHAPTER 6

E.1 Geochemical profiles of shelf stations

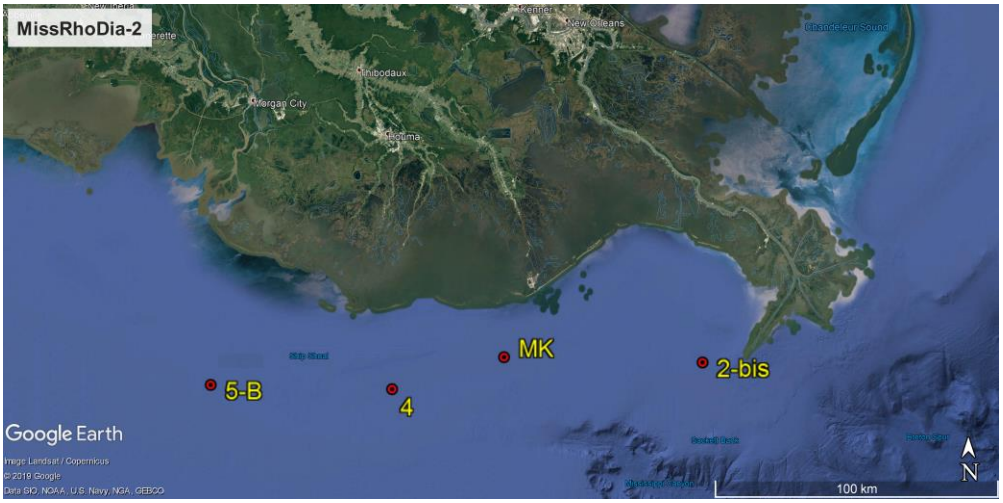

Figure E 1 Station locations of shelf sediment cores collected during the research cruise in July-August 2017.

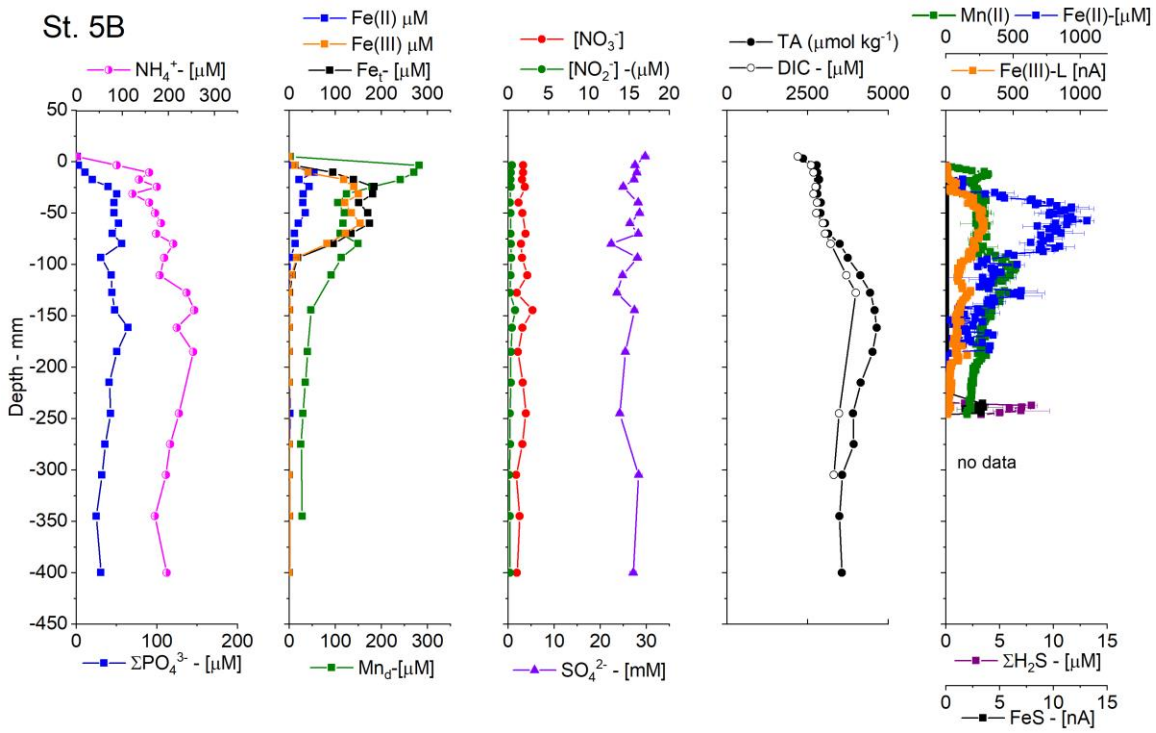

Figure E 2 Depth profiles at St. 5B of pore water species NH_4^+ and ΣPO_4^{3-}(first panel), Fe^{2+}, $Fe(III)_d$, Fe_t, Mn_d (second panel), NO_3^-, NO_2^-, and SO_4^{2-} (third panel) and DIC and total alkalinity (TA) (forth panel) as well as depth microprofiles of O_2, Mn^{2+}, Fe^{2+}, H_2S, org-Fe(III) complexes and FeS_{aq} (last panel) obtained with voltammetric and potentiometric microelectrodes.

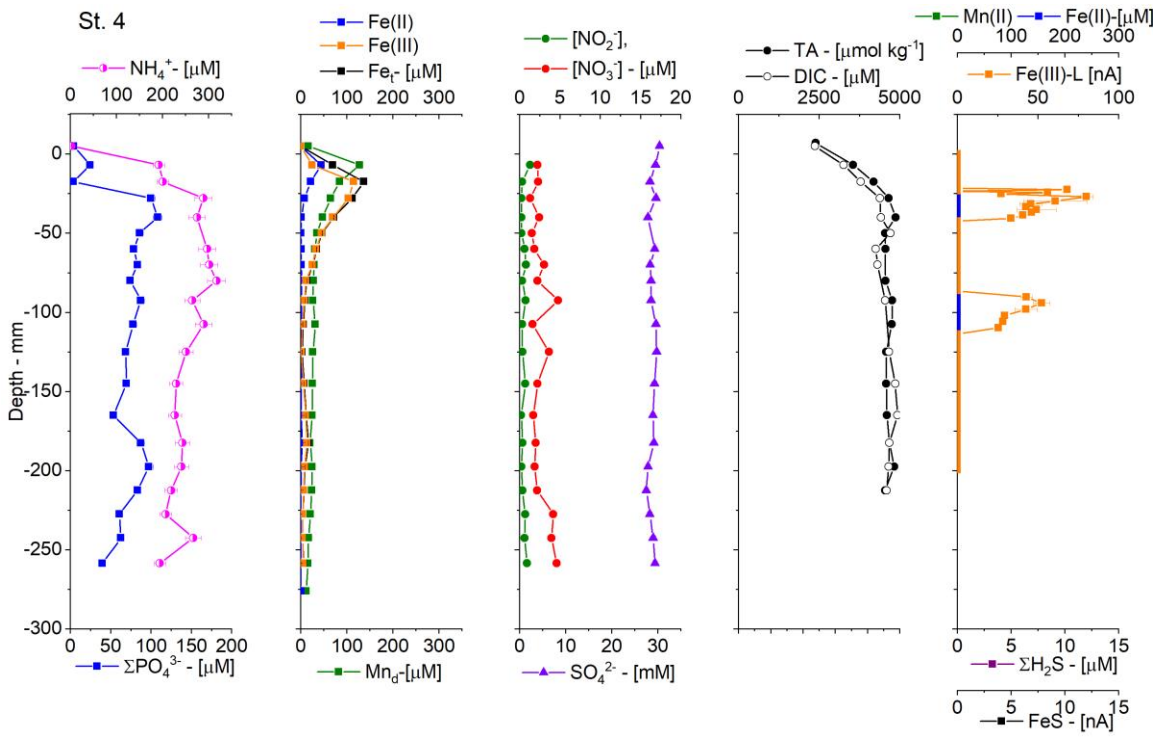

Figure E 3 Depth profiles at St. 4 of pore water species NH_4^+ and ΣPO_4^{3-}(first panel), Fe^{2+}, $Fe(III)_d$, Fe_t, Mn_d (second panel), NO_3^-, NO_2^-, and SO_4^{2-} (third panel) and DIC and total alkalinity (TA) (forth panel) as well as depth microprofiles of O_2, Mn^{2+}, Fe^{2+},

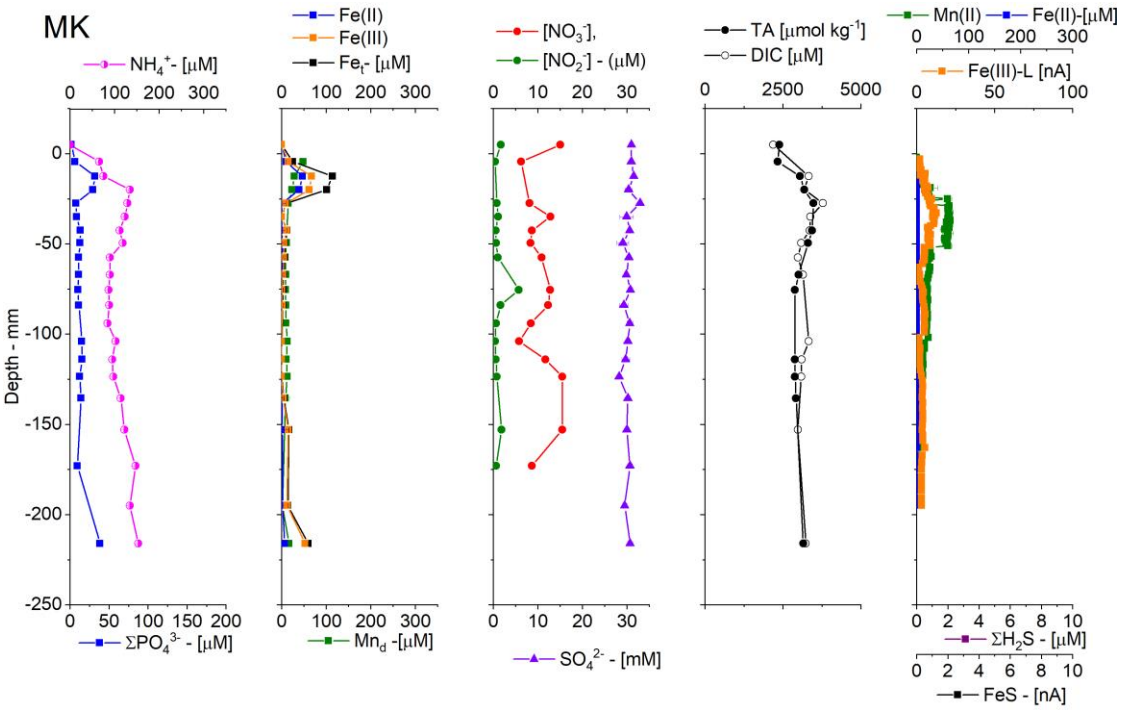

Figure E 4 Depth profiles at St. MK of pore water species NH_4^+ and ΣPO_4^{3-}(first panel), Fe^{2+}, $Fe(III)_d$, Fe_t, Mn_d (second panel), NO_3^-, NO_2^-, and SO_4^{2-} (third panel) and DIC and total alkalinity (TA) (forth panel) as well as depth microprofiles of O_2, Mn^{2+}, Fe^{2+}, H_2S, org-Fe(III) complexes and FeS_{aq} (last panel) obtained with voltammetric and potentiometric microelectrodes.

E.2 Thermodynamic calculations

The Gibbs free energy of reaction (ΔGr) was calculated for the reduction of ferrihydrite ($Fe(OH)_3$), goethite (FeOOH), pyrolusite (MnO_2), and sulfate (SO_4^{2-}) coupled to the oxidation of acetate (CH_3COOH) (Eqs. 1-3) in each section of the sediment cores using in-situ concentrations. ΔG_r was computed over a range of the reduced product concentrations (Fe(II), Mn(II), and HS^- 10^{-9}-1 M) in standard seawater conditions: 1 bar, I=0.73, $[SO_4^{2-}]$= 28 mM, pH=7.4, $[HCO_3^-]$= 2.5 mM at 2, 13 and 25°C (Beckler et al. 2016). Gibbs free energies of reaction in standard state conditions (ΔG_r^0) for ferrihydrite (ΔG_f^0 $Fe(OH)_3$ = - 705 kJ mol^{-1}), goethite (ΔG_f^0 FeOOH = - 488.6 kJ mol^{-1}), pyrolusite (ΔG_f^0 MnO_2 = - 465.1 kJ mol^{-1}), and sulfate (ΔG_f^0 SO_4^{2-} = -744.6 kJ mol^{-1}) were obtained from the literature (Stumm and Morgan, 1996).

$$CH_3COOH + 8Fe(OH)_3 + 14H^+ \rightarrow 8Fe^{2+} + 2HCO_3^- + 20H_2O \quad \text{(E1)}$$

$$CH_3COOH + 4MnO_2 + 6H^+ \rightarrow 4Mn^{2+} + 2HCO_3^- + 4H_2O \quad \text{(E2)}$$

$$CH_3COOH + SO_4^{2-} \rightarrow HS^- + 2HCO_3^- + H^+ \quad \text{(E3)}$$

E.3 Reaction network, rate laws, overall rates laws, and kinetic parameters used in the one-dimensional transient reactive transport model

Table E 1: Respiration reactions involved in the remineralization of natural organic matter used in the 1D transient reactive transport model MATSEDLAB (R1 = aerobic respiration; R2 = denitrification; R3 = dissimilatory manganese reduction; R4 = dissimilatory iron reduction; and R5 = sulfate reduction). The C:N ratio is used to set up the stoichiometric coefficients x and y in the model.

Reaction	Rate
$(CH_2O)_x(NH_3)_y(H_3PO_4) + xO_{2(aq)} \rightarrow xHCO_3^- + yNH_4^+ + HPO_4^{2-} + (x + y + 2)H^+$	R1
$5(CH_2O)_x(NH_3)_y(H_3PO_4) + 4xNO_3^- \rightarrow 2xN_2 + 5xHCO_3^- + 5yNH_4^+ + 5HPO_4^{2-} + (x - 5y + 10)H^+ + 2xH_2O$	R2
$(CH_2O)_x(NH_3)_y(H_3PO_4) + 2xMnO_{2(s)} + (3x + y - 2)H^+ \rightarrow 2xMn^{2+} + xHCO_3^- + yNH_4^+ + HPO_4^{2-} + 2xH_2O$	R3
$(CH_2O)_x(NH_3)_y(H_3PO_4) + 4xFe(OH)_{3(s)} + (7x + y - 2)H^+ \rightarrow 4xFe^{2+} + xHCO_3^- + yNH_4^+ + HPO_4^{2-} + 10xH_2O$	R4
$2(CH_2O)_x(NH_3)_y(H_3PO_4) + xSO_4^{2-} \rightarrow xHS^- + 2xHCO_3^- + 2yNH_4^+ + 2HPO_4^{2-} + (x - 2y + 4)H^+$	R5

Table E 2: Side abiotic and bacterial reactions used in the 1D transient reactive transport model MATSEDLAB (R6 = oxygenic oxidation of Fe2+; R7 = oxygenic oxidation of Mn^{2+}; R8 = aerobic nitrification; R9 = oxygenic sulfide oxidation; R10 = manganese reduction by dissolved sulfide; R11 = manganese reduction by Fe^{2+}; R12 = iron reduction by dissolved sulfide; R13 = precipitation and dissolution of manganese carbonates; R14 = precipitation and dissolution of iron carbonates; R15 = precipitation and dissolution of iron sulfide minerals).

Reaction	Rate
$4Fe^{2+} + O_2 + 10\,H_2O \rightarrow 4Fe(OH)_{3(s)} + 8H^+$	R6
$2Mn^{2+} + O_2 + 2H_2O \rightarrow 2MnO_{2(s)} + 4H^+$	R7
$NH_4^+ + 2O_2 \rightarrow NO_3^- + H_2O + 2H^+$	R8
$2H_2S + O_2 \rightarrow 2S^{(0)} + 2H_2O$	R9
$MnO_2 + H_2S + 2H^+ \rightarrow Mn^{2+} + S^{(0)} + 2H_2O$	R10
$2Fe(OH)_{3(s)} + H_2S + 4H^+ \rightarrow 2Fe^{2+} + S^{(0)} + 6H_2O$	R11
$Mn^{2+} + HCO_3^- \leftrightarrow MnCO_{3(s)} + H^+$	R12
$Fe^{2+} + HCO_3^- \leftrightarrow FeCO_{3(s)} + H^+$	R13
$Fe^{2+} + H_2S \leftrightarrow FeS_{(s)} + 2H^+$	R14

Table E 3: Rate laws used in the reaction network of the 1D transient reactive transport model MATSEDLAB.

$$R_1 = -R_c \frac{R_{m1}[O_2]}{(K_{m1} + [O_2])}$$

$$R_2 = -R_c \frac{R_{m2}[NO_3^-]}{(K_{m2} + [NO_3^-])} \frac{k_{inO2}}{(k_{inO2} + [O_2])}$$

$$R_3 = -R_c \frac{R_{m3}[MnO_2]}{(K_{m3} + [MnO_2])} \frac{k_{inO2}}{(k_{inO2} + [O_2])} \frac{k_{inNO3}}{(k_{inNO3} + [NO_3^-])}$$

$$R_4 = -R_c \frac{R_{m4}[Fe\{OH)_3]}{(K_{m4} + [Fe\{OH)_3])} \frac{k_{inO2}}{(k_{inO2} + [O_2])} \frac{k_{inNO3}}{(k_{inNO3} + [NO_3^-])}$$

$$R_5 = -R_c \frac{R_{m5}[SO_4^{2-}]}{(K_{m5} + [SO_4^{2-}])} \frac{k_{inO2}}{(k_{inO2} + [O_2])} \frac{k_{inNO3}}{(k_{inNO3} + [NO_3^-])} \frac{k_{inFeOH3}}{(k_{inFeOH3} + [Fe\{OH)_3])}$$

$$R_c = k_{org}[NOM]$$

$$R_6 = -k_6[Fe^{2+}][O_2][OH^-]^2$$

$$R_7 = -k_7[Mn^{2+}][O_2][OH^-]^2$$

$$R_8 = -k_8[NH_4^+][O_2]$$

$$R_9 = -k_9[H_2S][O_2]$$

$$R_{10} = -k_{10}[MnO_2][H_2S]$$

$$R_{11} = -k_{12}[Fe\{OH)_3][H_2S]$$

$R_{12} = -\delta k_{12}(\Omega_{MnCO3} - 1)$ with $\delta = 0$ *when* $\Omega_{MnCO3} > 1$[a]
$\delta = 1$ *when* $\Omega_{MnCO3} < 1$[a]

$R_{-12} = -\delta k_{21}(\Omega_{MnCO3} - 1)$ with $\delta = 1$ *when* $\Omega_{MnCO3} > 1$[a]
$\delta = 0$ *when* $\Omega_{MnCO3} < 1$[a]

$R_{13} = -\delta k_{13}(\Omega_{FeCO3} - 1)$ with $\delta = 0$ *when* $\Omega_{FeCO3} > 1$[b]
$\delta = 1$ *when* $\Omega_{FeCO3} < 1$[b]

$R_{-13} = -\delta k_{31}(\Omega_{FeCO3} - 1)$ with $\delta = 1$ *when* $\Omega_{FeCO3} > 1$[b]
$\delta = 0$ *when* $\Omega_{FeCO3} < 1$[b]

$R_{14} = -\delta k_{14}(\Omega_{FeS} - 1)$ with $\delta = 0$ *when* $\Omega_{FeS} > 1$[c]
$\delta = 1$ *when* $\Omega_{FeS} < 1$[c]

$R_{-14} = -\delta k_{41}(\Omega_{FeS} - 1)$ with $\delta = 1$ *when* $\Omega_{FeS} > 1$[c]
$\delta = 0$ *when* $\Omega_{FeS} < 1$[c]

[a] where $\Omega_{MnCO3} = \frac{[Mn^{2+}][HCO_3^-]}{K_{s12}[H^+]}$ with $K_{s12} = 10^{-5.39}$ (Jensen et al., 2002)

[b] where $\Omega_{FeCO3} = \frac{[Fe^{2+}][HCO_3^-]}{K_{s13}[H^+]}$ with $K_{s13} = 10^{-5.03}$ (Jensen et al., 2002)

[c] where $\Omega_{FeS} = \frac{[Fe^{2+}][HS^-]}{K_{s14}[H^+]}$ with $K_{s14} = 10^{-3.5}$ (Rickard, 2005)

Table E 4: Overall rates laws used in the reaction network of the 1D transient reactive transport model MATSEDLAB.

$$\frac{d[O_2]}{dt} = R_1 + \frac{1}{4}R_6 + \frac{1}{2}R_7 + 2R_8 + 2R_9$$

$$\frac{d[NO_3^-]}{dt} = \frac{4}{5}R_2 - R_8$$

$$\frac{d[MnO_2]}{dt} = 2R_3 - R_7 + R_{10}$$

$$\frac{d[Fe\{OH)_3]}{dt} = 4R_4 - R_6 + 2R_{11}$$

$$\frac{d[SO_4^{2-}]}{dt} = \frac{1}{2}R_5 - R_9$$

$$\frac{d[Fe^{2+}]}{dt} = -4R_4 - 2R_{11} + R_6 - R_{13} - R_{-13} - R_{14} - R_{-14}$$

$$\frac{d[Mn^{2+}]}{dt} = -2R_3 + R_7 - R_{10} - R_{12} - R_{-12}$$

$$\frac{d[NH_4^+]}{dt} = R_8 + \frac{1}{CNr}R_c$$

$$\frac{d[H_2S]}{dt} = -\frac{1}{2}R_5 + R_9 + R_{10} + R_{11} - R_{14} - R_{-14}$$

$$\frac{d[MnCO_3]}{dt} = R_{12} + R_{-12}$$

$$\frac{d[FeCO_3]}{dt} = R_{13} + R_{-13}$$

$$\frac{d[FeS]}{dt} = R_{14} + R_{-14}$$

Table E 5: Kinetic constants fixed at each station in the 1D transient reactive transport model MATSEDLAB.

Parameter (units)	Values	Reference
k_6 (mM^{-3} yr^{-1})	$10^{12.1}$	Millero et al., 1987a
k_7 (mM^{-3} yr^{-1})	$10^{9.89}$	Sung and Morgan, 1981
k_8 (mM^{-1} yr^{-1})	50	Wang and Van Cappellen, 1996
k_9 (mM^{-1} yr^{-1})	10^{6}	Millero et al., 1987b
k_{10} (mM^{-1} yr^{-1})	$10^{4.7}$	Yao and Millero, 1993
k_{11} (mM^{-1} yr^{-1})	$10^{-1.32}$	Yao and Millero, 1996

Table E 6: Kinetic constants adjusted at each station in the 1D transient reactive transport model MATSEDLAB to obtain the best fit to the data.

Parameter (units)	St. 2b	St. 13	St. 11	St. 15	St. 12
R_{m1} (mM yr^{-1})	5	0.8	10	55	3
K_{m1} (mM)	0.01	0.02	0.001	0.001	0.01
R_{m2} (mM yr^{-1})	200	20	20	20	10
K_{m2} (mM)	0.05	0.05	0.05	0.01	0.05
R_{m3} (mM yr^{-1})	6	6	7	20	5
K_{m3} (mM)	100	300	3000	300	300
R_{m4} (mM yr^{-1})	1.2	0.5	0.12	6	0.18
K_{m4} (mM)	1000	1000	1000	3000	3000
R_{m5} (mM yr^{-1})	4	12	0.12	0.12	3.97
K_{m5} (mM)	1.6	1.6	1.6	1.6	1.6
k_{inO2}	5	0.5	0.05	0.5	0.5
k_{inNO3}	100	100	100	100	100
$k_{inFe(OH)3}$	5	1.27	1.27	1	0.5
k_{12} (μmol g^{-1} yr^{-1})	$10^{-2.55}$	$10^{-2.55}$	$10^{-3.42}$	$10^{-1.91}$	$10^{-3.63}$
k_{21} (μmol g^{-1} yr^{-1})	0	$10^{-3.1}$	$10^{-3.72}$	$10^{-3.06}$	$10^{-3.13}$
k_{13} (μmol g^{-1} yr^{-1})	$10^{-0.23}$	$10^{-0.22}$	$10^{-0.23}$	$10^{-2.13}$	$10^{-0.45}$
k_{31} (μmol g^{-1} yr^{-1})	0	0	0	0	0
k_{14} (μmol g^{-1} yr^{-1})	$10^{0.09}$	$10^{0.22}$	$10^{0.09}$	$10^{0.09}$	$10^{-1.18}$
k_{41} (μmol g^{-1} yr^{-1})	$10^{-3.72}$	$10^{-3.72}$	$10^{-3.72}$	$10^{-3.72}$	$10^{-3.72}$
k_{org}	2.47	1.37	5.7	14.8	40

Table E 7: Other parameters adjusted at each station in the 1D transient reactive transport model MATSEDLAB to obtain the best fit to the data. BC0 = boundary condition at sediment-water interface

Parameter (units)	St. 2b	St. 13	St. 11	St. 15	St. 12
NOM (mM)	12	4	10	0.5	12
C:N ratio	10	10	15.5	10	15.5
Mean Porosity	0.86	0.87	0.86	0.8	0.75
Sedimentation (cm yr^{-1})	2.5	0.7	0.07	0.5	0.09
Bioturbation Coefficient at sediment-water interface (cm^2 yr^{-1})	6.94	6.94	6.94	6.94	6.94
Bioturbation decay constant (yr^{-1})	0.45	0.25	0.25	0.25	0.25
Bioturbation coefficient at depth (cm^2 yr^{-1})	0.001	0.001	0.001	0.001	0.001
BC0 MnO_2 (µmol g^{-1})	63.2	20.4	15.8	8.1	43.1
BC0 $Fe(OH)_3$ (µmol g^{-1})	73.7	22.9	2.6	18.6	11.9

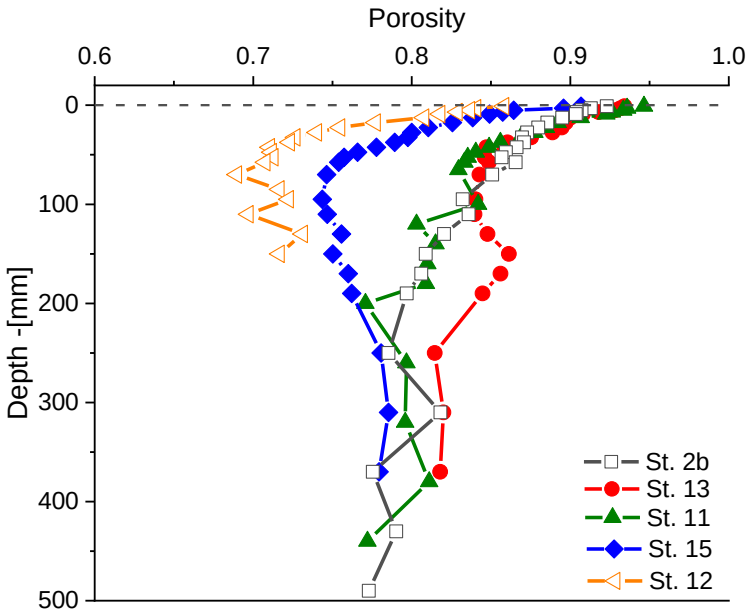

Figure E 5 Porosity as a function of depth for each core collected across the western and eastern transects

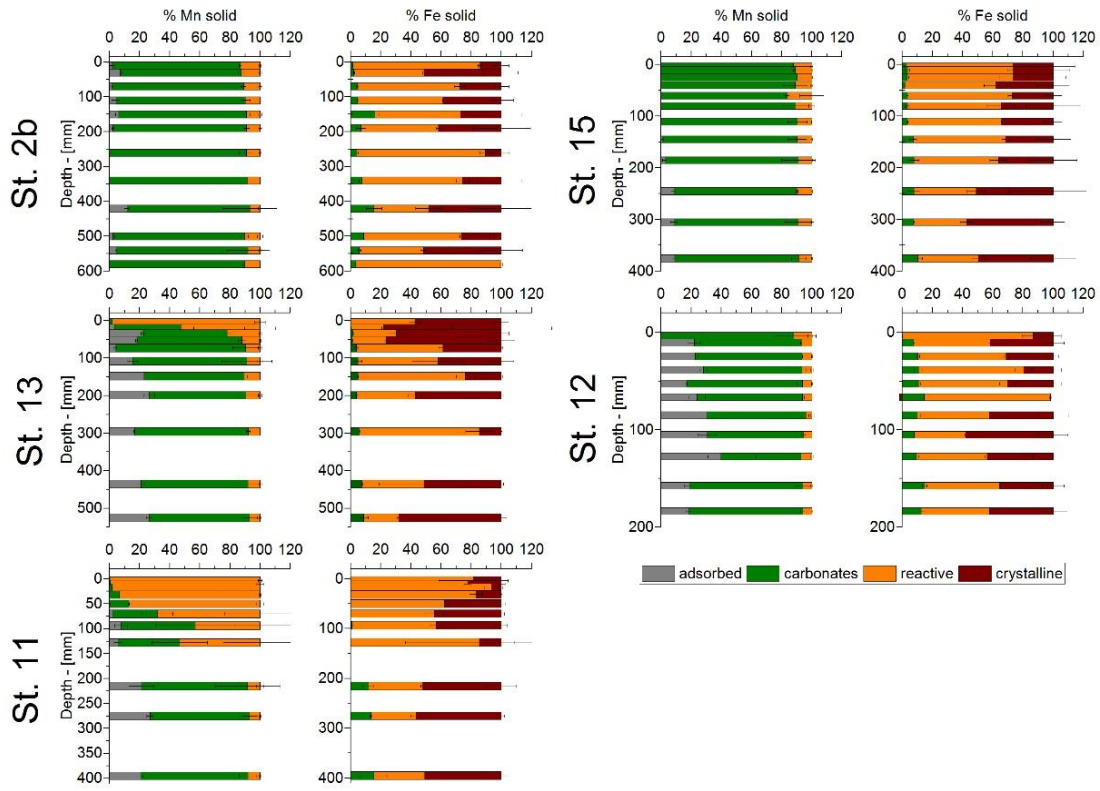

Figure E 6: Percentage of solid phase Mn (left) and Fe (right) partitioned into the adsorbed, carbonate, reactive and crystalline phases at each station. Note, the depth scales vary based on the length of the core.

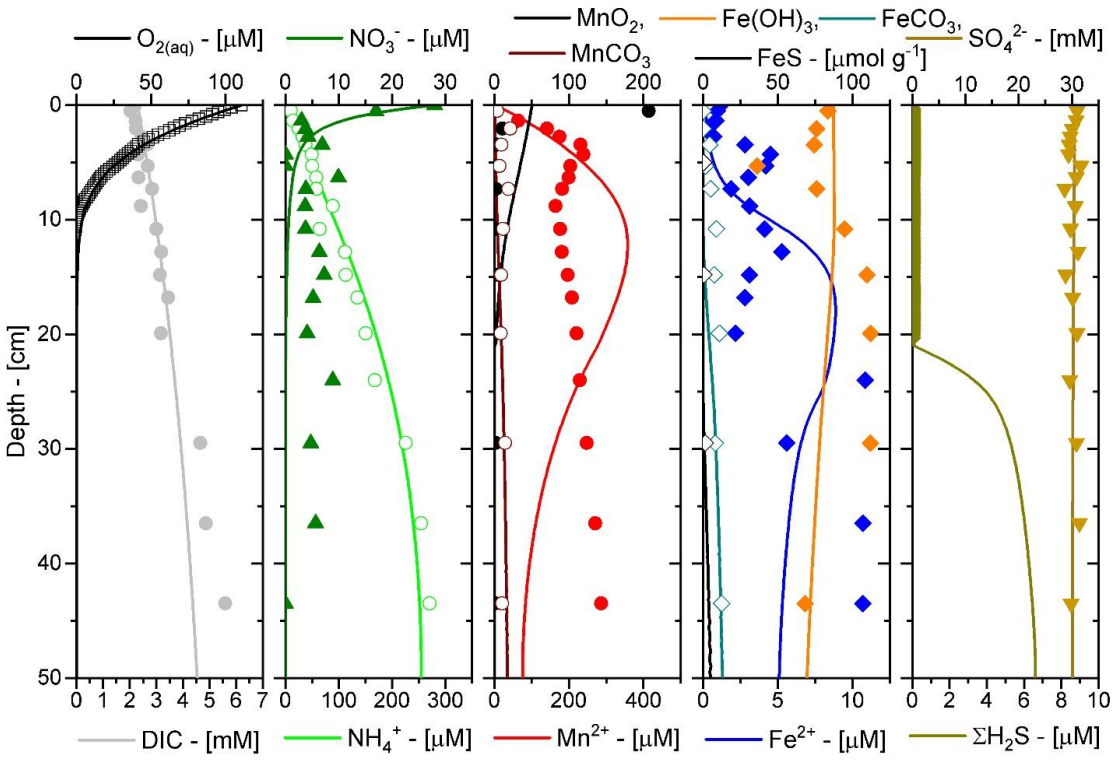

Figure E 7: Example of modeled depth profiles of the main species involved in diagenetic processes at St. 13 (plain lines) compared to experimental depth profiles (scatter points). Only respiration rates (aerobic, denitrification, Mn reduction, Fe reduction, and SO_4^{2-} reduction) were optimized to fit the experimental data at steady-state. Rate constants of abiotic processes and biological oxidation of NH_4^+, ΣH_2S, and Mn^{2+} by $O_{2(aq)}$ were fixed at each station.

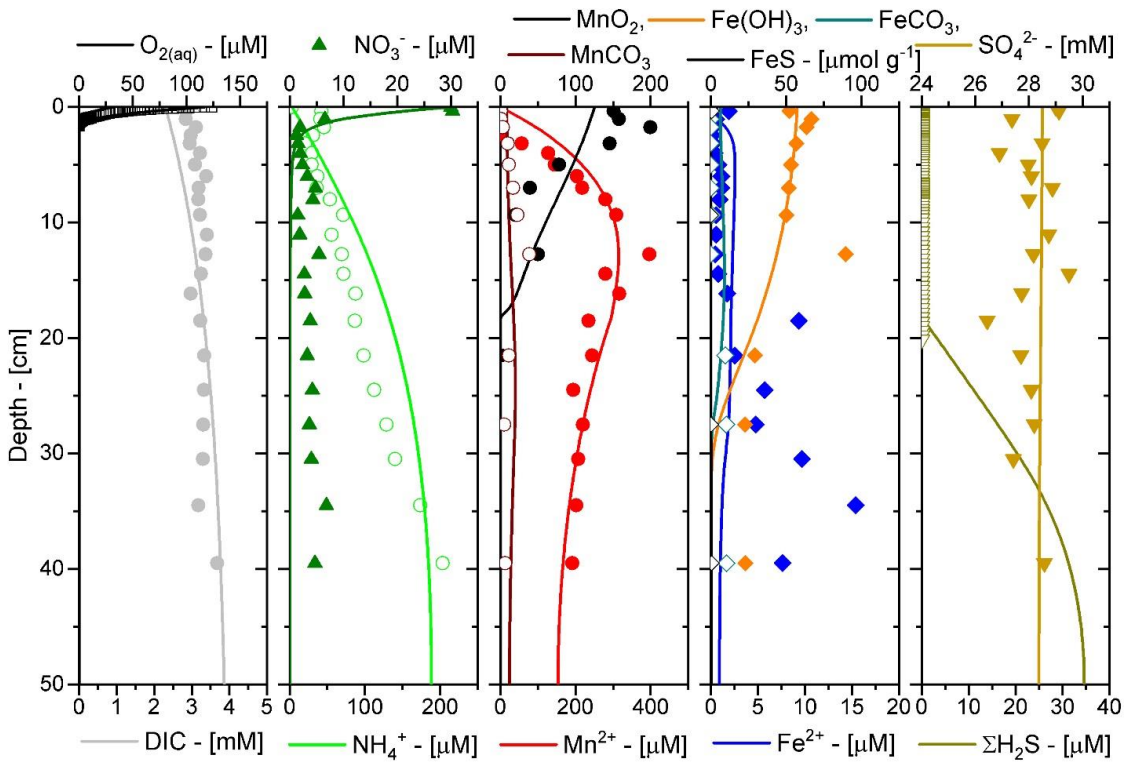

Figure E 8: Example of modeled depth profiles of the main species involved in diagenetic processes at St. 11 (plain lines) compared to experimental depth profiles (scatter points). Only respiration rates (aerobic, denitrification, Mn reduction, Fe reduction, and SO_4^{2-} reduction) were optimized to fit the experimental data at steady-state. Rate constants of abiotic processes and biological oxidation of NH_4^+, ΣH_2S, and Mn^{2+} by $O_{2(aq)}$ were fixed at each station.

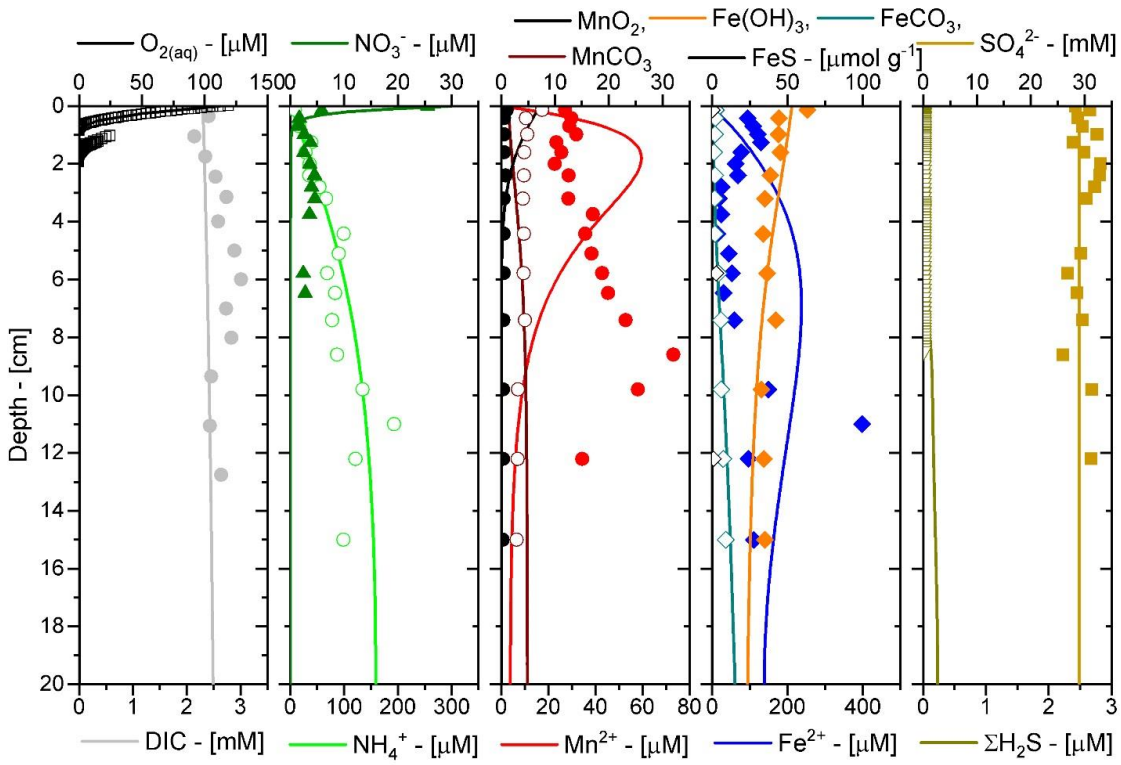

Figure E 9: Example of modeled depth profiles of the main species involved in diagenetic processes at St. 15 (plain lines) compared to experimental depth profiles (scatter points). Only respiration rates (aerobic, denitrification, Mn reduction, Fe reduction, and SO_4^{2-} reduction) were optimized to fit the experimental data at steady-state. Rate constants of abiotic processes and biological oxidation of NH_4^+, ΣH_2S, and Mn^{2+} by $O_{2(aq)}$ were fixed at each station.

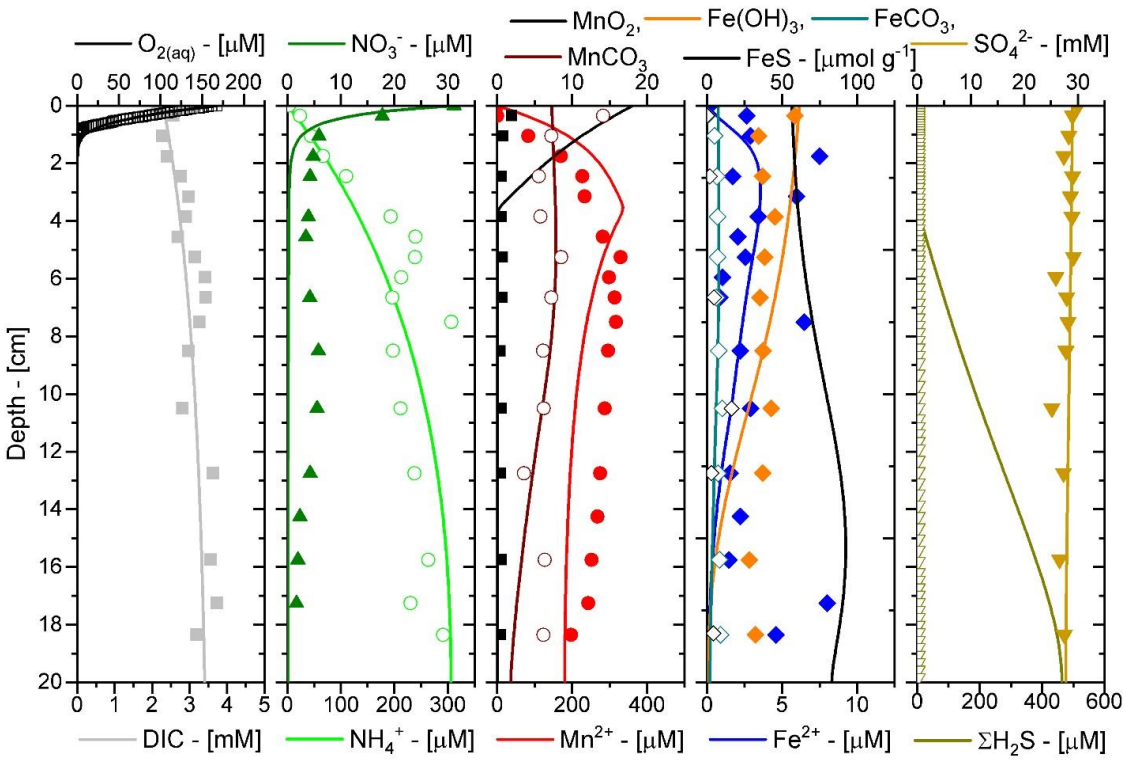

Figure E 10: Example of modeled depth profiles of the main species involved in diagenetic processes at St. 12 (plain lines) compared to experimental depth profiles (scatter points). Only respiration rates (aerobic, denitrification, Mn reduction, Fe reduction, and SO_4^{2-} reduction) were optimized to fit the experimental data at steady-state. Rate constants of abiotic processes and biological oxidation of NH_4^+, ΣH_2S, and Mn^{2+} by $O_{2(aq)}$ were fixed at each station.

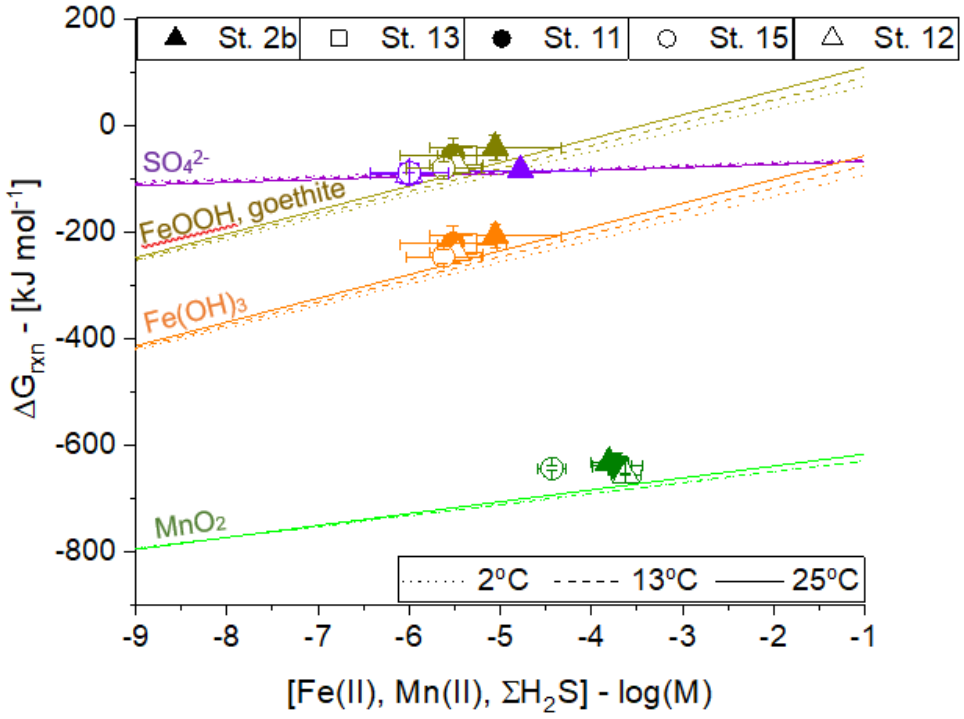

Figure E 11: Theoretical (lines) and experimental (scatter points) Gibbs Free energy of reaction for the anaerobic respiration of pyrolusite (MnO_2), ferrihydrite ($Fe(OH)_3$), goethite (FeOOH), and SO_4^{2-} as a function of the reduced metabolite concentration (Mn(II), Fe(II), and HS^-). See the text for details of these calculations.

REFERENCES

Ahmed, K.M., Bhattacharya, P., Hasan, M.A., Akhter, S.H., Alam, S.M.M., Bhuyian, M.A.H., Imam, M.B., Khan, A.A. and Sracek, O. (2004) Arsenic enrichment in groundwater of the alluvial aquifers in Bangladesh: an overview. Applied Geochemistry 19, 181-200.

Ajees, A.A. and Rosen, B.P. (2015) As(III) S-Adenosylmethionine Methyltransferases and Other Arsenic Binding Proteins. Geomicrobiology Journal 32, 570-576.

Aller, R.C. (1982) Carbonate Dissolution in Nearshore Terrigenous Muds: The Role of Physical and Biological Reworking. The Journal of Geology 90, 79-95.

Aller, R.C. (1994) The sedimentary Mn cycle in Long Island Sound: Its role as intermediate oxidant and the influence of bioturbation, O2, and Corg flux on diagenetic reaction balances. Journal of Marine Research 52, 259-295.

Aller, R.C. (1998) Mobile deltaic and continental shelf muds as suboxic, fluidized bed reactors. Marine Chemistry 61, 143-155.

Aller, R.C. and Aller, J.Y. (1998) The effect of biogenic irrigation intensity and solute exchange on diagenetic reaction rates in marine sediments. Journal of Marine Research 56, 905-936.

Aller, R.C., Blair, N.E., Xia, Q. and Rude, P.D. (1996) Remineralization rates, recycling, and storage of carbon in Amazon shelf sediments. Continental Shelf Research 16, 753-786.

Aller, R.C., Charnock, H., Edmond John, M., McCave, I.N., Rice, A.L. and Wilson, T.R.S. (1990) Bioturbation and manganese cycling in hemipelagic sediments. Philosophical Transactions of the Royal Society of London. Series A, Mathematical and Physical Sciences 331, 51-68.

Allison, M.A., Demas, C.R., Ebersole, B.A., Kleiss, B.A., Little, C.D., Meselhe, E.A., Powell, N.J., Pratt, T.C. and Vosburg, B.M. (2012) A water and sediment budget for the lower Mississippi–Atchafalaya River in flood years 2008–2010: Implications for sediment discharge to the oceans and coastal restoration in Louisiana. Journal of Hydrology 432-433, 84-97.

Allison, M.A. and Pratt, T.C. (2017) Discharge controls on the sediment and dissolved nutrient transport flux of the lowermost Mississippi River: Implications for export to the ocean and for delta restoration. Journal of Hydrology 555, 1-14.

Amirbahman, A., Kent, D.B., Curtis, G.P. and Davis, J.A. (2006) Kinetics of sorption and abiotic oxidation of arsenic(III) by aquifer materials. Geochimica et Cosmochimica Acta 70, 533-547.

Amstaetter, K., Borch, T., Larese-Casanova, P. and Kappler, A. (2010) Redox Transformation of Arsenic by Fe(II)-Activated Goethite (α-FeOOH). Environmental Science & Technology 44, 102-108.

Anderson, P.R. and Benjamin, M.M. (1990) Surface and bulk characteristics of binary oxide suspensions. Environmental Science & Technology 24, 692-698.

Andrews, D. and Bennett, A. (1981) Measurements of diffusivity near the sediment-water interface with a fine-scale resistivity probe. Geochimica et Cosmochimica Acta 45, 2169-2175.

Anschutz, P., Dedieu, K., Desmazes, F. and Chaillou, G. (2005) Speciation, oxidation state, and reactivity of particulate manganese in marine sediments. Chemical Geology 218, 265-279.

Anschutz, P., Sundby, B., Lefrancois, L., Luther, G.W. and Mucci, A. (2000) Interactions between metal oxides and species of nitrogen and iodine in bioturbated marine sediments. Geochimica Et Cosmochimica Acta 64, 2751-2763.

Arai, Y., Elzinga, E.J. and Sparks, D.L. (2001) X-ray Absorption Spectroscopic Investigation of Arsenite and Arsenate Adsorption at the Aluminum Oxide–Water Interface. Journal of Colloid and Interface Science 235, 80-88.

Arnold, R.G., DiChristina, T.J. and Hoffmann, M.R. (1988) Reductive dissolution of fe(III) oxides by Pseudomonas sp. 200. 32, 1081-1096.

Arrigo, K.R. (2005) Marine microorganisms and global nutrient cycles (vol 437, pg 349, 2005). Nature 438, 122-122.

Bahr, M., Crump, B.C., Klepac-Ceraj, V., Teske, A., Sogin, M.L. and Hobbie, J.E. (2005) Molecular characterization of sulfate-reducing bacteria in a New England salt marsh. Environmental Microbiology 7, 1175-1185.

Balashova, V. and Zavarzin, G. (1979) Anaerobic reduction of ferric iron by hydrogen bacteria. Mikrobiologiia 48, 773-778.

Ballantyne, J. and Moore, J. (1987) Arsenic geochemistry in geothermal systems. Geochimica et Cosmochimica Acta 53, 475-483.

Bartlett, R., Mortimer, R.J.G. and Morris, K. (2008) Anoxic nitrification: Evidence from Humber Estuary sediments (UK). Chemical Geology 250, 29-39.

Bartlett, R., Mortimer, R.J.G. and Morris, K.M. (2007) The biogeochemistry of a manganese-rich Scottish sea loch: Implications for the study of anoxic nitrification. Continental Shelf Research 27, 1501-1509.

Bauer, J.E., Cai, W.-J., Raymond, P.A., Bianchi, T.S., Hopkinson, C.S. and Regnier, P.A. (2013) The changing carbon cycle of the coastal ocean. Nature 504, 61-70.

Beckler, J.S., Kiriazis, N., Rabouille, C., Stewart, F.J. and Taillefert, M. (2016) Importance of microbial iron reduction in deep sediments of river-dominated continental-margins. Marine Chemistry 178, 22-34.

Beckler, J.S., Nuzzio, D.B. and Taillefert, M. (2014) Development of single-step liquid chromatography methods with ultraviolet detection for the measurement of inorganic anions in marine waters. Limnology and Oceanography: Methods 12, 563-576.

Bednar, A.J., Garbarino, J.R., Burkhardt, M.R., Ranville, J.F. and Wildeman, T.R. (2004) Field and laboratory arsenic speciation methods and their application to natural-water analysis. Water Research 38, 355-364.

Bendschneider, K. and Robinson, R. (1952) A new spectrophotometric method for the determination of nitrite in seawater. Journal of Marine Research 11, 87-96.

Bentley, R. and Chasteen, T.G. (2002) Microbial Methylation of Metalloids: Arsenic, Antimony, and Bismuth. Microbiology and Molecular Biology Reviews 66, 250-271.

Bertrand, J.-C., Bonin, P., Ollivier, B., Alain, K., Godfroy, A., Pradel, N. and Normand, P. (2018) Evolutionary success of prokaryotes, Prokaryotes and Evolution. Springer, pp. 131-240.

Beulig, F., Røy, H., Glombitza, C. and Jørgensen, B.B. (2018) Control on rate and pathway of anaerobic organic carbon degradation in the seabed. Proceedings of the National Academy of Sciences 115, 367.

Beulig, F., Røy, H., McGlynn, S. and Jørgensen, B. (2019) Cryptic CH 4 cycling in the sulfate–methane transition of marine sediments apparently mediated by ANME-1 archaea. The ISME journal 13, 250-262.

Bianchi, T.S. (2011) The role of terrestrially derived organic carbon in the coastal ocean: A changing paradigm and the priming effect. Proceedings of the National Academy of Sciences 108, 19473.

Bianchi, T.S., Allison, M.A., Canuel, E.A., Corbett, D.R., McKee, B.A., Sampere, T.P., Wakeham, S.G. and Waterson, E. (2006) Rapid export of organic matter to the Mississippi Canyon. Eos, Transactions American Geophysical Union 87, 565-573.

Bianchi, T.S., Cui, X., Blair, N.E., Burdige, D.J., Eglinton, T.I. and Galy, V. (2018) Centers of organic carbon burial and oxidation at the land-ocean interface. Organic Geochemistry 115, 138-155.

Bianchi, T.S., Galler, J.J. and Allison, M.A. (2007) Hydrodynamic sorting and transport of terrestrially derived organic carbon in sediments of the Mississippi and Atchafalaya Rivers. Estuarine, Coastal and Shelf Science 73, 211-222.

Biddle, J.F., Lipp, J.S., Lever, M.A., Lloyd, K.G., Sørensen, K.B., Anderson, R., Fredricks, H.F., Elvert, M., Kelly, T.J. and Schrag, D.P. (2006) Heterotrophic Archaea dominate sedimentary subsurface ecosystems off Peru. Proceedings of the National Academy of Sciences 103, 3846-3851.

Bienhold, C., Boetius, A. and Ramette, A. (2012) The energy–diversity relationship of complex bacterial communities in Arctic deep-sea sediments. The ISME journal 6, 724-732.

Bienhold, C., Zinger, L., Boetius, A. and Ramette, A. (2016) Diversity and biogeography of bathyal and abyssal seafloor bacteria. PLoS One 11.

Blair, N.E. and Aller, R.C. (2012) The Fate of Terrestrial Organic Carbon in the Marine Environment. Annual Review of Marine Science 4, 401-423.

Bode, A.M. and Dong, Z. (2002) The paradox of arsenic: molecular mechanisms of cell transformation and chemotherapeutic effects. Critical Reviews in Oncology/Hematology 42, 5-24.

Boudreau, B.P. (1997) Diagenetic Models and Their Implementation. Springer, Berlin.

Boudreau, B.P., Mucci, A., Sundby, B., Luther, G.W. and Silverberg, N. (1998) Comparative diagenesis at three sites on the Canadian continental margin. Journal of Marine Research 56, 1259-1284.

Bowles, M.W., Mogollón, J.M., Kasten, S., Zabel, M. and Hinrichs, K.-U. (2014) Global rates of marine sulfate reduction and implications for sub–sea-floor metabolic activities. Science 344, 889.

Brendel, P.J. and Luther, G.W., III (1995) Development of a Gold Amalgam Voltammetric Microelectrode for the Determination of Dissolved Fe, Mn, O2, and S(-II) in Porewaters of Marine and Freshwater Sediments. Environmental Science & Technology 29, 751-761.

Bristow, G. and Taillefert, M. (2008) VOLTINT: A Matlab®-based program for semi-automated processing of geochemical data acquired by voltammetry. Computers & Geosciences 34, 153-162.

Broecker, W.S. and Peng, T.H. (1974) Gas exchange rates between air and sea. Tellus 26, 21-35.

Buffle, J. (1988) Complexation reactions in aquatic systems: An analytical approach. Ellis Horwood Limited, Chichester, England.

Bukin, S.V., Pavlova, O.N., Manakov, A.Y., Kostyreva, E.A., Chernitsyna, S.M., Mamaeva, E.V., Pogodaeva, T.V. and Zemskaya, T.I. (2016) The ability of microbial community of Lake Baikal bottom sediments associated with gas

discharge to carry out the transformation of organic matter under thermobaric conditions. Frontiers in microbiology 7, 690.

Burdige, D.J. (1993) The biogeochemistry of manganese and iron reduction in marine sediments. Earth-Science Reviews 35, 249-284.

Cai, W.-J., Hu, X., Huang, W.-J., Murrell, M.C., Lehrter, J.C., Lohrenz, S.E., Chou, W.-C., Zhai, W., Hollibaugh, J.T., Wang, Y., Zhao, P., Guo, X., Gundersen, K., Dai, M. and Gong, G.-C. (2011) Acidification of subsurface coastal waters enhanced by eutrophication. Nature Geoscience 4, 766.

Cai, W.-J. and Sayles, F.L. (1996) Oxygen penetration depths and fluxes in marine sediments. Marine Chemistry 52, 123-131.

Canfield, D.E. (1994) Factors influencing organic matter preservation in marine sediments. Chemical Geology 114, 315-329.

Canfield, D.E., Jørgensen, B.B., Fossing, H., Glud, R., Gundersen, J., Ramsing, N.B., Thamdrup, B., Hansen, J.W., Nielsen, L.P. and Hall, P.O.J. (1993a) Pathways of organic carbon oxidation in three continental margin sediments. Marine Geology 113, 27-40.

Canfield, D.E., Thamdrup, B. and Hansen, J.W. (1993b) The anaerobic degradation of organic matter in Danish coastal sediments: Iron reduction, manganese reduction, and sulfate reduction. Geochimica et Cosmochimica Acta 57, 3867-3883.

Carey, E. and Taillefert, M. (2005) The role of soluble Fe(III) in the cycling of iron and sulfur in coastal marine sediments. Limnology and Oceanography 50, 1129-1141.

Castelle, C.J., Wrighton, K.C., Thomas, B.C., Hug, L.A., Brown, C.T., Wilkins, M.J., Frischkorn, K.R., Tringe, S.G., Singh, A. and Markillie, L.M. (2015) Genomic expansion of domain archaea highlights roles for organisms from new phyla in anaerobic carbon cycling. Current biology 25, 690-701.

Catts, J.G. and Langmuir, D. (1986) Adsorption of Cu, Pb and Zn by δMnO2: applicability of the site binding-surface complexation model. Applied Geochemistry 1, 255-264.

Challenger, F. (1945) Biological Methylation. Chemical Reviews 36, 315-361.

Chaves, M.G.d., Silva, G.G.Z., Rossetto, R., Edwards, R.A., Tsai, S.M. and Navarrete, A.A. (2019) Acidobacteria subgroups and their metabolic potential for carbon degradation in sugarcane soil amended with vinasse and nitrogen fertilizers. Frontiers in microbiology 10, 1680.

Chen, J., Bhattacharjee, H. and Rosen, B.P. (2015a) ArsH is an organoarsenical oxidase that confers resistance to trivalent forms of the herbicide monosodium methylarsenate and the poultry growth promoter roxarsone. Molecular Microbiology 96, 1042-1052.

Chen, J., Madegowda, M., Bhattacharjee, H. and Rosen, B.P. (2015b) ArsP: a methylarsenite efflux permease. Molecular Microbiology 98, 625-635.

Chen, J. and Rosen, B.P. (2016) Organoarsenical Biotransformations by Shewanella putrefaciens. Environmental Science & Technology 50, 7956-7963.

Chen, S., Wang, P., Liu, H., Xie, W., Wan, X.S., Kao, S.-J., Phelps, T.J. and Zhang, C. (2020) Population dynamics of methanogens and methanotrophs along the salinity gradient in Pearl River Estuary: implications for methane metabolism. Applied Microbiology and Biotechnology 104, 1331-1346.

Cherry, J.A., Shaikh, A.U., Tallman, D.E. and Nicholson, R.V. (1979) Arsenic species as an indicator of redox conditions in groundwater. Journal of Hydrology 43, 373-392.

Chiu, V.Q. and Hering, J.G. (2000) Arsenic Adsorption and Oxidation at Manganite Surfaces. 1. Method for Simultaneous Determination of Adsorbed and Dissolved Arsenic Species. Environmental Science & Technology 34, 2029-2034.

Chow, S.S. and Taillefert, M. (2005) Biogeochemical cycling of arsenic at the sediment–water interface of a recently flooded freshwater sediment.

Chow, S.S. and Taillefert, M. (2009) Effect of arsenic concentration on microbial iron reduction and arsenic speciation in an iron-rich freshwater sediment. Geochimica et Cosmochimica Acta 73, 6008-6021.

Christen, K. (2001) Chickens, manure, and arsenic. Environmental Science & Technology 35, 184A-185A.

Cismasu, A.C., Levard, C., Michel, F.M. and Brown, G.E. (2013) Properties of impurity-bearing ferrihydrite II: Insights into the surface structure and composition of pure, Al- and Si-bearing ferrihydrite from Zn(II) sorption experiments and Zn K-edge X-ray absorption spectroscopy. Geochimica et Cosmochimica Acta 119, 46-60.

Clayton, T.D. and Byrne, R.H. (1993) Spectrophotometric seawater pH measurements: total hydrogen ion concentration scale calibration of m-cresol purple and at-sea results. Deep Sea Research Part I: Oceanographic Research Papers 40, 2115-2129.

Cleland, W.W. and Hengge, A.C. (2006) Enzymatic Mechanisms of Phosphate and Sulfate Transfer. Chemical Reviews 106, 3252-3278.

Cline, J.D. and Richards, F.A. (1969) Oxygenation of hydrogen sulfide in seawater at constant salinity, temperature and pH. Environmental Science & Technology 3, 838-843.

Corbett, D.R., McKee, B. and Allison, M. (2006) Nature of decadal-scale sediment accumulation on the western shelf of the Mississippi River delta. Continental Shelf Research 26, 2125-2140.

Corbett, D.R., McKee, B. and Duncan, D. (2004) An evaluation of mobile mud dynamics in the Mississippi River deltaic region. Marine Geology 209, 91-112.

Cornwell, J.C. and Morse, J.W. (1987) The characterization of iron sulfide minerals in anoxic marine sediments. Marine Chemistry 22, 193-206.

Cotton, A.F., Wilkinson, G., Murillo, C.A. and Bochmann, M. (1999) Advanced Inorganic Chemistry, 6th ed. John Wiley & Sons, Inc.

Couture, R.-M., Shafei, B., Van Cappellen, P., Tessier, A. and Gobeil, C. (2010) Non-Steady State Modeling of Arsenic Diagenesis in Lake Sediments. Environmental Science & Technology 44, 197-203.

Cowie, G.L. and Hedges, J.I. (1984) Carbohydrate sources in a coastal marine environment. Geochimica et Cosmochimica Acta 48, 2075-2087.

Cowie, G.L. and Hedges, J.I. (1992) Sources and reactivities of amino acids in a coastal marine environment. 37, 703-724.

Cytryn, E., van Rijn, J., Schramm, A., Gieseke, A., de Beer, D. and Minz, D. (2005) Identification of bacteria potentially responsible for oxic and anoxic sulfide oxidation in biofilters of a recirculating mariculture system. Appl. Environ. Microbiol. 71, 6134-6141.

D'Hondt, S., Jørgensen, B.B., Miller, D.J., Batzke, A., Blake, R., Cragg, B.A., Cypionka, H., Dickens, G.R., Ferdelman, T. and Hinrichs, K.-U. (2004) Distributions of microbial activities in deep subseafloor sediments. Science 306, 2216-2221.

D'Hondt, S., Rutherford, S. and Spivack, A.J. (2002) Metabolic activity of subsurface life in deep-sea sediments. Science 295, 2067-2070.

Dagg, M., Benner, R., Lohrenz, S. and Lawrence, D. (2004) Transformation of dissolved and particulate materials on continental shelves influenced by large rivers: plume processes. Continental Shelf Research 24, 833-858.

Daims, H., Lebedeva, E.V., Pjevac, P., Han, P., Herbold, C., Albertsen, M., Jehmlich, N., Palatinszky, M., Vierheilig, J. and Bulaev, A. (2015) Complete nitrification by Nitrospira bacteria. Nature 528, 504.

Dale, J.R., Wade, R. and DiChristina, T.J. (2007) A Conserved Histidine in Cytochrome c Maturation Permease CcmB of Shewanella putrefaciens Is Required for Anaerobic Growth below a Threshold Standard Redox Potential. Journal of Bacteriology 189, 1036.

Danovaro, R., Molari, M., Corinaldesi, C. and Dell'Anno, A. (2016) Macroecological drivers of archaea and bacteria in benthic deep-sea ecosystems. Science advances 2, e1500961.

Davies, S.H.R. and Morgan, J.J. (1989) Manganese(II) oxidation kinetics on metal oxide surfaces. Journal of Colloid and Interface Science 129, 63-77.

Dellwig, O., Schnetger, B., Brumsack, H.-J., Grossart, H.-P. and Umlauf, L. (2012) Dissolved reactive manganese at pelagic redoxclines (part II): Hydrodynamic conditions for accumulation. Journal of Marine Systems 90, 31-41.

Devereux, R., Lehrter, J.C., Cicchetti, G., Beddick, D.L., Yates, D.F., Jarvis, B.M., Aukamp, J. and Hoglund, M.D. (2019) Spatially variable bioturbation and physical mixing drive the sedimentary biogeochemical seascape in the Louisiana continental shelf hypoxic zone. Biogeochemistry 143, 151-169.

Devereux, R., Mosher, J.J., Vishnivetskaya, T.A., Brown, S.D., Beddick, D.L., Yates, D.F. and Palumbo, A.V. (2015) Changes in northern Gulf of Mexico sediment bacterial and archaeal communities exposed to hypoxia. Geobiology 13, 478-493.

Dhar, R.K., Zheng, Y., Rubenstone, J. and van Geen, A. (2004) A rapid colorimetric method for measuring arsenic concentrations in groundwater. Analytica Chimica Acta 526, 203-209.

Dheeman, D.S., Packianathan, C., Pillai, J.K. and Rosen, B.P. (2014) Pathway of Human AS3MT Arsenic Methylation. Chemical Research in Toxicology 27, 1979-1989.

Dickson, A.G. (1993) pH buffers for sea water media based on the total hydrogen ion concentration scale. Deep Sea Research Part I: Oceanographic Research Papers 40, 107-118.

Dickson, A.G., Sabine, C.L. and Christian, J.R. (2007) Guide to best practices for ocean CO2 measurements. PICES Special Publication 3.

Diem, D. and Stumm, W. (1984) Is dissolved Mn2+ being oxidized by O2 in absence of Mn-bacteria or surface catalysts? Geochimica et Cosmochimica Acta 48, 1571-1573.

Dixit, S. and Hering, J.G. (2003) Comparison of Arsenic(V) and Arsenic(III) Sorption onto Iron Oxide Minerals: Implications for Arsenic Mobility. Environmental Science & Technology 37, 4182-4189.

Dollhopf, M.E., Nealson, K.H., Simon, D.M. and Luther, G.W. (2000) Kinetics of Fe(III) and Mn(IV) reduction by the Black Sea strain of Shewanella putrefaciens using in situ solid state voltammetric Au/Hg electrodes. Marine Chemistry 70, 171-180.

Donner, M.W., Javed, M.B., Shotyk, W., Francesconi, K.A. and Siddique, T. (2017) Arsenic speciation in the lower Athabasca River watershed: A geochemical investigation of the dissolved and particulate phases. Environmental Pollution 224, 265-274.

Duckworth, O.W. and Martin, S.T. (2004) Role of molecular oxygen in the dissolution of siderite and rhodochrosite1 1Associate editor: U. Becker. Geochimica et Cosmochimica Acta 68, 607-621.

Duckworth, O.W. and Sposito, G. (2005) Siderophore−Manganese(III) Interactions II. Manganite Dissolution Promoted by Desferrioxamine B. Environmental Science & Technology 39, 6045-6051.

Duckworth, O.W. and Sposito, G. (2007) Siderophore-promoted dissolution of synthetic and biogenic layer-type Mn oxides. Chemical Geology 242, 497-508.

Durbin, A.M. and Teske, A. (2011) Microbial diversity and stratification of South Pacific abyssal marine sediments. Environmental Microbiology 13, 3219-3234.

Durbin, A.M. and Teske, A. (2012) Archaea in organic-lean and organic-rich marine subsurface sediments: an environmental gradient reflected in distinct phylogenetic lineages. Frontiers in microbiology 3, 168.

Eary, E. and Schramke, J. (1990) Rates of Inorganic Oxidation Reactions Involving Dissolved Oxygen. ACS Symposium Series 416, 379-396.

Ellis, A.J. and Golding, R.M. (1959) 25. Spectrophotometric determination of the acid dissociation constants of hydrogen sulphide. Journal of the Chemical Society (Resumed), 127-130.

Ellis, P.J., Conrads, T., Hille, R. and Kuhn, P. (2001) Crystal Structure of the 100 kDa Arsenite Oxidase from Alcaligenes faecalis in Two Crystal Forms at 1.64 Å and 2.03 Å. Structure 9, 125-132.

Elzinga, E.J. (2011) Reductive Transformation of Birnessite by Aqueous Mn(II). Environmental Science & Technology 45, 6366-6372.

Elzinga, E.J. (2016) 54Mn Radiotracers Demonstrate Continuous Dissolution and Reprecipitation of Vernadite (δ-MnO2) during Interaction with Aqueous Mn(II). Environmental Science & Technology 50, 8670-8677.

Elzinga, E.J. and Kustka, A.B. (2015) A Mn-54 Radiotracer Study of Mn Isotope Solid–Liquid Exchange during Reductive Transformation of Vernadite (δ-MnO2) by Aqueous Mn(II). Environmental Science & Technology 49, 4310-4316.

Evans, P.N., Parks, D.H., Chadwick, G.L., Robbins, S.J., Orphan, V.J., Golding, S.D. and Tyson, G.W. (2015) Methane metabolism in the archaeal phylum Bathyarchaeota revealed by genome-centric metagenomics. Science 350, 434-438.

Fahy, A., Giloteaux, L., Bertin, P., Le Paslier, D., Médigue, C., Weissenbach, J., Duran, R. and Lauga, B. (2015) 16S rRNA and As-Related Functional Diversity: Contrasting Fingerprints in Arsenic-Rich Sediments from an Acid Mine Drainage. Microbial Ecology 70, 154-167.

Fan, X. and Xing, P. (2016) Differences in the composition of archaeal communities in sediments from contrasting zones of Lake Taihu. Frontiers in microbiology 7, 1510.

Fang, Y., Pan, Y., Li, P., Xue, M., Pei, F., Yang, W., Ma, N. and Hu, Q. (2016) Simultaneous determination of arsenic and mercury species in rice by ion-pairing reversed phase chromatography with inductively coupled plasma mass spectrometry. Food Chemistry 213, 609-615.

Feng, X., Wang, P., Shi, Z., Kwon, K.D., Zhao, H., Yin, H., Lin, Z., Zhu, M., Liang, X., Liu, F. and Sparks, D.L. (2018) A Quantitative Model for the Coupled Kinetics of Arsenic Adsorption/Desorption and Oxidation on Manganese Oxides. Environmental Science & Technology Letters 5, 175-180.

Ferdelman, T.G., Fossing, H., Neumann, K. and Schulz, H.D. (1999) Sulfate reduction in surface sediments of the southeast Atlantic continental margin between 15 degrees 38'S and 27 degrees 57'S (Angola and Namibia). Limnology and Oceanography 44, 650-661.

Forsberg, C. (1989) IMPORTANCE OF SEDIMENTS IN UNDERSTANDING NUTRIENT CYCLINGS IN LAKES. Hydrobiologia 176, 263-277.

Franz, B., Lichtenberg, H., Dahl, C., Hormes, J. and Prange, A. (2009) Utilization of'elemental'sulfur by different phototrophic sulfur bacteria (Chromatiaceae, Ectothiorhodospiraceae): A sulfur K-edge XANES spectroscopy study, Journal of Physics: Conference Series. IOP Publishing, p. 012200.

Fredrickson, J.K. and Gorby, Y.A. (1996) Environmental processes mediated by iron-reducing bacteria. Current opinion in biotechnology 7, 287-294.

Froelich, P.N., Klinkhammer, G.P., Bender, M.L., Luedtke, N.A., Heath, G.R., Cullen, D., Dauphin, P., Hammond, D., Hartman, B. and Maynard, V. (1979) Early oxidation of organic matter in pelagic sediments of the eastern equatorial Atlantic: suboxic diagenesis. Geochimica et Cosmochimica Acta 43, 1075-1090.

Geyer, W.R., Hill, P.S. and Kineke, G.C. (2004) The transport, transformation and dispersal of sediment by buoyant coastal flows. Continental Shelf Research 24, 927-949.

Gihring, T.M. and Banfield, J.F. (2001) Arsenite oxidation and arsenate respiration by a new Thermus isolate. FEMS Microbiology Letters 204, 335-340.

Ginder-Vogel, M., Landrot, G., Fischel, J.S. and Sparks, D.L. (2009) Quantification of rapid environmental redox processes with quick-scanning x-ray absorption spectroscopy (Q-XAS). Proceedings of the National Academy of Sciences 106, 16124-16128.

Glud, R.N. (2008) Oxygen dynamics of marine sediments. Marine Biology Research 4, 243-289.

Glud, R.N., Thamdrup, B., Stahl, H., Wenzhoefer, F., Glud, A., Nomaki, H., Oguri, K., Revsbech, N.P. and Kitazato, H. (2009) Nitrogen cycling in a deep ocean margin sediment (Sagami Bay, Japan). Limnology and Oceanography 54, 723-734.

Gomez-Caminero, A., Howe, P., Hughes, M., Kenyon, E., Lewis, D.R., Moore, M., Ng, J., Aitio, A. and Becking, G. (2001) Arsenic and arsenic compounds, Environmental Health Criteria 224, 2nd ed. World Health Organization, Geneva, pp. 1-5.

Grégoire, M. and Friedrich, J. (2004) Nitrogen budget of the northwestern Black Sea shelf inferred from modeling studies and in situ benthic measurements. Marine Ecology Progress Series 270, 15-39.

Gustafsson, J.P. (2019) Visual MINTEQ, version 3.1. KTH Royal Institute of Technology, Stockholm, Sweden.

Hall, P.J. and Aller, R.C. (1992) Rapid, small-volume, flow injection analysis for SCO2, and NH4+ in marine and freshwaters. Limnology and Oceanography 37, 1113-1119.

Hartnett, H.E., Keil, R.G., Hedges, J.I. and Devol, A.H. (1998) Influence of oxygen exposure time on organic carbon preservation in continental margin sediments. Nature 391, 572-575.

Hayakawa, T., Kobayashi, Y., Cui, X. and Hirano, S. (2005) A new metabolic pathway of arsenite: arsenic–glutathione complexes are substrates for human arsenic methyltransferase Cyt19. Archives of Toxicology 79, 183-191.

He, Z., Geng, S., Cai, C., Liu, S., Liu, Y., Pan, Y., Lou, L., Zheng, P., Xu, X. and Hu, B. (2015) Anaerobic oxidation of methane coupled to nitrite reduction by halophilic marine NC10 bacteria. Appl. Environ. Microbiol. 81, 5538-5545.

Hedrich, S., Schlömann, M. and Johnson, D.B. (2011) The iron-oxidizing proteobacteria. Microbiology 157, 1551-1564.

Henneke, E., Luther, G.W. and de Lange, G.J. (1991) Determination of inorganic sulphur speciation with polarographic techniques: Some preliminary results for recent hypersaline anoxic sediments. Marine Geology 100, 115-123.

Hersman, L., Maurice, P. and Sposito, G. (1996) Iron acquisition from hydrous Fe (III)-oxides by an aerobic Pseudomonas sp. Chemical Geology 132, 25-31.

Herszage, J. and dos Santos Afonso, M. (2003) Mechanism of Hydrogen Sulfide Oxidation by Manganese(IV) Oxide in Aqueous Solutions. Langmuir 19, 9684-9692.

Hinger, I., Pelikan, C. and Mußmann, M. (2019) Role of the ubiquitous bacterial family Woeseiaceae for N2O production in marine sediments, Geophysical Research Abstracts.

Hinrichs, K.-U., Hayes, J.M., Sylva, S.P., Brewer, P.G. and DeLong, E.F. (1999) Methane-consuming archaebacteria in marine sediments. Nature 398, 802-805.

Hoeft, S.E., Lucas, F.o., Hollibaugh, J.T. and Oremland, R.S. (2002) Characterization of Microbial Arsenate Reduction in the Anoxic Bottom Waters of Mono Lake, California. Geomicrobiology Journal 19, 23-40.

Hoke, K.R., Cobb, N., Armstrong, F.A. and Hille, R. (2004) Electrochemical Studies of Arsenite Oxidase: An Unusual Example of a Highly Cooperative Two-Electron Molybdenum Center†. Biochemistry 43, 1667-1674.

Hu, X., Cai, W.-J., Wang, Y., Guo, X. and Luo, S. (2011) Geochemical environments of continental shelf-upper slope sediments in the northern Gulf of Mexico. Palaeogeography, Palaeoclimatology, Palaeoecology 312, 265-277.

Hulth, S., Aller, R.C. and Gilbert, F. (1999) Coupled anoxic nitrification/manganese reduction in marine sediments. Geochimica et Cosmochimica Acta 63, 49-66.

Hunter, E.M., Mills, H.J. and Kostka, J.E. (2006) Microbial Community Diversity Associated with Carbon and Nitrogen Cycling in Permeable Shelf Sediments. Appl Environ Microb 72, 5689-5701.

Hyacinthe, C., Anschutz, P., Carbonel, P., Jouanneau, J.M. and Jorissen, F.J. (2001) Early diagenetic processes in the muddy sediments of the Bay of Biscay. Marine Geology 177, 111-128.

Hyun, J.H., Kim, S.H., Mok, J.S., Cho, H., Lee, T., Vandieken, V. and Thamdrup, B. (2017) Manganese and iron reduction dominate organic carbon oxidation in surface sediments of the deep Ulleung Basin, East Sea. Biogeosciences 14, 941-958.

Imhoff, J.F. and Wiese, J. (2014) The order Kiloniellales. Springer.

J.D.H Strickland, T.R.P. (1972) Determination of Dissolved Oxygen, in: Stevenson, J.C. (Ed.), A Practical Handbook of Seawater Analysis, 2 ed. Minister of Supply and Services Canada, Ottawa, Canada, pp. 21-25.

Jahnke, R.A., Reimers, C.E. and Craven, D.B. (1990) Intensification of recycling of organic matter at the sea floor near ocean margins. Nature 348, 50-54.

Jain, A. and Loeppert, R.H. (2000) Effect of competing anions on the adsorption of arsenate and arsenite by ferrihydrite. Journal of Environmental Quality 29, 1422.

Jakobsen, R. and Postma, D. (1989) Formation and solid solution behavior of Ca-rhodochrosites in marine muds of the Baltic deeps. Geochimica et Cosmochimica Acta 53, 2639-2648.

Javanaud, C., Michotey, V., Guasco, S., Garcia, N., Anschutz, P., Canton, M. and Bonin, P. (2011) Anaerobic ammonium oxidation mediated by Mn-oxides: from sediment to strain level. Research in Microbiology 162, 848-857.

Ji, G. and Silver, S. (1992) Reduction of arsenate to arsenite by the ArsC protein of the arsenic resistance operon of Staphylococcus aureus plasmid pI258. Proceedings of the National Academy of Sciences 89, 9474-9478.

Jia, Y., Huang, H., Zhong, M., Wang, F.-H., Zhang, L.-M. and Zhu, Y.-G. (2013) Microbial Arsenic Methylation in Soil and Rice Rhizosphere. Environmental Science & Technology 47, 3141-3148.

Jiang, S., Lee, J.-H., Kim, D., Kanaly, R.A., Kim, M.-G. and Hur, H.-G. (2013) Differential Arsenic Mobilization from As-Bearing Ferrihydrite by Iron-Respiring Shewanella Strains with Different Arsenic-Reducing Activities. Environmental Science & Technology 47, 8616-8623.

Johnson, K.S., Chavez, F.P. and Friederich, G.E. (1999) Continental-shelf sediment as a primary source of iron for coastal phytoplankton. Nature 398, 697-700.

Jones, L.C., Lafferty, B.J. and Sparks, D.L. (2012) Additive and Competitive Effects of Bacteria and Mn Oxides on Arsenite Oxidation Kinetics. Environmental Science & Technology 46, 6548-6555.

Jones, M.R., Oldham, V.E., Luther, G.W., Mucci, A. and Tebo, B.M. (2019) Distribution of desferrioxamine-B-extractable soluble manganese(III) and particulate MnO2 in the St. Lawrence Estuary, Canada. Marine Chemistry 208, 70-82.

Jørgensen, B.B. (1982) Mineralization of organic matter in the sea bed—the role of sulphate reduction. Nature 296, 643-645.

Julies Elsabé, M., Brüchert, V. and Fuchs, B.M. (2012) Vertical shifts in the microbial community structure of organic-rich Namibian shelf sediments. African Journal of Microbiology Research 6, 3887-3897.

Jung, H.S., Jeong, S.E., Kim, K.H. and Jeon, C.O. (2017) Parahaliea aestuarii sp. nov., isolated from the Asan Bay estuary. International journal of systematic and evolutionary microbiology 67, 1431-1435.

Kandegedara, A. and Rorabacher, D. (1999) Noncomplexing Tertiary Amines and "Better" Buffers Covering the Range of pH 3-11. Temperature Dependence of Their Acid Dissociation Constants. Analytica Chimica Acta 71, 3140-3144.

Kim, M.-J. and Nriagu, J. (2000) Oxidation of arsenite in groundwater using ozone and oxygen. Science of The Total Environment 247, 71-79.

Kim, Y.-S., Noh, E.S., Lee, D.-E. and Kim, K.-H. (2017) Complete genome of a denitrifying Halioglobus sp. RR3-57 isolated from a seawater recirculating aquaculture system. 미생물학회지 53, 58-60.

Kostka, J.E. and Luther, G.W. (1994) Partitioning and speciation of solid phase iron in saltmarsh sediments. Geochimica et Cosmochimica Acta 58, 1701-1710.

Kozich, J.J., Westcott, S.L., Baxter, N.T., Highlander, S.K. and Schloss, P.D. (2013) Development of a Dual-Index Sequencing Strategy and Curation Pipeline for Analyzing Amplicon Sequence Data on the MiSeq Illumina Sequencing Platform. Appl Environ Microb 79, 5112-5120.

Krafft, T. and Macy, J.M. (1998) Purification and characterization of the respiratory arsenate reductase of Chrysiogenes arsenatis. European Journal of Biochemistry 255, 647-653.

Kümmel, S., Herbst, F.-A., Bahr, A., Duarte, M., Pieper, D.H., Jehmlich, N., Seifert, J., von Bergen, M., Bombach, P. and Richnow, H.H. (2015) Anaerobic naphthalene degradation by sulfate-reducing Desulfobacteraceae from various anoxic aquifers. FEMS microbiology ecology 91.

Lafferty, B.J., Ginder-Vogel, M. and Sparks, D.L. (2010a) Arsenite Oxidation by a Poorly Crystalline Manganese-Oxide 1. Stirred-Flow Experiments. Environmental Science & Technology 44, 8460-8466.

Lafferty, B.J., Ginder-Vogel, M. and Sparks, D.L. (2011) Arsenite Oxidation by a Poorly-Crystalline Manganese Oxide. 3. Arsenic and Manganese Desorption. Environmental Science & Technology 45, 9218-9223.

Lafferty, B.J., Ginder-Vogel, M., Zhu, M., Livi, K.J.T. and Sparks, D.L. (2010b) Arsenite Oxidation by a Poorly Crystalline Manganese-Oxide. 2. Results from X-ray Absorption Spectroscopy and X-ray Diffraction. Environmental Science & Technology 44, 8467-8472.

Lan, S., Wang, X., Xiang, Q., Yin, H., Tan, W., Qiu, G., Liu, F., Zhang, J. and Feng, X. (2017) Mechanisms of Mn(II) catalytic oxidation on ferrihydrite surfaces and the formation of manganese (oxyhydr)oxides. Geochimica et Cosmochimica Acta 211, 79-96.

Lan, S., Ying, H., Wang, X., Liu, F., Tan, W., Huang, Q., Zhang, J. and Feng, X. (2018) Efficient catalytic As(III) oxidation on the surface of ferrihydrite in the presence of aqueous Mn(II). Water Research 128, 92-101.

Larsen, I., Little, B., Nealson, K.H., Ray, R., Stone, A. and Tian, J. (1998) Manganite reduction by Shewanella putrefaciens MR-4. American Mineralogist 83, 1564-1572.

Law, G.T.W., Shimmield, T.M., Shimmield, G.B., Cowie, G.L., Breuer, E.R. and Martyn Harvey, S. (2009) Manganese, iron, and sulphur cycling on the Pakistan margin. Deep Sea Research Part II: Topical Studies in Oceanography 56, 305-323.

Lazar, C.S., Baker, B.J., Seitz, K.W. and Teske, A.P. (2017) Genomic reconstruction of multiple lineages of uncultured benthic archaea suggests distinct biogeochemical roles and ecological niches. The ISME journal 11, 1118-1129.

Learman, D.R., Henson, M.W., Thrash, J.C., Temperton, B., Brannock, P.M., Santos, S.R., Mahon, A.R. and Halanych, K.M. (2016) Biogeochemical and microbial variation across 5500 km of Antarctic surface sediment implicates organic matter as a driver of benthic community structure. Frontiers in Microbiology 7, 284.

Learman, D.R., Voelker, B.M., Vazquez-Rodriguez, A.I. and Hansel, C.M. (2011) Formation of manganese oxides by bacterially generated superoxide. Nature Geoscience 4, 95.

Lee, T., Hyun, J.H., Mok, J.S. and Kim, D. (2008) Organic carbon accumulation and sulfate reduction rates in slope and basin sediments of the Ulleung Basin, East/Japan Sea. Geo-Mar. Lett. 28, 153-159.

Lehrter, J.C., Beddick, D.L., Jr., Devereux, R., Yates, D.F. and Murrell, M.C. (2012) Sediment-water fluxes of dissolved inorganic carbon, O-2, nutrients, and N-2 from the hypoxic region of the Louisiana continental shelf. Biogeochemistry 109, 233-252.

Lesley, M.P. and Froelich, P.N. (2003), Georgia Water Resources Conference.

Li, H. and Smart, R.B. (1996) Determination of sub-nanomolar concentration of arsenic(III) in natural waters by square wave cathodic stripping voltammetry. Analytica Chimica Acta 325, 25-32.

Lin, B., Braster, M., van Breukelen, B.M., van Verseveld, H.W., Westerhoff, H.V. and Röling, W.F. (2005) Geobacteraceae community composition is related to hydrochemistry and biodegradation in an iron-reducing aquifer polluted by a neighboring landfill. Appl. Environ. Microbiol. 71, 5983-5991.

Lin, H. and Taillefert, M. (2014) Key geochemical factors regulating Mn(IV)-catalyzed anaerobic nitrification in coastal marine sediments. Geochimica et Cosmochimica Acta 133, 17-33.

Lin, S., Huang, K.-M. and Chen, S.-K. (2002) Sulfate reduction and iron sulfide mineral formation in the southern East China Sea continental slope sediment. Deep Sea Research Part I: Oceanographic Research Papers 49, 1837-1852.

Lin, S. and Morse, J.W. (1991) Sulfate reduction and iron sulfide mineral formation in Gulf of Mexico anoxic sediments. American Journal of Science 291, 55-89.

Lipsewers, Y.A. (2017) Role of chemolithoautotrophic microorganisms involved in nitrogen and sulfur cycling in coastal marine sediments. Utrecht University.

Liu, P. and Conrad, R. (2017) Syntrophobacteraceae-affiliated species are major propionate-degrading sulfate reducers in paddy soil. Environmental microbiology 19, 1669-1686.

Liu, P., Klose, M. and Conrad, R. (2018) Temperature effects on structure and function of the methanogenic microbial communities in two paddy soils and one desert soil. Soil Biology and Biochemistry 124, 236-244.

Lloyd, K.G., Alperin, M.J. and Teske, A. (2011) Environmental evidence for net methane production and oxidation in putative ANaerobic MEthanotrophic (ANME) archaea. Environmental Microbiology 13, 2548-2564.

Lloyd, K.G., Schreiber, L., Petersen, D.G., Kjeldsen, K.U., Lever, M.A., Steen, A.D., Stepanauskas, R., Richter, M., Kleindienst, S. and Lenk, S. (2013) Predominant archaea in marine sediments degrade detrital proteins. Nature 496, 215-218.

Lovley, D.R. and Phillips, E.J.P. (1988) Novel Mode of Microbial Energy Metabolism: Organic Carbon Oxidation Coupled to Dissimilatory Reduction of Iron or Manganese. Applied and Environmental Microbiology 54, 1472-1480.

Lovley, D.R., Phillips, E.J.P., Gorby, Y.A. and Landa, E.R. (1991) Microbial reduction of uranium. Nature 350, 413-416.

Lozupone, C.A. and Knight, R. (2007) Global patterns in bacterial diversity. Proceedings of the National Academy of Sciences 104, 11436-11440.

Luther, G.W. (2005) Manganese(II) Oxidation and Mn(IV) Reduction in the Environment—Two One-Electron Transfer Steps Versus a Single Two-Electron Step. Geomicrobiology Journal 22, 195-203.

Luther, G.W. (2010) The Role of One- and Two-Electron Transfer Reactions in Forming Thermodynamically Unstable Intermediates as Barriers in Multi-Electron Redox Reactions. Aquat Geochem 395-420.

Luther, G.W., Findlay, A.J., MacDonald, D.J., Owings, S.M., Hanson, T.E., Beinart, R.A. and Girguis, P.R. (2011) Thermodynamics and kinetics of sulfide oxidation by oxygen: a look at inorganically controlled reactions and biologically mediated processes in the environment. Frontiers in Microbiology 2, 9.

Luther, G.W., Glazer, B.T., Ma, S., Trouwborst, R.E., Moore, T.S., Metzger, E., Kraiya, C., Waite, T.J., Druschel, G., Sundby, B., Taillefert, M., Nuzzio, D.B., Shank, T.M., Lewis, B.L. and Brendel, P.J. (2008) Use of voltammetric solid-state (micro)electrodes for studying biogeochemical processes: Laboratory measurements to real time measurements with an in situ electrochemical analyzer (ISEA). Marine Chemistry 108, 221-235.

Luther, G.W. and Popp, J.I. (2002) Kinetics of the Abiotic Reduction of Polymeric Manganese Dioxide by Nitrite: An Anaerobic Nitrification Reaction. Aquatic Geochemistry 8, 15-36.

Luther, G.W., Reimers, C.E., Nuzzio, D.B. and Lovalvo, D. (1999) In Situ Deployment of Voltammetric, Potentiometric, and Amperometric Microelectrodes from a ROV To Determine Dissolved O2, Mn, Fe, S(−2), and pH in Porewaters. Environmental Science & Technology 33, 4352-4356.

Luther, G.W., Sundby, B., Lewis, B.L., Brendel, P.J. and Silverberg, N. (1997) Interactions of manganese with the nitrogen cycle: Alternative pathways to dinitrogen. Geochimica et Cosmochimica Acta 61, 4043-4052.

Luther, G.W., Thibault de Chanvalon, A., Oldham, V.E., Estes, E.R., Tebo, B.M. and Madison, A.S. (2018) Reduction of Manganese Oxides: Thermodynamic, Kinetic and Mechanistic Considerations for One- Versus Two-Electron Transfer Steps. Aquatic Geochemistry 24, 257-277.

Madison, A.S., Tebo, B.M. and Luther, G.W. (2011a) Simultaneous determination of soluble manganese(III), manganese(II) and total manganese in natural (pore)waters. Talanta 84, 374-381.

Madison, A.S., Tebo, B.M. and Luther Iii, G.W. (2011b) Simultaneous determination of soluble manganese(III), manganese(II) and total manganese in natural (pore)waters. Talanta 84, 374-381.

Madison, A.S., Tebo, B.M., Mucci, A., Sundby, B. and Luther, G.W. (2013) Abundant Porewater Mn(III) Is a Major Component of the Sedimentary Redox System. Science 341, 875-878.

Manceau, A., Lanson, B. and Drits, V. (2002) Structure of heavy metal sorbed birnessite. Part III: Results from powder and polarized extended X-ray absorption fine structure spectroscopy Geochimica et Cosmochimica Acta 66, 2639-2663.

Manning, B.A., Fendorf, S.E., Bostick, B. and Suarez, D.L. (2002) Arsenic(III) Oxidation and Arsenic(V) Adsorption Reactions on Synthetic Birnessite. Environmental Science & Technology 36, 976-981.

Marapakala, K., Packianathan, C., Ajees, A.A., Dheeman, D.S., Sankaran, B., Kandavelu, P. and Rosen, B.P. (2015) A disulfide-bond cascade mechanism for arsenic(III) S-adenosylmethionine methyltransferase. Acta Crystallographica Section D 71, 505-515.

McCarthy, M.J., Newell, S.E., Carini, S.A. and Gardner, W.S. (2015) Denitrification Dominates Sediment Nitrogen Removal and Is Enhanced by Bottom-Water Hypoxia in the Northern Gulf of Mexico. Estuaries and Coasts 38, 2279-2294.

McGlynn, S.E. (2017) Energy metabolism during anaerobic methane oxidation in ANME archaea. Microbes and environments, ME16166.

McIlroy, S.J., Kirkegaard, R.H., Dueholm, M.S., Fernando, E., Karst, S.M., Albertsen, M. and Nielsen, P.H. (2017) Culture-independent analyses reveal novel anaerolineaceae as abundant primary fermenters in anaerobic digesters treating waste activated sludge. Frontiers in microbiology 8, 1134.

McKee, B.A., Aller, R.C., Allison, M.A., Bianchi, T.S. and Kineke, G.C. (2004) Transport and transformation of dissolved and particulate materials on continental margins influenced by major rivers: benthic boundary layer and seabed processes. Continental Shelf Research 24, 899-926.

McKenzie, R.M. (1971) The synthesis of birnesssite, crypomelane, and some other oxides and hydroxides of manganese. Mineralogical Magazine 38, 493-502.

McKinzi, A.M. and DiChristina, T.J. (1999) Microbially Driven Fenton Reaction for Transformation of Pentachlorophenol. Environmental Science & Technology 33, 1886-1891.

Meiggs, D. and Taillefert, M. (2011) The effect of riverine discharge on biogeochemical processes in estuarine sediments. Limnology and Oceanography 56, 1797-1810.

Mikutta, C. and Kretzschmar, R. (2011) Spectroscopic Evidence for Ternary Complex Formation between Arsenate and Ferric Iron Complexes of Humic Substances. Environmental Science & Technology 45, 9550-9557.

Millero, F.J., Sotolongo, S. and Izaguirre, M. (1987) The oxidation kinetics of Fe(II) in seawater. Geochimica et Cosmochimica Acta 51, 793-801.

Milliman, J.D. and Meade, R.H. (1983) World-Wide Delivery of River Sediment to the Oceans. The Journal of Geology 91, 1-21.

Montoya, L., Lozada-Chávez, I., Amils, R., Rodriguez, N. and Marín, I. (2011) The sulfate-rich and extreme saline sediment of the ephemeral tirez lagoon: a biotope for acetoclastic sulfate-reducing bacteria and hydrogenotrophic methanogenic archaea. International journal of microbiology 2011.

Morgan, J.J. (2005) Kinetics of reaction between O2 and Mn(II) species in aqueous solutions. Geochimica et Cosmochimica Acta 69, 35-48.

Morgan, J.J. and Stumm, W. (1964) Colloid-Chemical Properties of Manganese Dioxide. Journal of Colloid Sciences 19, 347-359.

Mori, K., Suzuki, K.-i., Urabe, T., Sugihara, M., Tanaka, K., Hamada, M. and Hanada, S. (2011) Thioprofundum hispidum sp. nov., an obligately chemolithoautotrophic sulfur-oxidizing gammaproteobacterium isolated from the hydrothermal field on Suiyo Seamount, and proposal of Thioalkalispiraceae fam. nov. in the order

Chromatiales. International journal of systematic and evolutionary microbiology 61, 2412-2418.

Morse, J.W. and Rowe, G.T. (1999) Benthic biogeochemistry beneath the Mississippi River plume. Estuaries 22, 206-214.

Mossa, J. (1996) Sediment dynamics in the lowermost Mississippi River. Engineering Geology 45, 457-479.

Mouret, A., Anschutz, P., Lecroart, P., Chaillou, G., Hyacinthe, C., Deborde, J., Jorissen, F.J., Deflandre, B., Schmidt, S. and Jouanneau, J.-M. (2009) Benthic geochemistry of manganese in the Bay of Biscay, and sediment mass accumulation rate. Geo-Mar. Lett. 29, 133-149.

Mucci, A. (2004) The Behavior of Mixed Ca–Mn Carbonates in Water and Seawater: Controls of Manganese Concentrations in Marine Porewaters. Aquatic Geochemistry 10, 139-169.

Mukhopadhyay, R., Manjaiah, K.M., Datta, S.C., Yadav, R.K. and Sarkar, B. (2017) Inorganically modified clay minerals: Preparation, characterization, and arsenic adsorption in contaminated water and soil. Applied Clay Science 147, 1-10.

Mukhopadhyay, R., Rosen, B.P., Phung, L.T. and Silver, S. (2002) Microbial arsenic: from geocycles to genes and enzymes. FEMS Microbiology Reviews 26, 311-325.

Murphy, J. and Riley, J.P. (1962) A modified single solution method for the determination of phosphate in natural waters. Analytica Chimica Acta 27, 31-36.

Murray, J.W. (1973) The Surface Chemistry of Hydrous Manganese Dioxide. Journal of Colloid and Interface Science 46, 357-371.

Myers, C.R. and Nealson, K.H. (1988) Bacterial Manganese Reduction and Growth with Manganese Oxide as the Sole Electron Acceptor. Science 240, 1319-1321.

Nair, S., Karimzadeh, L. and Merkel, B.J. (2014) Sorption of uranyl and arsenate on SiO2, Al2O3, TiO2 and FeOOH. Environ Earth Sci 72, 3507-3512.

Nesbitt, H.W., Canning, G.W. and Bancroft, G.M. (1998) XPS study of reductive dissolution of 7Å-birnessite by H3AsO3, with constraints on reaction mechanism. Geochimica et Cosmochimica Acta 62, 2097-2110.

Newman, D.K., Kennedy, E.K., Coates, J.D., Ahmann, D., Ellis, D.J., Lovley, D.R. and Morel, F.M.M. (1997) Dissimilatory arsenate and sulfate reduction in Desulfotomaculum auripigmentum sp. nov. Arch Microbiol 168, 380-388.

Nickson, R.T., McArthur, J.M., Ravenscroft, P., Burgess, W.G. and Ahmed, K.M. (2000) Mechanism of arsenic release to groundwater, Bangladesh and West Bengal. Applied Geochemistry 15, 403-413.

Nordstrom, D.K. (2002) Worldwide Occurrences of Arsenic in Ground Water. Science 296, 2143-2145.

Obuekwe, C.O., Westlake, D.W.S. and Cook, F.D. (1981) Effect of nitrate on reduction of ferric iron by a bacterium isolated from crude oil. Canadian Journal of Microbiology 27, 692-697.

Oldham, V.E., Mucci, A., Tebo, B.M. and Luther, G.W. (2017) Soluble Mn(III)–L complexes are abundant in oxygenated waters and stabilized by humic ligands. Geochimica et Cosmochimica Acta 199, 238-246.

Oldham, V.E., Owings, S.M., Jones, M.R., Tebo, B.M. and Luther, G.W. (2015) Evidence for the presence of strong Mn(III)-binding ligands in the water column of the Chesapeake Bay. Marine Chemistry 171, 58-66.

Oldham, V.E., Siebecker, M.G., Jones, M.R., Mucci, A., Tebo, B.M. and Luther, G.W. (2019) The Speciation and Mobility of Mn and Fe in Estuarine Sediments. Aquatic Geochemistry.

Oremland, R.S., Hoeft, S.E., Santini, J.M., Bano, N., Hollibaugh, R.A. and Hollibaugh, J.T. (2002) Anaerobic Oxidation of Arsenite in Mono Lake Water and by a Facultative, Arsenite-Oxidizing Chemoautotroph, Strain MLHE-1. Applied and Environmental Microbiology 68, 4795-4802.

Oremland, R.S. and Stolz, J.F. (2003) The Ecology of Arsenic. Science 300, 939-944.

Orsi, W.D., Vuillemin, A., Rodriguez, P., Coskun, Ö.K., Gomez-Saez, G.V., Lavik, G., Morholz, V. and Ferdelman, T.G. (2019) Metabolic activity analyses demonstrate that Lokiarchaeon exhibits homoacetogenesis in sulfidic marine sediments. Nature Microbiology, 1-8.

Oscarson, D.W., Huang, P.M., Defosse, C. and Herbillon, A. (1981a) Oxidative power of Mn(IV) and Fe(III) oxides with respect to As(III) in terrestrial and aquatic environments. Nature 291, 50-51.

Oscarson, D.W., Huang, P.M., Defosse, C. and Herbillon, A. (1981b) Oxidative power of Mn(IV) and Fe(III) oxides with respect to As(III) in terrestrial and aquatic environments. Nature 291, 50.

Oscarson, D.W., Huang, P.M. and Liaw, W.K. (1981c) Role of Manganese in the Oxidation of Arsenite by Freshwater Lake Sediments Clays and Clay Minerals 29, 219-225.

Oscarson, D.W., Huang, P.M., Liaw, W.K. and Hammer, U.T. (1983) Kinetics of Arsenite by Various Manganese Dioxides. Soil Sci. Soc. Am. J. 47, 644-648.

Overholt, W.A., Schwing, P., Raz, K.M., Hastings, D., Hollander, D.J. and Kostka, J.E. (2019) The core seafloor microbiome in the Gulf of Mexico is remarkably

consistent and shows evidence of recovery from disturbance caused by major oil spills. Environmental microbiology 21, 4316-4329.

Owings, S.M., Luther, G.W. and Taillefert, M. (2019) Development of a rate law for arsenite oxidation by manganese oxides. Geochimica et Cosmochimica Acta 250, 251-267.

Parikh, S.J., Lafferty, B.J. and Sparks, D.L. (2008) An ATR-FTIR spectroscopic approach for measuring rapid kinetics at the mineral/water interface. Journal of Colloid and Interface Science 320, 177-185.

Pastor, L., Cathalot, C., Deflandre, B., Viollier, E., Soetaert, K., Meysman, F.J.R., Ulses, C., Metzger, E. and Rabouille, C. (2011) Modeling biogeochemical processes in sediments from the Rhône River prodelta area (NW Mediterranean Sea). Biogeosciences 8, 1351-1366.

Pedersen, H.D., Postma, D. and Jakobsen, R. (2006) Release of arsenic associated with the reduction and transformation of iron oxides. Geochimica et Cosmochimica Acta 70, 4116-4129.

Picardal, F.W., Arnold, R.G., Couch, H., Little, A.M. and Smith, M.E. (1993) Involvement of cytochromes in the anaerobic biotransformation of tetrachloromethane by Shewanella putrefaciens 200. Applied and Environmental Microbiology 59, 3763.

Postma, D. (1985) Concentration of Mn and separation from Fe in sediments—I. Kinetics and stoichiometry of the reaction between birnessite and dissolved Fe(II) at 10°C. Geochimica et Cosmochimica Acta 49, 1023-1033.

Postma, D. and Appelo, C.A.J. (2000) Reduction of Mn-oxides by ferrous iron in a flow system: column experiment and reactive transport modeling. Geochimica et Cosmochimica Acta 64, 1237-1247.

Power, L.E., Arai, Y. and Sparks, D.L. (2005) Zinc Adsorption Effects on Arsenite Oxidation Kinetics at the Birnessite−Water Interface. Environmental Science & Technology 39, 181-187.

Pylro, V.S., Roesch, L.F.W., Ortega, J.M., do Amaral, A.M., Tótola, M.R., Hirsch, P.R., Rosado, A.S., Góes-Neto, A., da Silva, A.L.d.C. and Rosa, C.A. (2014) Brazilian microbiome project: revealing the unexplored microbial diversity—challenges and prospects. Microbial ecology 67, 237-241.

Pyzik, A.J. and Sommer, S.E. (1981) Sedimentary iron monosulfides: Kinetics and mechanism of formation. Geochimica et Cosmochimica Acta 45, 687-698.

Rabalais, N.N., Díaz, R.J., Levin, L.A., Turner, R.E., Gilbert, D. and Zhang, J. (2010) Dynamics and distribution of natural and human-caused hypoxia. Biogeosciences 7, 585-619.

Rabalais, N.N. and Turner, R.E. (2015) Press release, Bottom water dissolved oxygen-2015.

Rabalais, N.N. and Turner, R.E. (2017) Summary of 2017 Research Cruise Press release.

Rabalais, N.N., Turner, R.E., Sen Gupta, B.K., Boesch, D.F., Chapman, P. and Murrell, M.C. (2007) Hypoxia in the northern Gulf of Mexico: Does the science support the Plan to Reduce, Mitigate, and Control Hypoxia? Estuaries and Coasts 30, 753-772.

Rasheed, H., Kay, P., Slack, R., Gong, Y.Y. and Carter, A. (2017) Human exposure assessment of different arsenic species in household water sources in a high risk arsenic area. Science of The Total Environment 584–585, 631-641.

Rassmann, J., Lansard, B., Pozzato, L. and Rabouille, C. (2016) Carbonate chemistry in sediment porewaters of the Rhône River delta driven by early diagenesis (northwestern Mediterranean). Biogeosciences 13, 5379-5394.

Raven, K.P., Jain, A. and Loeppert, R.H. (1998) Arsenite and Arsenate Adsorption on Ferrihydrite: Kinetics, Equilibrium, and Adsorption Envelopes. Environmental Science & Technology 32, 344-349.

Raymann, K., Moeller, A.H., Goodman, A.L. and Ochman, H. (2017a) Unexplored Archaeal Diversity in the Great Ape Gut Microbiome. Msphere 2.

Raymann, K., Moeller, A.H., Goodman, A.L. and Ochman, H. (2017b) Unexplored Archaeal Diversity in the Great Ape Gut Microbiome. mSphere 2, e00026-00017.

Redman, A.D., Macalady, D.L. and Ahmann, D. (2002) Natural Organic Matter Affects Arsenic Speciation and Sorption onto Hematite. Environmental Science & Technology 36, 2889-2896.

Reese, B.K., Mills, H.J., Dowd, S.E. and Morse, J.W. (2013) Linking molecular microbial ecology to geochemistry in a coastal hypoxic zone. Geomicrobiology Journal 30, 160-172.

Reese, B.K., Witmer, A.D., Moller, S., Morse, J.W. and Mills, H.J. (2014a) Molecular assays advance understanding of sulfate reduction despite cryptic cycles. Biogeochemistry 118, 307-319.

Reese, B.K., Witmer, A.D., Moller, S., Morse, J.W. and Mills, H.J. (2014b) Molecular assays advance understanding of sulfate reduction despite cryptic cycles. Biogeochemistry 118, 307-319.

Reese, B.K., Zinke, L.A., Sobol, M.S., LaRowe, D.E., Orcutt, B.N., Zhang, X., Jaekel, U., Wang, F., Dittmar, T., Defforey, D., Tully, B., Paytan, A., Sylvan, J.B., Amend, J.P., Edwards, K.J. and Girguis, P. (2018) Nitrogen Cycling of Active Bacteria within Oligotrophic Sediment of the Mid-Atlantic Ridge Flank. Geomicrobiology Journal 35, 468-483.

Reiman, J.H., Xu, Y.J., He, S. and DelDuco, E.M. (2018) Metals geochemistry and mass export from the Mississippi-Atchafalaya River system to the Northern Gulf of Mexico. Chemosphere 205, 559-569.

Remucal, C.K. and Ginder-Vogel, M. (2014) A critical review of the reactivity of manganese oxides with organic contaminants. Environmental Science: Processes & Impacts 16, 1247-1266.

Revsbech, N.P. (1989) An oxygen microsensor with a guard cathode. Limnology and Oceanography 34, 474-478.

Richard, D., Sundby, B. and Mucci, A. (2013) Kinetics of manganese adsorption, desorption, and oxidation in coastal marine sediments. Limnology and Oceanography 58, 987-996.

Richey, C., Chovanec, P., Hoeft, S.E., Oremland, R.S., Basu, P. and Stolz, J.F. (2009) Respiratory arsenate reductase as a bidirectional enzyme. Biochemical and Biophysical Research Communications 382, 298-302.

Rickard, D. and Luther, G.W. (1997) Kinetics of pyrite formation by the H2S oxidation of iron(II) monosulfide in aqueous solutions between 25 and 125 degrees C: The mechanism. Geochimica Et Cosmochimica Acta 61, 135-147.

Rochette, E.A., Bostick, B.C., Li, G. and Fendorf, S. (2000) Kinetics of Arsenate Reduction by Dissolved Sulfide. Environmental Science & Technology 34, 4714-4720.

Rosen, B., Bhattacharjee, H. and Shi, W. (1995) Mechanisms of metalloregulation of an anion-translocating ATPase. J Bioenerg Biomembr 27, 85-91.

Rosen, B.P. (2002) Biochemistry of arsenic detoxification. FEBS Letters 529, 86-92.

Rosenberg, H., Gerdes, R.G. and Chegwidden, K. (1977) Two systems for the uptake of phosphate in Escherichia coli. Journal of Bacteriology 131, 505-511.

Rosenfeld, C.E., Sabuda, M.C., Hinkle, M.A.G., James, B.R. and Santelli, C.M. (2020) A Fungal-Mediated Cryptic Selenium Cycle Linked to Manganese Biogeochemistry. Environmental Science & Technology 54, 3570-3580.

Rowe, G.T., Kaegi, M.E.C., Morse, J.W., Boland, G.S. and Escobar Briones, E.G. (2002) Sediment community metabolism associated with continental shelf hypoxia, Northern Gulf of Mexico. Estuaries 25, 1097-1106.

Rowe, G.T., Morse, J., Nunnally, C. and Boland, G.S. (2008) Sediment community oxygen consumption in the deep Gulf of Mexico. Deep Sea Research Part II: Topical Studies in Oceanography 55, 2686-2691.

Sakurai, H., Ogawa, T., Shiga, M. and Inoue, K. (2010) Inorganic sulfur oxidizing system in green sulfur bacteria. Photosynthesis research 104, 163-176.

Saltikov, C.W., Cifuentes, A., Venkateswaran, K. and Newman, D.K. (2003) The ars Detoxification System Is Advantageous but Not Required for As(V) Respiration by the Genetically Tractable Shewanella Species Strain ANA-3. Applied and Environmental Microbiology 69, 2800-2809.

Saltikov, C.W. and Newman, D.K. (2003) Genetic identification of a respiratory arsenate reductase. Proceedings of the National Academy of Sciences 100, 10983-10988.

Saltikov, C.W., Wildman, R.A. and Newman, D.K. (2005) Expression Dynamics of Arsenic Respiration and Detoxification in Shewanella sp. Strain ANA-3. Journal of Bacteriology 187, 7390-7396.

Sampere, T.P., Bianchi, T.S., Allison, M.A. and McKee, B.A. (2011) Burial and degradation of organic carbon in Louisiana shelf/slope sediments. Estuarine, Coastal and Shelf Science 95, 232-244.

Sanders, O.I., Rensing, C., Kuroda, M., Mitra, B. and Rosen, B.P. (1997) Antimonite is accumulated by the glycerol facilitator GlpF in Escherichia coli. Journal of Bacteriology 179, 3365-3367.

Sanford, R.A., Wu, Q., Sung, Y., Thomas, S.H., Amos, B.K., Prince, E.K. and Löffler, F.E. (2007) Hexavalent uranium supports growth of Anaeromyxobacter dehalogenans and Geobacter spp. with lower than predicted biomass yields. Environmental Microbiology 9, 2885-2893.

Santini, J.M., Sly, L.I., Schnagl, R.D. and Macy, J.M. (2000) A New Chemolithoautotrophic Arsenite-Oxidizing Bacterium Isolated from a Gold Mine: Phylogenetic, Physiological, and Preliminary Biochemical Studies. Applied and Environmental Microbiology 66, 92-97.

Saunders, J.K., Fuchsman, C.A., McKay, C. and Rocap, G. (2019) Complete arsenic-based respiratory cycle in the marine microbial communities of pelagic oxygen-deficient zones. Proceedings of the National Academy of Sciences, 201818349.

Schacht, L. and Ginder-Vogel, M. (2018) Arsenite Depletion by Manganese Oxides: A Case Study on the Limitations of Observed First Order Rate Constants. Soil Systems 2, 39.

Schippers, A., Neretin, L.N., Kallmeyer, J., Ferdelman, T.G., Cragg, B.A., Parkes, R.J. and Jørgensen, B.B. (2005) Prokaryotic cells of the deep sub-seafloor biosphere identified as living bacteria. Nature 433, 861-864.

Scott, M.J. (1991) Kinetics of adsorptoin and redox processes on iron and manganese oxides:reactions of As(III) and Se(IV) at Goethite and Birnessite Surfaces, Environmental Quality Laboratory. California Institute of Technology, Pasadena, California.

Scott, M.J. and Morgan, J.J. (1995) Reactions at Oxide Surfaces. 1. Oxidation of As(III) by Synthetic Birnessite. Environmental Science & Technology 29, 1898-1905.

Sekar, R. and DiChristina, T.J. (2017) Degradation of the recalcitrant oil spill components anthracene and pyrene by a microbially driven Fenton reaction. FEMS Microbiology Letters 364.

Sekar, R., Taillefert, M. and DiChristina, T.J. (2016) Simultaneous Transformation of Commingled Trichloroethylene, Tetrachloroethylene, and 1,4-Dioxane by a Microbially Driven Fenton Reaction in Batch Liquid Cultures. Applied and Environmental Microbiology 82, 6335.

Senn, D.B. and Hemond, H.F. (2002) Nitrate Controls on Iron and Arsenic in an Urban Lake. Science 296, 2373-2376.

Sforna, M.C., Philippot, P., Somogyi, A., van Zuilen, M.A., Medjoubi, K., Schoepp-Cothenet, B., Nitschke, W. and Visscher, P.T. (2014) Evidence for arsenic metabolism and cycling by microorganisms 2.7 billion years ago. Nature Geoscience 7, 811-815.

Siebecker, M., Madison, A.S. and Luther, G.W. (2015) Reduction Kinetics of Polymeric (Soluble) Manganese (IV) Oxide (MnO2) by Ferrous Iron (Fe2+). Aquatic Geochemistry 21, 143-158.

Smedley, P.L. and Kinniburgh, D.G. (2002) A review of the source, behaviour and distribution of arsenic in natural waters. Applied Geochemistry 17, 517-568.

Smith, A., Lingas, E. and Rahman, M. (2000a) Contamination of drinking-water by arsenic in Bangladesh: a public health emergency. Bulletin of the World Health Organization 2000, 9.

Smith, A.H., Lingas, E.O. and Rahman, M. (2000b) Contamination of drinking-water by arsenic in Bangladesh: A public health emergency. World Health Organization. Bulletin of the World Health Organization 78, 1093-1103.

Snelgrove, P., Blackburn, T.H., Hutchings, P.A., Alongi, D.M., Grassle, J.F., Hummel, H., King, G., Koike, I., Lambshead, P.J.D., Ramsing, N.B. and Solis-Weiss, V. (1997) The importance of marine sediment biodiversity in ecosystem precesses. Ambio 26, 578-583.

Soetaert, K., Herman, P.M.J. and Middelburg, J.J. (1996) A model of early diagenetic processes from the shelf to abyssal depths. Geochimica et Cosmochimica Acta 60, 1019-1040.

Sørensen, J. and Jeørgensen, B.B. (1987) Early diagenesis in sediments from Danish coastal waters: Microbial activity and Mn-Fe-S geochemistry. Geochimica et Cosmochimica Acta 51, 1583-1590.

Spiro, T.G., Bargar, J.R., Sposito, G. and Tebo, B.M. (2010) Bacteriogenic Manganese Oxides. Accounts of Chemical Research 43, 2-9.

Stolz, J.F., Basu, P., Santini, J.M. and Oremland, R.S. (2006) Arsenic and Selenium in Microbial Metabolism*. Annual Review of Microbiology 60, 107-130.

Stookey, L.L. (1970) Ferrozine- A New Spectrophotometric Reagent for Iron. Analytical Chemistry 42, 779-781.

Strickland, J.D.H. and Parsons, T.R. (1972) A practical handbook of sea-water analysis, 2nd ed.

Stuckey, Jason W., Schaefer, Michael V., Kocar, Benjamin D., Benner, Shawn G. and Fendorf, S. (2016) Arsenic release metabolically limited to permanently water-saturated soil in Mekong Delta. Nature Geoscience 9, 70-76.

Stumm, W. and Morgan, J.J. (1996) Aquatic Chemistry: Chemical Equilibria and Rates in Natural Waters, 3rd ed. John Wiley & Sons, Inc., New York, New York

Sturt, H.F., Summons, R.E., Smith, K., Elvert, M. and Hinrichs, K.U. (2004) Intact polar membrane lipids in prokaryotes and sediments deciphered by high-performance liquid chromatography/electrospray ionization multistage mass spectrometry—new biomarkers for biogeochemistry and microbial ecology. Rapid Communications in Mass Spectrometry 18, 617-628.

Suess, E. (1979) Mineral phases formed in anoxic sediments by microbial decomposition of organic matter. Geochimica et Cosmochimica Acta 43, 339-352.

Sundby, B. and Silverberg, N. (1985) Manganese fluxes in the benthic boundary layer1. Limnology and Oceanography 30, 372-381.

Sundby, B., Silverberg, N. and Chesselet, R. (1981) Pathways of manganese in an open estuarine system. Geochimica et Cosmochimica Acta 45, 293-307.

Sutula, M., Bianchi, T.S. and McKee, B.A. (2004) Effect of seasonal sediment storage in the lower Mississippi River on the flux of reactive particulate phosphorus to the Gulf of Mexico. Limnology and Oceanography 49, 2223-2235.

Swan, B.K., Martinez-Garcia, M., Preston, C.M., Sczyrba, A., Woyke, T., Lamy, D., Reinthaler, T., Poulton, N.J., Masland, E.D.P. and Gomez, M.L. (2011) Potential for chemolithoautotrophy among ubiquitous bacteria lineages in the dark ocean. Science 333, 1296-1300.

Taillefert, M., Beckler, J.S., Cathalot, C., Michalopoulos, P., Corvaisier, R., Kiriazis, N., Caprais, J.-C., Pastor, L. and Rabouille, C. (2017) Early diagenesis in the sediments of the Congo deep-sea fan dominated by massive terrigenous deposits: Part II – Iron–sulfur coupling. Deep Sea Research Part II: Topical Studies in Oceanography 142, 151-166.

Taillefert, M., Bono, A.B. and Luther, G.W. (2000a) Reactivity of Freshly Formed Fe(III) in Synthetic Solutions and (Pore)Waters: Voltammetric Evidence of an Aging Process. Environmental Science & Technology 34, 2169-2177.

Taillefert, M., Hover, V.C., Rozan, T.F., Theberge, S.M. and Luther, G.W. (2002) The influence of sulfides on soluble organic-Fe(III) in anoxic sediment porewaters. Estuaries 25, 1088-1096.

Taillefert, M., Luther, G.W. and Nuzzio, D.B. (2000b) The Application of Electrochemical Tools for In Situ Measurements in Aquatic Systems. Electroanalysis 12, 401-412.

Tebo, B.M., Bargar, J.R., Clement, B.G., Dick, G.J., Murray, K.J., Parker, D., Verity, R. and Webb, S.M. (2004) BIOGENIC MANGANESE OXIDES: Properties and Mechanisms of Formation. Annual Review of Earth and Planetary Sciences 32, 287-328.

Tercier-Waeber, M.-L. and Taillefert, M. (2008) Remote in situ voltammetric techniques to characterize the biogeochemical cycling of trace metals in aquatic systems. Journal of Environmental Monitoring 10, 30-54.

Teske, A. and Sørensen, K.B. (2008) Uncultured archaea in deep marine subsurface sediments: have we caught them all? The ISME journal 2, 3-18.

Tessier, A., Campbell, P.G.C. and Bisson, M. (1979) Sequential extraction procedure for the speciation of particulate trace metals. Analytical Chemistry 51, 844-851.

Thamdrup, B., Rosselló-Mora, R. and Amann, R. (2000) Microbial manganese and sulfate reduction in Black Sea shelf sediments. Applied and environmental microbiology 66, 2888-2897.

Thanabalasingam, P. and Pickering, W. (1986a) Effect of ppH on Interaction Between As(III) or As(V) and Manganese(IV) oxide. Water Air Soil Pollut 29, 205-216.

Thanabalasingam, P. and Pickering, W.F. (1986b) Arsenic sorption by humic acids. Environmental Pollution Series B, Chemical and Physical 12, 233-246.

Theberge, S.M. and Luther, G.W. (1997) Determination of the Electrochemical Properties of a Soluble Aqueous FeS Species Present in Sulfidic Solutions. Aquatic Geochemistry 3, 191-211.

Tournassat, C., Charlet, L., Bosbach, D. and Manceau, A. (2002) Arsenic(III) Oxidation by Birnessite and Precipitation of Manganese(II) Arsenate. Environmental Science & Technology 36, 493-500.

Trefry, J.H. and Presley, B.J. (1982) Manganese fluxes from Mississippi Delta sediments. Geochimica et Cosmochimica Acta 46, 1715-1726.

Trouwborst, R.E., Clement, B.G., Tebo, B.M., Glazer, B.T. and Luther, G.W. (2006) Soluble Mn(III) in Suboxic Zones. Science 313, 1955-1957.

Troyer, L.D., Tang, Y. and Borch, T. (2014) Simultaneous Reduction of Arsenic(V) and Uranium(VI) by Mackinawite: Role of Uranyl Arsenate Precipitate Formation. Environmental Science & Technology 48, 14326-14334.

Tufano, K.J. and Fendorf, S. (2008) Confounding Impacts of Iron Reduction on Arsenic Retention. Environmental Science & Technology 42, 4777-4783.

Tufano, K.J., Reyes, C., Saltikov, C.W. and Fendorf, S. (2008) Reductive Processes Controlling Arsenic Retention: Revealing the Relative Importance of Iron and Arsenic Reduction. Environmental Science & Technology 42, 8283-8289.

Turekian, K.K. and Wedepohl, K.H. (1961) Distribution of the Elements in Some Major Units of the Earth's Crust. Geological Society of America Bulletin 72, 175-192.

Turner, R.E., Rabalais, N.N., Alexander, R.B., McIsaac, G. and Howarth, R.W. (2007) Characterization of nutrient, organic carbon, and sediment loads and concentrations from the Mississippi River into the northern Gulf of Mexico. Estuaries and Coasts 30, 773-790.

van de Vossenberg, J., Woebken, D., Maalcke, W.J., Wessels, H.J., Dutilh, B.E., Kartal, B., Janssen-Megens, E.M., Roeselers, G., Yan, J. and Speth, D. (2013) The metagenome of the marine anammox bacterium ‘Candidatus Scalindua profunda’illustrates the versatility of this globally important nitrogen cycle bacterium. Environmental microbiology 15, 1275-1289.

van der Zee, C., van Raaphorst, W. and Epping, E. (2001) Absorbed Mn2+ and Mn redox cycling in Iberian continental margin sediments (northeast Atlantic Ocean). Journal of Marine Research 59, 133-166.

van Kessel, M.A., Speth, D.R., Albertsen, M., Nielsen, P.H., den Camp, H.J.O., Kartal, B., Jetten, M.S. and Lücker, S. (2015) Complete nitrification by a single microorganism. Nature 528, 555-559.

van Niftrik, L. and Jetten, M.S. (2012) Anaerobic ammonium-oxidizing bacteria: unique microorganisms with exceptional properties. Microbiol. Mol. Biol. Rev. 76, 585-596.

vanden Hoven, R.N. and Santini, J.M. (2004) Arsenite oxidation by the heterotroph Hydrogenophaga sp. str. NT-14: the arsenite oxidase and its physiological electron acceptor. Biochimica et Biophysica Acta (BBA) - Bioenergetics 1656, 148-155.

vanLoon, G.W. and Duffy, S.J. (2011) Distribution of species in aquatic systems, Environmental Chemistry A Global Perspective, 3rd ed. Oxford University Press, New York, pp. 228-230.

Villalobos, M., Escobar-Quiroz, I.N. and Salazar-Camacho, C. (2013) The influence of particle size and structure on the sorption and oxidation behavior of birnessite: I. Adsorption of As(V) and oxidation of As(III). Geochimica et Cosmochimica Acta 125, 564-581.

Villalobos, M., Escobar-Quiroz, I.N. and Salazar-Camacho, C. (2014) The influence of particle size and structure on the sorption and oxidation behavior of birnessite: I. Adsorption of As(V) and oxidation of As(III). Geochimica et Cosmochimica Acta 125, 564-581.

Villalobos, M., Lanson, B., Manceau, A., Toner, B. and Sposito, G. (2006) Structural model for the biogenic Mn oxide produced by Pseudomonas putida. American Mineralogist 91, 489-502.

Villalobos, M., Toner, B., Bargar, J. and Sposito, G. (2003) Characterization of the manganese oxide produced by pseudomonas putida strain MnB1. Geochimica et Cosmochimica Acta 67, 2649-2662.

Viollier, E., Inglett, P.W., Hunter, K., Roychoudhury, A.N. and Van Cappellen, P. (2000) The ferrozine method revisited: Fe(II)/Fe(III) determination in natural waters. Applied Geochemistry 15, 785-790.

Wade, R., Jr. and DiChristina, T.J. (2000) Isolation of U(VI) reduction-deficient mutants of Shewanella putrefaciens. FEMS Microbiology Letters 184, 143-148.

Wade, T.L., Soliman, Y., Sweet, S.T., Wolff, G.A. and Presley, B.J. (2008) Trace elements and polycyclic aromatic hydrocarbons (PAHs) concentrations in deep Gulf of Mexico sediments. Deep Sea Research Part II: Topical Studies in Oceanography 55, 2585-2593.

Wang, J., Wu, M., Lu, G. and Si, Y. (2016) Biotransformation and biomethylation of arsenic by Shewanella oneidensis MR-1. Chemosphere 145, 329-335.

Wang, Y. and Van Cappellen, P. (1996) A multicomponent reactive transport model of early diagenesis: Application to redox cycling in coastal marine sediments. Geochimica et Cosmochimica Acta 60, 2993-3014.

Ward, L.M., Johnston, D. and Shih, P.M. (2019) Phanerozoic Radiation of Ammonia Oxidizing Bacteria. bioRxiv, 655399.

Ward, N.L., Challacombe, J.F., Janssen, P.H., Henrissat, B., Coutinho, P.M., Wu, M., Xie, G., Haft, D.H., Sait, M. and Badger, J. (2009) Three genomes from the phylum Acidobacteria provide insight into the lifestyles of these microorganisms in soils. Appl. Environ. Microbiol. 75, 2046-2056.

Wasmund, K., Schreiber, L., Lloyd, K.G., Petersen, D.G., Schramm, A., Stepanauskas, R., Jørgensen, B.B. and Adrian, L. (2014) Genome sequencing of a single cell of the

widely distributed marine subsurface Dehalococcoidia, phylum Chloroflexi. The ISME journal 8, 383-397.

Watanabe, J.i., Tani, Y., Chang, J., Miyata, N., Naitou, H. and Seyama, H. (2013) As(III) oxidation kinetics of biogenic manganese oxides formed by Acremonium strictum strain KR21-2. Chemical Geology 347, 227-232.

Waterson, E.J. and Canuel, E.A. (2008) Sources of sedimentary organic matter in the Mississippi River and adjacent Gulf of Mexico as revealed by lipid biomarker and δ13CTOC analyses. Organic Geochemistry 39, 422-439.

Webb, S.M., Dick, G.J., Bargar, J.R. and Tebo, B.M. (2005) Evidence for the presence of Mn(III) intermediates in the bacterial oxidation of Mn(II). Proceedings of the National Academy of Sciences of the United States of America 102, 5558-5563.

Wei, C.-L., Rowe, G.T., Escobar-Briones, E., Boetius, A., Soltwedel, T., Caley, M.J., Soliman, Y., Huettmann, F., Qu, F. and Yu, Z. (2010) Global patterns and predictions of seafloor biomass using random forests. PloS one 5.

Welch, A.H., Westjohn, D.B., Helsel, D.R. and Wanty, R.B. (2000) Arsenic in Ground Water of the United States: Occurrence and Geochemistry. Groundwater 38, 589-604.

White, A.K. and Metcalf, W.W. (2007) Microbial Metabolism of Reduced Phosphorus Compounds. Annual Review of Microbiology 61, 379-400.

Whitman, W.B., Coleman, D.C. and Wiebe, W.J. (1998) Prokaryotes: the unseen majority. Proceedings of the National Academy of Sciences 95, 6578-6583.

Wielinga, B., Mizuba, M.M., Hansel, C.M. and Fendorf, S. (2000) Iron Promoted Reduction of Chromate by Dissimilatory Iron-Reducing Bacteria. Environmental Science & Technology 35, 522-527.

Wilkin, R.T., Wallschlager, D. and Ford, R.G. (2003) Speciation of arsenic in sulfidic waters. Geochemical Transactions 4, 1-7.

Willsky, G.R. and Malamy, M.H. (1980a) Characterization of two genetically separable inorganic phosphate transport systems in Escherichia coli. Journal of Bacteriology 144, 356-365.

Willsky, G.R. and Malamy, M.H. (1980b) Effect of arsenate on inorganic phosphate transport in Escherichia coli. Journal of Bacteriology 144, 366-374.

Wu, Y., Kukkadapu, R.K., Livi, K.J.T., Xu, W., Li, W. and Sparks, D.L. (2018) Iron and Arsenic Speciation During As(III) Oxidation by Manganese Oxides in the Presence of Fe(II): Molecular-Level Characterization Using XAFS, Mössbauer, and TEM Analysis. ACS Earth and Space Chemistry 2, 256-268.

Wysocki, R., Chéry, C.C., Wawrzycka, D., Van Hulle, M., Cornelis, R., Thevelein, J.M. and Tamás, M.J. (2001) The glycerol channel Fps1p mediates the uptake of arsenite and antimonite in Saccharomyces cerevisiae. Molecular Microbiology 40, 1391-1401.

Xu, A.O.X.-W. (2014) 11 The Family Hyphomicrobiaceae.

Xu, K., Corbett, D.R., Walsh, J.P., Young, D., Briggs, K.B., Cartwright, G.M., Friedrichs, C.T., Harris, C.K., Mickey, R.C. and Mitra, S. (2014) Seabed erodibility variations on the Louisiana continental shelf before and after the 2011 Mississippi River flood. Estuarine, Coastal and Shelf Science 149, 283-293.

Yao, W. and Millero, F.J. (1993) The rate of sulfide oxidation by δMnO2 in seawater. Geochimica et Cosmochimica Acta 57, 3359-3365.

Yao, W. and Millero, F.J. (1996a) Adsorption of Phosphate on Manganese Dioxide in Seawater. Environmental Science & Technology 30, 536-541.

Yao, W. and Millero, F.J. (1996b) Oxidation of hydrogen sulfide by hydrous Fe(III) oxides in seawater. Marine Chemistry 52, 1-16.

Yeager, K.M., Santschi, P.H. and Rowe, G.T. (2004) Sediment accumulation and radionuclide inventories (239,240Pu, 210Pb and 234Th) in the northern Gulf of Mexico, as influenced by organic matter and macrofaunal density. Marine Chemistry 91, 1-14.

Ying, S.C., Kocar, B.D. and Fendorf, S. (2012) Oxidation and competitive retention of arsenic between iron- and manganese oxides. Geochimica et Cosmochimica Acta 96, 294-303.

Yoshinaga, M. and Rosen, B.P. (2014) A C·As lyase for degradation of environmental organoarsenical herbicides and animal husbandry growth promoters. Proceedings of the National Academy of Sciences 111, 7701-7706.

Zhou, Z., Pan, J., Wang, F., Gu, J.-D. and Li, M. (2018) Bathyarchaeota: globally distributed metabolic generalists in anoxic environments. FEMS Microbiology Reviews 42, 639-655.

Zhu, M., Paul, K.W., Kubicki, J.D. and Sparks, D.L. (2009) Quantum Chemical Study of Arsenic (III, V) Adsorption on Mn-Oxides: Implications for Arsenic(III) Oxidation. Environmental Science & Technology 43, 6655-6661.

Zhu, Y.-G., Xue, X.-M., Kappler, A., Rosen, B.P. and Meharg, A.A. (2017) Linking Genes to Microbial Biogeochemical Cycling: Lessons from Arsenic. Environmental Science & Technology 51, 7326-7339.

Zhu, Y. and Elzinga, E.J. (2015) Macroscopic and Spectroscopic Assessment of the Cosorption of Fe(II) with As(III) and As(V) on Al-Oxide. Environmental Science & Technology 49, 13369-13377.

Zhuang, G.-C., Montgomery, A. and Joye, S.B. (2019) Heterotrophic metabolism of C1 and C2 low molecular weight compounds in northern Gulf of Mexico sediments: Controlling factors and implications for organic carbon degradation. Geochimica et Cosmochimica Acta 247, 243-260.

Zinger, L., Amaral-Zettler, L.A., Fuhrman, J.A., Horner-Devine, M.C., Huse, S.M., Welch, D.B.M., Martiny, J.B., Sogin, M., Boetius, A. and Ramette, A. (2011) Global patterns of bacterial beta-diversity in seafloor and seawater ecosystems. PloS one 6.